This is to certify that the
dissertation entitled

PROCESSING AND CHARACATERIZATION OF PHASE BOUNDARIES IN CERAMIC AND METALLIC MATERIALS

presented by

Liang Zeng

has been accepted towards fulfillment
of the requirements for the

Ph.D. degree in Materials Science & Engineering

Major Professor's Signature

June 6, 2003

Date

PROCESSING AND CHARACTERIZATION OF PHASE BOUNDARIES IN CERAMIC AND METALLIC MATERIALS

By

Liang Zeng

A DISSERTATION

Submitted to

Michigan State University

in partial fulfillment of the requirements

for the degree of

DOCTOR OF PHILOSOPHY

Department of Chemical Engineering and Materials Science

2003

ABSTRACT

Processing and Characterization of Phase boundaries in Ceramic and Metallic Materials

By

Liang Zeng

The goal of this dissertation work was to explore and describe advanced characterization of novel materials processing. These characterizations were carried out using scanning and transmission electron microscopy (SEM and TEM), and X-ray diffraction techniques. The materials studied included ceramics and metallic materials.

The first part of this dissertation focuses on the processing, and the resulting interfacial microstructure of ceramics joined using spin-on interlayers. SEM, TEM, and indentation tests were used to investigate the interfacial microstructural and mechanical property evolution of polycrystalline zirconia bonded to glass ceramic MaCor™, and polycrystalline alumina to single crystal alumina. Interlayer assisted specimens were joined using a thin amorphous silica interlayer. This interlayer was produced by spin coating an organic based silica bond material precursor and curing at 200°C, followed by joining in a microwave cavity or conventional electric furnace. Experimental results indicate that in the joining of the zirconia and MaCor™ no significant interfacial microstructural and mechanical property differences developed between materials joined either with or without interlayers, due to the glassy nature of MaCor™. The bond interface was non-planar, as a result of the strong wetting of MaCor™ and silica and dissolution of the zirconia. However, without the aid of a silica interlayer, sapphire and 98% polycrystalline alumina failed to join under the experimental conditions under this study. A variety of interfacial morphologies have been

observed, including amorphous regions, fine crystalline alumina, and intimate contact between the sapphire and polycrystalline alumina. In addition, the evolution of the joining process from the initial sputter-cure to the final joining state and joining mechanisms were characterized.

The second part of this dissertation focused on the effects of working and heat treatment on microstructure, texture, phase boundary movement, and mechanical property evolution in Ti-6Al-4V wire. The as-received wire consisted of equilibrium α and metastable β phases and had a moderately strong fiber texture with prism plane normals aligned with the wire axis. The wire was worked by extrusion, solution heat-treatment and water quenching, and aging. The extrusion process strengthened the as-received texture. After solutionization and quenching, microstructural observations showed the presence of many needlelike martensitic platelets in the prior β phase regions. Texture analysis revealed that a secondary fiber with basal plane normals aligned with the wire axis emerged at the expense of the initial texture, indicating that highly preferred phase boundary motion (variant selection) occurred during the $\beta \rightarrow \alpha$ transformation. The strength of the variant selection consistently increased with solutionization temperature and time. In addition, the effects of dislocation type and density on variant selections were further investigated. This implies that strategic prior deformation and heat treatment can be exploited to design the resulting texture and microstructure and consequently optimize the properties of titanium products.

To my wife and my parents!

ACKNOWLEDGMENTS

I would like to thank my advisers, Professor Martin A. Crimp and Professor Thomas R. Bieler for providing me the opportunity to perform this research and to continue my graduate studies. Their continuous guidance, advice, and support were invaluable to the completion of this work. Without their support and patience, this work would not have been possible.

My thanks are extended to my guidance committee members Dr. Case, and Dr. Velbel for being my committee members. In particular, special thanks should go to Professor Case for his instruction, guidance and encouragement to complete this research.

The achievements of this work are also based on the help from the senior colleagues in our research group. I would like to appreciate the help of Hong Geng, John Heckman, Benjamin Simkin, Adwait Telang, and Jong-Gi Lee.

Many thanks go to Mr. Kenneth Singleton for the precious time he committed to proofreading of my dissertation.

I gratefully thank parents who gave me their endless love, care and support. Finally, I wish to thank my wife, Yanmei Li for her love and understanding. Especially, without my wife's patience and encouragement, I could not have completed this work.

Finally, I sincerely appreciate the support provided by the Composite Materials and Structures Center at Michigan State University and Fairchild Fasteners, City of Industry, CA, and Teaching assistant support from the Department which supplemented my research studies.

TABLE OF CONTENTS

LIST OF TABLES

PART I:
INTERFACIAL MICROSTRUCTURE OF CERAMICS JOINED USING SPIN-ON INTERLAYERS

PART II
EFFECTS OF WORKING AND HEAT TREATMENT ON MICROSTRUCTURAL AND CRYSTALLOGRAPHIC TEXTURE EVOLUTION IN TI-6AL-4V

LIST OF FIGURES

PART I:
INTERFACIAL MICROSTRUCTURE OF CERAMICS JOINED USING SPIN-ON INTERLAYERS

PART II
EFFECTS OF WORKING AND HEAT TREATMENT ON MICROSTRUCTURAL AND CRYSTALLOGRAPHIC TEXTURE EVOLUTION IN TI-6AL-4V

Figure 5.2 reveals the overall relationships between major texture intensities and the experiment processing conditions after solutionization for 40 minutes at 920°C. Different deformation, followed by the same heat treatment resulted in different texture development. (p. 257)

Figure 5.3 showing (a) the $(10\bar{1}0)_\alpha$, $(0002)_\alpha$, and $(110)_\beta$ pole figures of as–received wire with wire axis out of the page, and the (b) schematic α crystal orientations. The α phase consisted of one fiber texture with $(0002)_\alpha$ plane normal along radial directions. The β phase consisted of a fiber texture with the axisymmetric $(110)_\beta$ crystal orientations about the wire axis, and a few of rotated or tilted $(110)_\beta$ fiber texture aligned approximately 30° from the wire axis. (p. 258)

Figure 5.4 showing the $(10\bar{1}0)_\alpha$, $(0002)_\alpha$, and $(110)_\beta$ pole figures with wire axis out of the page of heat-treated specimens (a) L heat and (b) T heat after solutionization for 40 minutes at 920°C, followed by quenching in sealed quartz tube, and (c) the schematic α crystal orientations for both cases. Note, the crystal orientation of $(0001)_\alpha$ and $(110)_\beta$ plane normal along wire axis of T heat (deformed along transverse direction and heat treated) is 13.42 and 9.21 X random, respectively, which is 5.3 and 1.7 times higher than the corresponding textures of specimens L heat deformed along longitude direction and heat treated under the exact same conditions. (p. 260)

Figure 5.5 showing dislocations mutations based on the geometric and Burgers relationship between α and β phases. Compression along the wire axis is roughly out of the page. Compression in radial directions imposes compressive stresses in directions roughly in the plane of the page. Neither would activate much prism slip on $(10\bar{1}0)_\alpha$ planes. The prism $\vec{a}$ dislocations transform into $[1\bar{1}1](1\bar{1}2)_\beta$ dislocations, but they cannot mutate onto $(110)_\beta$ planes after $\alpha\rightarrow\beta$ transformation. However, either basal or prismatic $\vec{a}$ screw dislocations could cross slip onto the two inclined $(101)_\beta$, $(\bar{1}01)_\beta$ planes after $\alpha\rightarrow\beta$ transformation. The $\vec{c}+\vec{a}$ dislocations could be directly transferred onto β phase $(101)_\beta$, $(\bar{1}01)_\beta$ planes, but would have a large irrational Burgers vector. (p. 261)

Figure 5.6 shows the spatial construction of <100>, <110>, and <111> directions and {100}, {110}, and {112} planes in bcc metal, and (b) planer representation for projections of the ABCDX pyramids [After Zhi 1992]. In the ABCDX pyramids, sides of hexahedron represents {100} planes, sides of the dashed line pyramids represents {110} planes, and sides of the solids line pyramids represents {112} planes. (p. 262)

Chapter I

Introduction

In recent years there has been rapid progress toward the development of new and reliable ceramic joining techniques. Significant research in this area is being done on ceramic joining because of the commercial importance of joining ceramics. Reliable ceramic joining techniques would allow components to be joined from simpler parts that have been pre-tested for flaws, thus maintaining high mechanical properties and dimensional control, and lowering overall cost. The mechanical properties of joined ceramics depend on the composition and structure of the interface, the joining technology used, and reaction products that may be produced. Therefore, it is critical to have a fundamental understanding of ceramic interfaces and interfacial reactions to further the development of reliable ceramic joining methods. The first part of this project is an attempt to investigate the interfacial microstructure of ceramics joined using spin-on interlayers, which has significant advantages over other joining approaches. Analysis was carried out using optical, and scanning and transmission electron microscopy. The mechanical properties of the interface were characterized using Vickers indentation techniques to access the thermal residual stresses and interfacial strength. These techniques were used to further characterize the relation between interfacial microstructure and process variables such as time, temperature, and mechanical properties of the interfaces.

1.1 Ceramics and Ceramic Processing

Ceramics range from silicates and oxides such as zirconia, titania and alumina, to nonoxides such as nitrides, carbides, and borides of the transition elements. Ceramics are attractive for numerous reasons because of their properties. They may be electrical insulators, semiconductors, conductors, superconductors, heat conductors, or thermal insulators. Ceramics have large potential for high temperature applications such as heat engines or heat exchangers because they remain rigid at temperatures intolerable by metals and superalloys [Santellal 1997, Schwartz 1990, Moorhead 1990, Woods 1985].

In industry, most ceramic fabrication processes begin with fine powders. Pressing and slip casting are two major techniques used to form component shapes from ceramic powders [Richerson 1992]. Pressing is performed by placing the powders into a die and applying pressure to obtain a green compact. The main limitation to this approach is that the possible green compact shapes, such as rings or cylinders, are relatively simple [Richerson 1992]. Slip casting is performed by pouring particles that are suspended in water into a porous mold, followed by drying and sintering. Although slip casting offers more dimensional flexibility, it results in a relatively weak ceramic compact [Richerson 1992]. In particular, the introduction of precise channels or holes within the slip cast parts is problematic. Machining of ceramics is slow and expensive, making it impractical to machine ceramic parts with complicated shapes from a ceramic billet.

One alternative approach to fabricate ceramics of complex geometry is to join simpler subcomponents of densified ceramics to form the final component. This approach has motivated a sustained level of research and development in ceramic joining

over the past decades. There are at least three reasons for joining ceramics: (1) to assemble complex, multicomponent structures from simpler components of the same materials, (2) to join dissimilar materials so as to produce a functional gradient in material properties, and (3) to aid quality control by allowing defective sub-components to be identified and removed early in manufacturing process [Johnson 1985, Hauth 1989, Zdaniewski 1987, Shalz 1983]. Although improvement has been achieved in the fabrication of ceramic materials that are reliably strong and tough, the successful utilization of ceramics in many applications will depend on the ability to assemble or join simple components into structures that will function effectively [Shalz 1993, Locatelli 1997].

1.2 Joining ceramics

In recent years there has been rapid progress toward the development of new and reliable ceramic joining techniques. This work falls into a number of broad areas that include: (1) fundamental studies of interfaces, (2) joining without the use of interlayers, (3) joining using unconventional heating methods, such as microwave heating, (4) diffusion bonding [Urena 1992, Cross 1993, Yano 1998], (5) brazing [Sandhage 1996, Weldon, 1997], (6) the use of transient metal layers for joining [Shalz 1993, Gale 1999], and (7) joining with spin-on interlayers [Seiber 1997, Lee 1997, Case, 1997, 1998]. This list is not exhaustive and there are other ways to classify ceramic joining. However, the objective of this chapter is to review ceramic joining and focus on the recent literature and important findings related to the present research.

1.2.1 Joining without the use of interlayers

For direct ceramic-ceramic joining without the use of interlayer, adhesion and bonding generally takes place through an intergranular amorphous phase present in the base materials migrating to the joint [Binner 1998]; such intergranular phases can become viscous at elevated temperatures. The driving force for this adhesion comes from the tendency of the system to restore the equilibrium when a higher energy interface is introduced [Esposito 1998]. The interface between two polished ceramic parts put in contact can be viewed as a macroscopic inhomogeneity since no intergranular amorphous phase is present on the surface of the grains at the interface. Adhesion is therefore driven by the mass transport mechanisms that try to restore the equilibrium and minimize the macroscopic inhomogeneity between interfacial region and base ceramics. The possible mechanisms for bonding include liquid phase flow, grain boundary sliding and grain rotation, grain solution and precipitation, grain bridging and grain growth [Nakamura 1997]. The principle step of direct ceramic-ceramic joining processes without the use of interlayers is shown schematically in figure 1.1.

The presence of an intergranular phase appears to have two consequences: (1) it provides an adhesive medium to hold the two joining pieces together under proper temperature and pressure since the adhesion and chemical compatibility between intergranular glassy phases and base ceramics is generally good, (2) it can allow the grains near or at the interface in base materials to rotate and rearrange themselves at high temperatures, which can lead to the strengthening of the joint [Walls 1992, Binner 1998]. This grain rearrangement is strongly dependent on the softening temperature of the glassy phases, which in turn largely depends on the level of impurities, joining temperature and pressure, and sintering aids already present in the ceramics. For a number of ceramics,

impurities and sintering aids are added to enhance the sintering densification rate. The presence of these impurities and sintering aids can lead to significant intergranular amorphous phases, which in turn degrade the high temperature properties of the ceramics. Also, the need for additional fixtures to apply external loads to initiate grain rotation across the joint and cause bulk deformation [Binner 1998] complicates the furnace system and may be problematic in applying a large load to multiple parts simultaneously.

1.2.1.1 Diffusion Bonding

Diffusion bonding joins materials at high temperatures (from 0.6Tm to 0.8Tm, where T_m is the melting point of the material) and pressures. Ideally, diffusion bonding produces local deformation and/or melting at the joint, promoting surface contact, and subsequently allowing atomic or ionic migration across the joined interface to produce a bond (Figure 1.2) [Santellal 1992, Sandhage 1996]. However, advanced structural ceramics like alumina, silicon carbide, and zirconia do not deform easily except at very high temperatures. In addition, they are difficult to densify due to the low diffusivities of the chemical species of the base ceramics [Bates 1990]. Therefore, diffusion bonding can be difficult and impractical, especially without interlayers [Santellal 1992]. For example, Elssner et al. [1981] found that 18 μm coarse-grained alumina components could not be bonded to each other via heating at 1700°C and 9.0 MPa applied pressure, due to the high creep resistance of the alumina. However, under identical joining temperature and applied stress conditions, diffusion bonding of an 18 μm coarse-grained alumina to a 1 μm fine-grained alumina was achieved because the fine-grained alumina creeps enough to facilitate the joining. Consequently, diffusion bonding has to occur within the range of

stresses and temperatures that induce creep in materials, leading to dimensional changes and instability [Bates 1990, Elssner 1981].

1.2.2 Joining with interlayers

1.2.2.1 Brazing

Brazing with glasses, glass ceramics, or metals has been utilized by various researchers for ceramic-ceramic joining. For example, SiC can be brazed using a calcia-alumina glass ceramic [Ferraris 1998], a SiO_2-CaO-Al_2O_3 glass [Ahn 1998], an Ag-Cu-Ti alloy [Boadi 1997], and zirconia by CaO-MgO-SiO_2-Al_2O_3 glass [Ashizuka 1996].

There are two main advantages of glass brazing for ceramic joining [1]: (1) the adhesion and chemical compatibility between glass and base ceramics is good, (2) the physical properties of glass such as viscosity and melting characteristics can be controlled over wide ranges. However, glass bonds for high temperature applications are limited by the relatively low glass transformation point, low fracture toughness, and susceptibility to stress corrosion [Zdaniewski 1987, Sandhage 1996]. To increase the glass interlayer fracture toughness and stress corrosion resistance, Zdaniewski et al. [1987, 1975] used glass adhesives that can be crystallized under controlled joining conditions. Formation of interlocking grains or needles across the joint is expected to result in joint toughening, called crystallization toughening [Zdaniewski 1987, 1975]. However, the major difficulty encountered in crystallization toughening of ceramic adhesives is the persistent porosity in the joints, probably due to the evolution of gases absorbed in the ceramic [Zdaniewski 1987, 1975].

Metal brazing generally relies on selective oxidation to achieve bonding between the metal and base ceramics [Sandhage 1996]. However, the selection of available active

braze alloys is limited [Santella 1992]. Many common metal braze alloys are either ductile, such as aluminum [Suganuma 1987] and nickel [Vegter 1998], or contain indium or tin to allow melting at relatively low temperatures, such as Ag-Cu based alloys [Boadi 1997]. However, metal brazing often results in complicated interfacial reaction phases and thick bond layers, with dimensions several microns thick or more [Locatelli 1997, Ferraris 1998] that can result in large thermal residual stress at the joint. This stress is caused by thermal expansion differences between brazing metal and base ceramic that sometimes results in cracks or failure [Kovalev, Colombo 1998, Singh 1999]. As an example of the complicated reaction phases generated due to metal brazing, Zurbuchen et al. [1999] identified a series of complicated reaction layers and interfacial phases between the parent ceramics, an alumina-silicon carbide whisker (Al_2O_3-SiC_w) composite, and the brazing alloy, Ag-Cu-Ti, using TEM and EPMA (Figure 1.3). The local interfacial phase distribution sequence from the SiC is SiC/TiC/Ti_5Si_3/Ti_3(Cu,Al,Si)$_3$O/Ag-Cu. The local interfacial phase distribution sequence at the Al_2O_3 side is Al_2O_3/γ-TiO/Ti_3 (Cu,Al,Si)$_3$O/Ag-Cu [Zurbuchen 1999]. Figure 1.3 shows the phase development for Al_2O_3-SiC composite brazed by Ag-Cu-Ti alloy.

1.2.2.2 Transient liquid phase bonding

In metal systems, the use of a transient liquid phase (TLP) for bonding superalloys using alloys or layers of alloys is well known [Duvall 1974]. TLP has the ability to produce a bond at a lower temperature than that at which it will be ultimately used. The technology is currently being adapted to ceramic-ceramic joining, either using thin glass layers such as oxynitrides for joining SiAlON [Walls 1992] or alloy layers such as Cu/Pt/Cu and Cu/Ni/Cu for joining alumina [Shalz 1993]. In theory, it should be possible

to disperse the interlayer over time [Gale 1999]. This transient liquid phase will eventually disappear and result in a microstructurally homogeneous joint that is similar to the parent ceramics [Gale 1999]. However, in practice this has rarely been demonstrated, and would take very long times [Gale 1999], probably even days or weeks especially for bond layers several microns or more thick. In addition, the metal alloys or glassy layers that have the desired phase behavior, wetting behavior, and physical properties for joining are limited [Loehman 1999]. For example, Loehman [1981] investigated the joining of Si_3N_4 using oxynitride glasses whose compositions match the intergranular amorphous phases of the base Si_3N_4. During the joining, the oxynitride glassy interlayer must redistribute itself and penetrate into the adjoining base Si_3N_4 ceramics [Loehman 1981, Shalz 1993]. Thus, this joining approach requires the development of different interlayers to join different materials.

A few researchers have investigated interfacial microstructural evolutions of the TLP bonded ceramics using transmission electron microscopy (TEM) and other analytical techniques [Walls 1992, Hanson 1998]. In β-SiAlON/β-SiAlON ceramics joined using β-SiAlON glass-forming composite adhesives (mixture of Si_3N_4, Y_2O_3, Al_2O_3, SiO_2 powders), the microstructure of the joint consisted of a primary joint zone and a secondary joint zone on both sides of the primary joint zone (Figure 1.4) [Walls 1992, Hanson 1998]. At the joining temperature of 1400°C and above and 2.0 MPa pressure, the oxide components react to form a Y-Si-Al-O liquid phase, leading to densification and sintering of the interlayer. The Si_3N_4 then dissolves into the liquid, altering the composition to β-SiAlON. At the same time, the newly formed β-SiAlON grains grow and form an interlocking network across the joint. TEM analysis showed

that the joint thickness was approximately 1~2 μm, with an indistinct interface between the base β-SiAlON and the newly formed β-SiAlON materials. The secondary joint zone, determined by elemental analysis of the concentration across the joint into the surrounding base material using electron micro-probe analysis (EPMA), had a thickness of around 250 μm from the primary joint zone. The authors suggested that a gradual change of the ceramic composition within the secondary joint zone is an ideal way of relieving residual stresses at the joint that is introduced during the joining [Walls 1992, Hanson 1998].

1.2.2.3 Joining with spin-on interlayers

Joining with spin-on interlayers, which uses high rpm spinning to produce very thin (typically around 200 nm thick) interlayers, has been developed at Michigan State University (MSU) [Case 1997, 1998]. The spin-on coating typically consists of an organic based ceramic precursor such as Silicafilm™, Blackglas™, or sodium silicate, deposited as a liquid onto the surface of the ceramics to be joined. The ceramics to be joined are spun on a substrate spinner and pyrolyzed at low temperature to form a ceramic layer. The thickness of the ceramic precursor can be controlled by adjusting the spin rate, with films approximately 200~300 nm thick are produced at a spin rate of 3000 rpm for 20 seconds. This joining approach, which has many advantages over other joining methods, produces joined interfaces with interlocking microstructures that have little or no observable bond layer(s) or second phases [Zeng 2001] and have relatively high interfacial strength. Other characteristics of joining with spin-on interlayers can be listed as [Case 1997, 1998]:

1. This ceramic joining technique uses either zero loading or a minimal (20~85 gram) external loading that leads to zero or minimum dimensional changes and eliminates the need for a fixture to apply large external loads to the specimens and during joining.
2. It can accommodate complex exterior geometries and internal channels or holes. The spin-on interlayers can be applied to only one of the surfaces to be joined. Therefore, holes or channels can remain at precise dimensions, which would be impossible for brazing or transient liquid phase bonding since interlayers would melt, flow and obliterate the holes or channels.
3. Both conventional and microwave heating can be used to join the spin-on interlayer ceramics.
4. However, spin-on interlayer joining requires that the surfaces be flat and polished and may require the development of the different spin-on interlayers to join different materials.

To date, a variety of ceramics have been successfully joined by the spin-on interlayer techniques, including similar and dissimilar materials such as alumina/alumina, MaCor™/MaCor™, SiC/SiC, alumina/zirconia, and zirconia/MaCor™ [Lee 1997, Case 1998]. Indentation tests showed that these bonds have relatively high interfacial toughness with Vickers indentation induced crack near the interface propagated across the interface without deflection [Lee 1997, Case 1998].

1.2.3 Microwave heating and joining

One limitation of conventional ceramic–ceramic joining is that the entire assembly needs to be heated to the desired joining temperature. This requirement could lead to many practical difficulties. Therefore, ceramic-ceramic joining by selective heating using unconventional heating methods, such as microwave heating, has been the subject of considerable attention.

1.2.3.1 Microwave processing and microwave effect

Microwave heating is fundamentally different from conventional heating (Figure 1.5). Electrical furnaces used for conventional heating of materials are composed of heating elements, such as SiC, and insulation. For microwave heating, the cavity used to heat the materials is composed of a metal shell and microwave port through which electromagnetic waves are allowed into the cavity from the microwave power supply [Sutton 1992]. In conventional processing, heat is generated from an external source which transfers thermal energy to the surface, and further into the center of the material by conduction. However, in microwave heating, heat is generated within the material through the interaction between the electromagnetic field and induced molecular motions. When compared to conventionally heated materials, materials will be heated more uniformly, and typically more rapidly, when heated using microwaves, within the limits set by microwave absorption [Loehman 1983].

Due to the inherent heating characteristics associated with the microwave, many attractive advantages have been experimentally demonstrated. In addition to reduced processing times and energy savings, a number of researchers [Palaith 1989, Fanslow, Janney 1991] have reported that microwave processing produces chemical and physical reactions that are different from the reactions that would have occurred if the only effect

of the microwaves were to increase the temperature. For example, increased diffusion coefficients [Janney 1991], enhanced chemical and physical reactions [Fanslow 1991], improved microstructures and mechanical properties [Patterson 1992], smaller grain sizes [Tian 1988], and lowered sintering activation energies [Janney 1988] have been observed in microwave heating. These enhancements are known as the "microwave effect".

Janney et al. [1988] reported that Al_2O_3 doped with 0.1 wt% MgO sintered under vacuum using 28 GHz microwaves densified much faster than by conventional sintering. The activation energy observed for conventional sintering was 575 KJ/mol. However, the activation energy for microwave sintering, 160 KJ/mol, was only one-third of that for conventional sintering [Janney 1988], suggesting the sintering process and mechanisms were quite different for microwave and conventional sintering. In addition, Janney et al. [1988] also compared the kinetics of grain growth in both microwave and conventional annealed alumina samples. The rate of grain growth is greatly accelerated in microwave annealing. The activation energy for microwave grain growth was 480 KJ/mol, which was around 20% lower than 590 KJ/mol for conventional grain growth (Figure 1.6) [Janney 1988, 1991], suggesting the grain growth process may be more similar for both microwave and conventional annealing. To account for the observed athermal microwave effects, Janney et al. [1991] have speculated that these enhancements occur as a result of the electromagnetic field "coupling to lattice defects and other bulk crystalline effects". In addition, Lee and Lin [1998] measured and compared the dielectric loss factor (tan δ) of sintered $BaO{\cdot}La_2O_3{\cdot}4.7TiO_2$ ceramics with and without glasses addition. The tan δ of the sintered ceramics with an addition of glass is significantly higher than the theoretically calculated values of ceramics and glass based on the sum rule weighted

by constituent volume fractions, due to the heterogeneous interface between glasses and ceramics. This difference between the measured and calculated tan δ indicates that large dielectric losses occur at interfaces between materials with large differences in dielectric loss factors, leading to a large increase in tan δ at the interface [Lee and Lin 1998].

Recently, Rybakov et al. [1994] proposed a model in which a microwave field induces oscillatory fluxes of ionic point defects near surfaces, generating a net current of charged defects. Furthermore, Booske and their co-workers [Booske 1997, 1998, Freeman 1995, 1998] illustrated theoretically and numerically, and confirmed experimentally, that microwave fields induce an additional driving force (ponderomotive force or pmf) that enhances the mass transport rate and ionic diffusion, not seen with conventional heating. The pmf is an electromagnetic force that tends to move mass and can be expressed as the following:

$$pmf = \left\langle \frac{C_n^p}{C_n^i} q_n \left(E^{mw} + E^p \right) \right\rangle$$ [Booske 1997, 1998]

Where $\langle\ \rangle$ denotes time averaging over one cycle,

q_n denotes electric charge of the species n,

C_n^i denotes the initial, equilibrium concentration value of the species n,

C_n^p denotes the concentration perturbation from the initial value due to microwave excitation for species n,

E^{mw} denotes the microwave field or potential,

E^p denotes the microwave potential perturbation from the initial value due to microwave excitation.

The numerical model, based on continuum equations, predicted that the microwave fields do not enhance the ionic mobility, but rather are responsible for a new driving force for ionic diffusion [Booske 1997, 1998, Freeman 1995, 1998]. During powder sintering, this new additional driving force pmf could drive defects to the crystal boundary and enhance the long-range mass transport into the interior of the crystal. In addition, the model predicted that the pmf should predominate near material surfaces or any abrupt discontinuities, such as interfaces. Table 1.1 compares the microwave pmf with other calculated thermochemical driving forces for ionic transport in NaCl. The authors [Booske 1997, 1998, Freeman 1995, 1998] state that the value of the pmf is higher than the solid-state diffusion driving force for materials joining between two flat NaCl/NaCl surfaces. This can explain the rate enhancement during microwave joining observed by many authors.

1.2.3.2 Interaction between microwaves and materials

Depending on the material type, microwave energy can be transmitted, absorbed, or reflected. Metals are opaque to microwaves and thus are very difficult to heat by microwave energy (Figure 1.7). Low loss ceramics such as Al_2O_3, MgO, SiO_2, and most glasses are transparent to microwaves at ambient temperatures [Sutton 1992]. However, for these low loss ceramics, there is a critical temperature above which the ceramics begin to absorb and couple more efficiently with microwave radiation. In addition, adding conductive or magnetic phases or other additives in the form of fibers or particles to the low loss or microwave transparent ceramics can greatly enhance their microwave energy absorption. The added conductive and magnetic phases can absorb microwave energy more rapidly than the matrix and thus can be selectively heated [Sutton 1992]. On

the other hand, ceramics exhibiting high dielectric losses such as CuO, NiO, and MnO_2 can absorb microwave energy efficiently at room temperatures and heat up very rapidly [Sutton 1992, Tinga 1988].

When microwaves penetrate and propagate through a material, internal electric fields will be generated. These internal electric fields induce complicated motions of charges such as electrons, ions, and dipoles. "The resistance to the induced motions due to inertial, elastic, and frictional forces causes losses and attenuates the electric fields", resulting in volumetric heating [Sutton 1992]. Generally, the dielectric loss factor (tan δ) is used to describe these losses as the following [Sutton 1992]:

$$\tan\delta = \frac{\dot{\varepsilon}_{eff}}{\dot{\varepsilon}_r}$$

Where $\dot{\varepsilon}_{eff}$ denotes effective relative dielectric loss factor

$\dot{\varepsilon}_r$ denotes relative dielectric loss factor

Therefore, when a material exhibits a high dielectric loss factor in the microwave frequency range, it is expected that the dielectric material will absorb microwaves easily and with very efficient energy conversion, resulting in rapid heating.

1.2.3.3 Microwave joining

Since the absorption of microwave energy varies with the composition and structure of different phases, selective heating is certainly possible and presents opportunities for commercial applications where partial or local heating is highly desirable. One of the greatest characteristics of microwave heating that can be used for ceramic joining is the possibility of selectively heating the interface. A large tan δ dielectric interlayer can be heated preferentially and join the base ceramics without heating the bulk materials,

minimizing the volume of thermally stressed ceramics [Loehman 1993, 1999]. Another potential advantage of selective heating is the possibility of protecting certain heat sensitive components by shielding them with a piece of metal during joining since metals are opaque to microwaves [Loehman 1993].

Other advantages of microwave joining include (1) enhanced diffusion and lower joining temperatures and (2) lower processing times and energy saving costs. For example, Binner et al. [1998] investigated the microwave and conventional joining of different grades of polycrystalline alumina. They found that relatively low purity alumina, such as 85% and 94%, can be readily joined. However, higher purity 99.8% alumina was "insufficient to lossy to couple" with microwaves, and thus could not be heated to sufficient high temperatures due to the negligible amount of grain boundary phases present, making joining difficult. Despite the similarity in bonding mechanism based on viscous flow of the grain boundary phase, microwave joining can be a factor of at least four times faster than conventional diffusion joining, resulting in significantly less deformation associated with joining for the 85% alumina. Similar results were found by Fukushima et al. [1988] when joining different grades of alumina. Although 92 to 96% purity alumina were directly joined via microwave heating, higher purity 99% alumina failed to join together without the use of a layer of lower purity alumina.

Although microwave joining of ceramics exhibits great potential for commercial applications, many important process variables associated with microwave heating cannot be adequately controlled, such as heating and cooling rates, accurate temperature control, and temperature uniformity in the ceramics. As pointed out by Loehman [1993], "there

has not been enough experiences with microwave joining of ceramics to provide the needed data on process control and reproducibility".

1.3 Indentation tests

Vickers indentation tests, which use a pyramidal diamond indenter, are extensively used to study the toughness, fracture and deformation properties of brittle polycrystalline ceramics [Marshall 1977]. Cracks that initiate from the central deformation zone and develop as "half-pennies" along indentation diagonals can provide deep insight into the fundamental nature of damage modes in brittle solids and establish a basis for models of wear and erosion resistance [Marshall 1979]. Furthermore, understanding the behavior of indentation cracks near surfaces and interfaces is beneficial to the understanding of failure mode of bonded dissimilar materials and the further development of joining approaches [Lardner 1990, Lee 1998].

To evaluate the interfacial strength of bonded materials in comparison to the strength of the bulk ceramics, various researchers have utilized Vickers indentation testing on joined ceramics [Ye 1994, Nakamura-A 1997, Rodriguez 1998]. For example, by placing a series of Vickers indentations across the joint interface and comparing the crack lengths of the far and near field interface indentations, the residual stress σ_r can be determined from the following relationship [Lee 1996, Ye 1994]:

$$\sigma_r = K_c \left(\frac{4C_r}{\pi}\right)^{-0.5} \left[\left(\frac{C}{C_r}\right)^{1.5} - 1\right]$$

Where K_c denotes critical stress intensity factor,

C_r denotes indentation crack length near the interface,

C denotes indentation crack length far away the interface.

In addition, Vickers indentation cracks placed near the joint can also be used to estimate the interfacial fracture toughness of the joint [Lee 1996]. In the absence of an elastic mismatch across the joined materials, a crack can penetrate across the interface without deflection when the interfacial fracture energy reaches approximately 60% of the bulk fracture energy [Lee 1996]. For indentation tests on bonded dissimilar materials, distortion of radial cracks may result from elastic mismatch. Lardner et al. [1990] investigated the mechanisms of indentation crack propagation in cracks placed in glass near a joined glass/epoxy interface. Initially, the crack propagated toward the interface due to the modulus of glass being much higher than that of the epoxy. However, as the crack approached the interface, the crack reoriented in a direction away from or parallel to the interface due to the changing stress fields near the interface [Lardner 1990].

1.4 Characterization techniques

Development of ceramic joining methods requires a fundamental understanding of ceramic interfaces and reactions. The ultimate goal of ceramic joining is to develop joints with high interfacial strength and desirable interfacial microstructures between similar or dis-similar materials. Therefore, knowledge of the relationships between interfacial reactions and adhesion, the composition and structure of the interface, the joining mechanism, and the nature of any reaction products is crucial for the development of joining technology. Unfortunately, instead of using transmission electron microscopy (TEM), most researchers have only use optical microscopy (OM) and scanning electron microscopy (SEM) to characterize the interfaces. The reason may be related to the difficulty of TEM sample preparation (described in Chapter II). Although OM and SEM are useful for noting the presence of large-scale interfacial phases or interlayers, the

resolution of these techniques is still somewhat limited. Fine scale interlayers or defects that can be revealed using TEM may not be visible using OM or SEM. Therefore, more detailed characterization and structural analysis of interfaces should be carried out using TEM in conjunction with OM and SEM. More importantly, interface examinations will help in understanding the fundamental process in ceramic joining.

1.5 Research strategy

It is known that the mechanical properties of joined ceramics depend on the composition and structure of the interface, the joining technology used, and reaction products that may be produced [Loehman 1993, 1999]. Therefore, the initial objective of this research was to characterize the interfacial microstructures of ceramics joined using spin-on interlayers.

The interfacial microstructure of microwave joined polycrystalline partially stabilized zirconia and glass-ceramics MaCor™ using spin-on interlayers were first studied. In microwave joined zirconia/MaCor™ specimens, no silica interlayer, interfacial phase(s) or other reaction products were observed. Presumably, the interlayer diffused into the surrounding parent ceramics, leaving a perfectly bonded interface.

Because the glass-ceramic composite MaCor™ contains an amorphous matrix phase, it is not clear if the spin-on interlayer is in fact necessary to successfully bond zirconia and MaCor™ specimens. Thus, the initial objective of this study was modified to more comprehensively and intensively assess the nature of microstructure development in the bond region of partially stabilized zirconia and MaCor™ joined via conventional versus microwave heating with or without a spin-on interlayer in relation to a number of other processing variables. However, as the research progressed, it became clear that no

significant differences in the interfacial microstructure developed between conventional versus microwave joined zirconia and MaCor™, due to the glassy nature of the MaCor™. Thus, the final objective of this research was to focus on the interfacial microstructures of joined crystalline ceramics. Because of the difficulties in identifying interfaces in joined polycrystalline ceramics/polycrystalline ceramics, and because of the broad applications of single and polycrystalline alumina in industry, the interfacial microstructures of polycrystalline alumina and single crystal sapphire joined using spin-on interlayers have been investigated. Through a step-by-step process, better understanding of the nature of the joint associated with joining mechanisms and the joining technology has now been successfully achieved.

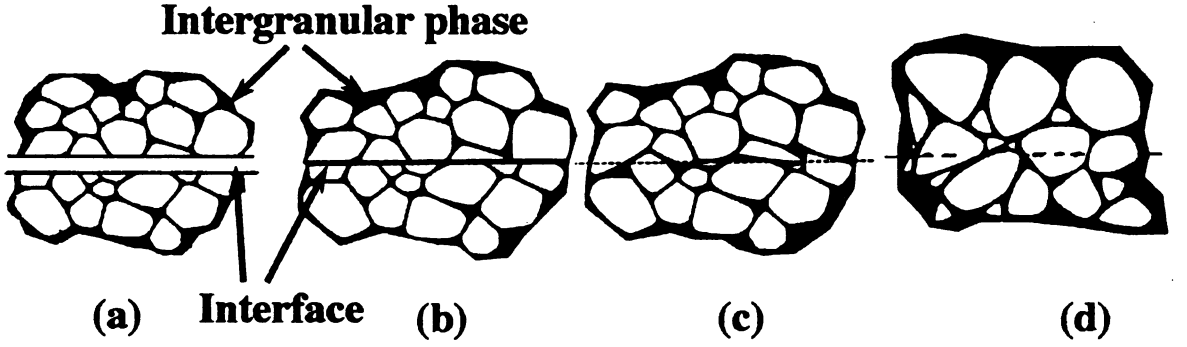

Figure 1.1 Schematic representation of the direct ceramic-ceramic joining process without the use of interlayers carried out at elevated joining temperature and pressure [Redrawn from Esposito 1998]. At the first stage of the joining process (a), the interface between the two polished ceramic parts can be seen as a macroscopic inhomogeneity since no intergranular amorphous phase is present on the surface of the grains at the interface. Driven by thermodynamic capillary force (b), the intergranular amorphous phase flows to the interface at elevated temperatures. As the process continues (c), liquid phase flow, grain boundary sliding, and grain rotation can be activated to minimize the macroscopic inhomogeneity between joint and base ceramics. Finally (d), grain growth and grain bridging occur, leading to an indistinguishable interface from the base ceramics.

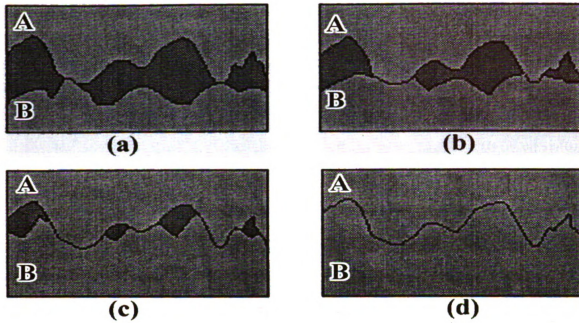

Figure 1.2 Schematic representation of the sequence for diffusion bonding at a proper joining temperature and pressure [after http://www.twi.co.uk/j32k]. Initially (a) two ceramic surfaces are placed in contact, (b) at least one of the surfaces begins to deform under high temperature and stress, (c) deformation continues, leading to void shrinkage, and (d) the formation of interface or joint.

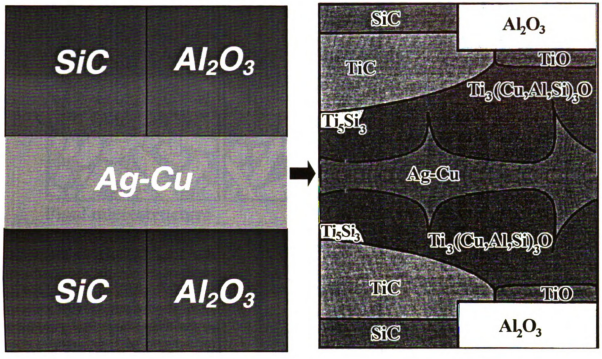

(a) (b)

Figure 1.3 shows the phase development of a Al_2O_3-SiC composite brazed by Ag-Cu-Ti alloy from (a) the initial phase distribution to (b) the final experimentally determined complicated phase distribution at the joint after brazing [Redrawn from Zurbuchen 1999].

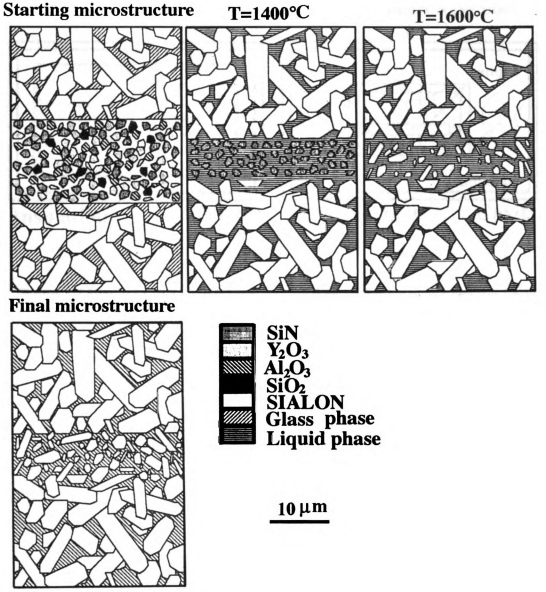

Figure 1.4 shows the sequential stages of the transient liquid phase bonding process for the joining of β-SiAlON/β-SiAlON ceramics using β-SiAlON glass-forming composite adhesives (mixture of Si_3N_4, Y_2O_3, Al_2O_3, SiO_2 powders) [Redrawn from Walls 1992, Hanson 1998]. Prior to the joining, adhesive powders are sprayed onto one of the base materials. Around 1400°C, oxide components react to form a Y-Si-Al-O liquid phase, leading to densification and sintering of the interlayer. At approximately 1600°C, the Si_3N_4 dissolves quickly into the liquid. At the same time, the newly formed β-SiAlON grains grow and form an interlocking network across the joint, leading to an indistinct interface between the base β-SiAlON and the newly formed β-SiAlON materials. The final microstructure is composed of the base β-SiAlON and the newly formed β-SiAlON grains with an almost indistinct interface.

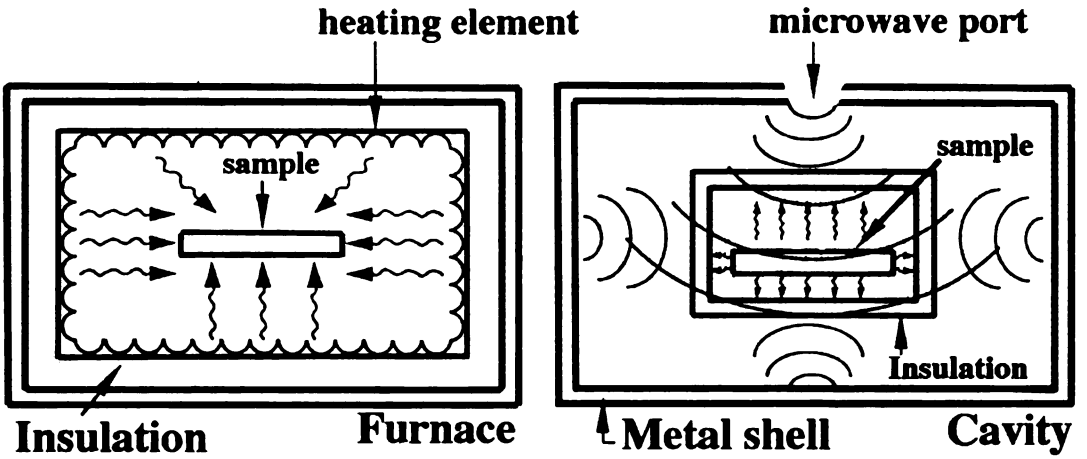

Figure 1.5 Heating patterns in (a) conventional and (b) microwave heating furnaces [Redrawn from Sutton 1992].

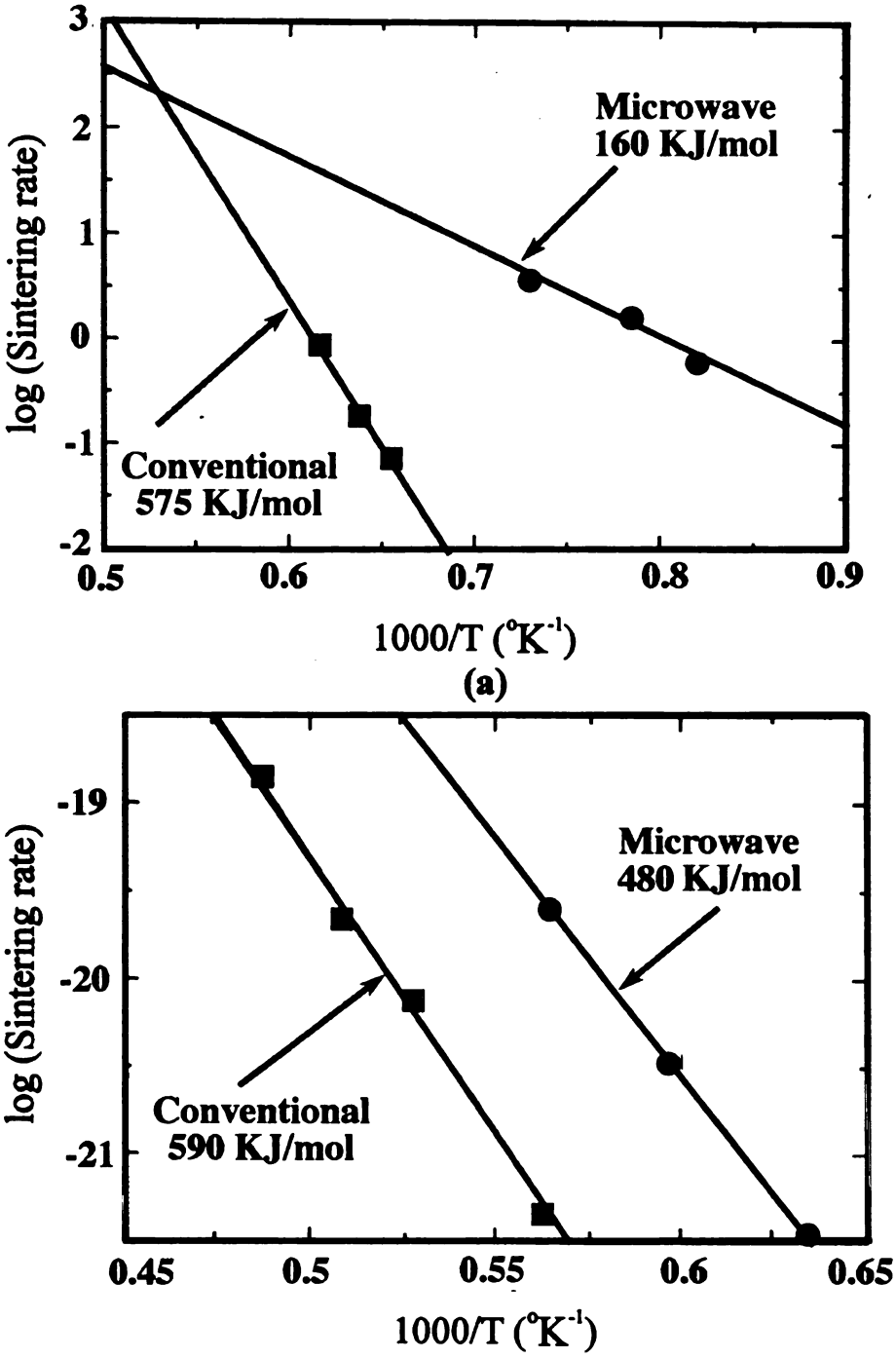

(b)

Figure 1.6 shows the activation energy for (a) sintering process in microwave and conventional sintered Al_2O_3 doped with MgO [Redrawn from Janney 1988] and (b) grain growth in microwave and conventional heated Al_2O_3 doped with MgO [Redrawn from Janney 1991].

Table 1.1 Comparison of microwave *pmf* and other thermochemical driving forces for ionic transport in NaCl [Booske 1997, 1998, Freeman 1995, 1998].

	Transport driving force	Typical magnitude (N)
1	Sintering 1μm powder—initial stage	$\sim 10^{-16}$
2	Sintering 1μm powder—intermediate stage	$\sim 10^{-18}$
3	Joining two flat faces	$< 10^{-18}$
4	Chemical interdiffusion (depending on concentration gradient	$\sim 10^{-16}$ to ∞
5	Tracer isotope diffusion	$<< 10^{-19}$
6	Microwave *pmf*	$\sim 10^{-19}$ to 10^{-15}

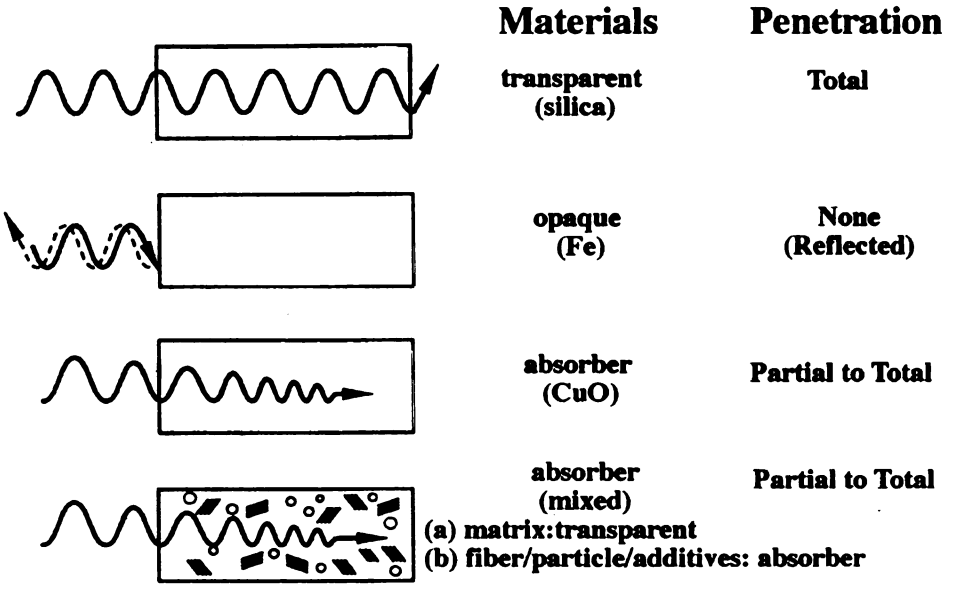

Figure 1.7 Interactions of microwaves with different materials [Redrawn from Sutton 1992].

Chapter II

Experimental procedures

2.1 Goals and objectives of the proposed research

This research program focused on the interfacial microstructures of ceramics joined using spin-on interlayers. The joined ceramic samples were characterized using different techniques including optical microscopy (OM), scanning electron microscopy (SEM), and transmission electron microscopy (TEM). The primary goal of the interfacial assessment was to gain a complete understanding of the nature of the joint. The mechanical properties of the interface were characterized using Vickers indentation techniques to access the thermal residual stresses and interfacial strength. The microstructure and mechanical characterization resulted in information about the structure of the interfaces, and the fundamental ceramic joining processes. Furthermore, the degree of bonding was assessed and related to mechanical properties of the joined ceramics.

2.2 Materials and spin-on interlayers used in the current research

2.2.1 Joining materials

Three mol.% yttria-zirconia, glass-ceramics MaCor™, polycrystalline alumina, and single crystalline alumina (sapphire) were joined in this research.

The polycrystalline partially stabilized zirconia (PSZ) specimens used in this research were sintered from powder compacts which were pressed in a uniaxial die at approximately 32 MPa using commercial powders (TZ-3Y, Tosoh Corporation, Japan). The powder compacts were sintered at 1375°C for one hour in a 2.45 GHz single-mode

microwave cavity (Model CMPR-250, Wavemat Inc., Plymouth, MI) [Case 1997, 1998]. During sintering, the temperature was controlled by adjusting an input power with automatic sliding short and probe. After sintering, the zirconia specimens were approximately 17 mm in diameter and 2 mm thick.

MaCor™ (Corning Code 9658, Corning, NY) is a fluorophlogopite mica reinforced glass ceramics in the system of Si_2O-Al_2O_3-MgO-K_2O-F, composed of approximately 55 volume percent of a randomly oriented fluorophlogopite mica platelet and 45 percent of borosilicate glass matrix [Corning]. MaCor™ is widely used as an electrical or thermal insulator for structural components in semi-conductor industry.

Two different commercial grades of polycrystalline alumina were used in this research; 96% and 98%, which are often used as insulators for precision resistors, wear resistant components for pump seals, and lids for hybrid microwave applications. Commercial 96% and 98% grades of polycrystalline alumina were purchased from the Coors Corporation.

Sapphire wafers with $(11\bar{2}0)$ surface normals (±0.3°), with flatness better than 25 micrometer (μm) and a metallic impurity level less than 100 ppm, were purchased from the Union Carbide Corporation.

2.2.2 spin-on interlayers

The spin-on interlayer used as the bonding agent was produced from Silicafilm™ (Emulsitone Co., Whippany, NJ). Silicafilm™ is an organically based silica precursor that was applied to the polished surface to yield a pure amorphous SiO_2 film [Emulsitone]. This thin, amorphous silica film coating was the interlayer that aided in joining the specimens. The Silicafilm™ was applied as a liquid and spun on a substrate

spinner to produce a thin film. The film was then cured or heated in air to provide an amorphous silica layer with the high purity required for integrated circuit applications. Silicafilm™ has an impurity level of less than one part per million of metallic ions [Emulsitone].

2.3 Joining

2.3.1 Joining procedures

The technique used to join densified ceramics using spin-on interlayers was developed here at Michigan State University (MSU) by previous researchers [Case 1997, 1998]. Figure 2.1 shows an overview of the typical spin-on interlayer ceramic joining procedure used in the current study. More detailed system specific procedures follow the common outline. The general joining procedure was as follows:

1. Mount the specimens to be joined to a flat aluminum disk with thermoplastic using a hot plate.
2. Polish the specimens using an automated polishing system (LECO Corporation, St. Joseph, MI) and a series of an abrasive diamond paste with grits ranging from 35, 25, 17, 15, 10, 6, to 1 μm for 2~20 minutes.
3. Demount the specimens from the aluminum disk by heating on the hot plate.
4. Clean all specimens in a 50:50 mixture of acetone and alcohol for 10~20 minutes in an ultrasonic bath.
5. Adhere the ceramic components to a substrate spinner (Headway Research, Inc. Garland, Texas) using a double-sided tape.

6. Apply four to five drops of Silicafilm™ (Emulsitone Co., Whippany, NJ) to the polished and cleaned surfaces of the ceramic components using a pipette.
7. Turn on the substrate spinner and spin at a rate of 3000 rpm for 20 seconds.
8. Separate the coated ceramic components from the double-sided tape using a single sided razor blade.
9. Cure the liquid Silicafilm™ in a conventional resistance furnace for 20 minutes at 200°C to form a thin amorphous silica layer (approximately 200~300 nm). This thin amorphous silica coating was the interlayer that aids in joining the specimens.
10. Put the specimens to be joined on an alumina setter and place the coated surfaces of the specimens in contact.
11. Apply a small (20~85g) polycrystalline alumina deadweight (Figure 2.2) to the specimens.
12. Heat the specimens to be joined in a single-mode cylindrical 2.45 GHz microwave cavity or conventional resistance furnace.
13. Cool the joined specimens in a furnace-cooling mode.

The microwave heating was carried out using a cylindrical zirconia casket refractory and the TM_{111} microwave cavity (Model CMPR-250, Wavemat Inc., Plymouth, MI) mode with a stepped input power sequence typically starting from 100 Watts and increasing to approximately 1200 Watts in steps of 100 Watts every 3 minutes. During the microwave joining, the joining temperatures were measured using an optical pyrometer system (Accufiber Optical Fiber Thermometer, Model 10, Luxtron Co.,

Beaverton, OR), which is capable of measuring temperatures ranging from 500~1900°C with an accuracy of ±2°C [Case 1997, 1998].

The conventional joining was performed using a conventional electrical resistance furnace (Carbolite, Aston Lane, Sheffield, England) with SiC heating elements. The temperature was controlled to ±2°C. The heating and cooling rates were approximately 10°C per minute. For all microwave and conventional joining, the joining time refers to the time at the desired temperature.

2.3.2 Materials joining systems

Three different joint systems were produced via microwave heating: 3 mol.% yttria-zirconia/MaCor™, polycrystalline alumina/polycrystalline alumina, and polycrystalline alumina/3 mol.% yttria-zirconia. Conventional furnace heating was used to produce MaCor™/MaCor™, polycrystalline alumina/single crystalline alumina (sapphire), and 3 mol.% yttria-zirconia/MaCor™ joins. Table 2.1-2.3 list all of the different joined specimens produced in this study.

2.3.2.1 joining of crystalline materials with non-crystalline materials

2.3.2.1.1 Microwave and conventional joining of zirconia and MaCor™

In this study, 3 mol% yttria-zirconia specimens were joined to MaCor™ using microwave and conventional heating to assess the differences between microwave joining and conventional joining by comparing the times and temperatures necessary to achieve successful joining using these two approaches. 10-mm X 10-mm X 1.8-mm specimens were cut from the as-received MaCor™ billets using a low speed diamond saw. After polishing, coating and curing, 3 mol% yttria-zirconia specimens were joined to MaCor™ using microwave heating at 1020°C for 20 minutes. During the joining process, a 20-

gram polycrystalline alumina deadweight was applied to the specimens, providing a very small normal load of 2000 Pa.

Table 2.1 outlines various experimental conditions and combinations of joined specimens via conventional heating. In addition to the joining of MaCor™/zirconia with spin-on interlayers, two polished but uncoated MaCor™/zirconia specimen pairs were joined via conventional heating to compare the results with spin-on interlayer joining and to determine the effect of the silica spin-on interlayer.

2.3.2.2 Joining of crystalline ceramics

In addition to the joining of crystalline materials with non-crystalline materials, joining of crystalline ceramics was performed via microwave and conventional heating. Table 2.2 outlines the experimental conditions for the joining of polycrystalline alumina/3 mol% yttria-zirconia and 98% polycrystalline alumina/polycrystalline alumina. Zirconia/alumina, microwave and conventional joining 98% polycrystalline alumina/alumina specimens were joined using microwave heating at 1500°C for 20 minutes, and 1340°C for 20 minutes, 1340°C for 180 minutes, respectively. During the joining process, a 20-gram polycrystalline alumina deadweight was applied to the specimens, providing a very small normal load of 2000 Pa.

2.3.2.3 Joining of polycrystalline alumina and sapphire

Sapphire wafers with $(11\bar{2}0)$ surface normals (±0.3°), and commercial 96% and 98% polycrystalline alumina were used in this study. Ten-mm diameter and 2~3 mm thick specimens were cut from 96% and 98% polycrystalline alumina rods, respectively. Initially, the polycrystalline alumina specimens were finely polished, and cleaned in a 50:50 mixture of acetone and alcohol for 10~20 minutes in an ultrasonic bath.

Fifty mm diameter and 0.45 mm thick of sapphire disks were sectioned into rectangular 10mm X 10mm squares. The as-received sapphires were only cleaned in an ultrasonic bath. Polishing was not required due to the high flatness of the sapphire. After spin coating and curing, the coated surfaces were put in contact and joined by heating in a conventional electric furnace. During the joining process, an 85 gram polycrystalline alumina deadweight was applied to the specimen, providing a very small normal load of 8000 Pa. Table 2.3 outlines the experimental conditions for the joining of 96%, 98% polycrystalline alumina with sapphire using silica interlayers at temperatures from 1400° C, 1450°C and 1475°C for 3 hours via conventional heating.

2.4 Characterization

2.4.1 Optical microscopy and SEM

2.4.1.1 Sample preparation

Specimens were prepared for optical and SEM examination by cross-sectioning with a low speed diamond saw. A portion of each sectioned specimen was mounted in diallyl phthalate powder (LECO Corporation, MI). Using an automatic polisher, the mounted specimens were polished using a series of diamond abrasive grit ranging from 25, 10, 3, to 1 microns. The final cleanings were done in a 50:50 mixture of acetone and alcohol for 10~20 minutes in an ultrasonic bath. Thus, the specimens were ready for optical microscopy examinations. In addition, prior to SEM examination, the polished and cleaned specimens were carbon coated using a carbon evaporator (Denton Vacuum DV-502) to avoid charging effects.

2.4.1.2 Characterization techniques

Optical microscopy was used to initially assess the integrity and thoroughness of the bonds. Optical microscopy was performed using a Nikon optical microscope (Model EPIPHOT 200, Japan). More detailed characterization of the interfaces was carried out using SEM. The SEM observations were carried out using a Hitachi S-2500C, a CamScan 44 FE SEM, or a JEOL JSM-35CF operated at an accelerating voltages of 15~25 kV and working distance of 15 mm using secondary and backscattered electron imaging techniques.

2.4.2 TEM

2.4.2.1 TEM sample preparation

To carry out TEM analysis, cross-sectional TEM thin foils were prepared by sectioning, mounting the sections to 3 mm molybdenum rings, polishing, dimpling and ion milling until perforation. Figure 2.3 shows an overview of the cross-sectional TEM sample preparation procedure. The detailed sample preparation sequence used to form a cross-sectional TEM thin foil is as follow:

1. Section the joined specimens into a 1 mm thickness slab using a low speed diamond saw.
2. Continually section the slab into a 2.5×2.5 mm squares using a low speed diamond saw.
3. Clean the joined specimen squares in a 50:50 mixture of acetone and alcohol.
4. Mount the 2.5×2.5 mm joined specimens square onto a 19 mm diameter sapphire flat with Crystalbond™ mounting wax on a hot plate.

5. Mechanically attach the sapphire flat with the mounted joined specimens square into a sapphire flat holder that fits into the polishing block.
6. Polish the joined specimen squares with a series of diamond lapping films, ranging from 35, 25, 10, 3, 1, to 0.5 μm.
7. Separate the joined specimen squares from the sapphire flat using acetone, followed by a rinse with ethanol.
8. Measure the joined specimen square thicknesses using a micrometer.
9. Glue the polished side of the joined specimen square to a 3 mm diameter molybdenum ring using Gatan™ G-1 epoxy and hardener, followed by curing on the hot plate for 10 minutes at 130°C.
10. Mount the joined specimen squares with molybdenum ring onto the sapphire flat with Crystalbond™ mounting wax on the hot plate.
11. Re-measure the total thickness of the sample assembly to determine the amount of materials needed to be removed by polishing.
12. Mechanically re-attach the sapphire flat into the sapphire flat holder that fits into the polishing block.
13. Polish the joined specimen squares to a thickness of approximately 70~90 μm with a series of diamond lapping films, ranging from 35, 25, to 10 μm.
14. Mount the joined sample assembly on a VCR™ Model D500i dimpler.
15. Dimple the joined specimen squares to a thickness of approximately 15~20 μm using a 3 μm diamond coated dimpling wheel with 1 μm diamond slurry.
16. Dismount the dimpled joined specimens square from the sapphire flat with acetone, followed by a rinse with ethanol.

17. Mount the joined sample assembly on a Gatan DuoPost™ support
18. Ion mill using a Gatan PIPS at an angle of ±3~±6° with 5 Kev Ar^+ beam until perforation.
19. Carbon coat the thin foil using a carbon evaporator (Denton Vacuum DV-502) to avoid charging under the electron beam.

The original pieces and interfaces for joining of like ceramics such as 98% polycrystalline alumina/98% polycrystalline alumina, may be indistinguishable optically, leaving the original specimens are almost perfectly joined together. Thus, the standard cross-sectional TEM sample preparation procedures (described above) had to be changed to examine the interfacial microstructures. To determine the interfaces for dimpling, after polishing and gluing, the specimens were ion milled at a high angle of 10° for a short time. After ion milling, the interfaces were distinguishable with an observable thin interface line. This preferential thinning was probably due to the difference in chemistry and strength between the interfacial region and base ceramics. Following the short time ion millings, the specimens were then dimpled to 15~20 μm and further ion milled to electron transparency.

2.4.2.2 TEM Characterization

Detailed characterization of the interfaces was carried out using TEM. TEM was used to investigate the effect of interlayers on the joining process and check for the presence of interfacial phases or interlayer at the interface. In addition, the overall interface microstructural features, such as interface roughness, wetting behavior, grain sizes, and the possible base microstructural changes due to joining process, were

characterized using TEM to facilitate the understanding of the fundamental materials joining process. In this study, TEM examinations were performed using a Hitachi H-800 electron microscope operated at 200 kV. Both bright and dark field imaging were carried out in conjunction with selected area diffraction. A double tilt holder allowed the interface planes to be oriented parallel with the electron beam. The EMS software package was used to assist indexing the experimental diffraction patterns [EMS].

2.5 Indentation tests

Vickers indentation tests were done on the joined ceramic 3 mol% yttria-zirconia/MaCor™ and polycrystalline alumina/sapphire to assess residual stresses and interfacial fracture toughness of the joint at the gross scale. The joined ceramics were cross-sectioned with a minimum thickness of 2.5 mm, mounted, and finely polished using a series of diamond abrasive grits, ranging from 35, 25, 10, 3, to 1 μm. A series of Vickers indentations were placed across the joint interface with a minimum spacing of 2.5 times the Vickers indentation crack length to avoid the effect of strain field around the prior indent (Figure 2.4). By comparing the crack lengths of the far and near field interface indentations, the residual stress and interfacial toughness were determined [Lee 1996, Ye 1994].

Vickers indentation tests were done at a load of 5 Kg for 10 seconds with load speed of 60 um/sec. The indentation tests were done on the 3-mol% yttria-zirconia side for joined zirconia/MaCor™ specimens because indentation cracks in MaCor™ would be repeatedly deflected, blunted, and arrested due to the randomly orientated fluorophlogopite mica crystals in glass matrix [Grossman 1972, 1978]. In addition, the indentation tests were done on the polycrystalline alumina side for joined polycrystalline

alumina/sapphire specimens to protect the expensive diamond indenter. The indentation crack lengths were measured using both optical microscopy and SEM. Prior to SEM observations, the indented specimens were carbon coated using carbon evaporator (Denton Vacuum DV-502) to avoid charging under the electron beam.

Table 2.1 the experimental conditions and results for the joining of zirconia/MaCor™ in the current research. Please note, all experiments were done twice to verify joining results.

Specimens to be joined	Joining temperature (°C)	Joining time (min)	Heating mode	Coating
MaCor™/zirconia	1020	20	Microwave	Silicafilm™
MaCor™/zirconia	1020	20	Conventional	Silicafilm™
MaCor™/zirconia	1020	40	Conventional	Silicafilm™
MaCor™/zirconia	1020	60	Conventional	Silicafilm™
MaCor™/zirconia	1070	20	Conventional	Silicafilm™
MaCor™/zirconia	1070	40	Conventional	Silicafilm™
MaCor™/zirconia	1070	60	Conventional	Silicafilm™
MaCor™/zirconia	1070	60	Conventional	No coating
MaCor™/zirconia	1070	120	Conventional	Silicafilm™

Table 2.2 outlines the experimental conditions for the joining of 3 mol% yttria-zirconia/polycrystalline alumina, and 98% polycrystalline alumina/98% polycrystalline alumina. Please note, all experiments were done twice to verify joining results.

Specimens to be joined	Joining temperature (°C)	Joining time (min)	Coating	Heating mode
Polycrystalline alumina/polycrystalline alumina	1340	20	Silicafilm™	Microwave
Polycrystalline alumina/polycrystalline alumina	1340	180	Silicafilm™	Conventional
3 mol% yttria-zirconia/polycrystalline alumina	1500	20	Silicafilm™	Microwave

Table 2.3 outlines the experimental conditions and results for the joining of 98% polycrystalline alumina/alumina, 98% polycrystalline alumina/sapphire, and 96% polycrystalline alumina/sapphire via conventional heating. Please note, all experiments were done twice to verify joining results.

Specimens to be joined	Joining temperature (°C)	Joining time (min)	Coating
Sapphire/98% polycrystalline alumina	1400	180	Silicafilm™
Sapphire/98% polycrystalline alumina	1450	180	Silicafilm™
Sapphire/98% polycrystalline alumina	1475	180	Silicafilm™
Sapphire/98% polycrystalline alumina	1475	180	No coating
Sapphire/98% polycrystalline alumina	1475	180+300	Silicafilm™
Sapphire/96% polycrystalline alumina	1475	180	Silicafilm™
Sapphire/96% polycrystalline alumina	1475	180	No coating
Sapphire/96% polycrystalline alumina	1475	180+300	Silicafilm™

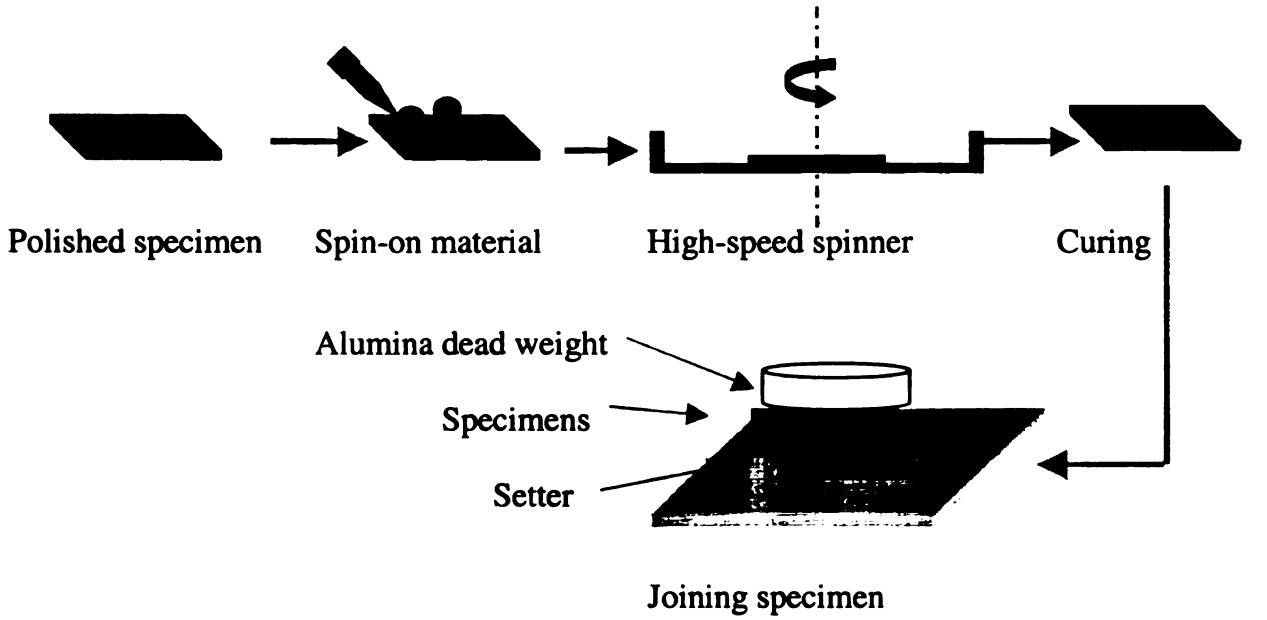

Figure 2.1 Schematic representation of spin-on interlayer joining method used in the current study.

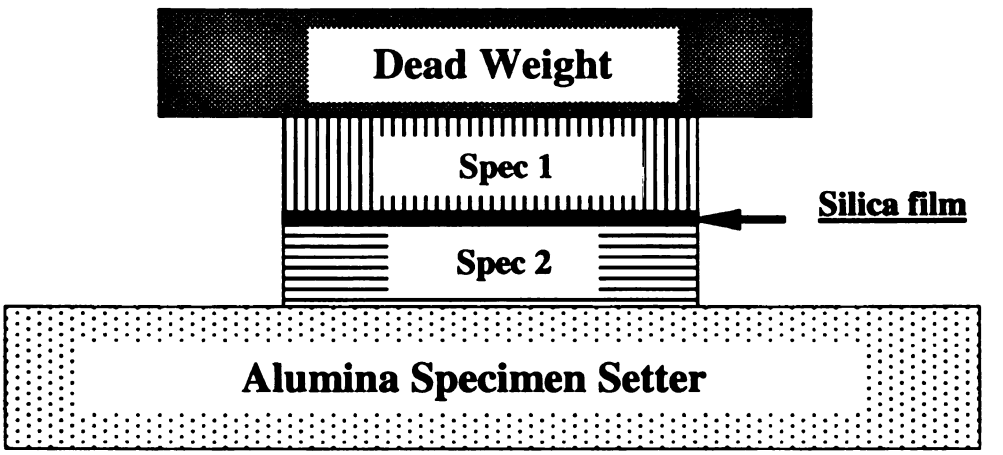

Figure 2.2 Representation of the ceramic joining set-up used in the current study. The joined specimens are loaded using a small (20~85g) polycrystalline alumina deadweight, to prevent slippage of the specimens.

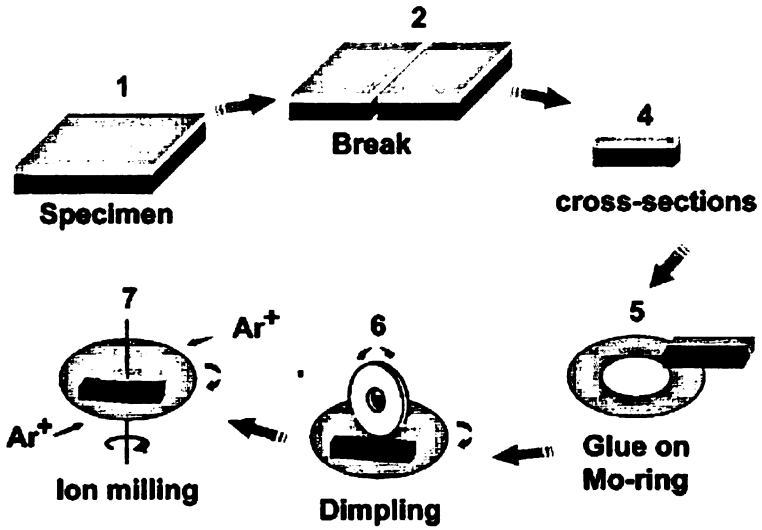

Figure 2.3. Schematic representation of the cross-sectional TEM sample preparation procedure used in the current study [after Geng 2003].

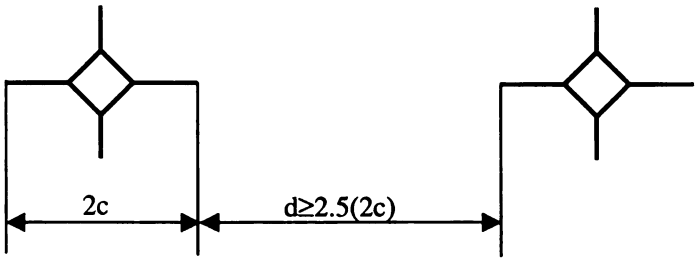

(a)

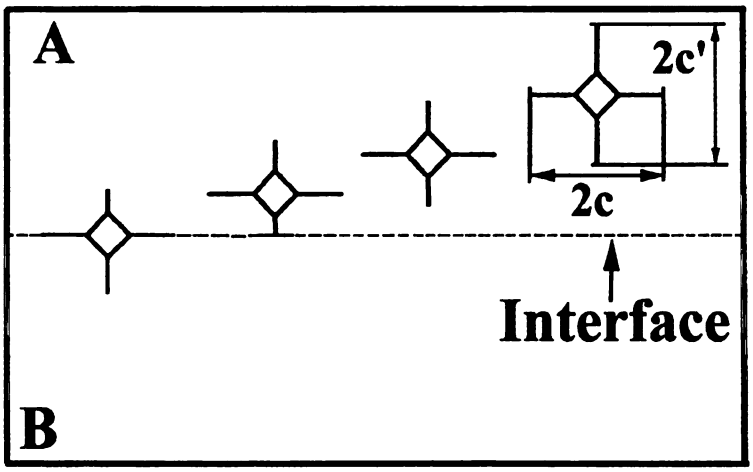

(b)

Figure 2.4 shows (a) the indentation spacing and the (b) scheme of the test to check the strength of the interface.

Chapter III

Experimental Results

3.1 Introduction

This section of the thesis describes the microwave and conventional spin-on interlayer joining of zirconia and MaCor™, the microwave joining of polycrystalline alumina with polycrystalline alumina, and polycrystalline alumina with polycrystalline partially stabilized zirconia, and the conventional joining of polycrystalline and single crystal alumina. The interfacial microstructures of these joined samples have been examined using optical microscopy (OM), scanning electron microscopy (SEM), and transmission electron microscopy (TEM). The interfacial toughness evaluation of these joined samples have been examined using indentation tests. These comprehensive interfacial microstructural and mechanical properties studies of the joined specimens resulted in a better understanding of the relationship between interfacial microstructures and mechanical properties associated with the joining process.

3.2 As-received materials

Prior to joining, the microstructures of the sintered 3 mol% yttria-zirconia, as-received glass ceramics MaCor™, and 96% and 98% polycrystalline alumina specimens were evaluated using TEM. In addition, the silica spin-on interlayer thickness was measured using SEM.

3.2.1 MaCor™ and 3-mol% yttria-zirconia

Figure 3.1 shows the microstructures of (a) MaCor™ and (b) zirconia. The commercial glass ceramic MaCor™ consisted of approximately 55% uniformly and

randomly distributed fluorophlogopite mica ($KMg_3AlSi_3O_{10}F_2$) crystals in glass matrix. This highly interlocked microstructure is the key to MaCor™'s machinability, which results from the fractures propagating by broaching along cleavage planes of the mica or the mica-glass interfaces [Grossman 1978]. Then micro-cracks are repeatedly deflected, blunted, and arrested, resulting in excellent machinability. Diffraction patterns (Figure 3.1(a)) of the matrix phase reveal an amorphous structure, consistent with that expected for the borosilicate glass [Corning].

The sintered zirconia consisted of monoclinic/tetragonal plates in equiaxial cubic grains with grain sizes approximately 0.5 μm (Figure 3.1(b)). The cross-sectional surface grain morphology of the sintered and finely polished zirconia prior to coating was evaluated using TEM. After polishing and cleaning, the zirconia shows an almost perfectly flat surface without any wetting or surface grain boundary grooves (Figure 3.2).

3.2.2 Polycrystalline alumina

Figure 3.3 shows the microstructures of as-received 98% (a) and 96% (b) polycrystalline alumina. The commercial 96% polycrystalline alumina consisted of elongated α-Al_2O_3 grains, with approximately 20% intergranular grain boundary phase, due to the presence of impurities CaO, BaO, and SiO_2. Diffraction patterns (Figure 3.3(b) inset) of the intergranular grain boundary phase reveal an amorphous structure, consistent with that expected for the aluminosilicate glass [Brydson 1998]. In contrast, the 98% alumina contained equiaxial α-Al_2O_3 grains with little grain boundary phase. Diffraction patterns from these alumina grains revealed the α-Al_2O_3 structure, with the particular grain in figure 3.3(a) oriented to $[0\bar{3}1]$.

3.2.3 As-spun and cured interlayer thickness

The silica spin-on interlayer thickness is an important factor in joining that can affect the final interfacial microstructure and strength. Excess interlayer may result in a thick bond region and modify the local microstructure. To determine the as-spun and cured silica interlayer thickness, one coated sapphire sample was sectioned in half after curing and examined using SEM. Figure 3.4 shows that the interlayer has a thickness in the range of 250~320 nm in the current research, slightly thicker than the 200 nm of manufacturer's specification [Emulsitone].

3.3 Joining of crystalline ceramics with non-crystalline ceramics

3.3.1 Microwave joining of Zirconia/MaCor™

This section describes the interfacial microstructure of polycrystalline 3 mol% yttria-zirconia/commercial glass ceramics MaCor™ joined by spin-on layer bonding. After polishing, coating, and curing, 3 mol% yttria-zirconia specimens were joined to MaCor™ using microwave heating at 1020°C for 20 minutes.

3.3.1.1 The interfacial microstructure of MaCor™/zirconia joined at 1020°C for 20 minutes using a spin-on interlayer

Cross-sectional SEM examination of the microwave joined zirconia/MaCor™ specimens revealed no observable reaction layers or interfacial phases in the join region. Figure 3.5 shows an example of a cross-sectional SEM image taken from one of the zirconia/MaCor™ specimens joined at 1020°C for 20 minutes. In these images, the interface is wavy and an interlocking microstructure results from grain boundary grooving of the zirconia grains at the zirconia/MaCor™ interface. The grain boundary grooves observed in the zirconia are roughly 0.25 μm deep and 0.5 μm wide (Figure 3.5). At some locations along the interface, porosity was observed in the MaCor™ near the

interface. Apparently, the joining process changes the surface grain morphology of the zirconia near the interface, resulting in a non-planar surface in the zirconia grains at the 3 mol% yttria-zirconia/MaCor™ interface (for example compare figures 3.2 and 3.5). Within the resolution limits of the SEM, no local modification of either the zirconia or the MaCor™ was observed near the interface.

In addition to the SEM examinations, TEM analysis of the joined specimens was carried out to provide a more detailed understanding of the interfacial and bulk microstructures present. At the higher magnifications and resolution offered by TEM, no silica bond interlayer was observed in the joined 3 mol% yttria-zirconia/MaCor™ interfacial region (Figure 3.6, 3.7 and 3.8). Presumably the spin-on interlayer silica and/or any other possible reaction product(s) diffused or dispersed into the surrounding parent ceramics, leaving a perfectly bonded interface. Figure 3.6 shows an example of a cross-sectional TEM image, which shows an interlocking microstructure resulting from grain boundary grooving of the zirconia grains at the zirconia/MaCor™ interface. Diffraction patterns of the MaCor™ matrix near the interface (Figure 3.7(b)) reveal an amorphous structure, consistent with that expected for the borosilicate glass phase present in the as-received MaCor™ specimens. A diffraction pattern from a mica plate near the interface (Fig. 3.7(a)) shows that this particular plate is oriented to the $[3\bar{1}1]$-zone axis of the fluorophlogopite mica [Corning]. The 3-mol% yttria-zirconia near the interface has a grain size about 0.5 μm (Figure 3.8).

The 3 mol% yttria-zirconia grains have been wet and dissolved along the grain boundaries by the borosilicate glass matrix phase of the MaCor™, resulting in intimate bonding between the zirconia and MaCor™ and a non-planer interface with significant

interlocking (Figure 3.6, 3.7 and 3.8). The grain boundary grooves observed using TEM, approximately 0.2 μm deep and 0.4 μm wide, are consistent with the SEM observations (Figure 3.5).

The joining process does not appear to change the microstructure of either the MaCor™ or the zirconia near the interface, other than the grain boundary grooves in the zirconia grains at the zirconia/MaCor™ interface. The interfacial microstructures were compared to the microstructures of the base materials examined at locations away from the interface. The specimens were examined up to the electron transparency limits imposed by the sample thinning process. The microstructure at the interface was found to be similar to the microstructure at these electron transparency limits, 10 μm away from the interface for the zirconia (Figure 3.9) and 100 μm for the MaCor™ (Figure 3.10). In the zirconia (Figure 3.9), the grain size remained consistent at approximately 0.5 μm, with a distribution of monoclinic plates consistent with the base material. In the MaCor™ (Figure 3.10), the size distribution and volume fraction of mica plates did not change with distance from the interface. This shows that the microstructure of both the zirconia and the MaCor™ near the joint region has not been significantly affected by the joining process, except for the zirconia grain boundary grooves at the interface. Microstructures similar to those shown in figure 3.5-3.9 were observed in other joined zirconia/MaCor™ samples.

3.3.1.2 Indentation tests

In addition to microstructural analysis, Vickers indentation tests were carried out on the joined zirconia/MaCor™ to estimate the interfacial fracture toughness of the joint at the gross scale. By placing a series of Vickers indentations in the zirconia side of the

interface and comparing the crack lengths at different orientations of the far and near field interface indentations, the residual stress and interfacial fracture toughness of the joint can be estimated.

Vickers indentation tests (Figure 3.11(a)) showed that the radial crack length near the zirconia/MaCor™ interface in the zirconia was longer in the direction of parallel to the interface than perpendicular to the interface. This thermal residual stress profile is evidently caused by a thermal expansion coefficient difference and elastic mismatch between the zirconia and MaCor™. This means that the radial crack experiences a compressive stress field in the direction of parallel to the interface and a tensile stress field in the direction perpendicular to the interface. Zirconia, which has a lower thermal expansion coefficient than that of MaCor™, experiences a compressive stress in the direction of parallel to the interface. Correspondingly, MaCor™ experiences a tensile stress in the direction of parallel to the interface. Furthermore, the porosity in the MaCor™ near the interface did not appear to affect the crack propagation (Figure 3.11(a) and (b)). In addition, due to the Young's modulus of zirconia being much higher than that of MaCor™, the indentation cracks in the direction of parallel to the interface (Figure 3.11(b)) propagated toward the interface [Lardner 1990].

Furthermore, a radial crack (Figure 3.11(c)) placed in the zirconia near the interface propagated across the interface into the MaCor™ without deflection at the interface, indicating the interfacial toughness was at least 60 percent of that of the bulk ceramics. This suggests that this joining method, unlike others [Ureña 1992, Ferraris 1998], can result in reasonably strong interfaces without major modification of the parent ceramics.

3.3.2 Conventional joining of zirconia/MaCor™

Similar to the microwave joining of zirconia/MaCor™ using a silica spin-on layer bonding, conventional joining of polycrystalline 3 mol% yttria-zirconia and commercial glass ceramics MaCor™ was carried out with and without a spin-on interlayer in relation to a number of processing variables, such as joining temperature and time. Joining via conventional versus microwave heating was assessed by comparing the experimental temperatures and times required for successful bonding. Cross-sectional SEM, TEM, and indentation tests were used to investigate the interfacial microstructure and interfacial toughness development of MaCor™ and zirconia joined at different temperatures with or without the aid of an amorphous interlayer, respectively.

3.3.2.1 Effect of heating mode on the joining of zirconia and MaCor™

Although MaCor™ and zirconia were completely joined with a spin-on interlayer by heating at 1020°C for 20 minutes using microwave heating, successful joining of the MaCor™ and zirconia with the same silica spin-on interlayer was not achieved under the same conditions of joining time, temperature, and specimen size, when conventional heating was employed. Instead, conventional heating at 1070°C for 60 minutes was required to achieve good bonding (Table 3.1). This difference in joining behavior is most likely due to differences in the mechanisms involved in microwave and conventional heating. Although the silica interlayer has a very low dielectric loss factor that makes it essentially transparent to microwaves, the difference between the dielectric behavior of the interlayer and surrounding base materials could result in preferential heating at the interface, resulting in faster interface development during microwave heating [Loehman 1993, 1999]. In contrast, in conventional heating, the heat flows from the surrounding bulk material to the interface without preferential heating at the interface.

3.3.2.2 Conventional joining of MaCor™/zirconia at 1070°C for 60 minutes using a spin-on interlayer

Similar to the studies of MaCor™/zirconia joined with microwave heating, cross-sectional SEM examination of the MaCor™/zirconia specimens joined at 1070°C for 60 minutes using conventional heating revealed no observable reaction layers or interfacial phases in the bond region (Figure 3.12). The MaCor™/zirconia interface was wavy and no porosity was observed in the MaCor™ near the interface.

In addition to the SEM examinations, TEM examination of the MaCor™/zirconia specimens joined at 1070°C for 60 minutes using conventional heating revealed intimate contact between the zirconia and MaCor™ without any observable reaction layers in the joint (Figure 3.13 and 3.14). This non-planer interface between zirconia and MaCor™ appears to have resulted from the wetting and dissolution of zirconia along the grain boundaries (Figure 3.13 and 3.14), similar to the interfacial microstructure of microwave MaCor™/zirconia joined at 1020°C for 20 minutes (Figure 3.7). Near the interface, the mica plates were more rounded than those further from the interface, suggesting the mica plate morphology changes. Despite this change in morphology, a diffraction pattern (Figure 3.13(a)) from one of these rounded plates near the interface revealed the fluorophlogopite ($KMg_3AlSi_3O_{10}F_2$) mica structure, with the particular plate oriented to $[5\bar{4}2]$. As expected for the borosilicate glass matrix phase of MaCor™, an amorphous diffraction pattern is observed from the MaCor™ matrix (Figure 3.13(b)). The microstructures of the MaCor™ (Figure 3.15) and zirconia (Figure 3.16) in the joined MaCor™/zirconia specimens were consistent with those observed in unjoined samples of MaCor™ and zirconia heat treated at 1070°C for 60 minutes, respectively.

3.3.2.2.1 Indentation tests

As in indentation studies of microwave joined MaCor™/zirconia, Vickers indentation testing (Figure 3.17) of the zirconia/MaCor™ joined at 1070°C for 60 minutes using conventional heating shows that a radial crack placed in the zirconia near the interface propagated across the interface into the MaCor™ without deflection at the interface, indicating the interfacial toughness was at least 60 percent of that of the bulk ceramics. This suggests that this joining approach, using either conventional or microwave heating, can result in reasonably strong interfaces. No significant differences in the interfacial microstructure and interfacial toughness developed between conventional versus microwave joined zirconia and MaCor™.

3.3.2.3 Conventional joining of MaCor™/zirconia at 1070°C for 120 minutes using a spin-on interlayer.

Extending the time to join the MaCor™ to zirconia to 120 minutes of conventional heating at 1070°C using the silica spin-on interlayer resulted in further microstructure development at the interface (Table 3.1). As with samples joined for 60 minutes, cross-sectional TEM images revealed no silica bond layer or reaction phases in the joint region (Figure 3.18 and 3.19). Further rounding of the mica plates near the interface was observed, forming a nearly continuous mica interfaces layer, with many mica plates now incorporated into the interface. This morphology dominates the entire observable joint region (Figure 3.18 and 3.19), suggesting more extensive interlocking. However, the distorted plates continue to display the fluorophlogopite ($KMg_3AlSi_3O_{10}F_2$) mica structure, as shown in the figure 3.19. Again, except for the molding of the mica platelets

into the zirconia/MaCor™ interface, the morphology of the MaCor™ did not change near or at a distance from the interface.

3.3.2.4 Conventional joining of MaCor™/zirconia joined at 1070°C for 60 minutes without the use of a spin-on interlayer.

To determine the role of the spin-on interlayer, samples joined without an interlayer were compared to samples joined with an interlayer. These comparisons were made using the MaCor™/zirconia samples joined using conventional furnace heating at 1070°C for 60 minutes (Table 3.1). Without the aid of a silica interlayer, MaCor™ and zirconia were successfully joined at 1070°C for 60 minutes. Cross-sectional SEM examinations revealed grain boundary grooving of the zirconia grains without any observable interfacial phases (Figure 3.20), similar to the interfacial microstructure of the MaCor™/zirconia joined using a spin-on interlayer.

TEM studies of the MaCor™/zirconia joined without an interlayer showed intimate bonding between the zirconia and MaCor™ without any interfacial phases (Figure 3.21). However, near the interface in the MaCor™, no rounding of the mica plates was observed, which is different than the interfacial microstructure of MaCor™/zirconia joined using spin-on interlayer. As expected, the microstructures of the base MaCor™ in the zirconia/MaCor™ joined with and without a silica interlayer were the same, consistent with that of unjoined MaCor™ annealed at 1070°C for 60 minutes (Figure 3.22).

The above results show that the zirconia and MaCor™ can be successfully joined with or without the aid of a silica spin-on interlayer. Thus, despite the fact that a spin-on interlayer has been shown to greatly enhance the joining of crystalline ceramics [Lee

2000], the interlayer, which has an amorphous structure, is not necessary to successfully bond the zirconia to MaCor™. This is because MaCor™ is a glass-ceramic composite containing a 45% volume fraction of amorphous matrix phase and this amorphous matrix phase has the similar joining characteristics as the silica interlayer. Therefore, no significant microstructural differences developed between using and without using a silica spin-on interlayer in the joining of the zirconia and MaCor™.

3.3.2.4.1 Indentation tests

Similar to the indentation studies of MaCor™/zirconia joined using a spin-on interlayer (Figure 3.11), Vickers indentation testing (Figure 3.23) carried out on MaCor™/zirconia specimens joined without the use of a silica interlayer showed that a indentation induced crack placed in the zirconia propagated across the interface into the MaCor™ without deflection at the interface, indicating reasonably strong interfaces. This suggests that the joining of zirconia and MaCor™ is not greatly enhanced or hindered by the presence of a silica spin-on interlayer. Therefore, no significant microstructural and interfacial toughness differences developed between joining using a interlayer versus joining without the use of a silica interlayer of zirconia and MaCor™.

3.3.2.5 Joining of MaCor™/MaCor™ and zirconia/zirconia.

To further examine the microstructure development of the early stages of the zirconia and the MaCor™ joining process, zirconia/zirconia and MaCor™/MaCor™ specimens were joined using silica spin-on interlayers and conventional heating. When conventionally heated at 1070°C, zirconia and zirconia failed to join for times as long as 60 minutes, but MaCor™ and MaCor™ were successfully joined using a silica spin-on interlayer, in as little as 10 minutes (Table 3.1).

TEM observation of MaCor™/MaCor™ joined at 1070°C for 10 minutes using a spin-on interlayer revealed a varying microstructure along the interface. At some locations, an interfacial phase was observed in the middle of the joint region (Figure 3.24). In these regions, the interface between this interfacial phase and the MaCor™ was wavy and evidence of wetting and dissolution of the MaCor™ along the interface was observed, suggesting an interfacial reaction has occurred between the MaCor™ and the silica. The bond region was less than 0.5 μm thick and diffraction pattern analysis showed that the interfacial phase is amorphous (Figure 3.24 inset). At other locations along the joint, Mica platelets incorporated into the interface (Figure 3.25).

3.4 Joining of crystalline ceramics with crystalline ceramics

The nature of the interfacial microstructures of joined ceramics is key to understanding the fundamental materials joining process. However, the cross-sectional SEM, TEM, and indentation studies clearly indicated that the interfacial microstructural and mechanical property differences between conventional versus microwave joined zirconia and MaCor™ is trivial due to the glassy nature of MaCor™. In addition, no significant interfacial microstructural and mechanical property differences developed between joining with and without using interlayers in the joining of the zirconia and MaCor™. Thus, the final objective of current study was to focus on the interfacial microstructures of joined crystalline ceramics with crystalline ceramics. The nature of microstructure and interfacial toughness development in the bond region of zirconia and 98% polycrystalline alumina, 98% polycrystalline alumina and 98% polycrystalline alumina, sapphire and 98% polycrystalline alumina, and sapphire and 96% polycrystalline alumina were assessed.

3.4.1 Effect of heating mode on the joining of alumina/alumina

98% polycrystalline alumina and alumina were joined with a silica spin-on interlayer by heating at 1340°C for 20 minutes using microwave and conventional heating under the same conditions (Table 3.2). The joint developed via microwave heating was successful and robust. However, the joint developed via conventional heating did not appear very robust, with the samples falling apart during attempts at SEM sample preparation. Similar to the joining behavior of the zirconia and MaCor™, this difference in joining behavior is most likely due to the preferential heating at the interface and faster interface development during microwave heating.

3.4.2 The interfacial microstructure of polycrystalline alumina/alumina joined at 1340°C for 20 minutes

TEM examinations performed on the microwave joined 98% polycrystalline alumina/98% polycrystalline alumina revealed the interface to be nearly indistinguishable from the base polycrystalline alumina. The approximate location of the interface can only be identified due to residual porosity in the interfacial region. Figure 3.26 shows the interfacial microstructure of joined 98% polycrystalline alumina/alumina via microwave joining. The grains along the joint were found to be equiaxial and interlocked, with no evidence of the interlayer or any interfacial phases. This essentially perfect joining made it impossible to identify the original interface (Figure 3.26). The alumina grains have equilibrated along the joint, leading to a non-planar interface with a structure comparable with the bulk grain boundary structure. In addition, no observable microstructural difference is identified between the 98% polycrystalline alumina near the interface and the parent ceramics up to the electron transparency limit, 10 μm away from the interface

for both sides of alumina. This shows that the microstructure of the polycrystalline alumina near the joint region has not been greatly affected by the joining process.

3.4.3 The interfacial microstructure of polycrystalline zirconia/alumina joined at 1500°C for 20 minutes

As in the studies of 98% polycrystalline alumina/alumina joined with microwave heating, cross-sectional TEM examination of the 3 mol% yttria-zirconia/polycrystalline alumina specimens joined at 1500°C for 20 minutes using microwave heating revealed no observable reaction layers or interfacial phases in the joint region. Presumably the interlayer diffused into the surrounding parent ceramics, leaving a perfectly bonded interface. Figure 3.27 shows a TEM micrograph of an interface in an alumina/zirconia specimen joined at 1500°C for 20 minutes using silica interlayer. In these images, the interface is wavy and an interlocking microstructure is evident. The interlocking is on the scale of grain sizes within the specimens. At the higher magnifications offered by TEM, the interface boundaries appear to have taken up low energy orientations, with morphologies similar to normal grain boundaries [Case 2001] (Figure 3.28). As before, the joining process does not greatly affect the microstructures of the base ceramics.

3.4.4 Joining of sapphire and polycrystalline alumina

The work summarized in the following section was carried out to investigate the interfacial microstructural and interfacial toughness development in joined single crystal and polycrystalline alumina. Single and polycrystalline alumina were chosen for this study because the sapphire/polycrystalline alumina interface, unlike in the joining of like polycrystals (Figure 3.26), will always be distinguishable, even for perfect bonding. In addition, the effects of alumina purity, joining temperature, time, and the use of

interlayers on the interfacial microstructure evolution were assessed using a combination of OM, SEM and TEM.

3.4.4.1 Joining of sapphire and 98% polycrystalline alumina

Sapphire and 98% polycrystalline alumina were successfully joined in 180 minutes at temperatures of 1400°C, 1450°C, and 1475°C with the aid of a silica interlayer. In contrast, two pairs of sapphire and 98% alumina samples failed to join under the same conditions without a silica interlayer (Table 3.3), indicating that the silica interlayer substantially promotes the joining of sapphire and 98% polycrystalline alumina.

Figure 3.29 shows optical microscopy images of 98% alumina/sapphire joined at 1400°C, 1450°C, and 1475°C for 180 minutes using a silica interlayer. With increasing joining temperature, the thickness of the interfacial reaction layer decreased and joining was more complete. At 1400°C (Figure 3.29(a)), a reaction layer approximately 5 μm thick, characterized by regions of both light contrast and larger amounts of dark-gray contrast, was found in the joint region. Note that this thickness is more than an order of magnitude greater than the spin-on interlayer thickness. Energy dispersive spectroscopy (EDS) revealed similar spectra for the dark-gray contrast at the joint and the base mounting material Bakelite. This mounting material most likely flowed into the joint during the sample polishing and indicates the joining was not complete and voids or porosity existed between the sapphire and alumina at this stage of joining. In addition, the joint did not appear very robust, with the samples falling apart during attempts at TEM sample preparation. Figures 3.29(b) shows cross-sectional optical microscopy image of 98% alumina and sapphire joined at 1450°C for 180 minutes. The joining was more complete than in the specimen joined at 1400°C, and only small amount of residual

mounting material was observed. Cross-sectional optical microscopy images of 98% alumina and sapphire joined at 1475°C for 180 minutes (Figures 3.29(c) and (d)) illustrate two slightly different interfacial microstructures in the same joined bulk specimen. The joining was more complete than in the specimen joined at 1450°C and no evidence of residual mounting materials was observed. At some locations, the reaction layer was found to be as thin as 1 μm (Figure 3.29(c)), while at other locations the reaction layer was up to of 3 μm thick (Figure 3.29(d)).

In addition to the optical microscopy, cross-section TEM examination of the sapphire/alumina interface joined at 1475°C for 180 minutes was carried out to investigate if any additional reaction phases were present on a finer scale. Consistent with the optical microscopy observations (Figure 3.29(c) and (d)), TEM examination of the sapphire and alumina joined at 1475°C for 180 minutes showed two different interfacial microstructures in the same joined bulk specimen. At some locations (Figure 3.30(a)), the interlayer between the sapphire and alumina has apparently wet and dissolved alumina along the grain boundaries, leaving an amorphous interfacial phase (see inserted diffraction pattern in figure 3.30(a)) along the sapphire and alumina interface and the near-interface alumina grain boundaries. The wetting penetrated the alumina grain boundaries to a depth of approximately 1 μm. The amorphous interfacial layer has a thickness around 0.5~1 μm, consistent with some of the optical microscopy observations (Figure 3.29(c)). The thickness is in the range expected from the combination of two coated surfaces (each 250~320 nm thick), but may also be enhanced somewhat by the additional dissolution of the base alumina into the amorphous phase. At other locations along the interface, a very fine crystalline phase, with a grain size of about

100 nm, was observed (Figure 3.30(b)). In these regions the joint between the sapphire and alumina has a thickness of approximately 3 μm, again consistent with optical microscopy observations (Figure 3.29(d)). Diffraction patterns from the joint show fine rings, typical of randomly oriented fine crystalline grains or particles (Figure 3.30(c)). These ring patterns were found to be consistent with the α-Al_2O_3 structure. As expected, no significant microstructural differences were observed, beyond those immediately at the 2~3 μm interfacial region.

To investigate the microstructural evolution, sapphire and 98% alumina joined at 1475°C for 180 minutes were re-heated at 1475°C for an additional 300 minutes. Optical microscopy revealed close contact between the sapphire and alumina, without any observable residual reaction layer (Figure 3.31(a)). However, TEM examination (Figure 3.31(b)) found that the amorphous layer had decreased in thickness to approximately 0.1~0.5 μm. The sapphire interface remained smooth, with the alumina interface becoming wavy, due to continued wetting by the amorphous phase. As before, the base 98% alumina and sapphire showed no microstructural changes for 180+300 minutes heat treatment at 1475°C. Furthermore, no regions of fine polycrystalline alumina were observed at this longer joining time.

3.4.4.2 Joining of sapphire and 96% polycrystalline alumina

Similar to the joining of sapphire with 98% polycrystalline alumina, sapphire and 96% polycrystalline alumina were successfully joined together using a silica interlayer at 1475°C for 180 minutes (Table 3.3). However, unlike the joining of sapphire with 98% polycrystalline alumina, sapphire and 96% polycrystalline alumina were also successfully joined together without the use of a silica interlayer at 1475°C for 180 minutes. The

interfacial microstructures developed in joining sapphire and 96% alumina varied depending on if an interlayer was used (Figure 3.32). With the aid of a silica interlayer, the amorphous reaction layer was approximately 0.5~1 μm thick (Figure 3.32(a)). In contrast, when an interlayer was not used, the resulting amorphous interfacial phase was, somewhat surprisingly, much thicker, on the order of 5~10 μm thick (Figure 3.32(b)). The thicker interfacial phase appears to result from a capillary flow of the amorphous grain boundary phase in the 96% alumina to the interface, driven by the tendency of the system to restore the equilibrium when a higher energy interface is introduced. It appears that the silica interlayer could inhibit this flow.

In addition to the SEM examinations, cross-section TEM examination of the sapphire and 96% alumina interface joined at 1475°C for 180 minutes using a silica interlayer revealed no silica bond interlayer or interfacial phases in the joint (Figure 3.33). Presumably the silica spin-on interlayer diffused into the surrounding parent ceramics. In addition, the amorphous interfacial layer has a thickness around 0.5~2 μm, consistent with SEM observations (Figure 3.33). As before, the joining process does not appear to change the microstructure of the polycrystalline alumina near the interface.

Reheating the interlayer joined sapphire/96% alumina samples for additional 300 minutes resulted in a decrease in the interfacial phase thickness. Figure 3.34 shows (a) secondary electron and (b) backscattered electron SEM images of the sapphire and 96% polycrystalline alumina joined at 1475°C for 180+300 minutes using a silica spin-on interlayer. With this longer joining time, the interfacial phase was no longer observable and the base polycrystalline alumina and sapphire were in direct contact (Figure 3.34). TEM analysis of the sapphire/96% polycrystalline alumina joined at 1475°C for 180+300

minutes (Figure 3.35) revealed a thin amorphous interfacial phase between the sapphire and the alumina. The sapphire and the alumina interfaces remained wavy. At some locations, the polycrystalline alumina grains and sapphire were in direct bonding without any interfacial phase.

3.4.4.3 Indentation tests

Vickers indentation testing showed that the radial crack length near the 96% polycrystalline alumina/sapphire interface joined at 1475°C for 180 minutes using a silica interlayer in the alumina equals in the direction of parallel to the interface and perpendicular to the interface (Figure 3.36(a)). This means that the thermal residual stress is negligible. In addition, an indentation induced crack (Figure 3.36(b)) placed in the polycrystalline alumina near the joint propagated across the polycrystalline alumina/sapphire interface into the sapphire without deflection, indicating the interfacial toughness was at least 60 percent of that of the bulk ceramics. However, crack deflection occurred at the polycrystalline alumina/sapphire interface joined at 1475°C for 180 minutes without the use of a silica interlayer, suggesting that the fracture energy of the interface is less than about 10~20 % of the bulk materials [Lee 1996]. This difference suggests that the silica interlayer dramatically promotes the joining of sapphire and 96% polycrystalline alumina, resulting a relatively strong interface.

Reheating the interlayer joined sapphire/96% alumina samples for additional 300 minutes resulted in a similar behavior in the indentation tests. The indentation induced crack propagated across the interface with no deflection (Figure 3.37). In addition, the radial crack length near the polycrystalline alumina/sapphire interface in the alumina was

equal in the direction of parallel and perpendicular to the interface, indicating that the thermal residual stresses due to joining are minimum.

Unfortunately, indentation tests were not carried out on the joined 98% polycrystalline alumina/sapphire because the limited number of joined specimens were instead sectioned for TEM analysis.

Table 3.1 The experimental condition and results for ceramics/ceramics joining via conventional heating in the present study. Please note, all experiments were done twice to verify joining results.

Specimens to be joined	Joining temperature (°C)	Joining time(min)	Coating	Results
MaCor™/zirconia	1020	20	Silicafilm™	Failed to join
MaCor™/zirconia	1020	40	Silicafilm™	Failed to join
MaCor™/zirconia	1020	60	Silicafilm™	Failed to join
MaCor™/zirconia	1070	20	Silicafilm™	Failed to join
MaCor™/zirconia	1070	40	Silicafilm™	Failed to join
MaCor™/zirconia	1070	60	Silicafilm™	Joined
MaCor™/zirconia	1070	60	No coating	Joined
MaCor™/zirconia	1070	120	Silicafilm™	Joined
MaCor™/MaCor™	1070	10	Silicafilm™	Joined
zirconia/zirconia	1070	60	Silicafilm™	Failed to Join

Table 3.2 outlines the experimental conditions and results for the joining of 3 mol% yttria-zirconia/polycrystalline alumina, and 98% polycrystalline alumina/98% polycrystalline alumina. Please note, all experiments were done twice to verify joining results.

Specimens to be joined	Joining temperature (°C)	Joining time (min)	Coating	Heating mode	Results
Polycrystalline alumina/alumina	1340	20	Silicafilm™	Microwave	Joined
Polycrystalline alumina/alumina	1340	180	Silicafilm™	Conventional	Joined
zirconia/alumina	1500	20	Silicafilm™	Microwave	Joined

Table 3.3 The experimental conditions and results for the joining of sapphire and polycrystalline alumina via conventional heating in the current research. Please note, all experiments were done twice to verify joining results.

Specimens to be joined	Joining temperature (°C)	Joining time (minutes)	Coating	Heating mode	Results
Sapphire/98% alumina	1400	180	Silicafilm™	Microwave	Joined
Sapphire/98% alumina	1475	180	Silicafilm™	Microwave	Joined
Sapphire/98% alumina	1475	180	No coating	Microwave	Failed
Sapphire/98% alumina	1475	180+300	Silicafilm™	Microwave	Joined
Sapphire/96% alumina	1475	180	Silicafilm™	Microwave	Joined
Sapphire/96% alumina	1475	180	No coating	Microwave	Joined
Sapphire/96% alumina	1475	180+300	Silicafilm™	Microwave	Joined

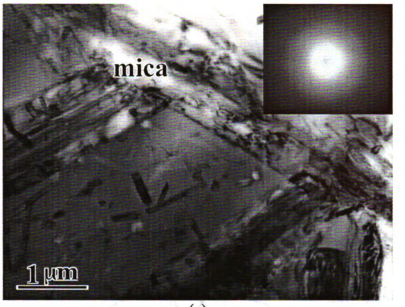

(a)

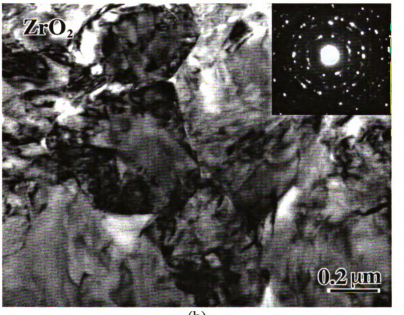

(b)

Figure 3.1 TEM images of the sintered as-received glass-ceramics MaCor™ (a) and 3 mol% yttria-zirconia specimens (b).

Figure 3.2 A cross-sectional TEM image showing the polished surface of the sintered, and cleaned 3 mol% yttria-zirconia specimens prior to coating showing the surface grains morphology.

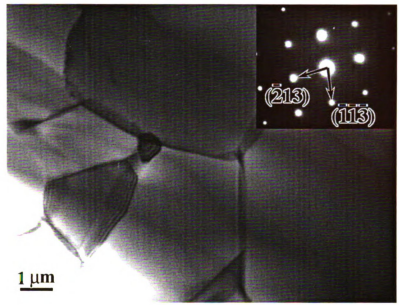

(a)

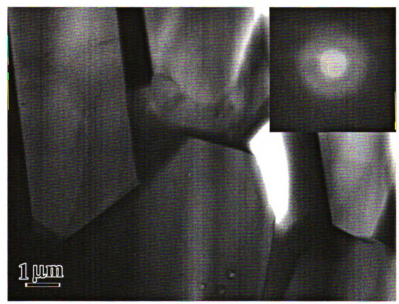

(b)

Figure 3.3 TEM images of the as-received microstructures of 98% (a) and 96% (b) polycrystalline alumina. The commercial 96% polycrystalline alumina (b) consists of platelike or elongated α-Al_2O_3 grains, with approximately 20% intergranular grain boundary phase. The diffraction pattern of the intergranular grain boundary phase reveals an amorphous structure, consistent with that expected for the aluminosilicate glass [Brydson 1998]. However the 98% alumina (a) contains equiaxial α-Al_2O_3 grains with little grain boundary phase.

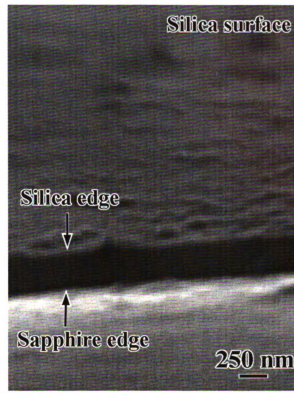

Figure 3.4 SEM image of silica interlayer showing the interlayer has a thickness in the range of 250~320 nm thick after spinning at 3000 rpm and curing at 200°C for 20 minutes.

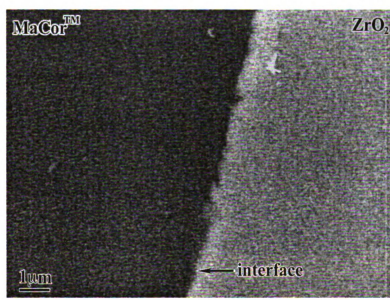

Figure 3.5 An SEM micrograph of the microwave joined zirconia/MaCor™ showing the bond interface. At the gross scale the interface is straight, locally the zirconia contains grain boundary grooves. No interfacial phase(s) were observed.

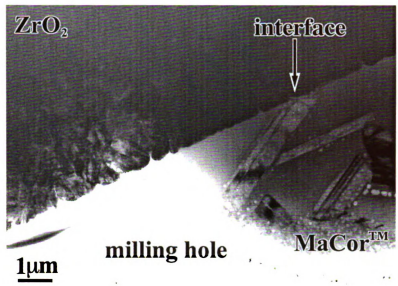

Figure 3.6 Low magnification TEM image of the interface between the 3 mol% yttria-zirconia and the MaCor™ joined at 1020°C for 20 minutes using microwave heating. Differential ion milling in the specimens results in the MaCor™ being thinned back with respect to the zirconia, resulting in occasional perforation of the MaCor™ specimen near the interface.

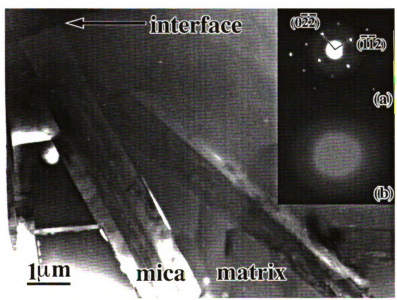

Figure 3.7 A TEM image of the MaCor™ near the interface. Inserts showing (a) a diffraction pattern from a single mica plate and (b) a diffraction pattern from matrix areas between the mica plates.

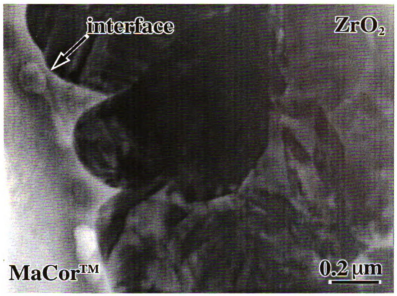

Figure 3.8 A TEM image of the interface between the 3 mol% yttria-zirconia and the MaCor™ showing that the zirconia has been strongly wetted and dissolved along grain boundaries, resulting in a non-planer interface.

Figure 3.9 A TEM image of the microstructure of the zirconia in a joined 3 mol% yttria-zirconia/MaCor™ specimen at a location at about 10 μm away from the interface. The microstructure of the zirconia at this location is similar to that of the zirconia microstructure near the interface (Figure 3.6).

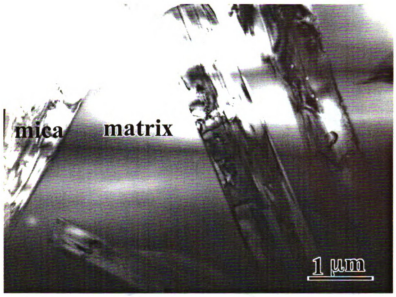

Figure 3.10 A TEM image of the MaCor™ microstructure in a joined 3 mol% yttria-zirconia/MaCor™ specimen at a location at about 100 μm away from the interface. The microstructure at this location is similar to the microstructure of the MaCor™ near the interface (Figure 3.5). Due to a range of mica platelet orientations, the apparent dimensions differ from platelet to platelet.

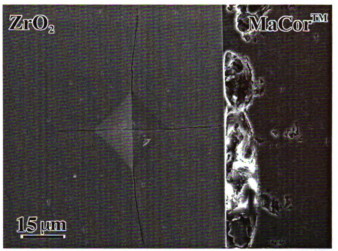

(a)

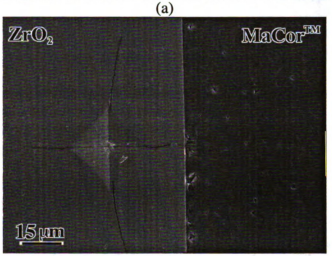

(b)

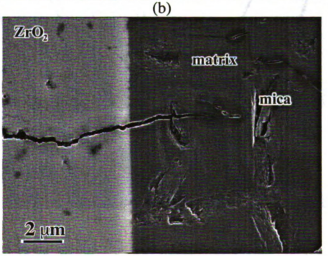

(c)

Figure 3.11 A Vickers indentation testing shows that the radial crack near the microwave joined zirconia/MaCor™ interface with (a) and without (b) observable porosity in the MaCor™ has different length on the vertical and horizontal directions, and (c) propagates across the interface from zirconia into the MaCor™ without deflection

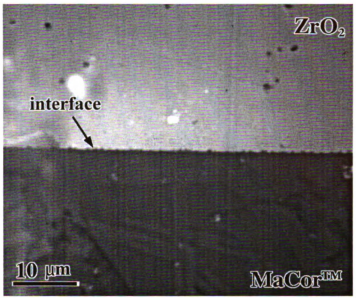

Figure 3.12 An SEM micrograph of the zirconia/MaCor™ joined at 1070°C for 60 minutes using a silica spin-on interlayer showing the bond interface.

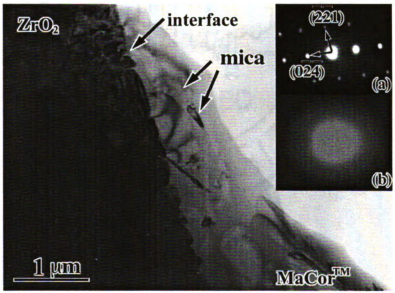

Figure 3.13 A TEM image of the zirconia/MaCor™ joined at 1070°C for 60 minutes using a silica spin-on interlayer. Diffraction pattern from one of the rounded plates near the interface revealed the mica structure (a), oriented to [$5\bar{4}2$]. Diffraction pattern from the matrix of MaCor™ revealed an amorphous structure (b).

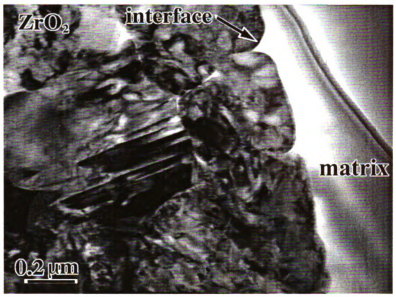

Figure 3.14 The interfacial microstructure of the zirconia/MaCor™ joined at 1070°C for 60 minutes using a silica spin-on interlayer showing intimate bonding between zirconia and the matrix of MaCor™.

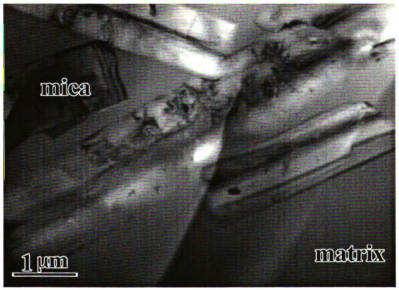

Figure 3.15 A TEM image of the bulk MaCor™ microstructure. The center of the image is about 5 μm away from the zirconia/MaCor™ interface. The specimens were joined at 1070°C for 60 minutes using a spin-on interlayer.

Figure 3.16 A TEM image of the bulk zirconia microstructure. The center of the image is about 5 μm away from the zirconia/MaCor™ interface. The diffraction pattern is consistent with a two phases partially stabilized zirconia structure.

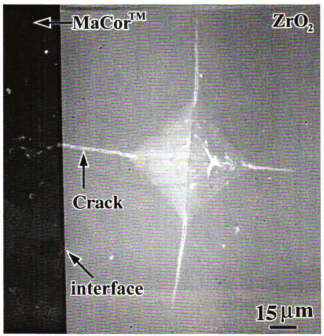

Figure 3.17 A Vickers indentation testing shows that the radial crack near the joined zirconia/MaCor™ interface propagates across the interface from zirconia into the MaCor™ without deflection.

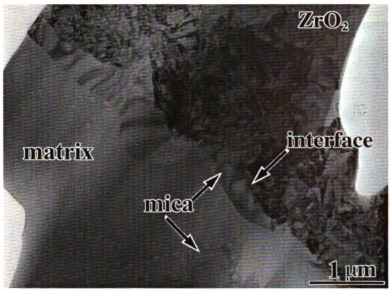

Figure 3.18 TEM brightfield micrograph of the zirconia/MaCor™ interface joined at 1070°C for 120 minutes using a silica spin-on interlayer shows mica plates incorporated into the MaCor™/zirconia interface.

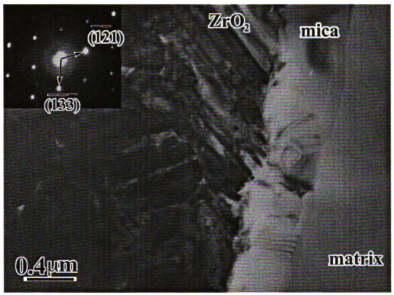

Figure 3.19 The interfacial microstructure of MaCor™ and zirconia joined at 1070°C for 120 minutes using a silica spin-on interlayer. Insert showing that selected area diffraction pattern of the distorted plates continue to display the mica structure.

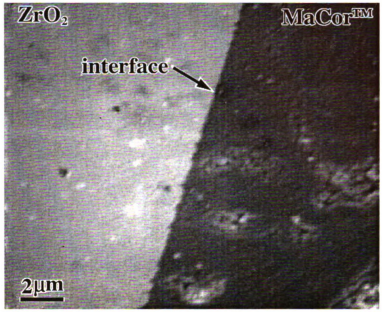

Figure 3.20 An SEM micrograph of the zirconia/MaCor™ joined at 1070°C for 60 minutes without the use of a silica interlayer showing the bond interface.

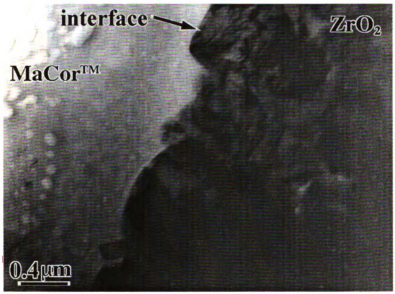

Figure 3.21 A TEM image of the zirconia and MaCor™ joined at 1070°C for 60 minutes without the use of a silica interlayer. No interfacial phase(s) were observed at the interface.

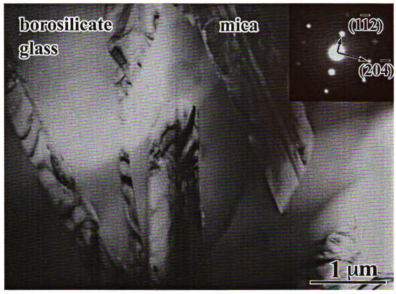

Figure 3.22 A TEM micrograph of MaCor™ (unjoined control) that was heated at 1070°C for 60 minutes. Insert shows the diffraction pattern from a single mica platelet ([241] orientation). MaCor™ heated at 1070°C for 120 minutes showed similar microstructure.

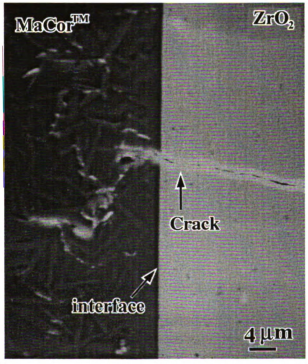

Figure 3.23 An SEM image of the Vickers indentation crack on the zirconia/MaCor™ joined at 1070°C for 60 minutes without the use of a silica spin-on interlayer in the zirconia side showing the radial crack propagates across the interface without deflection.

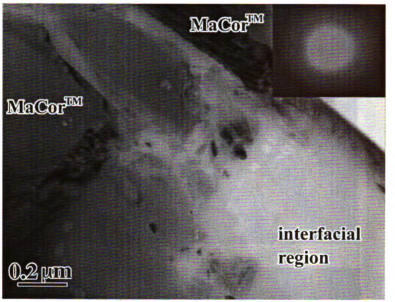

Figure 3.24 The interfacial microstructure of MaCor™ and MaCor™ joined at 1070°C for 10 minutes using a silica interlayer showing an amorphous interfacial region, as indicated by the inset diffraction pattern.

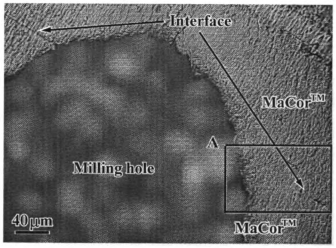
Interface
MaCor™
A
Milling hole
40 μm
MaCor™

(a)

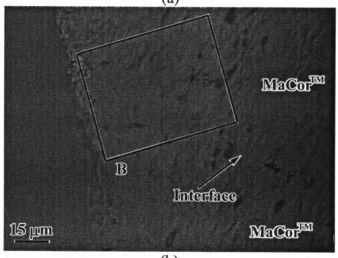
MaCor™
B
Interface
15 μm
MaCor™

(b)

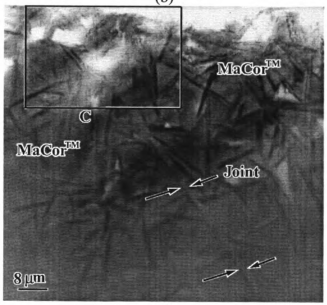
MaCor™
C
MaCor™
Joint
8 μm

(c)

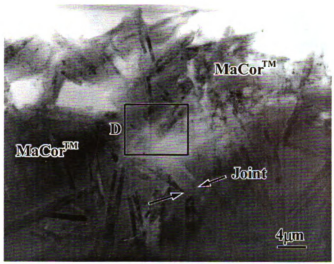

(d)

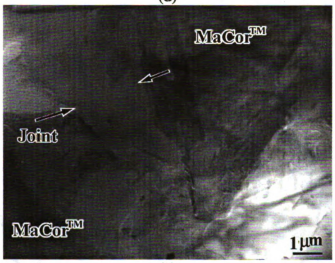

(e)

Figure 3.25 A series of images of the MaCor™ and MaCor™ joined at 1070°C for 10 minutes using a silica interlayer (a) optical micrograph of the TEM thin foil showing the MaCor™/MaCor™ interface, (b) higher magnification optical micrograph of the TEM thin foil showing the MaCor™/MaCor™ interface from box A, (c) low magnification TEM image from the area indicated on (b) showing the foil edge and interfacial region, (d) higher magnification TEM image from the area indicated on (c) showing the foil interfacial region, and (e) further higher magnification image showing mica plates incorporate into interface.

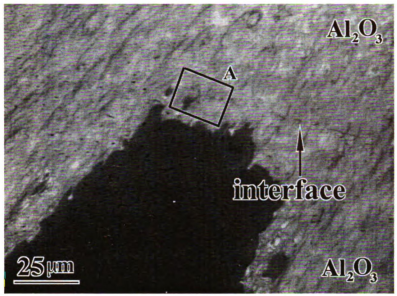

(a)

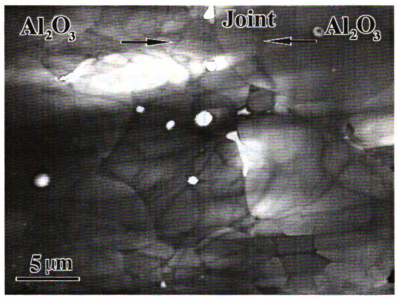

(b)

Figure 3.26 The interfacial microstructure of the microwave joined 98% polycrystalline alumina/98% polycrystalline alumina using a silica interlayer silica interlayer (a) optical micrograph of the TEM thin foil showing the alumina/alumina interface, (b) higher magnification TEM micrograph showing the equiaxed alumina grains cross the whole joint region, making the interface very difficult to distinguish from the base material.

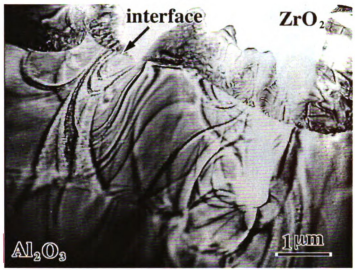

Figure 3.27 Low magnification TEM image of the interface between the 3 mol% yttria-zirconia and the polycrystalline alumina joined at 1500°C for 20 minutes using microwave heating.

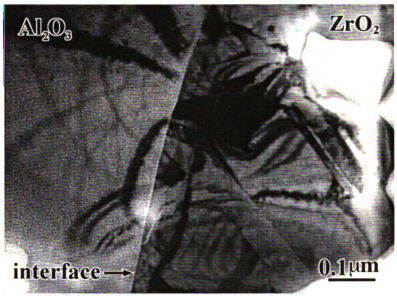

Figure 3.28 A TEM image of the interface between the 3 mol% yttria-zirconia and the polycrystalline alumina showing that no observable reaction layers or interfacial phases in the join region.

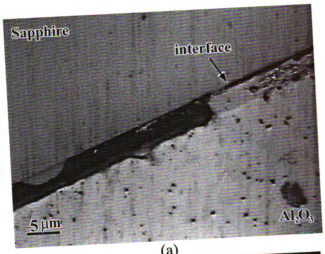
Sapphire
interface
5 μm
Al_2O_3

(a)

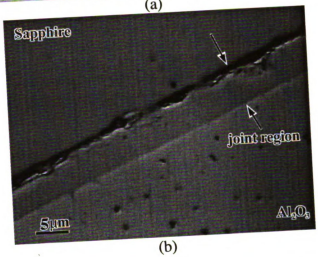
Sapphire
joint region
5 μm
Al_2O_3

(b)

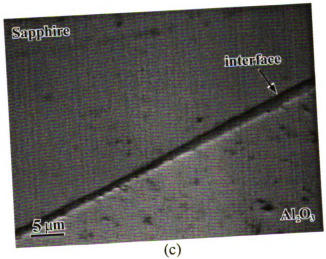
Sapphire
interface
5 μm
Al_2O_3

(c)

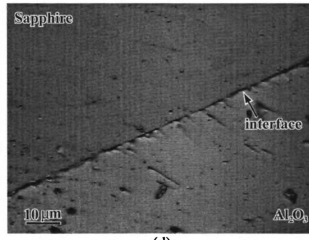

(d)

Figure 3.29 Optical microscopy images of sapphire/98% polycrystalline alumina joined at (a) 1400°C for 180 minutes, (b) 1450°C for 180 minutes, and (c, d) 1475°C for 180 minutes using silica interlayer that illustrate two different interfacial microstructures on the same joined bulk specimen. At some locations, the reaction layer is approximately 3 μm thick (c) while at other location reaction layer has a thickness only around 1 μm (d).

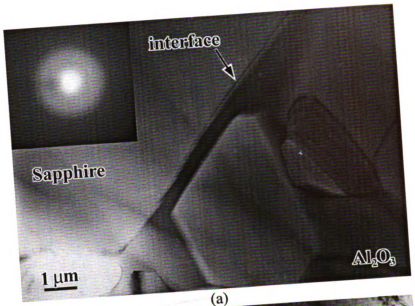
interface
Sapphire
Al_2O_3
1 μm

(a)

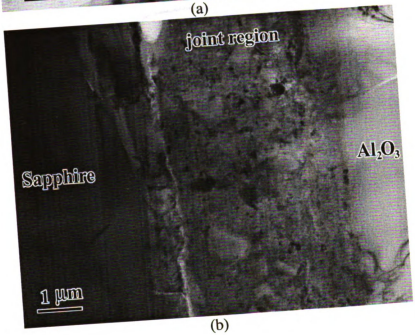
joint region
Al_2O_3
Sapphire
1 μm

(b)

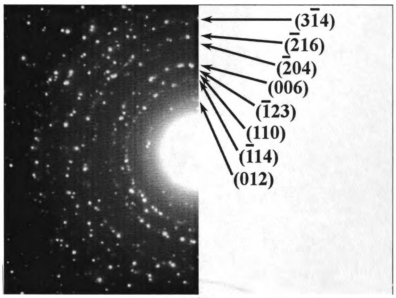

(C)

Figure 3.30 TEM images of sapphire/98% polycrystalline alumina joined at 1475°C for 180 minutes revealed two distinct interfacial microstructures at the joint. At some locations (a), the interfacial phase has a thickness around 0.5~1 μm, while at other locations, a fine distribution of alumina crystalline phase occurred at the joint (b) with indexed diffraction pattern (c).

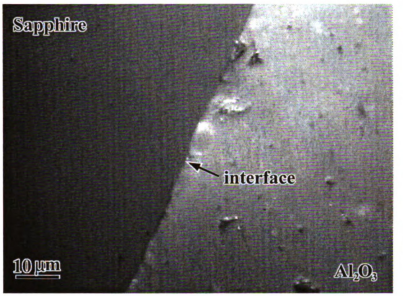

(a)

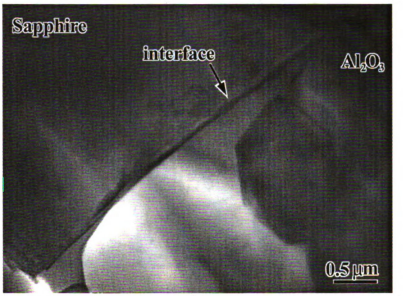

(b)

Figure 3.31 (a) Optical microscopy and (b) TEM images of the sapphire/98% polycrystalline alumina joined at 1475°C for 180+300 minutes using a silica spin-on interlayer.

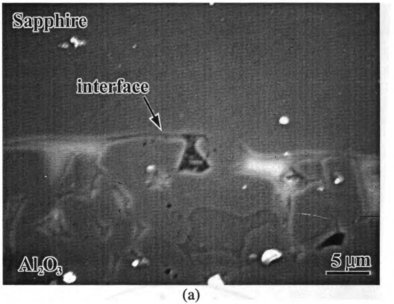

(a)

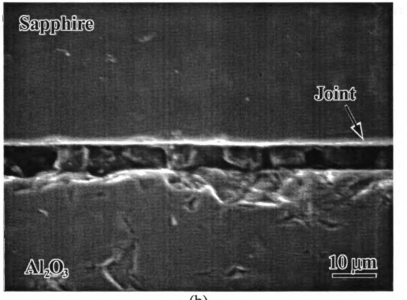

(b)

Figure 3.32 SEM images of the sapphire/96% polycrystalline alumina joined at 1475°C for 180 minutes (a) with and (b) without the use of a silica spin-on interlayer.

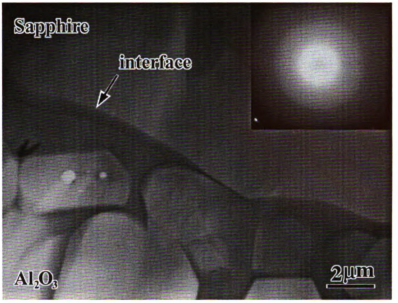

Figure 3.33 A TEM image of sapphire/96% polycrystalline alumina joined at 1475°C for 180 minutes using a silica interlayer. Insert shows the diffraction pattern from the amorphous interlayer.

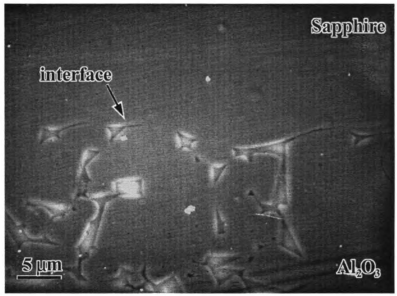

(a)

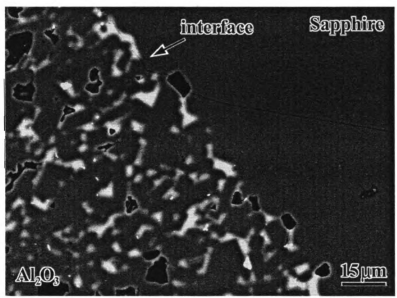

(b)

Figure 3.34 (a) Secondary and (b) backscattered electron SEM images of the sapphire/96% polycrystalline alumina joined at 1475°C for 180+300 minutes using a silica spin-on interlayer. The bright contrast in the polycrystalline alumina in the BSEM image (b) corresponds to grain boundary phases, the gray contrast corresponds to α-Al_2O_3 phase, and the black contrast corresponds to porosity.

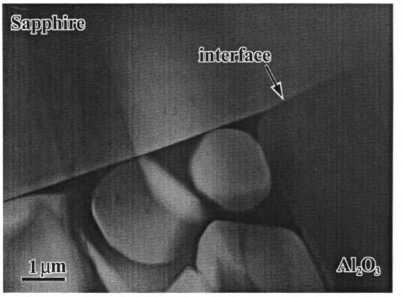

Figure 3.35 A TEM image of the sapphire/96% polycrystalline alumina joined at 1475°C for 180+300 minutes using a silica spin-on interlayer.

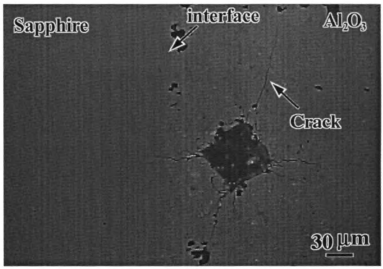

(a)

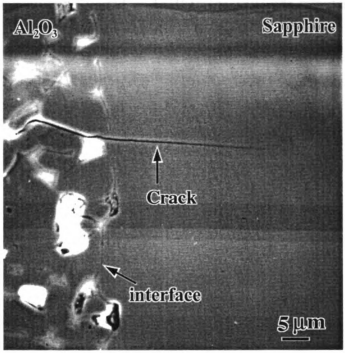

(b)

Figure 3.36 An optical microscopy (a) and SEM (b) images of the Vickers indentation crack on the sapphire/polycrystalline alumina joined at 1450°C for 180 minutes using a silica spin-on interlayer in the alumina side neat the joint showing the radial crack propagates across the interface from polycrystalline alumina into the sapphire without deflection.

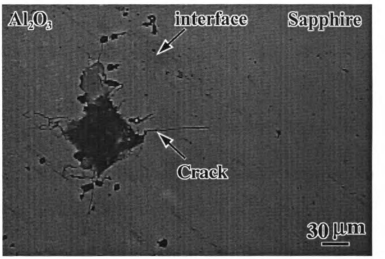

Figure 3.37 An optical microscopy image of the Vickers indentation crack on the sapphire/polycrystalline alumina joined at 1450°C for 180+300 minutes using a silica spin-on interlayer in the alumina side neat the joint.

Chapter IV

Discussion

4.1 Spin-on interlayer joining mechanisms

The results presented in Chapter III show that joining involving MaCor™ is not substantially enhanced or hindered by the presence of a spin-on bonding agent. This effect is very different from the joining of crystalline ceramics, such as high purity 98% polycrystalline alumina and sapphire, where bonding was not achieved without the use of a silica spin-on interlayer. However, sapphire and low purity 96% polycrystalline alumina can be successfully joined together with or without the use of a silica interlayer. Thus, it is of interest to compare the nature of bonding in these two classes of ceramics in relation to previous ceramic/ceramic joining studies, pertinent phase diagrams, and microstructure studies of other crystalline ceramics and glass ceramics that are similar in composition to MaCor™. In addition, it is critical to fully characterize the evolution of the joining process from initial sputter-cure to final joining state in order to further the understanding of ceramic joining mechanisms, reaction kinetics, and the development of reliable ceramic joining approaches.

4.1.1 Surface and interface diffusion

Despite growing interest in joining ceramics, there has been little research on the detailed mechanisms or modeling of ceramic-ceramic joining. Consequently, process conditions are often chosen by trial and error, rather than from scientific predictions that ensure complete bonding. The reason for the trial and error approach may be related to the complicated diffusion, mass transport, reaction, and interface formation mechanisms.

For example, Derby and Wallach [1982, 1984] developed a theoretical model of the simplest joining process, metal–metal diffusion bonding without reaction phase formation. They assumed that diffusion bonding has some similarity with powder pressure sintering processes. The geometry of the contacting surfaces was simplified as a series of asperities touching at their tips to form holes, voids and pores [Wallach 1989]. The difference in free energy and chemical potential between the contacting area and the surface of the asperities forming the voids provides a driving force which causes the diffusion of materials, similar to mass diffusion in powder pressure sintering process [Kingery 1976, Barsoum 1997]. Thus, they postulated that following three bonding mechanisms could be initiated to close the interface porosities (Figure 4.1) [Derby 1982, 1984]:

- Mechanism 1: Surface and volume diffusion from surface source to neck, driven by differences in surface curvatures across the surface of an interfacial void.
- Mechanism 2: Boundary diffusion and volume diffusion along the bond interface from interface source to neck, driven by the chemical potential differences along the bond line.
- Mechanism 3: Local yielding or creep, driven by the applied force during diffusion joining.

Figure 4.1 shows a schematic representation of the three mass transport mechanisms for interface formation. However, for heterogeneous metal-ceramic or ceramic-ceramic bond formation, additional processes certainly need to be considered. For example, interdiffusion between bulk materials, a possible eutectic reaction at the interface to form a liquid phase, wetting and dissolution of the ceramic or metal phase

into the liquid phase, diffusion activation energies, maximum solubility, and chemical reactions at interface to form reaction products. Each of these mass-transport mechanisms has to be taken into account to understand the detailed bonding interface formation process. These factors suggest that diffusion is crucial to the understanding of bonding, interface formation, and interface morphology.

In the current research, when two flat surfaces, such as zirconia and MaCor™, silica and MaCor™, and silica and alumina, were placed in contact, voids, porosity, or channels were formed. This is consistent with what would form between ridges, and is consistent with the original polished surface roughness being as a series of straight-sided ridges [Derby 1982, 1984]. At elevated temperatures, driven by differences in surface curvatures and chemical potential, mechanisms 1 and 2, surface and volume diffusion from high radius ridge surface source to ridge neck area and/or along the bond interface, can be initiated, leading to a gradual shrinking of these pores or voids (Figure 4.1). However, the current spin-on interlayer joining approach uses very small nominal joining pressure which is in the range of 2000~8500 Pa. Thus, mechanism 3, local yielding or creep requiring a large stress concentration, is not likely to occur at the interface. Therefore, as bonding progresses, the mass transport across the interface via mechanisms 1 and 2, surface and volume diffusion, resulted in the gradual shrinkage of interfacial voids and interdiffusion between similar and dis-similar ceramics, such as silica and MaCor™, and silica and alumina.

4.1.2 Interfacial eutectic reactions

In the current study, the silica interlayer would not become liquid or spread through wetting action along the interface, to assist the bonding at the joining temperature of

1020°C, due to its high melting point (1720°C) and high viscosity at this temperature [Emulsitone]. However, the interfacial interdiffusion between similar and dis-similar ceramics continues, and as such, eutectic liquid phase formation could occur at the silica/MaCor™ and silica/alumina interfaces. The interfacial liquid phases may increase interfacial wetting and dissolution, and assist the interface formation since wetting of surface is a measure of the adhesion of the two joining materials [Burger 1998].

4.1.2.1 Silica and MaCor™

According to the SiO_2-MgO-K_2O-Al_2O_3 equilibrium quaternary phase diagram [Schairper 1954], liquid is present down to the ternary eutectic temperature of 715°C in the three phases field of $K_2O{\cdot}MgO{\cdot}5SiO_2$\$SiO_2$\$K_2O{\cdot}4SiO_2$ (Figure 4.2). Likewise, liquid is present down to the ternary eutectic temperature of 963°C in the three phase field of $K_2O{\cdot}5MgO{\cdot}12SiO_2$\$SiO_2$\$K_2O{\cdot}MgO{\cdot}5SiO_2$, while liquid is also present to the ternary eutectic temperature of 1013°C in the three phase field of $2MgO{\cdot}SiO_2$\$K_2O{\cdot}MgO{\cdot}5SiO_2$\$K_2O{\cdot}MgO{\cdot}5SiO_2$. MaCor™ contains 47.2% SiO_2, 16.7% Al_2O_3, 9.5% K_2O, 14.5% MgO, and 8.5% B_2O_3 (wt%) [Pinckney 1991]. Thus, as the silica interlayer reacts with the MaCor™ at the joining temperatures of 1020 or 1070°C, it is likely that a liquid silicate phase will form at the silica/MaCor™ interface.

4.1.2.2 Silica and alumina

Similar to the eutectic reaction between the silica spin-on interlayer and the borosilicate glass phase that may result in liquid phase formation, a eutectic reaction between the silica and the alumina phase (either polycrystalline or single crystal sapphire) could occur at the silica/polycrystalline alumina interface. According to the equilibrium Al_2O_3-SiO_2 phase diagram [Macdowell 1969], a liquid interfacial phase reaction between

SiO_2 and high purity bulk Al_2O_3 should only occur at temperatures higher than 1595°C. However, Sacks et al. [Sacks] found that fine micro-powders (around 200 nm) of alumina and silica could react at much lower temperatures, leading to the formation of mullite ($3Al_2O_3 \cdot 2SiO_2$) at temperatures as low as 1400°C, as a consequence of interfacial liquid phase formation [Davis 1972]. Thus, a liquid interfacial phase reaction could occur at the joining temperature of 1475°C used in the present study.

4.1.2.2.1 Effect of impurities

The temperatures at which liquid interfacial eutectic phase reactions can occur between Al_2O_3 (either polycrystalline or single crystal sapphire) and the SiO_2 interlayer depends on the particle size and the actual impurities present in the base component (such as magnesium oxide, calcium oxide, and silicon oxide) [Sacks 1996, 1997, Nakajima 1998, Staley 1969]. Impurities in the alumina may further lower the interfacial liquid phase formation temperature between the silica interlayer and the polycrystalline alumina in the same manner as small quantities of CaO, SiO_2, and MgO have been found to lower the liquid phase sintering temperature of alumina [Brydson, Nakajima 1998]. Because CaO is typically present as an impurity in 96% alumina, a eutectic liquid phase could form in the SiO_2-$CaO \cdot SiO_2$-$CaO \cdot Al_2O_3 \cdot 2SiO_2$ phase field at temperatures above 1170°C or in the SiO_2-$3Al_2O_3 \cdot 2SiO_2$-$CaO \cdot Al_2O_3 \cdot 2SiO_2$ phase field at temperatures above 1368°C [Levin 1964]. Thus, as a result of impurities, the formation of a liquid phase at silica/96% polycrystalline alumina might be expected.

4.1.3 Wetting and dissolutions

The eutectic liquid phase formation at the zirconia/MaCor™ and silica/alumina interfaces could expedite the mass transfer across the interfaces and the formation of

thermal grooving. Generally, thermal grooving forms at the interface between a polycrystalline solid phase and a liquid phase whenever a grain boundary meets the interface [Mullins 1957, 1958, 1960]. The thermodynamic driving force for the formation of thermal grooving is to develop an equilibrium condition of interfacial forces at solid/liquid triple junctions or groove root (solid/liquid interfacial energy γ_{sl}, and grain boundary energy γ_{gb}) (Figure 4.3(a)). As investigated by Mullins [Mullins 1957, 1958, 1960], the formation and growth of interfacial thermal grooving could take place through the following three mechanisms: (1) interfacial diffusion, (2) volume diffusion, and (3) interfacial reactions such as solution and precipitation, and evaporation and condensation for solid/liquid and solid/gas interfaces, respectively. In an idealized case where liquid/solid diffusion is dominated by one of the diffusion mechanisms, Mullins [1957, 1958, 1960] predicted that each thermal groove profile shape is determinative and independent of time. Figure 4.3 summarizes the expected thermal groove shape based on Mullin's analysis. When interfacial reactions are the dominant diffusion mechanism, the groove surface lies everywhere below the original polished surface (Figure 4.3(a)). However, in a case where the dominant mass transport mechanism for thermal grooving is either interfacial diffusion or volume diffusion, a hump develops adjacent to the groove that can lie above the original polished surface (Figure 4.3(b) and (c)). In addition, the expected dependence of the groove depth and width with solutionization time is linear. For example, the groove profile is proportional to $t^{1/2}$ for interfacial reactions mechanism, to $t^{1/3}$ for volume diffusion, and to $t^{1/4}$ for interfacial diffusion, where t is the time [Mullins 1957, 1958, 1960].

In the current study of joining of zirconia and MaCor™ via microwave (Figure 3.8) and conventional heating (Figure 3.13), polycrystalline alumina and sapphire (Figure 3.27), cross-sectional TEM observations revealed that the grain boundary groove shapes lack the humps above the original flat surfaces on either side, indicating mass-transport is mostly controlled by interfacial reactions. However, it is impossible to calculate the theoretical values of thermal groove depth since the physical and chemical characteristics of eutectic liquid phases were unknown (Figure 4.2 and 4.3).

4.1.4 Interface formation

The wetting experiments performed by Saiz et al. [1998] with molten drops of copper and nickel on polycrystalline alumina revealed mass transport involving grain boundary grooves near the metal/alumina interfaces is two to four orders of magnitude faster than on the free surface of the alumina. In addition, many authors [Dennalay 1987, Dalgleish 1994] illustrated theoretically and confirmed experimentally that there is a direct correlation between a good wetting and a strong interfacial bonding that results in a strong joint strength.

Thus, it is expected that the mass transport involving grain boundary grooves due to eutectic liquid phase formation could accelerate the interfacial interdiffusion across the interface. As many authors postulate the diffusion bonding process as a process analog to powder pressure sintering processes, the spin-on interlayer joining approach used in the current study can be viewed as a process analog to liquid phase sintering process. In liquid phase sintering, the presence of liquid phase provides a capillary force that pulls the solid particles together and promotes rapid densification in the compacts [Kingery 1976, Barsoum 1997]. However, for these effects to occur it is necessary to "have an

appreciable solubility and wetting of the solid in the liquid" [Kingery 1976]. The cross-sectional TEM observations revealed that liquid phases apparently wet the zirconia and alumina in the joining of zirconia and MaCor™ (Figure 3.8 and 3.13), and sapphire and alumina (Figure 3.27 and 3.30), respectively. Therefore, it is likely that liquid phases due to eutectic reactions will accelerate the ceramic-ceramic joining process.

Similar to sintering in the presence of a liquid phase [Kingery 1976, Barsoum 1997], the presence of a liquid phase during the joining could (1) generate an attractive force between neighboring ridges across the joining interface due to a capillary force resulting from surface tension, (2) introduce an additional mass transport mechanism through the liquid phase via dissolution of small particles and growth of large particles, (3) filling of interfacial pores or voids. Thus, the presence of eutectic liquid phase at the joint interfaces could expedite the mass transport across the joining interface, resulting in a dramatic enhancement of interface formation. Therefore, the interfacial reactions or wetting and dissolution that occurred during the joining of zirconia/Macor™ and silica/alumina could result in a dramatic enhancement in the joining sapphire and alumina, and alumina/alumina.

4.1.5 Phase development at the join interface

In the current spin-on interlayer joining approach, the silica interlayer thickness is in the range expected from the combination of two coated surfaces (each 250~320 nm thick). The presence of a eutectic liquid phase could expedite the materials transport across the interfaces and bond formation. Thus, the additional dissolution of the base ceramics into the amorphous eutectic liquid phase can broaden the reaction layer. For example, optical microscopy revealed that a reaction layer approximately 5 μm thick was

found at the joint region in 98% alumina/sapphire joined at 1400°C for 180 minutes using a silica interlayer (Figure 3.29(a)). This reaction layer thickness is more than an order of magnitude greater than the spin-on interlayer thickness.

However, following cooling from the joining temperatures, a variety of interfacial microstructures have been observed. For example, microstructural analysis revealed that no observable reaction phase or layer is observed for joining involving MaCor™ with and without the use of a silica spin-on interlayer, while joining of sapphire and 98% polycrystalline alumina, and sapphire and 96% polycrystalline alumina showed interfacial layers and/or non-equilibrium alumina phase. Although the equilibrium phase diagram illustrates the phases expected to develop under equilibrium conditions, the joining in the current study may be far from equilibrium conditions. Thus, it is beneficial to the development of joining procedures to investigate the details of the different joining scenery based on previous ceramic/ceramic joining studies, pertinent phase diagrams, and microstructure studies.

4.1.5.1 Joining of zirconia/MaCor™

Baik et al. [1995] reported that the microstructure of fluorophlogopite mica-based glass-ceramics, containing 50% SiO_2, 20% Al_2O_3, 8% K_2O, 15% MgO, 0.9% Li_2O and 6.1% F (wt%) similar to MaCor™, is not affected by 2-wt% ZrO_2 addition, but at a 4% addition level, crystallization is inhibited and spontaneous opalization occurs at 6% addition level. Thus, the addition of zirconia to the glass ceramic can (1) leave the microstructure unchanged, (2) inhibit crystallization, or (3) induce spherical precipitates (opalization) [Baik 1995]. The TEM studies presented (Figure 3.9 and 3.10) indicate that the microstructures of both the MaCor™ and the zirconia are unchanged near the

interface, which may indicate limited diffusion of zirconia into the liquid that is likely formed (according to the equilibrium phase diagrams) at the silica/MaCor™ interface. Therefore, during the following cooling after joining, the liquid silicate phase can form an amorphous matrix and fluorophlogopite mica platelet phase without additional interfacial phases or reaction layers.

4.1.5.2 Joining of sapphire and polycrystalline alumina

In the joining of polycrystalline alumina and sapphire, equilibrium may not have been reached due to slow reactions. Furthermore, impurities can shift the phase boundaries significantly. Many researchers [Risbud 1977, 1978, Aksaky 1975] have illustrated theoretically and confirmed experimentally the development of metastable phases in the SiO_2-Al_2O_3 system. This metastable system forms a simple eutectic of SiO_2-Al_2O_3 (eutectic point: ~12 mol% Al_2O_3 at ~1260°C), without the development of equilibrium mullite phase. This metastable behavior may explain why no mullite formation has been observed at the SiO_2-Al_2O_3 interfaces in the joining of sapphire and polycrystalline alumina. Furthermore, the oxide impurities CaO and BaO, which are present in the as-received 96% and 98% alumina, have been shown to inhibit the devitrification of glassy phases during cooling [Macdowell 1969]. This may also be a factor in inhibiting the formation of mullite at the interface. Instead of forming mullite, a number of researchers [Risbud 1978, Aksaky 1975, Kennard 1972] have found that alumina can precipitate from the glassy phase during cooling. This is consistent with the observation of the fine alumina grains developed at some points in the joint region (figure 3.27).

4.2 Microwave vs. conventional joining

Microwave heating is fundamentally different from conventional heating. In microwave heating, heat is generated from the electromagnetic energy losses associated with the interactions between the internal electric fields and induced molecular motions. This results in the heat being generated within the material, rather than flowing in from the surface, as in the case for conventional heating. When compared to conventionally heated materials, materials will be heated more uniformly, and typically more rapidly. This heating results in reduced processing times and energy costs within the limits set by microwave absorption, when heated using microwaves [Loehman 1999]. Thus, while microwave heating results in joining at lower nominal temperatures in the present study, the effective time at the joining temperature maybe longer than experienced with conventional heating. However, further localized heating may be occurring at the joined interfaces as a result of differences in the dielectric loss factor (tan δ) [Lee and Lin 1998].

4.2.1 Joining zirconia and MaCor™

The available information on dielectric loss factors for the joining of zirconia and MaCor™ using a silica interlayer used in this study is limited (See Table 4.1). However, it is clear that the dielectric loss factor (tan δ) is much lower in the silica interlayer at 1020°C and 2.45 GHz than it is in the zirconia (a comparable value for MaCor™ is not available) (Table 4.1). Given this, it might be expected that the silica interlayer would not heat as rapidly as the neighboring zirconia.

4.2.2 Joining of 98% polycrystalline alumina and alumina

Alumina, as a low loss ceramic, is transparent to microwaves at ambient temperatures [Sutton 1992]. Initially, the dielectric loss factor (tan δ) of the alumina rises slowly with increasing temperatures. However, above a critical temperature which is

approximately 1000°C for alumina, tan δ rises rapidly [Sutton 1992]. Thus, alumina can absorb and couple more efficiently with microwave radiation, resulting in more effective heating at high temperatures. The rapid increase of tan δ at high temperatures is associated with the softening of the grain boundary amorphous phase in alumina, causing an increase in a local electrical conductivity, as reported by Ho [1988]. Thus, the tan δ of higher purity alumina is less affected by temperature than that for the lower purity alumina. Therefore, in the joining of 98% polycrystalline alumina and alumina using a silica interlayer, the intergranular amorphous phase in the 98% alumina could result in a the rapid rise of tan δ, resulting in more effective heating at high temperatures. The available information on the tan δ for the 98% alumina is limited (Table 4.2). However, it is expected that the tan δ for the 98% alumina be between that of lower purity alumina AD85 and higher purity AD99.5. Furthermore, the tan δ is much lower in the silica interlayer at high temperatures and 2.45 GHz than it is in the alumina (Table 4.2). Therefore, it is expected that the silica interlayer would not heat as rapidly as the neighboring polycrystalline alumina.

4.2.3 Microwave joining

In the microwave joining, it is known that large dielectric losses occur at interfaces between materials with large differences in dielectric loss factors, leading to an additional term in the total dielectric loss factor and large increase of tan δ at the interface [Lee and Lin 1998]. Thus, significant local heating might be expected at the silica/zirconia and silica/MaCor™ interfaces. Similar differences and local heating might be expected at the silica/alumina interface, which may further push up the local temperature at the joint

relative to the nominal joining temperature. As the interlayer is very thin (less than 1 μm), it should also absorb heat readily from the surrounding, rapidly heated materials.

A number of researchers [Palaith 1989, Janney 1991, Fanslow 1990] have reported that microwave processing produces chemical and physical reactions that are different from the reactions that would have occurred if the only effect of the microwaves were to increase the temperature. For example, improved microstructures and mechanical properties [Janney 1991, Fanslow 1990, Patterson 1992], enhanced chemical and physical reactions [Fanslow 1990], increased diffusion coefficients [Janney 1991] and lowered sintering activation energies [Janney 1988] have been observed in microwave heating. These enhancements are known as the "microwave effect". Janney et al. [1988] have speculated that these enhancements occur as a result of the electromagnetic field "coupling to lattice defects and other bulk crystalline effects". The present results that indicate joining of zirconia/MaCor™ and 98% polycrystalline alumina/alumina can be achieved at shorter times and at lower nominal temperatures using microwave heating may also be a result of such athermal microwave effects. Booske and co-workers [Booske 1997, 1998, Freeman 1995, 1998] illustrated theoretically and numerically, and confirmed experimentally that microwave fields induce an additional driving force (ponderomotive force or pmf) that enhances the mass transport rate and ionic diffusion compared to conventional heating mode. The pmf can occur at any abrupt discontinuities, such as surfaces or interfaces. The authors [Booske 1997, 1998, Freeman 1995, 1998] state that the value of the pmf is higher than the solid-state diffusion driving force for joining of two flat NaCl/NaCl surfaces. Thus, ceramic-ceramic joining

processes could be substantially enhanced since diffusion is crucial to the development of eutectic liquid formation, wetting, dissolution, and interface formation.

Therefore, the additional pmf athermal driving force for mass transport across the zirconia/silica, MaCor™/silica, and silica/alumina interfaces, most likely enhances the interfacial diffusion rates and mass transport across the interfaces to a large degree. In addition, preferential interfacial heating can occur due to the large dielectric losses at interfaces [Lee and Lin 1998]. These conditions can result in a lower nominal microwave joining temperature, consistent with experimental results presented in this thesis that show that microwave heating has greatly enhanced the joining of zirconia/MaCor™, 98% polycrystalline alumina/alumina although the silica interlayer is essentially transparent to the microwave field. Furthermore, it is also expected that microwave heating would assist the bonding of the zirconia and MaCor™ without the use of a silica interlayer, due to increased mass transfer across the interface.

4.3 Joining without the use of interlayers

For direct ceramic-ceramic joining without the use of any interlayer, adhesion generally takes place through high temperature and pressure diffusion bonding or as a result of an intergranular amorphous phase present in the base materials migrating to the joint [Binner, Esposito 1998]. Ideally, diffusion bonding produces local deformation or melting at the joint, promoting surface contact, and subsequently allowing atomic or ionic migration across the interface to produce a bond [Santella 1992, Sandhage 1996]. For example, Glaeser et al. [1990] joined sapphire and polycrystalline alumina via hot pressing at 1370°C for 60 minutes at 15 MPa pressure (as compared to the 8000 Pa in the

present study). However, such high pressures have the potential to lead to creep in the base materials and a consequent change in shape of the joined components.

Because the adhesion and chemical compatibility between intergranular glassy phases and base ceramics is generally good, joining as a consequence of intergranular amorphous phase migration depends primarily on the existence and mobility of intergranular phases [Santella 1992, Sandhage 1996]. For example, Binner et al. [1998] joined reaction-bonded silicon carbide (RBSC) to RBSC via microwave heating without the use of an interlayer. During direct joining, the high temperature and pressure promoted the motion and "bleeding" of liquid free silicon from the matrix to the interface [Binner 1998], driven by the tendency of the system to restore the equilibrium when a higher energy interface is introduced [Esposito 1998]. Subsequently, the liquid free silicon spreads across the RBSC surface, generating a free silicon interlayer between the two RBSC specimens which assist the bonding.

4.3.1 Joining of sapphire and polycrystalline alumina

The joining of sapphire and 96% polycrystalline alumina without the use of a silica interlayer is similar to the joining of 92 to 96% purity alumina investigated by Fukushima et al. [1988] and RBSC to RBSC investigated by Binner et al [1998]. The interface between the two polished 96% polycrystalline alumina specimens put in contact can be regarded as a macroscopic inhomogeneity since no intergranular amorphous phase is present on the surface of the grains at the interface. Thus, mass transport occurs, which tries to minimize the macroscopic inhomogeneity between interfacial region and the base alumina, via migrating of the grain boundary amorphous phase through capillary flow to the free surface. At high temperatures, the amorphous grain boundary phase in the 96%

polycrystalline alumina can melt and migrate to the free surface, accounting for the successful joining of the sapphire and polycrystalline alumina [Case 2001]. However, due to the negligible amount of grain boundary phase in high purity 98% polycrystalline alumina, sapphire and 98% alumina will not form a wetting phase without the use of a silica interlayer.

4.3.2 Joining of zirconia and MaCor™

Similar to the joining of sapphire and 96% polycrystalline alumina without the use of a silica interlayer, the glassy matrix phase of the MaCor™ is sufficient to promote bonding in the joining of zirconia and MaCor™ without the use of an interlayer. Such a glassy borosilicate phase could become viscous or liquid at high temperatures and assist the bonding of the zirconia and MaCor™ [Santella 1992]. As an example of glassy phase assisted bonding, Fukushima [1988] directly joined 92 to 96% purity alumina via microwave heating, presumably as a result of intergrannular glassy phases being preferentially heated and spreading through capillary wetting action along the joint interface to assist the bonding. In the current study, evidence of the glassy nature of the MaCor™ appeared with the development of ripples on the free surfaces of the MaCor™ during the joining. Wunsche et al. [1999] reported similar ripples on the fracture surface of borosilicate glass (the matrix of MaCor™) that resulted from local melting. Thus, when heated to 1070°C, it is likely that liquid phase(s) will form at the MaCor™/zirconia interface even without the use of a silica interlayer (Figure 4.2). In addition, similar to the eutectic reactions that might be expected at the MaCor™/silica interface [Schairper 1954], liquid silicate phase formation could also be expected at the zirconia/MaCor™ interface or inside the MaCor™ since MaCor™ contains a total of 71% SiO_2, K_2O, and

MgO with additional amounts of Al_2O_3 and B_2O_3 [Corning]. Therefore, the interfacial liquid that forms at the MaCor™/zirconia interface wets and dissolves the zirconia along the grain boundaries for temperatures at or below the joining temperature of 1070°C (Figure 3.6), promoting a directly bonded interface between the MaCor™ and the zirconia even without the use of a silica interlayer.

4.4 Effect of silica spin-on interlayers

4.4.1 Joining involving glassy ceramics

For the joining involving non-crystalline ceramics, such as glass-ceramics, or crystalline ceramics containing fairly large amounts of amorphous intergranular phase under proper joining temperatures and low nominal pressures, adhesion could take place as a result of glassy amorphous matrix or intergranular amorphous phase present in the base materials migrating to the joint [Binner, Esposito 1998]. The presence of an amorphous phase appears to have two purposes: (1) it can directly hold the two joining pieces together under proper temperature and pressure, acting as an adhesive medium, similar to glass brazing, (2) it can allow the grains at or near the interface in base materials to rotate and rearrange themselves at very high temperatures, which can lead to the strengthening of the joint [Walls 1992, Binner 1998]. Therefore, the use of a silica spin-on interlayer for the joining of ceramics containing large amounts of amorphous phase, such as MaCor™ and 96% polycrystalline alumina, is not necessary.

4.4.2 Joining involving crystalline ceramics with little or no amorphous phase

In the joining of crystalline ceramics containing little or no amorphous phase using low nominal pressures, successful bonding was not achieved without the use of a silica spin-on interlayer. Since interfacial diffusion is critical to the development of bonding,

the interlayer should be properly chosen to assist the mass transport across the interfacial region. The eutectic liquid phase formation between the chosen silica spin-on interlayers and the base ceramics substantially enhanced the mass transport across the interfacial region, resulting in successful bonding of crystalline ceramics containing little or no amorphous phase. Thus, without the presence of a silica interlayer, liquid formation should not occur between sapphire and 98% polycrystalline alumina below the melting temperature of 98% alumina. Therefore sapphire and 98% polycrystalline alumina cannot be joined without the use of a silica interlayer at the temperature and pressures studied.

In addition, in the conventional joining of zirconia with zirconia using a silica interlayer, the zirconia-silica equilibrium phase diagram [Curtis 1953] shows that the zirconia-silica eutectic temperature is about 1680°C. Therefore, although interdiffusion between zirconia and silica is likely to occur at the zirconia/silica interface, it is unlikely that liquid formation will result at this side of the interface at the joining temperature of 1020°C. This is consistent with the experimental results that showed zirconia failed to join with zirconia using a silica interlayer when heated at 1070°C for 60 minutes.

Thus, similar to liquid phase sintering where the compositions of sintering aids can be chosen to result in an appreciable amount of liquid phase formation at elevated temperatures [Kingery 1976, Barsoum 1997], the chemical compositions of the spin-on interlayers could be chosen to assist the formation of a low melting point interfacial glassy phase upon joining, such as the liquid phase formation due to eutectic reactions between silica spin-on interlayer and the base joining ceramics in the present study.

Therefore, the wetting liquid phases formed upon heating could penetrate between the two joining surfaces and enhance mass diffusion to assist the joining process.

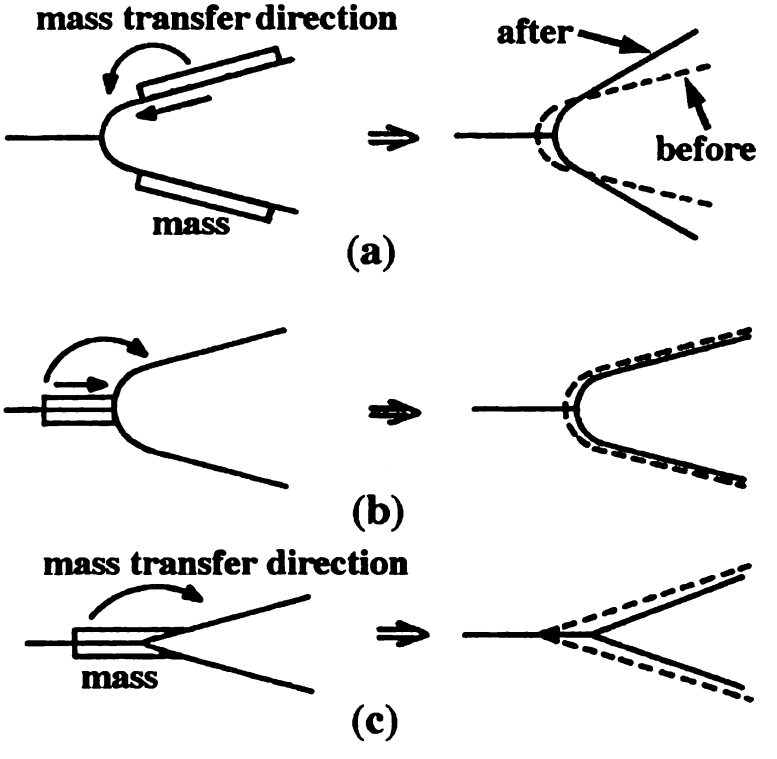

Figure 4.1 The schematic representation of the three mass transport mechanisms for interface formation due to (a) surface and volume diffusion from surface source to neck, (b) diffusion along the bond interface, and (c) bulk deformation mechanism after [Derby 1982, 1984]. The arrows denote the mass diffusion direction, while the dotted and bold lines represent the interfacial void geometry before and after diffusions, respectively.

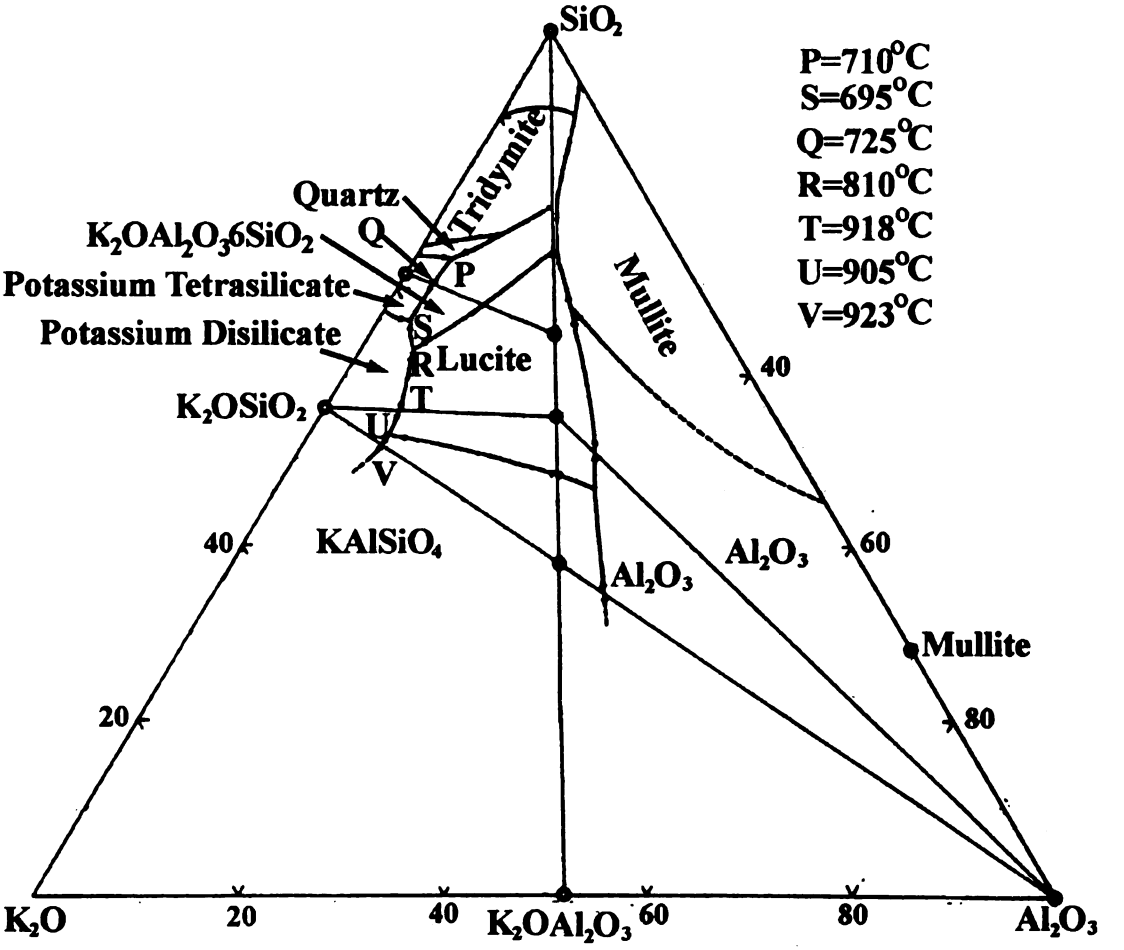

Figure 4.2 Equilibrium phase diagram of SiO_2-K_2O-Al_2O_3 [redrawn from Schairper 1954].

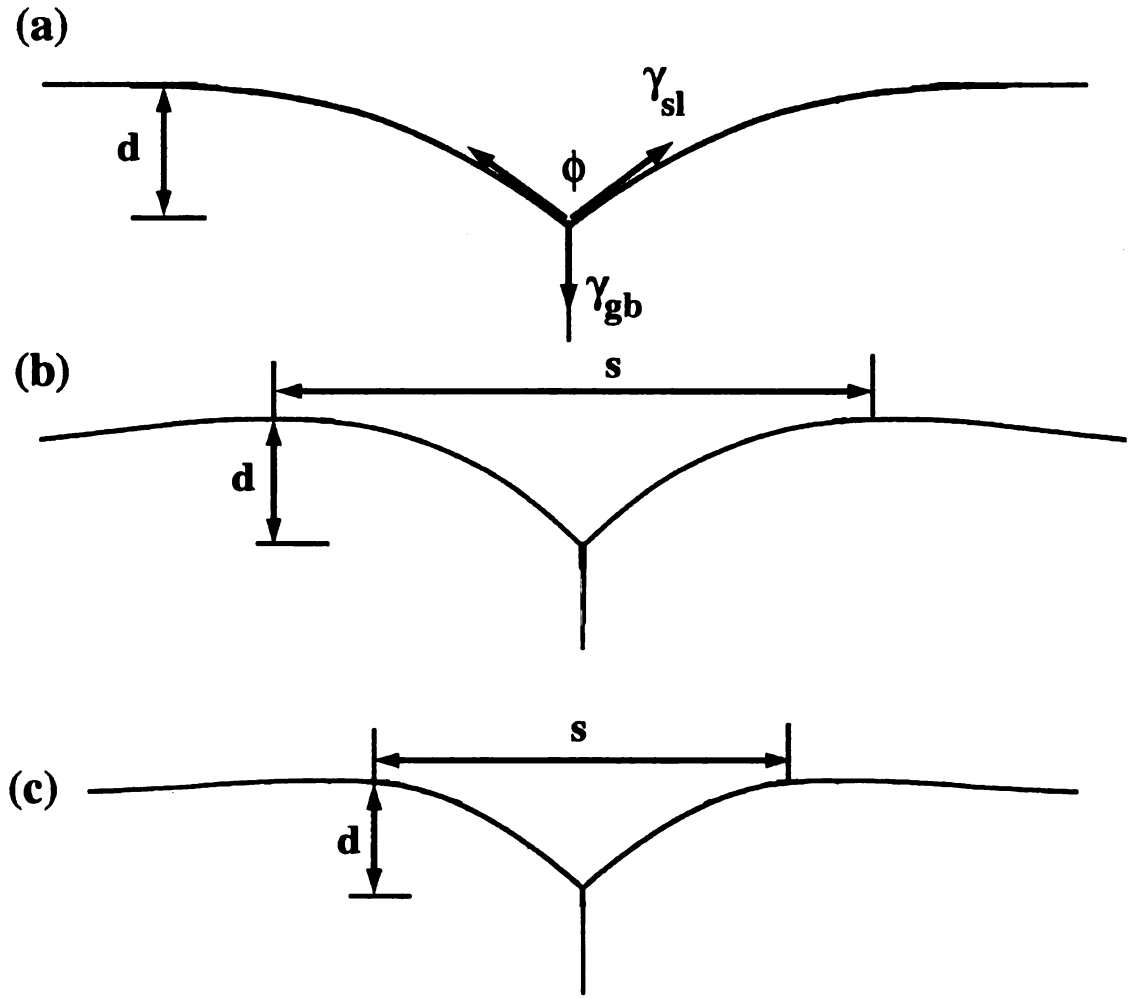

Figure 4.3 The expected thermal groove profile shapes due to (a) Interfacial reactions with groove depth $d = 1.13m(At)^{0.5}$, (b) surface diffusion with depth $d = 0.973m(B_s t)^{0.25}$ and width $s = 4.6(B_s t)^{0.25}$, and (c) volume diffusion with depth $d = 1.01m(B_v t)^{0.33}$ and width $s = 5(B_v t)^{0.33}$ [After Mullins 1957, 1958, 1960]. Constants $A = \frac{LC_0\gamma_{sl}\Omega^2}{kT}$, $L = \frac{J}{c - c_0}$, $B_s = \frac{\delta D_s \gamma_{sl}\Omega}{kT}$, and $B_v = \frac{xD_v\gamma_{sl}\Omega}{kT}$, where m is the slope of the solid/liquid interface at the groove root; C_0 is the initial concentration with a planar interface; C is the concentration; Ω is the molecular volume and weight; M is the molecular weight; x is the solubility of solid in the liquid; Dv and Ds are the volume and surface diffusion coefficients, respectively; δ is interfacial width; J is the flux, γ_{sl} is the solid/liquid interfacial energy, and γ_{gb} is the grain boundary energy.

Table 4.1 The dielectric properties of various ceramics used in the joining of zirconia and MaCor™ using a silica interlayer.

Materials	Frequency	ε'	ε"	tan δ	Temperature (°C)	Reference
MaCor™	1 kHz			0.0047	25	[Corning]
MaCor™	8.5 GHz			0.0071	25	[Corning]
Borosilicate glass*	1 MHz			0.004	20	[Corning]
Borosilicate glass*	1 MHz			0.11	350	[Corning]
Silica	8-10 GHz			0.0002	25	[Walton 1970]
Silica	3 GHz	3.78	0.00023	0.00006	25	[Palaith 1989]
Silica	0.5-5GHz	3.8		~0.0001	25	[Arai 1993]
Silica	0.1 MHz	4.2	0.0086	0.002	25	[Regnier 1996]
Silica	2.45 GHz			0.0032	1025	[Hassler 1988]
Zirconia	1 MHz			0.01	25	[Buchanan 1986]
Zirconia	5.4 GHz			0.0009	25	[Smith 1992]
Zirconia	2.45 GHz	25	15.5	0.62	1020	[Arai 1993]

*Borosilicate glass is the matrix phase of MaCor™ [Corning]. However, borosilicate glasses can have fairly broad composition ranges, and it is not clear if the borosilicate glass noted in the table has a composition comparable to the MaCor™ matrix. Thus, these compositions must be made with caution.

Table 4.2 The dielectric properties of polycrystalline alumina used in the joining of alumina and alumina using a silica interlayer at 2.45 GHz.

Materials	ε'	ε"	tan δ	Temperature (°C)	Reference
Alumina (AD85)	8.8	0.9	0.1	1000	[Arai 1993]
Alumina (AD85)	9.1	1	0.11	1200	[Arai 1993]
Alumina (AD99.8)	9	0.64	0.07	1000	[Arai 1993]
Alumina (AD99.8)	9.2	0.71	0.077	1200	[Arai 1993]
Silica			0.0032	1000	[Hassler 1988]
Silica			0.01	1200	[Hassler 1988]
Silica			0.016	1400	[Hassler 1988]

Chapter V

Conclusions and Future Studies

5.1 Summary and conclusions

The present study investigated the interfacial microstructure of ceramics joined using spin-on interlayers. The fist key experimental result was the finding of no reaction layers in the microwave joining of MaCor™ and zirconia, as described in detail in Chapter III. In the microwave joined zirconia/MaCor™ specimens using a silica interlayer, cross-sectional scanning and transmission electron microscopy (SEM and TEM) reveal a non-planer zirconia/MaCor™ interface. This interlocking microstructure appears to have resulted from the glass matrix of MaCor™ and silica strongly wetting and dissolving the zirconia along grain boundaries.

However, because the glass-ceramic composite MaCor™ contains a glassy matrix phase, it was not necessary to use a silica spin-on interlayer. Thus, the initial objective of this study was modified to more comprehensively investigate the interfacial microstructural development in the joining of zirconia and MaCor™ via conventional versus microwave heating with or without a spin-on interlayer in relation to a number of other processing variables. TEM analysis revealed similar interfacial microstructures were developed with all of the interfaces, showing direct bonding between the zirconia and MaCor™, without any additional interfacial or residual phases, regardless of joining time or the presence or lack of an interlayer. In addition, successful interlayer joining required higher temperatures for conventional heating than had been observed for

microwave heating, due to differences in the mechanisms involved in microwave and conventional heating.

Because of the difficulties in identifying interfaces in joined like polycrystalline ceramics/polycrystalline ceramics, the final objective of this research was to focus on the nature of microstructure development in the interface region of polycrystalline alumina bonded to sapphire. With the aid of silica interlayer, sapphire and 98% polycrystalline alumina were successfully joined in 180 minutes at 1400°C, while samples without a silica interlayer failed to join under these conditions, suggesting the silica interlayer substantially promotes the joining of sapphire and 98% polycrystalline alumina. TEM examinations revealed the formation of non-equilibrium alumina and amorphous phases at the joint interface in sapphire and 98% polycrystalline alumina joined at 1475°C. However, sapphire and 96% polycrystalline alumina were joined with and without the use of a silica interlayer, due to the presence of glassy grain boundary phases. SEM analysis showed that an amorphous reaction layer approximately 0.5 μm thick formed in sapphire/96% polycrystalline alumina samples joined with an interlayer. However, when an interlayer was not used, the resulting amorphous interfacial phase was much thicker, on the order of 5 μm thick, suggesting the silica interlayer may inhibit the flow of the amorphous intergranular phase. In both cases, higher joining temperatures and longer processing times resulted in more complete joints and thinner interfacial regions.

A more comprehensive understanding of the fundamental processes related to ceramic joining, such as reaction mechanisms, diffusion kinetics, wetting behavior, phase behavior, and microstructural development was achieved. The spin-on interlayer joining approach can be envisaged as a process similar to liquid phase sintering processes. The

eutectic liquid phase formation between the chosen silica spin-on interlayers and the base ceramics substantially enhanced the mass transport across the interfacial region, resulting in successful bonding of crystalline ceramics. Since interfacial diffusion is critical to the development of bonding, the spin-on interlayer should be properly chosen to assist the mass transport across the interfacial region.

Unlike other joining processes using interlayers that are several microns thick or more [Locatelli 1997, Ferraris 1998], the spin-on interlayer joining approach studied in this thesis employs a thin interlayer to produce an imperceptible or thin bond layer without the major modifications of the base ceramics. In addition, indentation tests suggested that the resulting interfaces are strong, at least 60% of the strength of the base ceramics.

5.2 Future studies

The nature of the interfacial microstructures of joined ceramics is key to understanding the fundamental materials joining process. Factors such as thermal expansion mismatch, interfacial roughness, surface energy, wetting, and adhesion will all affect the resulting structures. This study shows that TEM is capable of providing interfacial structural information at the micro level. However, to obtain information regarding the atomic structure of the interface, the chemical nature of the interface, or the mechanical properties of these joined ceramics, other techniques and further analysis are required.

Thus, research in this joining area could be continued with the following studies:

(1) Thermal residual stress analysis of the joined ceramics systems could be carried out using finite element analysis (FEA) to determine the optimal interfacial

microstructures and the related joining conditions. (2) High resolution TEM (HRTEM) studies of the interfacial microstructures of the joined crystalline ceramics with crystalline ceramics, to investigate atomic quality of the interfaces and lattice mismatch between dissimilar materials. The HRTEM studies could allow assessment of the interfaces at the micro and atomic level, the degree of joining, enhance our understanding of interfaces and should also help in determining the joining mechanism. (3) Other characterization techniques capable of obtaining additional information about the interfacial microstructures. Energy dispersive spectroscopy (EDS) and electron energy loss spectroscopy (EELS) in TEM could be used to obtain the chemical distribution of elements and to determine the elemental interdiffusion processes across the interfaces during joining.

References

Ahn, B.G., Shiraishi, Y., *High Temperature Materials and Processes (UK)*, 17(4) (1998) 209.

Aksaky, I.A., Pask, J.A., *J.Am.Ceram.Soc.*, 58(11-12)(1975) 507.

Arai, M., Binner, J.G.P., Bowden, A.L., Cross, T.E., Evans, N.G., Hamlyn, M.G., Hutcheon, R., Morin, G., Smith, B., in: D.E. Clark, W.R. Tinga, J.R. Laia Jr (Eds.), Microwaves: Theory and Application in Materials Processing II. Proc. Symp. Cincinnati, April 19-22, 1993, American Ceramic Soc. Inc.; *Ceram.Trans.* 36 (1993) 539.

Ashizuka, M., Ishida, E., *Journal of the Ceramic Society of Japan*, 104 (4)(1996)345.

Baik, D.S., No, K.S., Chun, J.S., *J. Am. Ceram. Soc.* 78 (5) (1995) 1217.

Barsoum, M.W., *Fundamentals of ceramics*, New York, McGraw Hill, 1997. p. 371-380.

Bates, C.H., Foley, M.R., Rossi, G.A., Sundberg, G.J., Wu, F.J., *Am. Ceram. Soc. Bull.*, 69(3)(1990)350.

Binner, J.G.P., Fernie, J.A., Whitaker, P.A., Cross, T.E., *J.Mat.Sci.* 33(12)(1998) 3017.

Binner, J.G.P., Fernie, J.A., Whitaker, P.A., *J.Mat.Sci.* 33(12)(1998) 3009.

Boadi, J.K., Yano, T., Iseki, T., *J. Mater. Sci.* 22(7)(1997)2431.

Booske, J.H., Cooper, R.F., Freeman, S.A., *Mater. Res. Innov.*, 1(2) (1997) 77.

Booske, J.H., Cooper, R.F., Freeman, S.A., Rybakov, K.I., Semenov, V.E.; *Physics of Plasmas*, 5(5) (1998) 1664.

Brydson, R., Chen, S.C., Riley, F.L., Milne, S.J., Pan, X., Ruhle, M., *J.Am.Ceram.Soc.*, 81(2)(1998) 369.

Buchanan, R.C., *Ceramic Materials for Electronics*, Marcel Dekker, Inc., New York, N.Y. 1986, pp. 33-47.

Burger, K., Ruhle, M., *Ultramicroscopy*, 29(1998)88.

Case, E. D., Lee, J. G., Lee, K. Y., "Joining of Optical and Infrared Materials Using Spin-On Layers", 1998, pp. 17 – 26 in *Joining of Advanced and Specialty Materials*, M. Singh, J. E. Indacochea, and D. Hauser, eds., ASM International, Materials Park, OH. (Invited paper)

Case, E. D., Lee, K. Y., Lee, J. G., "Joining of Polycrystalline Ceramics and Ceramic Composites Using Microwave Heating", 1997, pp. 17 – 20 in *Proceedings of the 33rd International Microwave Power Symposium, International Power Institute*, Manassas, VA.

Case, E. D., Lee, K. Y., Lee, J. G., Hoepfner, T., "Geometrical Stability of Holes and Channels During Joining of Ceramics and Ceramic Composites", 1998, pp. 27 – 34 in *Joining of Advanced and Specialty Materials*, M. Singh, J. E. Indacochea, and D. Hauser, eds., ASM International, Materials Park, OH. (Invited paper).

Case, E.D., Crimp, M.A., *Advanced Engineering Materials (Germany)*, 3(6)(2001) 395.

Colombo, P., Sglavo, V., Pippel, E., Woltersdorf, J., *J. Mater. Sci.* 33 (9) (1998)2405.

Corning information and Corning web site, http://www.corning.com.

Cross, T.H., Mayo, M.J., *Nanostructured Materials*, 3(1993) 163.

Curtis, C.E., Sowman, H.G., *J. Am. Ceram. Soc.* 36 (5) (1953) 190.

Dalgleish, B.J., Saiz, E., Tomsia, A.P., Cannon, R.M., Ritchie, R.O., *Scripta Met.*, 31(8) (1994)1109.

Davis, R.F., Pask, J.A., *J.Am.Ceram.Soc.*, 55(10)(1972) 525.

Derby, B., Wallach, E.R., *J. Mater. Sci.*, 19 (10) (1984)3140.

Derby, B., Wallach, E.R., *Metal Science*, 16 (1982)49.

Dennalay, F., Froyen, L., Deryttere, A., *J. Mater. Sci.*, 22(1987)1.

Duvall, D.S., Owczarski, W.A., Paulonis, D.F., *Welding Journal*, 53(4)(1974)203.

Elessner, G., Diem, W., Eallace, J.S., in: J.A. Park, A.G. Evans (Eds.), *Surfaces and Interfaces in Ceramics and Ceramic-Metal Systems*, Plenum Press, New York, 1981, pp629-939.

EMS, Electron microscopy image simulation online website, http://cimewww.epfl.ch.

Emulsitone Company Information and web site, http://www.emulsitone.com/sif.html.

Esposito, L., Bellosi, A., in A. Bellosi (Eds.), *Interfacial Science in Ceramic Joining*, Kluwer Academic Publishers, 1998, p. 211.

Fanslow, G.E., in: W.B. Snyder Jr, W.H. Sutton, M.F. Iskander, D.L. Johnson (Eds.), *Microwave Processing of Materials II. Proc. Symp.* San Francisco, April 17-20, 1990,

Material Research Society, Pittsburgh, Pennsylvania, Materials Research Society Symposium Proceedings, 189 (1991) 43.

Ferraris, M., Salvo, M., Isola, C., Montorsi, M.A., Kohyama, A., *Journal of Nuclear Materials*, 258-263(1998) 1546.

Freeman, S.A., Booske, J.H., Cooper, R.F., *J. Appl. Phys.*, 83(11) (1998) 5761.

Freeman, S.A., Booske, J.H., Cooper, R.F., *Rev. Sci. Instrum.*, 66(6) (1995) 3606.

Fukushima, H., Yamanaka, T., Matsui, M., in W.H. Sutton, M.H. Brooks and I.J. Chabinsky (Eds.), *Microwave Processing of Materials, Mat. Res. Symp. Proc.*, Materials Research Society, Pittsburgh, 124 (1988) 267.

Gale, W.F., *JOM*, 51(2) (1999) 49.

Geng, H., Ph.D dissertation, Michigan state university, 2003.

Grossman, D., *American Machinist*, May (1978) 21.

Grossman, D., *J.Am.Ceram.Soc.*, 55 (9)(1972) 448.

Hanson, W.. Fernie, J., *Materials World* 16 (9) (1998) 534.

Hassler, Y., Johansen, L., in: W.H. Sutton, M.H. Brooks, I.J. Chabinsky (Eds), Microwave Processing of Materials, April 5-8, 1988, Reno, Nevada, Material Research Society, Pittsburgh, Pennsylvania, *Materials Research Society Symposium Proceedings*, 124(1988) 273.

Hauth, W.E., *Am. Ceram. Soc. Bull.*, 58(1979)584.

Ho, W.W., in W.H. Sutton, M.H. Brooks and I.J. Chabinsky (Eds.), *Microwave Processing of Materials, Mat. Res. Symp. Proc.*, Materials Research Society, Pittsburgh, 124 (1988) 137.

Janney, M.A., Kimrey, H. D., in: W.B. Snyder Jr, W.H. Sutton, M.F. Iskander, D.L. Johnson (Eds.), *Microwave Processing of Materials II. Proc. Symp.* San Francisco, April 17-20, 1990, Material Research Society, Pittsburgh, Pennsylvania, Materials Research Society Symposium Proceedings, 189 (1991) 215.

Janney, M.A., Kimrey, H.D., in: G.L. Messing, E.R. Fuller, H. Hausner (Eds.), American Ceramic Society, Westerville, Ohio, 1988, Ceramic Powder Science II, B, *Ceramic Transactions*, 1(1988) 919.

Janney, M.A., Kimrey, H.D., Schmidt, M.A., Kiggans, J.O., *J.Am.Ceram.Soc.* 74(7) (1991)1675.

Johnson, S.M., Rowcliff, D.J., *J. Am. Ceram. Soc.*, 68(1985) 468.

Kennard, F.L., Bradt, R.C., Stubican, V.S., in J.S. Anderson (Eds.), *Reactivity of Solids*, North Holland, Amsterdam, 1972, p. 580.
Kingery, W.D., Bowen, H.K., Uhlmann, D.R., *Introduction to Ceramics*, Second Edition, John Wiley & Sons, Inc, New York, 1976, p. 466-513.

Kovalev, S.P., Miranzo, P., Osendi, M.I.,, *J. Amer. Ceram. Soc*, 81(9) (1998) 2342.

Lardner, T.J., Rotter, J.E., Shiao, M.L., Lin, M.R., *International Journal of Fracture*, 44(1990)133.

Lee, C.C., Lin, P., Jpn. *J. Appl. Phys.* 37(1998) 6048.

Lee, J.G., Case, E.D., in: N.P. Bansal, J.P. Singh, E. Ustundag (Eds.), Advances in Ceramic Matrix Composite V, American Ceramic Society, Inc., Westerville, OH, 2000, *Ceramic Trans.* 103, pp. 571-581.

Lee, K. Y., Case, E. D., Reinhard, D., *Ceramic Eng. And Sci. Proc.*, 18(1997)543.

Lee, K.S., Wuttiphan, S., Hu, X.Z., Lee, S.K., Lawn, B.R., *J.Am.Ceram.Soc.*, 81 (3)(1998) 571.

Lee, W., Howard, S. J., Clegg, W. J., *Acta Mater.* 44(10) (1996) 3905.

Levin, E.M., Robbins, C.R., McMurdie, H.F., Fig. 630 in *Phase Diagrams for Ceramists*, Edited by M.K. Reser. American Ceramic Society, Columbus, OH, 1964.

Locatelli, M.R., Dalgleish, B.J., Nakashima, K., Tomsia, A.P., Glaeser, A.M., *Ceramic International.* 23 (1997) 313.

Loehman, R.E., in: D.E. Clark, W.R. Tinga, J.R. Laia Jr (Eds.), Microwaves: Theory and Application in Materials Processing II. Proc. Symp. Cincinnati, 19-22 April, 1993, American Ceramic Soc. Inc.; *Ceram.Trans.* 36 (1993) 417.

Loehman, R.E., *Key Engineering Materials.* 161-163 (1999) 657.

Loehman, R.E., pp. 701-11 in *Surface and Interfaces in Ceramic and Ceramic-Metal Systems*, Edited by J. Pask and A. Evans. Plenum Publishing Co., New York, 1981.

Macdowell, J.F., Beall, G.H., *J.Am.Ceram.Soc.*, 52(1)(1969) 17.

Marshall, D.B., B.R. Lawn, *J. Mater. Sci.*, 14(8)(1979) 2001.

Marshall, D.B., B.R. Lawn, *J.Am.Ceram.Soc.*, 60 (1-2)(1977) 86.

Moorhead, A.J., *Adv. Ceram. Mater.*, 2(1987)159.

Moorhead, A.J., Keating, H., *Welding J.*, 65(1986)17.

Mullins, W.W., *Acta Met.*, 6(1958) 414.

Mullins, W.W., *J. Appl. Phys.*, 28(1957) 333.

Mullins, W.W., *Trans. Met. Soc. AIME.*, 218(1960) 354.

Nakajima, A., Messing, G.L., *J.Am.Ceram.Soc.*, 81(5)(1998) 1163.

Nakamura, M., Shigematsu, I., Nakanishi, M., Shigematsu, K., Yamada, Y., Shigegaki, Y., *J.Mat.Sci.Lett.*, 16(1997) 1654.

Nakamura-A, M., Shigematsu, I., Mabuchi, M., Yamada, Y., Shimojima, K., Saito, N., Nakanishi, M., *Journal of the Ceramic Society of Japan*, 105(1227)(1997) 1047.

Palaith, D., Silberglitt, R., *Am. Ceram. Soc. Bull.* 68(9) (1989) 1601.

Patterson, M.C.L., Apte, P.S., Kimber, R.M., Roy, R., in: R.L. Beatty, W.H. Sutton, M.F. Iskander (Eds.), *Microwave Processing of Materials III. Proc. Symp.* San Francisco, April 27-May 1,1992, Material Research Society, Pittsburgh, Pennsylvania, Materials Research Society Symposium Proceedings, 269 (1992) 301.

Pinckney, L.R., *Ceramics and Glasses*, ASM International, Engineered Materials Handbook. vol 4, ASM International, Materials Park, Ohio, 1991, p. 436.

Regnier, C., Tristant, P., Desmaison, J., *Surface and Coating Technology*, 80(1996) 18.
Richerson, D. W., *Modern Ceramic Engineering: Properties, processing and Use in Design*, 2nd edition, p. 419-497, Marcel Dekker, Inc., New York (1992).

Risbud, S.H., Pask, J.A., *Journal of Materials Science*, 13(1978) 2449.

Risbud, S.H., Pask, J.A., *Journal of Materials Science*, 60(1977) 418.

Rodel, J., Glaeser, A.M., *J.Am.Ceram.Soc.* 73(3)(1990) 592.

Rodriguez, A.D., Guiberteau, F., Melendo, M.J., *Journal of Materials Research (USA)*, 13(6) (1998) 1631.

Rybakov, K.I., ,V.E., *Phys. Rev. B* 49 (1994) 64.

Sacks, M.D., Wang, K., Scheiffele, G.W., Bozkurt, N., *J.Am.Ceram.Soc.*, 79(2)(1996) 571.

Sacks, M.D., Wang, K., Scheiffele, G.W., Bozkurt, N., *J.Am.Ceram.Soc.*, 80(3)(1997) 663.

Saiz, E., Tomsia, A.P., Cannon, R.M., in A. Bellosi (Eds.), *Interfacial Science in Ceramic Joining*, Kluwer Academic Publishers, 1998, p. 161.

Sandhage, K.H., Schmutzler, H.J., Wheeler, R., Frazer, H.L., *J. Amer. Ceram. Soc.*, 79 (7) (1996)1839.

Santellal, M.L., *Am. Ceram. Soc. Bull.*, 71(1992) 947.

Schairper, J.F., *J. Am. Ceram. Soc.* 37 (11) (1954) 501.

Schwartz, M.M., *Ceramic Joining*. ASM International, Materials Park, OH, 1990.

Seiber, K. N., Lee, K. Y., Case, E. D., "Microwave and Conventional Joining of Ceramics using Spin-on Materials," pp. 941-949, *Proceedings of the 12th Annual Advanced Composites Conference*, Technomic Publishing Co., Lancaster, PA., 1997.
Shalz, M.L., Dalgeish, B.J., Tomsia, A.P., Glaeser, A.M., *Ceramic Transactions*, 35 (1993) 301.

Singh, M.. 164-165(1999)415.

Smith, P.A., Davis, L.E., *Electronics Letters*, 28 (4) (1992) 424.

Staley, W.G., Brindley, G.W., *J.Am.Ceram.Soc.*, 32(11)(1969) 616.

Suganuma, K., Okamoto, T., Koizumi, M., Shimada, M., *J. Mater. Sci.*, 22 (4)(1987) 1359.

Sutton, W., *Ceramic Bulletin*, 68 (1992)376.

Tian, Y.L., Johnson, D.L., Brodwin, M.E., in: G.L. Messing, E.R. Fuller, H. Hausner (Eds.), American Ceramic Society, Westerville, Ohio, 1988, Ceramic Powder Science II, B, *Ceramic Transactions*, 1(1988) 925.

Tinga, W.R., Mat. Res. Soc. Sym. Proc., *Materials Research Society* (USA), 124 (1988)33.

Urena, A., Gomez de Salazar, J.M., Quinones, J., *J. Mater. Sci.* 27(3) (1992)599.

Vegter, R.H., Ouden, G.D., *J. Mater. Sci.* 33(18)(1998) 4225.

Wallach, E.R., Hill, A., *Acta Metall Mater*, 37 (9) (1989) 2425.

Walls, P.A., Ueki, M., *J. Am. Ceram. Soc.* 75 (9) (1992) 2491.

Walton, J.D., *Radome Engineering Handbook; Design and Principles: Inorganic Randomes*; Marcel Dekker, Inc., New York, 1970, pp. 229-344.
Weldon, L.M., Hampshire, S., Pomeroy, M.J., *J. Euro. Ceram. Soc.* 17(1997)1941.

Woods, M.E., Mandler, W.F., Scofield, T.L., *Am. Ceram. Soc. Bull.*, 64 (1985)287.

Wunsche, C., Radlein, E., Frischat, G.H., *Glass Sci. Technol.* 72(2) (1999) 49.

Yano, T., Suematsu, H., Iseki, T., *J. Mater. Sci.* 23(3)(1998)3362.

Ye, J., Rodriquez, A. D., *Scripta Metallurgica and Materialia*, 33, (1994) 441.

Zdaniewski, W.A., *J. Amer. Ceram. Soc.* 58(5-6)(1975)163.

Zdaniewski, W.A., Kirchner, H.P., Segall, A., Conway, J.C., *J. Amer. Ceram. Soc.* 70 (2) (1987) 110.

Zdaniewski, W.A., Shah, P.M., Kirchner, H.P., *Adv. Ceram. Mater.*, 2 (1987) 204.

Zeng, L., Case, E., Crimp, M.A., *Mat. Sci. and Eng.* A 307 (2001)74.

Zurbuchen, M.A., Carim, A.H., *J. Am. Ceram. Soc.*, 82 (3)(1999) 705.

PART II

EFFECTS OF WORKING AND HEAT TREATMENT ON MICROSTRUCTURAL AND CRYSTALLOGRAPHIC TEXTURE EVOLUTION IN TI-6AL-4V

Chapter I

Introduction

1.1 Introduction

As a commercial alloy with 6 wt% aluminum and 4 wt% vanadium, Ti-6Al-4V is currently the most widely used titanium alloy, accounting for more than 50% of all titanium output in the world [Boyer-A 1994]. To date, no other titanium alloy can replace its dominant position. Due to its good strength-to-weight-ratio or high specific strength, Ti-6Al-4V is frequently used in aviation and aerospace industry that accounts for more than 80% of this usage. The next largest application of Ti-6Al-4V is medical prostheses, which accounts for 3% of the market [Boyer-A 1994]. The automotive, marine, and chemical industries also use small amounts of Ti-6Al-4V [Boyer 1995]. The initial application of Ti-6Al-4V includes compressor blades in gas turbine and fasteners due to their good corrosion-resistance. However, the low modulus of elasticity and thermal resistance of titanium alloys designed for high strength at low to moderate up to 400°C gives them new opportunities in turbine engine and air frame applications. Unfortunately, cost continues to be a major factor for its use in industries where weight

and corrosion are critical considerations. In the aerospace industry, the superplastic characteristics of fine grained, equiaxial Ti-6Al-4V are being used increasingly [Boyer-A 1994], such as fabrication of very complex structures for military airplanes, by combining good diffusion bonding characteristics with superplastic forming.

In the medical industry, due to its biological compatibility, good tensile and fatigue strength, wrought Ti-6Al-4V is used for surgical implants, especially for bone screws, and for partial and total hip, knee, elbow, jaw, finger, and shoulder replacement joints [Ke 2001, Orr 1992].

1.2 Microstructure evolution in Ti-6Al-4V

As an $\alpha+\beta$ alloy, Ti-6Al-4V has received extensive research and development theoretically and experimentally since it was developed in the 1950s. Much progress has been accomplished through heat treatments, processing techniques, fundamental knowledge of phase transformations and deformation mechanisms, and the relationship between microstructure and the corresponding mechanical properties.

1.2.1 Phase transformations and heat treatments

Microstructure evolution control is necessary to change and control the physical and mechanical properties of Ti-6Al-4V. More importantly, the effective controls of microstructure evolution of Ti-6Al-4V mainly depend on the understanding of the phase transformations occurring during heat treatment and processing. Table 1.1 lists the main phase transformations and resulting phases that can occur in Ti-6Al-4V. Some of the transformations are understood better than others. A complete review and research of all phase transformations that occur in Ti-6Al-4V is beyond the scope of this research, so only the subjects relevant to this dissertation will be reviewed.

As an α+β alloy, Ti-6Al-4V can have different microstructures having different geometrical arrangements of many crystal phases, including α, β, α', α", α_2, and ω phases, depending on the particular thermomechanical treatment and interstitial (primarily oxygen) content. These phases are all minor distortions of the bcc β or the hcp α phase, such that boundaries between them are typically coherent. The β isomorphous phase diagram shown in figure 1.1 can be divided into three regions depending on the β stabilizer V concentration in primary β grains [Koul 1970]. In region I where the β stabilizer V concentration is approximately 4 wt%, the high temperature, bcc β phase can completely transform to hexagonal close packed equilibrium α and/or martensitic α' phases upon cooling. The needlelike α' phase is obtained upon quenching and it is frequently internally twinned on $\{10\bar{1}1\}_\alpha$ planes. Slow cooling or furnace cooling from above the β transus which is around 955~1010°C into the two phase (α+β) region leads to the formation of α-phase in plate form or plate-like alpha by nucleation and growth at preferred sites, such as primary β grain boundaries [Boyer-A 1994], since the kinetics of the α phase nucleation and growth reaction in region I that is lean in β stabilizers such as V, is very fast [Chesnutt 1976]. Air-cooling results in a fine needle-like alpha α, generally referred to as acicular alpha. Certain intermediate cooling rates develop Widmanstätten structures (Figure 1.1(b)) [Boyer-A 1994].

In region II where the β stabilizer V concentration is around 9~13 wt% V [Koul 1970], the beta phase can be retained at room temperature and/or transform to other non-equilibrium orthorhombic α" martensite by quenching, or it can partially decompose to a structure such as ω phase during iso-thermal annealing at temperatures below 400°C

[Boyer-B 1994]. In Ti-6Al-4V, the α' phase is obtained by quenching from above 900°C and α" is a rather soft martensite that forms when quenching from temperatures between 800 and 900°C. Slower cooling leads to the formation of platelet α-phase in β matrix generally referred to as "transformed β". In addition, stress induced α" martensite can form under stress in this region [Koul 1970].

Upon aging the α' and α" martensites can decompose into fine α phase since the structure of α' and α" is metastable. Just as in the case of ferrous martensites, the nature of tempering reactions in Ti martensites is rather complex and depends on the composition and crystal structure of the martensites. Several mechanisms have been proposed to explain the age hardening effects that raise the yield strength:

(1) The decomposition of α' into fine α and β by nucleation and growth process. During the precipitation of β phase which is preferentially oriented along the basal directions within the α' plates [Gil 1995], the composition of α' approaches the equilibrium composition of the α phase in equilibrium with the β phase at the tempering temperatures.

(2) The decomposition of α" into fine α and β. The α" martensite tempers first by spinodal precipitation of α phase with the attendant enrichment of the non-equilibrium orthorhombic structure that eventually approaches the composition of β phase [Williams 1970, 1972], unlike the decomposition of α'. The overall tempering reaction can be explained in terms of spinodal decomposition and reverse martensite transformation represented by $\alpha'' \rightarrow \alpha''_{lean} + \alpha''_{rich} \rightarrow \alpha + \beta$ [Davis 1977].

(3) The formation of finely ordered equilibrium hexagonal α_2 (Ti_3Al) phase within primary α phase. Due to the large, negative titanium and aluminum interaction energy, the formation of tightly and directionally bonded α_2 precipitates causes increases in modulus and yield strength [Gehlen 1970, Welsch 1977].

(4) The ordering of interstitials (primarily oxygen) within primary α phase. Due to the formation of short-range order of oxygen, oxygen induced internal friction and promotion of glide band with increasing oxygen concentration produce large increases in modulus and yield strength [Welsch 1977].

(5) The metastable $\beta \rightarrow \omega$ transformation that is generally thought to cause hardening and embrittlement of Ti-6Al-4V alloys. Generally the ordered hexagonal and/or cubic ω phase does not occur in Ti-6Al-4V alloy of commercial purity unless the β phase is highly enriched with vanadium (over 15 wt.%) that makes the formation of ω phase thermodynamically favorable instead of hexagonal α' and orthorhombic α" martensites [Fan 1994, Lasalmonie 1979]. The ω phase might occur during low temperature aging or during cooling through the same temperature range, or be maintained throughout processing due to its presence in as-received material [Boyer-A 1994].

In region III where the V concentration is more than 15%, the high temperature β phase can be completely retained or slowly transformed to more stable ω phase during cooling to room temperature [Koul 1970, Boyer-B 1994]. The $\beta \rightarrow \omega$ transformation kinetics in Ti-6Al-4V is very slow and thus this transformation takes very long time to accomplish. Therefore, it is generally believed that the β phase remains stable with

increasing solute concentration and therefore no further transformations occur in this region.

1.2.2 Crystallography of major phases in Ti-6Al-4V

Although the α, β, α', α", and ω phases fall into different crystallographic categories, their crystal structures are all really similar. Table 1.2(a) shows the main crystallography relations of α, β, α', α", and ω phases transformations in Titanium alloys. The generally accepted lattice correspondence between β and α(α') phases is the Burgers relationship [Burgers 1934] in $(110)_\beta \| (0001)_\alpha$ and $\langle 111 \rangle_\beta \| \langle 11\bar{2}0 \rangle_\alpha$. Davis et al. [1979] calculated the lattice strain and found the transformation between β and α(α') phases can be achieved via 10% contraction along $[100]_\beta$ which becomes $[2\bar{1}\bar{1}0]_\alpha$, a 10% expansion along the $[01\bar{1}]_\beta$ that becomes $[01\bar{1}0]_\alpha$ and 1% expansion along $[011]_\beta$ that becomes $[0001]_\alpha$. Similar to the β→α' transformations, [Davis 1979] the equivalent lattice correspondence of the β→α" transformation is: $[100]_\beta$ and $[100]_{\alpha"}$, $[01\bar{1}]_\beta$ and $[010]_{\alpha"}$, $[01\bar{1}]_\beta$ and $[001]_{\alpha"}$ with reduced corresponding lattice strain (Table 1.2(b)), suggesting the orthorhombic α" structure is an intermediate structure between β (bcc)→α' (hcp) transformations. The lattice correspondence between the β, α' and α" is shown in figure 1.2. It is generally known that the orthorhombic α" structure is derived from a distorted hexagonal lattice in which the c-axis of the α" corresponded to the c-axis of the hexagonal α' lattice with the a and b axes of orthorhombic α" structure corresponding to the orthogonal axes of the hexagonal lattice.

1.2.3 Solution quenching and aging (SQA)

Ti-6Al-4V alloy is most commonly used in the fully annealed conditions, often referred to as mill annealed. In an industry where high strength with adequate ductility is required, such as for fasteners, it is necessary to solution treat at a temperature high in the α-β field, normally 28~83°C (50~150°F) below the β-transus temperature which is generally around 975°C [Boyer-C 1994]. If high fracture toughness or improved resistance to stress corrosion is required, a solution treatment above the β transus that causes fully transformed α', may be desirable (Table 1.3(a)).

The microstructure obtained from solution treating in the α-β field depends on the degree of homogenization and cooling rate during the heat treatment. Mill annealed Ti-6Al-4V alloy is a mixture of Al-rich α grains and V-rich β grains. At elevated temperatures, α grains transform to β grains and upon subsequent quenching β may transform into α', α" or retained β, depending on the solution treating temperature, time [Boyer-D 1994] and oxygen concentration [Kahveci 1986]. The higher the solution treating temperature in the α-β field, the greater the amount of α grains that can transform to β (figure 1.3), which causes lower V content in the equilibrium β phase [Maykuth 1971] and higher strength after aging [Lasalmonie 1979]. Quenching from above 900°C, the V content in the equilibrium β phase is approximately 4 wt%, so α' phase is obtained, and soft α" martensite is formed when quenching from between 800 and 900°C, when the V content is around 9~13 wt%. However, when quenching from below 800°C, when 15 wt% or higher V content is in the primary β phase, the β phase is retained without transformation.

The effects of solutionization time and temperature on microstructural changes depend on diffusion coefficients [Boyer-D 1994]. Therefore, approximate assessment of

the extent of possible microstructure changes by solutionization or aging can be made on the basis of the magnitude of the Ti element self-diffusion, Al and V alloy elements diffusion coefficient in α and β grains, respectively. The available information on diffusion coefficients for the Ti-6Al-4V used in this study is limited (See Table 1.3(b)), so data comes from similar structure of different Titanium alloys. A rough estimate of the average distance χ traveled by an atom in one direction can be obtained from the random walk equation $\chi^2=2Dt$, where D is the diffusion coefficient and t is the diffusion time (Table 1.3(b)). For example, at normal aging temperature 500°C, the average diffusion distance of Titanium for 4 hours are approximately 0.5 and 0.25 μm in the α and β phase, respectively, suggesting that the aging process can only lead to local modification of microstructure and no obvious microstructure changes could occur when examined using optical and scanning electron microscopy. However, for 1 hour at 1000°C, they are 3 and 30 μm, respectively, suggesting homogenization of the microstructure occurs rapidly enough to facilitate observable microstructure changes.

In addition, oxygen, carbon and nitrogen interstitial impurities can increase the β-transus temperature, lattice parameters [Anderson 1957], notch sensitivity [Maykuth 1971], strength and α/β phase ratio. Kahveci et al. [1986] found oxygen significantly decreased the volume fraction of β phase (Figure 1.3) and raised the β-transus temperature in the following relation:

$$T_{\beta\text{-transus}}\,(°C) = 937 + 242.7 \times O$$

Where O is the oxygen content in wt%.

Recently, Boswell [1995] et al. researched the effects of solutionization temperature and time in β phase field on grain growth, texture and grain misorientation behaviors. With the higher solutionization temperature and longer solutionization time in β phase field, the preferred orientation or texture increases and the average degree of grain boundary misorientation decreases, leading to a decreasing grain growth rate at larger grain sizes. The authors suggested that slowing down grain growth and deviations from a classic grain growth law may be due to the decrease in grain boundary misorientation, occurrence of local grouping of similar boundaries and solute segregation at grain boundaries. However, Boswell et al. [1995] failed to correlate the $\alpha \leftrightarrow \beta$ phase transformation mechanisms to the observed phenomena.

1.2.4 Deformation and processing

1.2.4.1 Deformation mode of α phase

The deformation of Titanium alloys has been the subject of intensive study over the last 40 years. An understanding of deformation mechanisms is essential for the solution of problems such as the development of rolling texture, creep, and fracture toughness. Deformation in the α phase can occur by either slip or twinning. The slip and twinning modes reported in the literature are listed in table 1.4. At room temperature, the α phase slips along the basal {0001}, prism $\{10\bar{1}0\}$, and pyramidal $\{10\bar{1}1\}$ planes by the motions of $1/3\langle 11\bar{2}0\rangle$, or $\vec{a}$ dislocations, as well as the $\{10\bar{1}0\}$ and pyramidal $\{11\bar{2}\bar{2}\}$ systems with the $\vec{c}+\vec{a}$ dislocations $1/3\langle 11\bar{2}3\rangle$ (Figure 1.4) [Jones 1981, Boyer-B 1994]. $\vec{c}$ dislocation <0001> is restricted to only prismatic planes and always sessile and generally does not occur. The relative ease of activation for different slip systems is

controlled by the core structure of dislocations, impurity content, and temperature [Jones 1981]. Ti-6Al-4V can also deform by twinning (Figure 1.4). It has been reported to occur on a variety of pyramidal planes. $\{11\bar{2}3\}$, $\{10\bar{1}2\}$ and $\{11\bar{2}1\}$ twins allow an extension, while $\{11\bar{2}2\}$, $\{10\bar{1}1\}$ and $\{11\bar{2}4\}$ twins permits a contraction [Rosi 1953]. In polycrystalline Ti-6Al-4V, basal and prism slip of $\vec{a}$ dislocations do not support sufficient slip modes to satisfy von Mises criterion that every grain should be able to plastically deform generally to meet the shape changes imposed by its neighbors. Therefore, at least five independent slip systems are required, whereas basal and prism slip can only provide four, so twinning and $\vec{c}+\vec{a}$ dislocation slip must accommodate shear strain and displacement in the $\vec{c}$ directions [Boyer-B 1994].

The deformation modes of α phase as a function of stress, temperature, and the impurity level have been widely explored. Compression perpendicular to the c-axis, or along the $<10\bar{1}0>$, is accommodated by the prismatic $\{1\bar{1}00\}$ slip of $\vec{a}$ screw dislocations, either $1/3<11\bar{2}0>$ or $1/3<\bar{2}110>$ [Jones 1981] and $\{10\bar{1}2\}$ [Boyer-B 1994] or $\{11\bar{2}1\}$ twins [Paton 1969, 1970]. However, Jones et al. [1981] found no twins were ever observed due to (< 10 μm) fine grain size for compression normal to the c-axis, so $\vec{c}+\vec{a}$ dislocations on $\{1\bar{1}01\}$ satisfied the von Mises criterion. TEM analysis revealed dislocations arranged in planar glide. Although Jones et al. [1981] did not specify the oxygen content, a transition from planar to wavy glide was observed with decreasing temperature and increasing oxygen content [Williams 1972]. In the planar arrays, most of dislocations are jogged screws, suggesting edge dislocations move more quickly, and

the average distance between jogged screw dislocations is less within planer bands, leading to increased internal stress [Williams 1972], as compared to tangled dislocation arrangements.

Compression [Jones 1981] along the c-axis is mainly accommodated by the $\{1\bar{1}01\}$ slip of $\vec{c}+\vec{a}$ dislocations with extensive cross-slip on second $\{1\bar{1}01\}$ and dragging out edge dipoles until the neighboring segments also cross-slip and join them. In contrast, with c-axis tension, slip planes are clean without cross-slip, leading to increased CRSS in compression. However, Paton et al. [1969, 1970] found compression along the c-axis is accomplished only by wide and lenticular shaped $\{11\bar{2}2\}$ twins for single crystal Titanium via metallographic examinations, while increasing aluminum content tends to suppress the occurrence of twinning. For example, compression along the c-axis even at 77°K resulted in very limited amount of twinning for 6% Al addition and extensive $\vec{c}+\vec{a}$ was always seen. In addition, almost all dislocations [Jones 1981] are of screw $\vec{a}$ type gliding on (0001) and $(0\bar{1}1\bar{1})$ planes for compression along $<10\bar{1}1>$, implying edge components are more mobile.

TEM analysis also showed that the screw dislocation components are less mobile than edge components. Naka [1994] has proposed a complex core structure for screw dislocations. The screw components have a core spread on different planes, while the edge components have a planer core. Below the athermal temperature (~500°K), the motion of screw dislocations is controlled by the thermally activated recombination of the core and therefore the screw components move slower and thus control the deformation rate.

To explain the hcp↔bcc transformations, a few authors [Akhtar 1975, Regnier 1970] proposed a dissociation of $\vec{a}$ dislocations on $\{1\bar{1}01\}$ plane is similar to bcc structure based on the correlation between the ease of hcp transformations and a tendency for prismatic $\vec{a}$ slip. However, Jones et al. [1981] found no justification for such correlations and proposed that the hcp↔bcc transformations are a separate phenomenon influenced by the c/a ratio [Spedding 1916].

1.2.4.2 Deformation mode of β phase

In addition to the research of deformation mode in the α phase, the β phase has also received much attention. It is expected that deformation in single crystal β phase is the same as for other bcc metals, i.e. {110}, {112}, and {123} planes with <111> slip directions [Barrett 1966]. Studies on commercial binary and ternary β Titanium alloys in which the β phase is metastable or stable at room temperature revealed {332}<113> twinning or <111> slip as the dominant plastic deformation mode [Hanada 1986, 1987]. {332}<113> twinning appears in the most unstable β phase alloys where the diffraction pattern of the β phase reveals sharp ω phase reflections. As the stability of the β phase increases, the deformation mode changes from twinning to slip, and correspondingly, the diffraction pattern of the β phase changes from sharp ω reflections to diffuse streaking [Hanada 1987]. In addition, modeling of the high temperature β phase in a Ti-6Al-4V showed that mixed slip on {110}<111> and {112}<111> are the dominant deformation modes [Gey 1996, 1997].

1.3 Texture evolution in Ti-6Al-4V

Texture or preferred orientation plays an important role in the mechanical properties of Titanium and its alloys because of the highly anisotropic crystalline structure of the α phase, leading to pronounced anisotropy in stress, strain and strength. It is almost impossible to eliminate texture or preferred orientation in commercial manufacturing processes [Fujishiro 1980]. Further, texture strengthening or hardening can be beneficial. For example, it has long been realized that strong basal plane texture of Ti-6Al-4V is desirable for applications whenever the stress field is biaxial [Babel, Murayama 1968]. Therefore, it is necessary to study the formation and evolution of Ti-6Al-4V textures induced by different thermomechanical treatments since better adaptation of the mechanical properties for a given applications requires good control of the texture.

Based on the formation mechanisms, three kinds of textures are found in Ti-6Al-4V, deformation, recrystallization and phase transformation textures. Deformation texture, including fiber and sheet texture, is formed due to the tendency of polycrystalline grains in an aggregate to rotate during plastic deformation. For fiber texture, the individual grain in a wire is oriented so that the same crystallographic direction [uvw] in most grains is parallel or nearly parallel to the wire axis. Materials having a fiber texture have rotational symmetry (about [uvw] parallel to wire axis) such that all crystal rotations about the wire axis are equally probable. Therefore, fiber texture is expected in materials formed by forces that have rotational symmetry about an axis, such as, in wire drawing, swaging or extrusion [Cullity 1978]. Sheet texture implies that most of the grains are oriented with a certain crystallographic plane (hkl) roughly parallel to the sheet normal (SN), and a certain crystallographic direction roughly parallel to the rolling direction

(RD). Such a texture is described by the notation (hkl)[uvw] [Cullity 1978]. Recrystallization or annealing textures are formed when annealing cold or hot worked Titanium to initiate new grain structure that generally has a preferred orientation, possibly different from the deformation texture. A phase transformation texture is formed through following three steps: (1) development of transformation texture from $\alpha \rightarrow \beta$ phase, (2) development of β phase texture at elevated temperatures usually above 850°C, and (3) development of transformation texture from $\beta \rightarrow \alpha$ phase during cooling [Tanabe 1980]. In industry, texture of Ti-6Al-4V usually originates from hot working processes, which produce a combination of deformation, recrystallization and phase transformation textures [Fujishiro 1980]. Therefore, the overall influential factors on the texture formation are mainly: (1) deformation mode, (2) prior texture, (3) deformation temperature, and (4) subsequent processing after deformation.

1.3.1 Deformation and recrystallization texture

Due to its poor cold forming properties which are generally associated with cracking or excessive spring back problems, Ti-6Al-4V typically is formed using hot forming above 540°C [Boyer-F, G 1994]. At temperatures below 850°C, the hot rolled texture [Tanabe, Peters 1980] is composed of transverse, split RD, and split transverse direction (TD) components. The split TD texture due to hot rolling at 500°C with (0002) pole concentrated at 20~30° from the SN toward the TD is generated with a spread of (0002) poles. With increasing rolling temperature, an additional (0002) pole peak concentrated at 60~80° from the SN in the TD is generated, called transverse texture [Tanabe 1980]. This can be interpreted as α-rolling texture because the volume fraction

of the primary β phase is in the range of 25~30% from 500~850°C, so the newly formed α phase after the phase transformation cycle α→β→α is less than 10% (Figure 1.3).

Upon further annealing after hot rolling in the temperature range of 500~850°C, the split RD and transverse texture will not change [Tanabe, Peters 1980]. For example, Peters et al. [1980] investigated the hot rolling and annealing texture at 800°C starting from randomly orientated Ti-6Al-4V specimen. After hot rolling at 800°C followed by quenching to avoid recrystallization, two different types of texture, split RD and transverse, are developed (Figure 1.5(a)). Further annealing (Figure 1.5(b)) at 800°C for up to 96 hours will not change the texture significantly [Peters 1980], except for a slightly increased maximum intensity, even though the microstructure changes from deformed to equiaxed microstructure, suggesting that recrystallization texture is essentially the same as deformation texture for Ti-6Al-4V alloy.

The similar deformation and recrystallization texture behaviors are different from the high purity Titanium, where recrystallization due to selective growth of the newly formed nuclei [Hu 1968] leads to sharpening of texture and rotation of the basal plane [Keeler 1956]. Figure 1.5 shows the schematic representation of cold rolling deformation and recrystallization texture in pure Titanium sheet [Keeler 1956]. In addition, hot rolling at 700°C of randomly oriented pure Titanium yields a split RD and TD texture; while further annealing at 700°C leads to a crystal rotation with disappearance of the split RD texture [Tanabe 1980]. These different behaviors between pure Titanium and Ti-6Al-4V are generally considered to be caused by alloying elements.

1.3.2 Transformation texture and variant selections

At elevated temperatures above the $\alpha/\alpha+\beta$ transus, the low temperature hcp α phase transforms to the bcc β phase and the subsequent cooling results in the β phase transforming back to the hcp α phase, leading to the formation of many new orientations, or the phase transformation texture. This $\alpha \leftrightarrow \beta$ transformation behavior is based on the Burgers relationship in $(110)_\beta \| (0001)_\alpha$ and $<111>_\beta \| <11\bar{2}0>_\alpha$. Thus, upon heating, each α phase orientation can produce up to six cubic orientations with a $(110)_\beta$ plane parallel to the original $(0001)_\alpha$ plane and with the six possible combinations of parallel orientations, including two $<111>_\beta$ directions in the $(110)_\beta$ plane and three $<11\bar{2}0>_\alpha$ directions in the $(0001)_\alpha$ plane. With cooling to room temperature after solutionization, each one of the six cubic orientations can generate another twelve orientations of the hcp α phase, with two different ways to align the hcp cell with reference to the [110] directions on each of the six $(110)_\beta$ planes. Therefore, one orientation of α phase could generate an α phase texture with potentially $6 \times 12 = 72$ orientations on heating to above the transformation temperature followed by cooling to room temperature [Keeler 1956]. Figure 6 schematically shows the $\alpha \rightarrow \beta \rightarrow \alpha$ transformation texture cycle from an initial α single variant to the three possible variants of transformation β texture, and the six possible variants of room temperature α phase from single orientation of high temperature β phase. Due to crystal symmetry, only three variants of high temperature β phase and six variant of room temperature α phase are shown (Figure 1.6). However, many authors found each α phase orientation may not be able to equally provide 72 orientations after the transformation cycle $\alpha \rightarrow \beta \rightarrow \alpha$. Based on the three steps of

formation of transformation texture, some important aspect of variant selection will be discussed below.

First, each α phase orientation at room temperature will probably not be able to equally provide 6 orientations of β phase on heating to high temperatures [Gey 2000, Moustahfid 1997]. For example, heating initially randomly orientated α+β phases should be able to generate randomly orientated high temperature β phase without any significant texture if variant selection does not apply. However, Gey et al. [Gey 2000] simulated the high temperature β phase texture, based on the (1) measurement of room temperature retained β phase texture, and (2) simulation with a rate sensitive pancake Taylor model assuming mixed slip on {110}+{112}<111> [Toth 1998]. They found the high temperature β phase texture is essentially similar to room temperature retained β phase texture which has two distinct and strong fiber texture components characterized by the γ fiber and Eular angles (φ_1, 0, φ_2) in bcc. Furthermore Moustahfid et al. [1997] confirmed the relationship between high temperature β texture and the retained β phase texture, indicating variant selections can apply during α→β transformation on heating, resulting in some preferred β phase orientations.

Second, the complicated physical mechanisms that occur upon heating and high temperature solutionization that develop high temperature β phase texture remain unexplained [Moustahfid 1997]. Generally, high temperature solutionization will lead to β grain growth which could further modify or sharpen the existing β texture [Boswell 1995], and thus the subsequent transformation α texture. For example, Boswell [1995] et al. found that a higher solutionization temperature and longer solutionization time caused

a larger β grain size, stronger transformation α texture, and a smaller grain boundary misorientation angles. Apparently, all the factors that affecting the metallurgical state of the β phase can also affect the subsequent transformation texture [Keeler 1956, Gey 1997]. Therefore, Moustahfid et al. [1997] even thinks the physical mechanisms operating upon heating and solutionization might be more complex than the ones occurring during the β→α transformation.

Lastly, many authors found that each β phase orientation formed at high temperatures from the original α phase may not be able to equally provide 12 orientations of α phase upon cooling. In other words, it is highly possible that β grains can prefer one of these 12 α orientations. It has long been realized that constraint, such as residual stress, crystalline inclusion and an oriented overgrowth, can affect the β→α transformation texture, causing only one of the six $(110)_\beta$ planes to be favored in transforming to the $(0001)_\alpha$ with two strongly preferred α orientations [Keeler 1956]. This explanation is in agreement with the result that upon heat treatment in the β phase field without deformation, then α phase texture was developed from the high temperature β phase without variant selection. However, heat treatment in the α+β phase field or hot rolling in the β phase field with more than 30% reduction results in an α phase texture with variant selection [Gey 1996, 1997, Moustahfid 1997]. These observations can be correlated to residual stress generation since solution treating in the α+β phase field and deformation in the β phase field results in higher values of internal friction and/or residual stress than solution treating in the β phase field and undeformed β phase, respectively [Ouchi 1999]. In addition, if the β phase hot rolling was allowed to

recrystallize first then the subsequent α phase texture would have all six $(110)_\beta$ plane equally favored in transforming to the $(0001)_\alpha$ [Peters 1980]. Therefore, Gey et al. [1996, 1997] think the metallurgical state of the β phase, especially high temperature texture, is the key to the variant selections and affect the subsequent transformation texture. Noticeably, a model to simulate the transformation texture that correlated the favored variants and the most active slip system was developed, based on the assumptions that during high temperature rolling deformation the most active slip or the highest shear directions of β phase can be correlated to high defect density sites that are known to be nucleation sites of the new α phase, and further determine the later favored transformation texture. For example, $(0001)\ [2\bar{1}\bar{1}0]_\alpha$ α variant can be generated due to shear along the $(110)[\bar{1}1\bar{1}]_\beta$ or $(1\bar{1}2)[\bar{1}1\bar{1}]_\beta$ slip systems (Figure 1.7(a)). Therefore, based on the high temperature β phase texture and calculation of the highest resolved shear of all β slip systems, favored variants can be determined, so the simulated α phase transformation texture from the high temperature β phase texture is in general agreement with experimental texture. However, many authors reported that stress could speed the phase transformation by several orders of magnitude [Boyer-H 1994], such as dramatically reducing the time needed to complete the eutectoid reaction in Ti-12Cr. Furthermore, just as the growth of the pre-existing β nuclei inherited from high temperature forging determines the α→β transformation mechanism and the high temperature β phase texture upon heating, the "continuous dynamic recrystallization" with the appearance of small equiaxial grains during β phase hot rolling can also affect or even determine the subsequent β→α transformation [Gey 1996, 1997, 2000]. Therefore,

does hot rolling in the β phase field with more than 30% reduction lead to the α phase texture with variant selection by a stress, recrystallization or transformation texture effect, or a combination of these three effects?

In general, the variant selection rules for the transformation cycle α→β→α remain unanswered, especially the development of high temperature β phase texture upon heating and solutionization. The texture change due to β→α transformation has been widely studied and a little work has been done on the α→β transformation upon heating [Gey 2002]. As in the case of ferrous alloys, the martensite nucleation process involves the interaction of different defects to produce a configuration resembling the martensitic structure [Cahn 1996], so it is expected that different arrangements of defects, especially dislocations, may speed up or slow down the Ti-6Al-4V α→β and β→α transformations. Recently, Gey et al. [2002] found that cold rolling prior to the transformation cycle α→β→α leads to stronger high temperature β phase texture and stronger variant selections in pure Titanium sheet, suggesting strong initial α texture resulting in strong variant selections on both α→β and β→α transformations and vise versa.

Therefore, it is reasonable to assume that defects of certain arrangements in the initial α phase due to initial deformation can affect or even determine the α→β phase transformation texture and be kept or stored in the high temperature β phase to further influence the subsequent β→α transformations texture. In addition, it is also expected that not only the metallurgical state of high temperature β phase as discussed by Gey et al. [1996, 1997, 2000], but also the initial α phase texture prior to deformation.

1.4 Research strategy

The aim of this study is to achieve a better understanding of the relationship between texture and processing associated with the high temperature heat treatment in axisymmetric sample geometries. This research focuses on the effects of working and heat treatment on microstructural and crystallographic texture evolution in Ti-6Al-4V. The $\alpha \rightarrow \beta \rightarrow \alpha$ transformations, especially the texture variation, variant selections, and predictions were investigated using available analytical equipment. The effects of heat treatment, including solutionization and aging, on characteristics of variant selections of crystallographic texture evolution, major phases present, lattice parameters, grain sizes, and volume fractions of major phases were examined. These variables affect the deformation mode and phase/texture transformation. By deforming a textured sample in different deformation directions to introduce different internal defects or dislocations, the effects of crystallographic dislocations on the variant selections of transformation cycle $\alpha \rightarrow \beta \rightarrow \alpha$ were investigated. These results provide theoretical and experimental basis for extending the ability to manipulate Ti-6Al-4V into new and innovative textures that enable new applications by proper control of the texture and microstructure. This understanding will be critical in developing, commercializing and enhancing current or future applications.

In chapter three, crystallographic texture and microstructural features of Ti-6Al-4V were measured through several stages of processing, from as-received wire, extrusion, to solution heat-treating and then aging. In addition, a natural aging effect was found for the first time in Ti-6Al-4V. The main objective of this research is to gain comprehensive

understanding of the physical metallurgy of manufacturing processes that introduce variability in Ti-6Al-4V products such as inter-related effects of

- Intrinsic variability in source material
- Texture evolution,
- Phase transformation,
- Microstructure/property development.

In chapter four, effects of solution temperature and time on crystallographic texture and mechanical properties in Ti-6Al-4V were examined. The main purpose of this investigation is to gain a phenomenological understanding of the physical metallurgy of high temperature solution treating and water quenching that is widely used in industry on the following parameters and the correlation between them:

- Grain sizes
- Volume fraction of primary α and β
- Diffusion of Ti, Al and V in primary α and β grains
- Variant selections of $\beta \rightarrow \alpha$ transformation texture
- Texture
- Mechanical properties at different sample orientations

In chapter five, the α/β texture transformations mechanisms in Ti-6Al-4V were investigated. By deliberately deforming samples in different directions, different deformation modes and hence different dislocation densities and defect structures can be generated, so therefore different transformation texture might result. The main objective of this research is to investigate the effects of dislocation structure on the transformation texture and correlations of the following factors:

- Deformation mode
- Dislocations
- Variant selections of $\alpha \rightarrow \beta$ and $\beta \rightarrow \alpha$ transformation texture
- Development of high temperature β phase
- α/β phase transformation mechanism

Table 1.1 Main phase transformations in Ti-6Al-4V.

	Transformations	Process	Reference
1	Martensitic transformation	Martensite: $\beta \rightarrow \alpha'$, α''	[Williams 1967, 1970]
2	Stress-induced transformation	Martensite: $\beta \rightarrow \alpha''$	[Davis 1979]
		Athermal diffusionless ω phase: $\alpha \rightarrow \omega$	[Rabinkin 1981]
3	Decomposition of β phase (Nucleation and growth)	Iso-thermal ω phase: $\beta \rightarrow \omega$	[Fan 1994, Lasalmonie 1979]
		Acicular or basketwave α platelet: $\beta \rightarrow \alpha$ or $\beta \rightarrow$ Type1α, Type2α,	[Rhodes 1975, 1977]
4	Ordering of α phase	α_2 phase precipitation	[Welsch 1977]
5	Decomposition of martensites	Hexagonal $\alpha' \rightarrow \alpha+\beta$	[Williams 1967, 1970]
		Orthorhombic $\alpha'' \rightarrow \alpha+\beta$	
6	Spinodal decomposition	Phase separation: $\beta \rightarrow \beta'_{lean}+\beta'_{rich}$	[Fan 1994]
		Phase separation: $\alpha'' \rightarrow \alpha''_{lean}+\alpha''_{rich}$	[Davis 1979]

Table 1.2 The (a) main crystallography relations of α, β, α', α", and ω phase transformations in titanium alloys, the (b) lattice principle strains for β→α' and β→α" transformations

Process	Orientation relations	Reference
β→α (Type 1α)	Obeying Burgers relations: $(110)_\beta \| (0001)_\alpha$ $<111>_\beta \| <11\bar{2}0>_\alpha$	[Rhodes 1975]
β→α (Type 2α)	Not obeying Burgers relations but follows the $\{10\bar{1}2\}<10\bar{1}1>$ twin orientation with respect to the Burgers relations α	[Rhodes 1975]
β→α'	Obeying Burgers relations: $(110)_\beta \| (0001)_{\alpha'}$ $<111>_\beta \| <11\bar{2}0>_{\alpha'}$	[Burgers 1934, Rhodes 1975]
β→α"	$(110)_\beta \| (001)_{\alpha"}$ & $<1\bar{1}1>_\beta \| <110>_{\alpha"}$	[Davis 1979]
β→ω	$(110)_\beta \| (0001)_\omega$ & $<111>_\beta \| <11\bar{2}0>_\omega$	[Silcock 1956]
α→ω	$(0001)_\alpha \| (1\bar{2}10)_\omega$ & $<\bar{1}\bar{1}20>_\alpha \| <0001>_\omega$	[Rabinkin 1981]

(a)

Alloy	Transformations	ε_1(%)	ε_2(%)	ε_3(%)
Ti	β→α'	-10.1	10.1	0.9
Ti-8Mo	β→α"	-8.5	7.8	0.37

The calculations were made from the relations $\varepsilon_i=\eta_i-1$, $\eta_1=a/a_\beta$, $\eta_2=b/\sqrt{2}\,a_\beta$, $\eta_3=c/\sqrt{2}\,a_\beta$, where a, b, c are the lattice parameters of orthorhombic α" and a_β corresponding to the lattice parameter of β phase [from Davis 1979].

(b)

Table 1.3 The (a) relationship between microstructure characteristics, mechanical properties, and processing conditions [Boswell 1995, Boyer-B, C, E 1994], and the (b) diffusion coefficients in Titanium alloys.

Microstructure	Enhanced	Degrades	Processing
Bi-Modal α	Strength Ductility Fatigue initiation resistance Low-cycle fatigue resistance	Fatigue crack growth resistance Fracture toughness	STA in the α-β field
α' martensite	Fatigue performance	Fatigue crack growth resistance Fracture toughness	STA in the β field
Widmanstatten α	Fatigue crack growth resistance Fracture toughness High-cycle fatigue resistance Aqueous stress corrosion Creep	Ductility Strength Fatigue initiation resistance Low-cycle fatigue resistance	β field anneal

(a)

Temperature (°C)	Elements	α Phase		β Phase	
		D (m^2/s)	Materials	D (m^2/s)	Materials
500~1250	Ti	$1.3\times10^{-12}\times$ exp(-74500/RT)	Ti-4.1Al [Ouchi 1980]	$1.39\times10^{-6}\times$ exp(-173000/RT)	Ti-4.55 Al [Ouchi 1980]
500~1250	Al	$8.7\times10^{-13}\times$ exp(-70700/RT)	Ti-4.1Al [Ouchi 1980]	$2.9\times10^{-6}\times$ exp(-180000/RT)	Ti-4.55 Al [Ouchi 1980]
900~1550	V	---	---	$3.1\times10^{-6}\times$ exp(-32200/RT)+ $1.37\times10^{-4}\times$exp(-57200/RT)	Ti [Murdock 1964, 1968, Inouye, 1980]
700~950	O	$0.45\times$exp(-48000/RT)			Ti [David 1980]
690~850	Ti	$6.4\times10^{-12}\times$exp(-29300/RT)	Titanium [Libanati 1963]	---	---

(b)

Table 1.4(a). Slip and twin modes in α phase Titanium

	Slip mode	Reference
$\vec{a}$ Slip	$\{0001\}\langle 11\bar{2}0\rangle$	[Jones 1981]
	$\{10\bar{1}0\}\langle 11\bar{2}0\rangle$	[Jones 1981]
	$\{10\bar{1}\,\bar{1}\}\langle 11\bar{2}0\rangle$	[Jones 1981]
$\vec{c}+\vec{a}$ Slip	$\{11\bar{2}\,2\}\langle 11\bar{2}3\rangle$	[Boyer-B 1994]
	$\{10\bar{1}\,\bar{1}\}\langle 11\bar{2}3\rangle$	[Jones 1981]
Twin	$\{11\bar{2}3\}$	[Rosi 1953, Churchman 1954]
	$\{10\bar{1}2\}$	[Rosi 1953]
	$\{11\bar{2}1\}$	[Rosi 1953]
	$\{11\bar{2}2\}$	[Rosenbaum 1964]
	$\{10\bar{1}1\}$	[Paton 1969, 1970]
	$\{11\bar{2}4\}$	[Rosenbaum 1964]
$\vec{c}$ Slip	$\{11\bar{2}0\}\langle 0001\rangle$	[Boyer-B 1994]
	$\{10\bar{1}0\}\langle 0001\rangle$	[Boyer-B 1994]

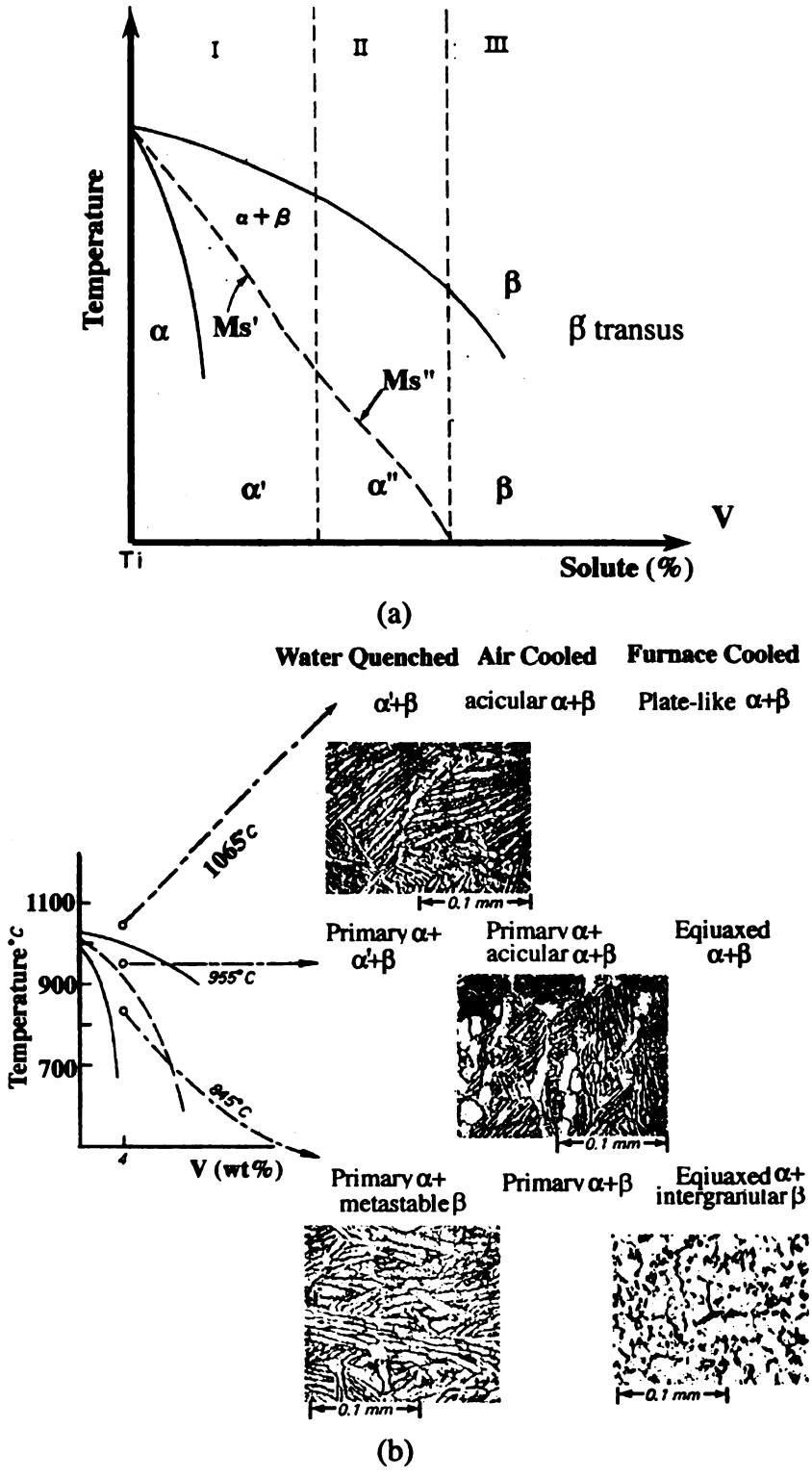

Figure 1.1 (a) Beta isomorphous phase diagram for Ti-6Al-4V showing three regions that undergo different transformation behaviors [After Koul 1970] and (b) a schematic diagram showing different microstructures under thermal treatment with three different cooling rates [Maykuth 1971, Boyer-B 1994].

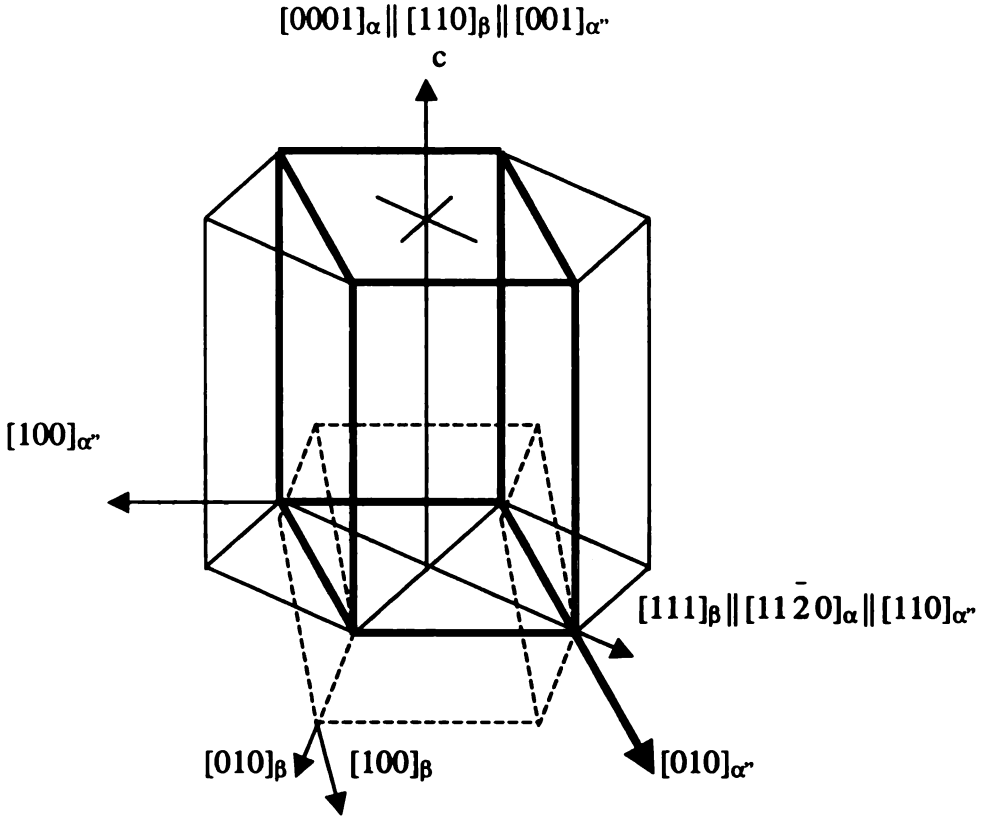

Figure 1.2 The lattice correspondence for β, α' and α" transformations [From Davis 1979].

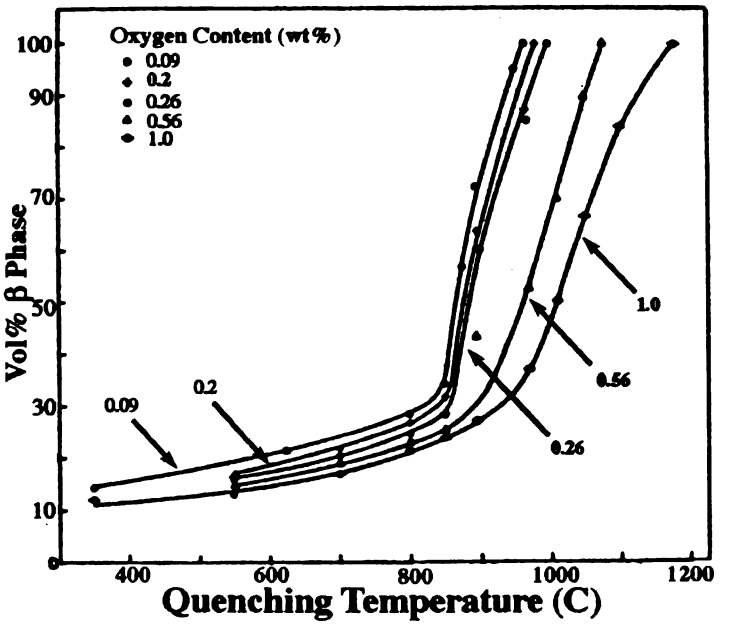

Figure 1.3 Primary β phase volume with different oxygen content as a function of temperature [After Kahveci 1986].

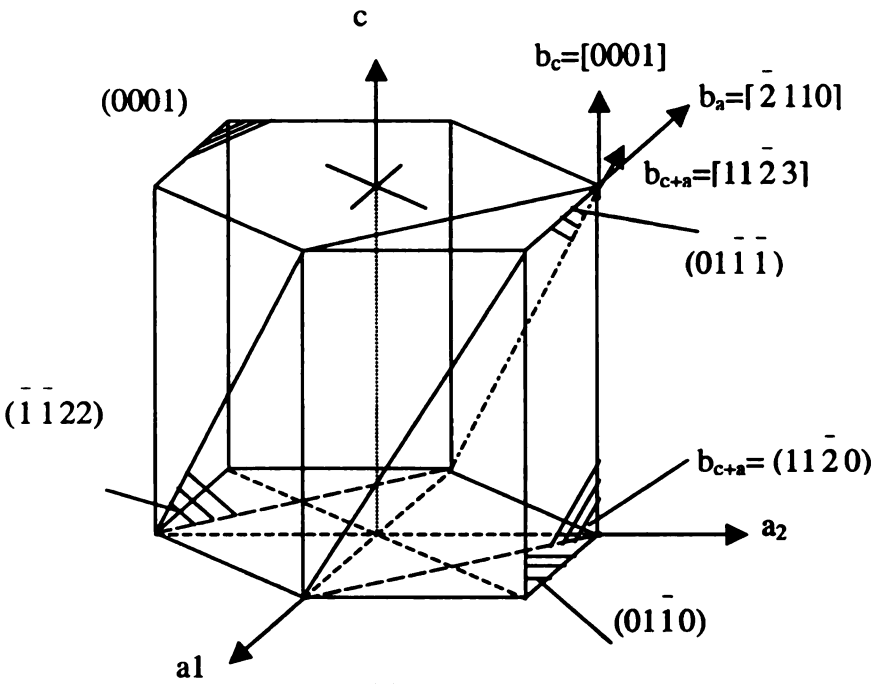

(a)

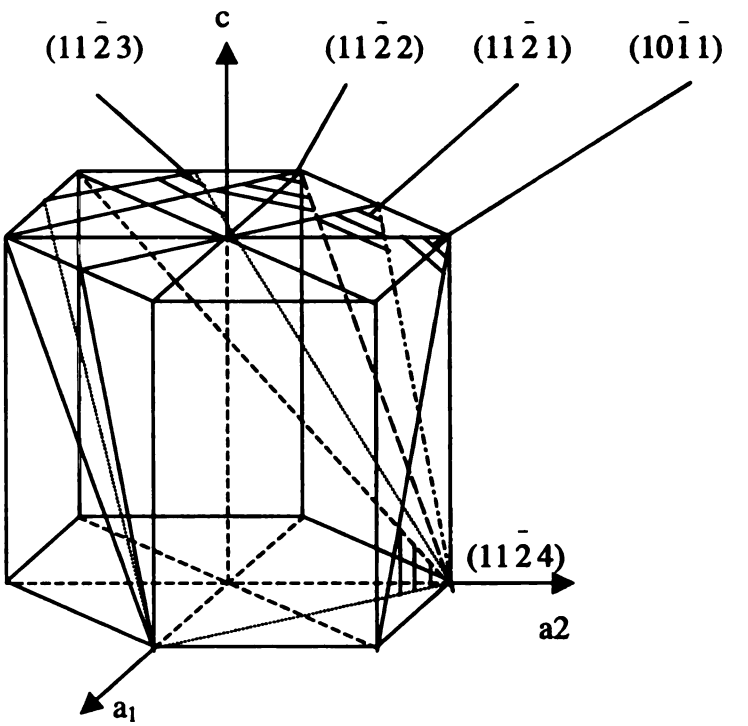

(b)

Figure 1.4 Major (a) slip and (b) twinning planes in α phase Titanium alloys.

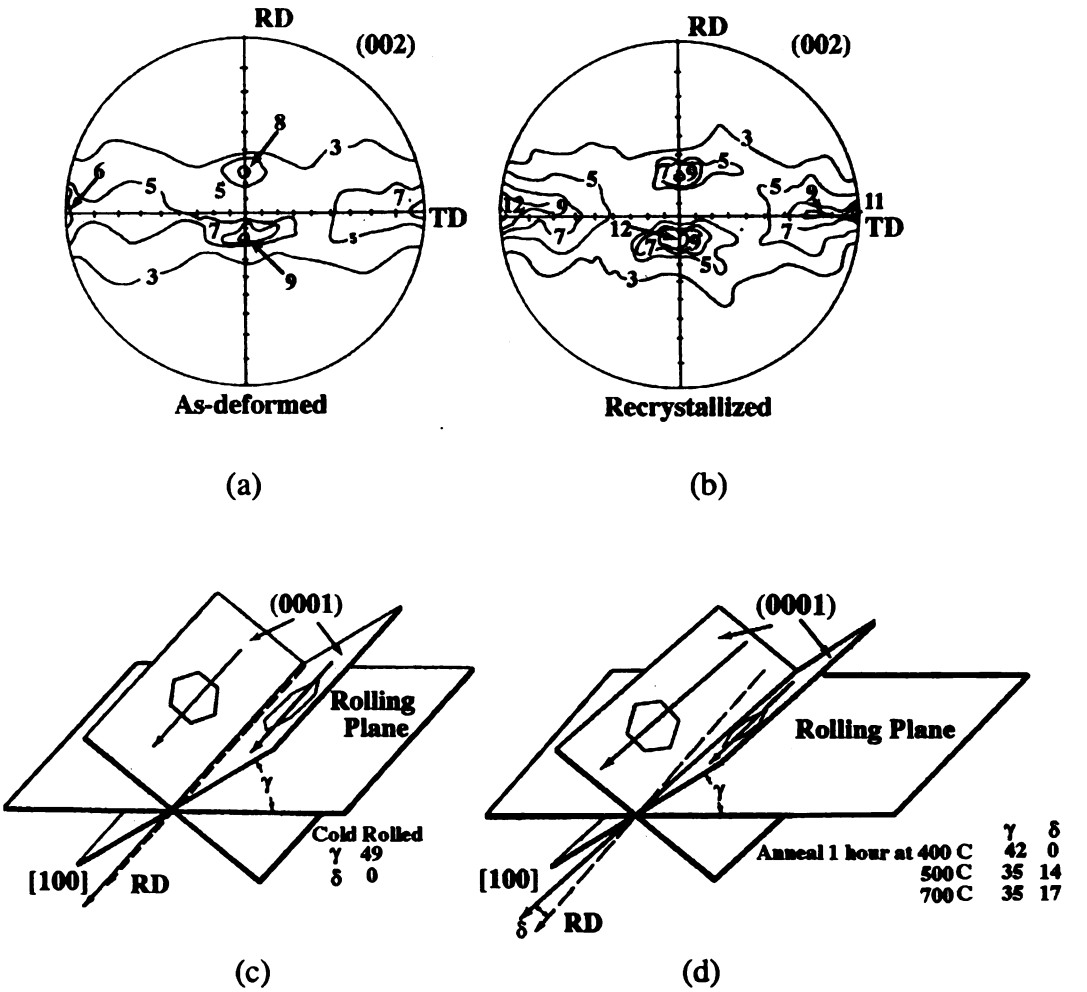

Figure 1.5 (0002) pole figures of Ti-6Al-4V starting from initially randomly oriented specimen rolled at 800°C followed by water quenching (a) and after further annealing at 800°C for 1 hour (b) results in minor texture variations [After Peters 1980]. Two major (002) pole intensity maxima are observed. One major component, transverse texture, belongs to basal plane normals in the TD aligned perpendicular to the SN and planes parallel to the RD. The other one splits RD texture belongs to basal planes in the RD align about 20° with the SN. The schematic representation of cold rolling deformation (c) and recrystallization texture (d) in pure Titanium sheet [After Keeler 1956], results in slightly different crystal rotations of the basal planes, indicated by γ and δ.

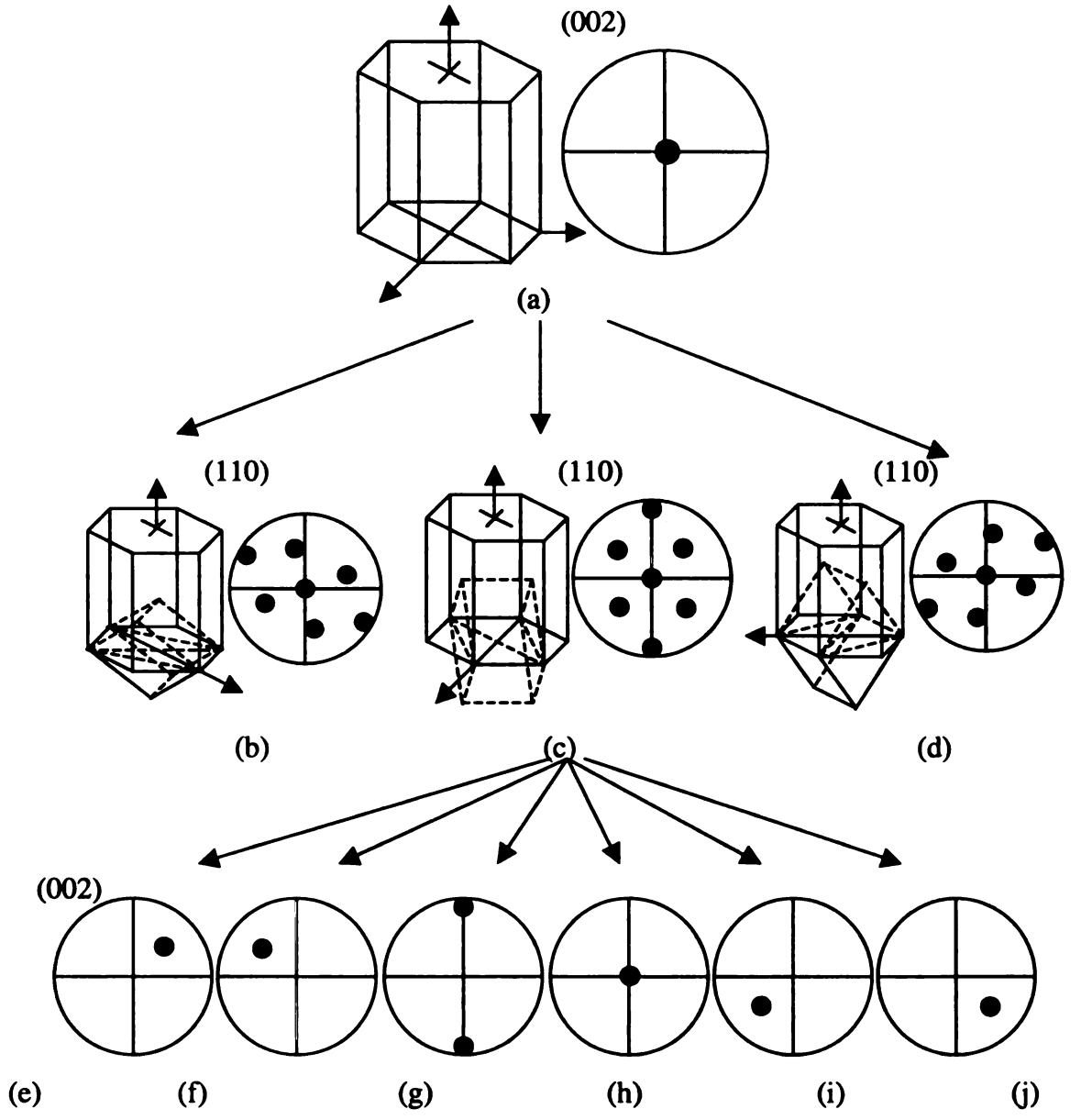

Figure 1.6 Schematically represent the α→β→α transformation texture cycle from (a) initial α single variant with crystal orientation and the (002) pole figure to the possible (b) (c) (d) variants of transformation β texture with the corresponding with crystal orientation between α and β and the (110) pole figures. (e) (f) (g) (h) (i) (j) are the possible six pole figures of room temperature α phase variants from a single variant of high temperature β phase (c) after the β→α transformation. Due to crystal symmetry, only three variants of the high temperature β phase and six variants of the room temperature α phase are shown.

	α Variants	Slip systems in {110}<111>	Slip systems in {112}<111>
1	135°/90°/355°	$(110)[\bar{1}1\bar{1}]$	$(1\bar{1}\,\bar{2})[\bar{1}11]$
2	225°/90°/346°	$(1\bar{1}0)[111]$	$(11\bar{2})[111]$
3	315°/90°/355°	$(110)[1\bar{1}1]$	$(1\bar{1}2)[1\bar{1}1]$
4	45°/90°/355°	$(1\bar{1}0)[11\bar{1}]$	$(112)[11\bar{1}]$
5	90°/45°/85°	$(101)[1\bar{1}1]$	$(12\bar{1})[1\bar{1}1]$
6	270°/45°/264°	$(10\bar{1})[1\bar{1}1]$	$(121)[1\bar{1}1]$
7	270°/135°/265°	$(101)[11\bar{1}]$	$(1\bar{2}1)[11\bar{1}]$
8	90°/135°/84°	$(10\bar{1})[111]$	$(1\bar{2}1)[111]$
9	180°/45°/85°	$(011)[11\bar{1}]$	$(2\bar{1}1)[11\bar{1}]$
10	0°/45°/265°	$(01\bar{1})[111]$	$(2\bar{1}\,\bar{1})[111]$
11	360°/135°/265°	$(011)[1\bar{1}1]$	$(21\bar{1})[1\bar{1}1]$
12	180°/135°/85°	$(01\bar{1})[1\bar{1}\,\bar{1}]$	$(211)[1\bar{1}\,\bar{1}]$

(a)

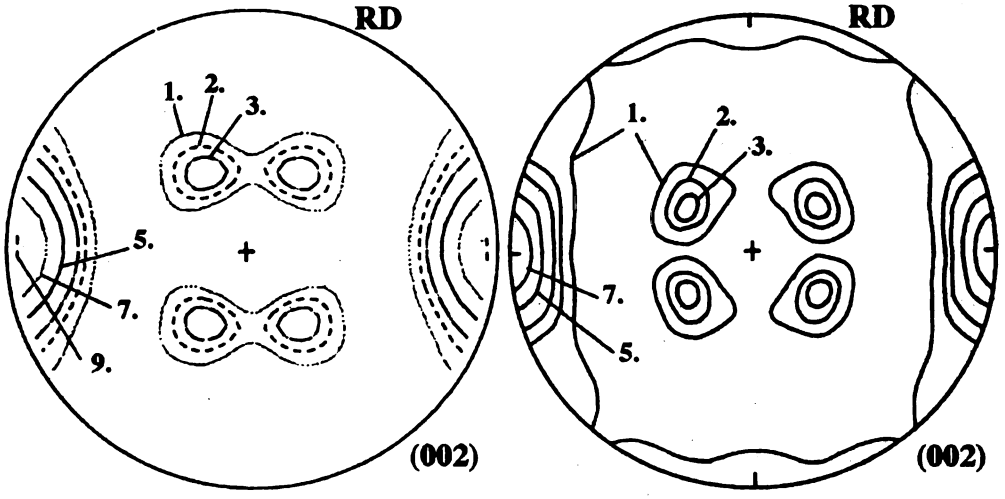

(b) (c)

Figure 1.7 (a) Relationship between the slip systems in {110}<111> and {112}<110> and the preferred α variants and the simulated (b) and experimental (c) α phase texture after α→β→α the transformation cycle with 75% reduction deformed specimen [After Gey 1997].

Chapter II

Experimental procedures

2.1 Research strategy

The overall objective of this research is to investigate the effects of working and heat treatment on crystallographic texture and microstructural (CTM) evolution during typical manufacturing processes in Ti-6Al-4V. The CTM features of Ti-6Al-4V were examined through several stages of the manufacturing processes, including as-received wire, extrusion, to solution heat-treating and then aging. Preliminary texture measurements showed that after solutionization and quenching, a new α phase orientation developed with a fiber texture with the crystal basal plane (0001) normal direction aligned with the wire axis, in addition to the $(10\bar{1}0)$ prism plane normal direction along to the wire axis, which was the only texture present before solutionization. The new orientation is rotated 90° from the prior texture due to a preferred variant selection transformation.

Because of the 90° texture rotation due to heat treatment, the specimens' mechanical strength changed, so the objective of this study was further focused to investigate the effects of solution temperature and time on crystallographic texture rotation and the associated mechanical properties, denoted as the SQA (solution quenching and aging) project. However, as the research progressed, it became clear that 90° texture rotation is clearly associated with primary α and β phase initial texture, working history, and defects generations and structures. Thus, a further project focused on the correlation between variant selections and α/β phase transformation mechanisms,

denoted as the variant selection (VS) project. Therefore, through this progression of research projects, better understanding of the mechanisms of microstructure and texture evolution associated with heat treatment, deformation modes, and working history in Ti-6Al-4V have now been successfully achieved.

2.2 Materials and fabrication

2.2.1 Materials and processing for the Crystallographic Texture & Microstructure project

The Ti-6Al-4V alloy used in the present study was all provided by Dynamet (195 Museum Road, Washington, PA 15301). The material came as 6.5 mm diameter cylindrical wire (rod), which had been forged above the β-transus temperature and subsequently cooled to room temperature. The chemical composition of this alloy is shown in Table 2.1. Figure 2.2 shows the specimen preparation procedures and naming nomenclature, from as-received wire, hot heading or extrusion, to solution and aging thermal treatment, simulated from typical industrial manufacturing processes (Figure 2.1). The samples were cut into approximately 20 mm long cylinders from the beginning of the as-received wire, middle of as-received wire, and end of as-received wire to evaluate metallurgical variations inside the as-received wire. Cylinders from the beginning of coil, middle of coil, and end of coil were partially extruded, so as to have samples with undeformed and deformed microstructures from each part of the coil. The extruded area was reduced to 5.7 mm in diameter, corresponding to ~30% area reductions. Extrusion was done in an industrial machine at a strain rate of approximately 1000/s, and followed by air cooling.

Since an equiaxed α phase in a transformed β matrix microstructure is generally preferred for aerospace applications where high strength with adequate ductility is required and desired, conventional solution treatment of the both extruded and the un-extruded cylinder pairs cut from middle of coil was done in the two-phase region at 920°C for 2.4 and 3.6 ks in an industrial resistance furnace with an argon atmosphere, and rapidly quenched in water at room temperature. To avoid diffusion bonding between Titanium specimens at elevated temperatures, the furnace floor was shaken periodically, which also moved them from the input end to the output end. During the solution treatment, the dew point was less than -40°C to minimize surface contamination from possible chemical reactions between Titanium and water vapor originating from the quench end of the furnace. Aging treatments at 500°C in air for 14.4 ks at temperature, and then air-cooled.

2.2.2 Materials and processing for the SQA project

The Ti-6Al-4V alloy used for the STA project was also provided by Dynamet. This lot of material was processed similarly as above, but the wire diameter was 4.9 mm in diameter (Table 2.1). The samples were cut to about 15 mm long cylinders from as-received wire, followed by partial extrusion of one end to 4.3 mm in diameter. The solution treatment of the partially extruded cylinders was done in two-phase region at temperatures of 905, 925, 940 and 960°C for of 1.2, 2.4, 3.6, or 4.8 ks in a resistance shaker furnace as described above. Aging treatments in air at 500°C were subsequently applied for 14.4 ks and then air-cooled. After solution treating and aging, the specimens were cross-sectioned to further microstructural, texture, and mechanical tests.

In addition, X-ray diffraction studies of certain selected specimens in a direction perpendicular to the wire axis via continuously gradual sectioning were used to examine the possible alloy elements local grouping or residual stress. Three representative parts were chosen, first one solutionized at 905°C for 1.2 ks and aged at 500°C for 14.4 ks, second one solutionized at 905°C for 4.8 ks and aged at 500°C for 14.4 ks, and the last one solutionized at 960°C for 4.8 ks and aged at 500°C for 14.4 ks. Initially, the chosen specimens were cross-sectioned and finely polished until 0.05 μm, followed by X-ray diffraction study, and then remove the surface layer of approximately 500 μm and finely polished, and followed by another X-ray diffraction study under the exact the same conditions as before, and so on (Figure 2.3). After a series of sectioning and diffraction studies and analyzes, the corresponding texture variation and lattice strain due to micro-residual stress, macro-residual stress, or solid solution of alloy or impurities can be determined.

2.2.3 Materials and fabrications for the Variant Selection project

For the VS project, the material came as cylinder rods of 10 mm in diameter, with the same type of prior processing as indicated above. (Dynamet) (Table 2.1). The samples were cut into approximately 10 mm long cylinders from as-received wire. This study included two parts of experimental work. The first part, samples were grouped into pairs that were adjacent to each other in the parent wire (Figure 2.4): one specimen from each pair was stress relief annealed at 525°C for 28.8 ks on a copper plate in a resistance furnace with a thermocouple attached to the copper plate near the location of the sample, followed by furnace cooling to room temperature which took approximately 40 ks. Thereafter, the stress relief annealed and un-annealed specimen pairs were flash heat

treated at a temperature of 920°C for either of 0.06 or 2.4 ks on the copper plate with thermocouple in the resistance furnace, and rapidly quenched in water to room temperature. After surface oxide removal, and light polishing, texture measurements were made on the surfaces of the specimens in contact with the copper plate.

In another part of the designed experiment, the 10 mm long cylinder wire sample pairs were further machined into approximately 6.8×4.4×5.0 rectangular shape specimens using low speed diamond saw, followed by metallurgical polishing. Figure 2.5 shows the specimen preparation procedures. Samples were grouped into pairs that were adjacent to each other in the parent wire. The texture measurements were always done on the transverse surface (perpendicular to the original wire axis). After texture measurements, one specimen of each pair was compressed along the transverse direction, the other along the longitude direction. These specimens were deformed at room temperature to approximately 5% strain level (See compression test description, below for details), followed by texture measurements on the exact same planes as before. Then, these deformed rectangular specimen pairs were put in a sealed quartz tube under a vacuum of 10^{-5} Torr to avoid surface oxidation at elevated temperatures. Solution heat treatments were done in the two-phase region at a temperature of 920°C for a 2.4 ks on a copper hot plate with a calibrated thermometer in the resistance furnace, and rapidly quenched in water at room temperature (the quartz did not break, so the quench was less severe). After solutionization and quenching, the rectangular specimen pairs were taken out from the quartz tube to measure the texture and microstructure on the exact same planes as before. Table 2.2 shows the detailed nomenclature used for this project. For this project, the texture measurements were made on the exact same surface after different processing

conditions, from as received, deformed, and solution heat-treated to monitor the surface texture evolution.

2.3 Mechanical tests

2.3.1 Compression tests

All the mechanical and static compression tests were conducted using a screw driven testing machine (Instron Model 4206, Canton, MA). All cylinder test specimens were prepared with equal length and diameter using electric discharging machining (EDM). In addition, all specimens, cylinder and rectangular shapes were cleaned using a 50:50 mixture of acetone and alcohol for 20~40 minutes in an ultrasonic bath prior to compression test. Figure 2.6 shows the representation of the experimental set up used for normal compression test and related specimen orientations and dimensions. No lubrication was used during the mechanical compression test. The compression tests were conducted at a crosshead speed of 2.54 mm/min. The cylinder or rectangular shape specimens with longitude direction (labeled as L) means the wire axis is parallel to the compression axis, while the specimens in transverse direction (labeled as T) means the wire axis is perpendicular to the compression axis. Young's Modulus, which represents the material's resistance to elastic deformation under external load, was characterized from the slope the elastic region in the stress-strain curve (though elastic deformation of the platen was not accounted for in post-test analysis that used the machine compliance to remove the effects of elastic deformation of the machine). The yield stress corresponds to the stress of the 0.2% permanent deformation from the stress-strain curve.

2.3.2 Micro-hardness tests

To evaluate micro-hardness variations in samples, Vickers hardness measurements were performed by applying a load of 500 g for 30 seconds on selected specimens. Prior to a micro-hardness test, specimens were cross-sectioned using a low speed diamond saw, followed by mounting and mechanical polishing to a 0.05 μm surface finish.

2.4 Optical microscopy and scanning electron microscopy (SEM)

For optical microscopy and scanning electron microscopy (SEM) analysis, specimens were cross-sectioned using a low speed diamond saw. A portion of each sectioned specimen was mounted in diallyl phthalate powder (LECO Corporation, MI). The specimens were then mechanically polished to a 0.05 μm (alumina powder) surface finish, and etched using Kroll's reagent (2 ml HF, 6 ml HNO_3, and 92 ml H_2O) using standard metallographic polishing and etching techniques. The primary α and β grains sizes were determined by the planimetric grain counting methods or linear intercept technique along both longitudinal and transverse directions, which effectively gives the mean areas of grains and mean section diameters in the selected areas. The intercept method was done by drawing a straight line of a specific length on a micrograph and counting the number of grains intercepted by the line. Volume fraction of the primary α and β phases were determined by point counting analysis along both longitudinal and transverse directions. The point counting was done by randomly distributing a grid of points over an optical, SEM or TEM micrograph and counting the fraction of total point count that falls in the given phase, which gives the volume fraction of the phases directly. The aspect ratio of primary α and β grains were determined by the intercept method, which is done by calculating the ratio of the grain size along the length and along the width using oriented lines.

The optical microscopy was done using a Nikon optical microscope (Model EPIPHOT 200, Japan). SEM observations were performed using a CamScan 44 FE SEM or Hitachi S-2500C equipped with energy dispersive spectroscopy (EDS) operated at 15 kV. In addition, all specimens had been cleaned using a 50:50 mixture of acetone and alcohol for 20~40 minutes in ultrasonic bath prior to optical or SEM examinations.

2.5 TEM sample preparation and analysis

Cross-sections for transmission electron microscopy TEM samples were sliced from the bulk specimens using a low-speed diamond saw, followed by gluing the two-mm by two-mm squares cut from the bulk specimens to 3-mm diameter molybdenum rings with epoxy resin. The orientation of the foil with respect to the specimen was always known, along the longitude specimen directions. All cross-sections were then polished, pre-thinned using a VCR Model D500i electronically damped dimpler, and low-angle ion milled to electron transparency using a Gatan Precision ion polishing system (PIPS). TEM observations were performed at 200 kV using a Hitachi H-800 with double-tilt specimen stage, using conventional amplitude contrast image techniques.

TEM, as one of the most powerful techniques to perform very fine microstructure analysis, was used to characterize the overall crystal structure of the thin foils Ti-6Al-4V. Both brightfield and darkfield imaging were carried out in conjunction with local selected area diffraction pattern (SAD) to provide unique and direct information on the local microstructure features, such as primary α and β grain sizes, α' and α'' platelet sizes, the orientation and texture of the primary α and β grains, the internal structures of primary α and β phases, and orientation relations.

2.6 X-ray techniques

2.6.1. X-ray diffraction techniques

X-ray diffraction was used to determine the "unknown" spacing and phases present. Samples for phase and lattice measurements were prepared by sectioning to obtain a surface normal in a direction along the transverse directions (Figure 2.7). Prior to X-ray diffraction measurements, the X-ray diffractometer was precisely calibrated using polycrystalline quartz to insure good alignment of the instrument. In addition, all specimens analyzed were polished using standard metallographic polishing technique to a 0.05 μm (alumina powder) surface finish. Furthermore, all specimens surface normal were adjusted to coincide as closely as possible with the diffractometer axis. X-ray normal diffraction was made using CuK_α radiation on a Scintag XDS-2000 system with Ni filter. The X-ray diffraction measurements were performed at 35 kV and 25 mA with a continuous scanning mode at 0.2° per minute. A 2 mm tube divergent and 3 mm tube scatter slits, and 0.5 mm detector scatter and 0.3 mm detector reference slits were used to control the spot size and sharpness of the X-ray peaks.

For simplicity, lattice parameter calculations were based on the 2θ locations of maximum peak intensities without using least squares method. The lattice parameter of β phase was calculated based on averaging the d-spacing of $(110)_\beta$ and $(200)_\beta$ peaks; while the lattice parameters of the α phase were calculated based on the $(002)_\alpha$ and $(100)_\alpha$ peaks, and α" based on the $(110)_{\alpha"}$, $(020)_{\alpha"}$, and (0002) peaks.

Analysis of the diffraction pattern was made using the software package Diffractometer Management System for windows NT (DMSNT). The measured raw diffraction patterns were processed to obtain normalized diffraction patterns using a series of programs, including Background removal with Box Car Curve Fit with filter

width 1.5° which determines how closely the background curve follows the ups and downs of the raw data files, followed by smoothing using a simple box car averaging algorithm with 3 points, and to remove the $K\alpha_2$ using $K\alpha_2$ Stripping. The peaks and maximum intensities were located using Lorenz correction analysis to correct the raw data for the polarization effects without fitting $K\alpha_2$.

2.6.2. Texture

Samples for texture measurements were prepared by sectioning to obtain a surface normal in a direction along the longitudinal or wire axis directions. This same specimen orientation was used to measure peak intensities in the wire axis direction, corresponding to the 90° texture rotation direction (Figure 2.7). Therefore, this sample orientation can provide direct measurement and evidence of 90° texture rotation without any tilting of pole figures, superior to the other sample configurations with the surface parallel to longitudinal directions. Texture measurements were made using CuK_α radiation on a Scintag XDS-2000 system equipped with a Huber ring goniometer and Ni filter without oscillation. A 1 mm collimator and 2 mm detector slit were used for the measurement of pole figures. During the pole figure measurements, 5° increments scan along the pole distance and azimuth for all pole figures were followed (to a tilt angle of 80°), resulting in an array of 72×16=1152 measurements that were subsequently used for processing and analysis. $(10\bar{1}0)$ and (0002) pole figures were measured for the primary α phase, and (110) pole figures were measured for the primary β phase.

The procedure for reflection pole figure measurements was the following.

1. Mount the specimen in the texture goniometer. The specimen surface normal should be at the correct height and exactly in the reflection plane for incoming and diffracting X-ray beam when no tilt of specimen, or α=0°.
2. Perform a θ-2θ scan on the goniometer over the 2θ range of interest and record it. For $(110)_{\alpha''}$, $(020)_{\alpha''}$, $(110)_{\beta}$, $(10\bar{1}0)_{\alpha}$ and $(0002)_{\alpha}$ pole figures, the 2θ scan ranged from 30~45° in step of 0.05° to find all possible α, α" and β peaks. For (200) pole figure, the 2θ scan ranged from 50~65° to find the possible β peak.
3. Repeat the θ-2θ scan at different tilt angle, such as α=30° or α=60° over the same angular range in step of 0.05° to find all peaks of interest and to locate the angular center of the peaks.
4. Locate the background 2θ angles on both sides of the peak for all tilts. For $(110)_{\alpha''}$, $(020)_{\alpha''}$, $(110)_{\beta}$, $(10\bar{1}0)_{\alpha}$ and $(0002)_{\alpha}$ pole figures, the experimentally measured intensities at 33° and 45° were determined as backgrounds (since these peaks were too close together to measure background close to each peak). For $(200)_{\beta}$ pole figures, intensities at 50° and 65° were determined as backgrounds.
5. Start the pole figure scan in a defined scanning pattern, such that net intensity is calculated by subtracting a weighted average of the two background intensities from the peak intensity for all tilts, followed by data processing.

Analysis of the pole figures was made using the preferred orientation package from Los Alamos (popLA). The measured raw texture data was processed to obtain normalized experimental pole figures using the program UNRAW which uses defocusing correction data generated by program MAKEDFB. The theoretical MAKEDFB files

were created according to the detector slit width used, the θ value of each crystallographic plane, and the width of each peak in degrees (1°). Then experimental raw pole figures were smoothed by 2.5° using a Gaussian filter and minor rotations were made to maximize the symmetry in the pole figure, followed by a harmonic analysis to complete the rim of pole figures using popLA software package without imposing any assumed symmetry. A maximum scale of 400 and lowest contour value of 3 were consistently chosen for final plotting of pole figures.

Table 2.1 Chemical compositions of as-received Ti-6Al-4V alloys in weight percentage.

Diameter (mm)	Al	V	Fe	C	O	N	H	Y	Ti
4.9	6.12	3.86	0.18	0.02	0.16	0.1	0.0029	<0.005	Bal
6.5	6.01	3.71	0.18	0.06	0.14	0.06	0.0037	<0.005	Bal
10	6.09	4.16	0.16	0.08	0.16	0.06	0.0046	<0.005	Bal

Table 2.2 Detailed nomenclature used in the Variant Selection project to evaluate the influence of different deformation mode on variant selections of $\alpha \rightarrow \beta \rightarrow \alpha$ transformation cycle.

Pairs	Name	Processing conditions
Pair1	S1Q	As-received+Heat treated 920°C for 1 min
	Ann+S1Q	Annealed+Heat treated 920°C for 1 min
Pair2	S40Q	As-received+Heat treated 920°C for 40 min
	Ann+S40Q	Annealed+Heat treated 920°C for 40 min
Pair3	L Wire	As-received
	L def	Deformed along longitudinal direction from L Wire
	L SQ	Heat treated 920°C for 40 min in quartz tube after deformation L def
	T Wire	As-received
	T def	Deformed along transverse direction from T Wire
	T SQ	Heat treated 920°C for 40 min in quartz tube after deformation T def

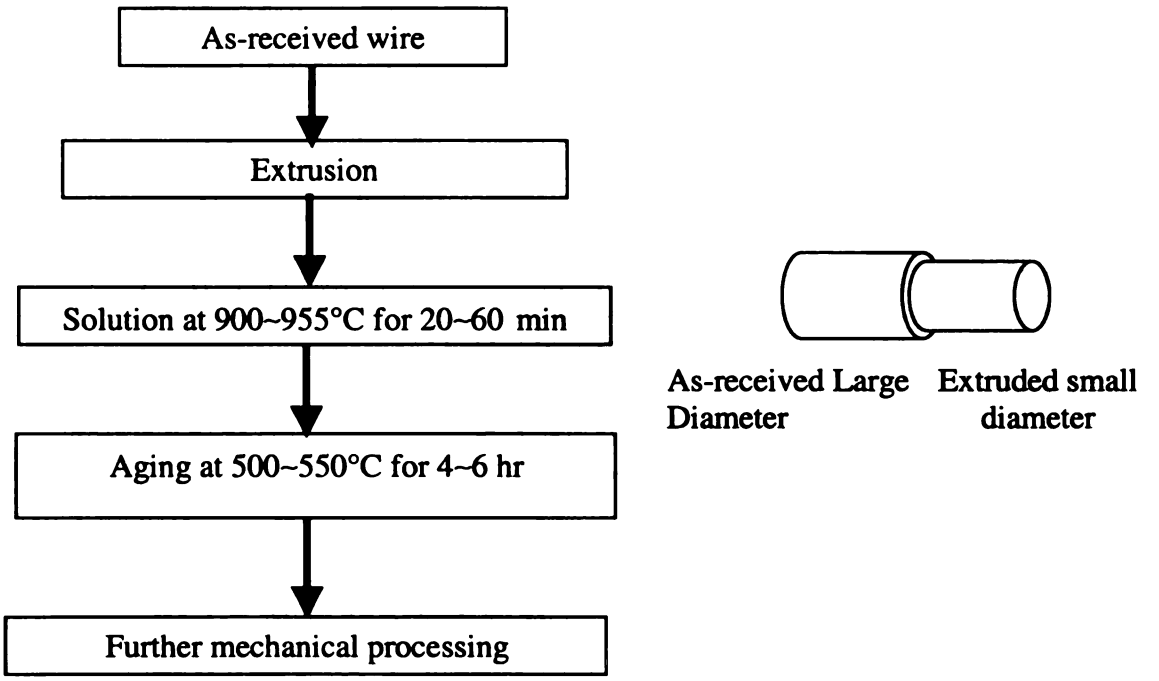

Figure 2.1 Schematical representation of typical industrial manufacturing flow chart.

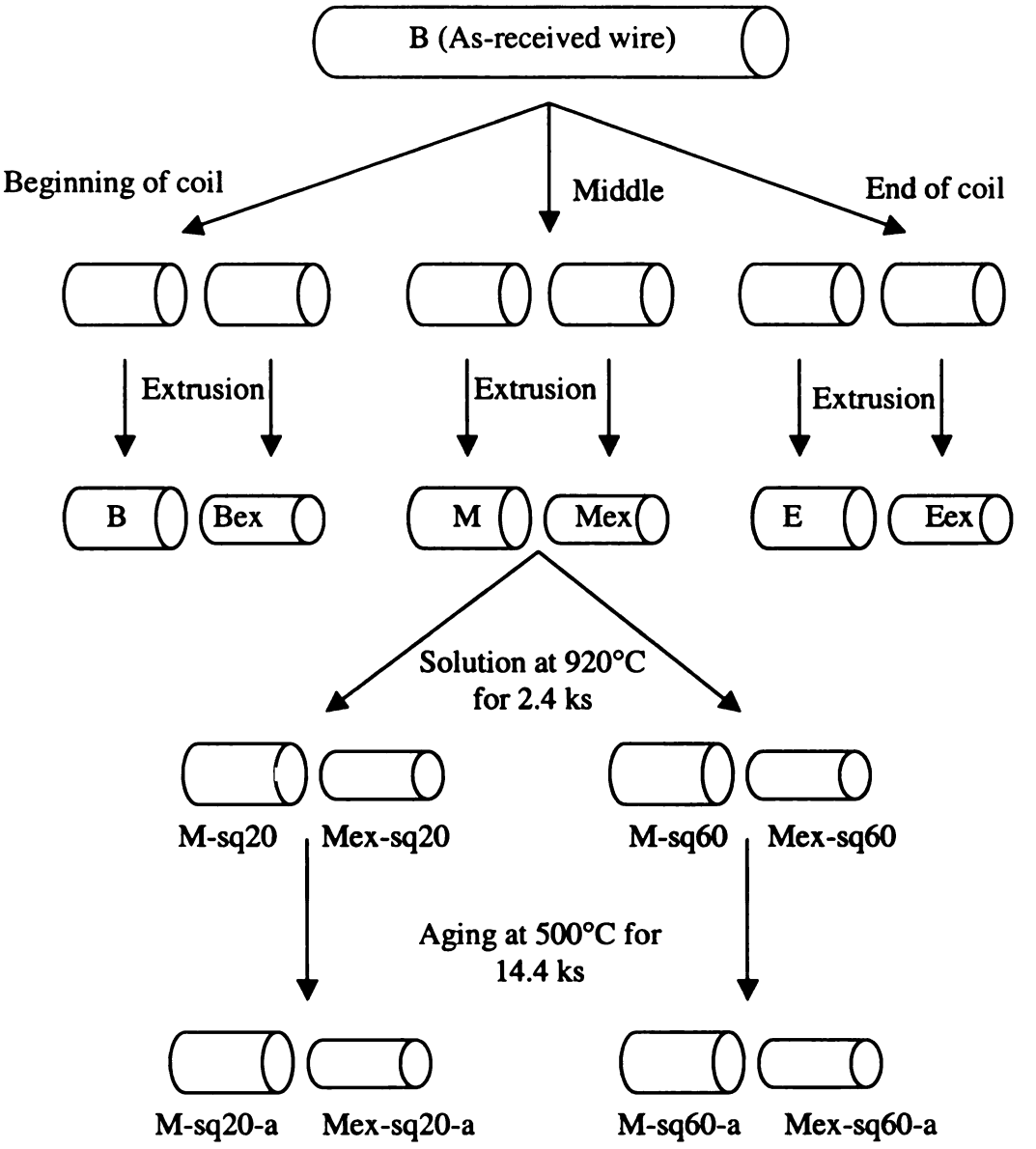

Figure 2.2 Schematic representations of the specimen preparation procedures and nomenclatures, from as-received wire, extrusion, to solution and aging thermal treatment.

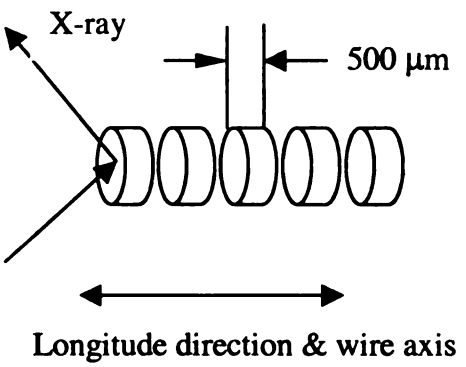

Figure 2.3 Schematic representations of the sample orientation for serial sectioning X-ray diffraction techniques used in the current study.

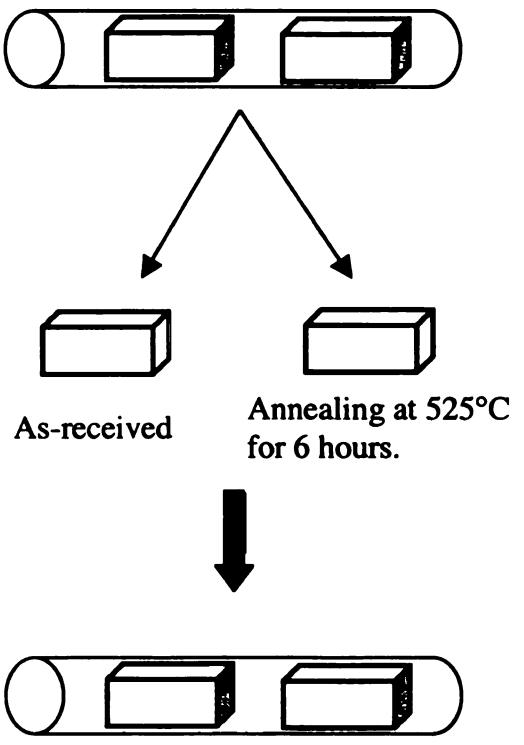

Figure 2.4 Schematic representation of the specimen preparation procedures, from as-received wire, to solution treated conditions. See table 2.2 for detailed nomenclatures. The arrow mark referred to specimens' orientations for texture measurements.

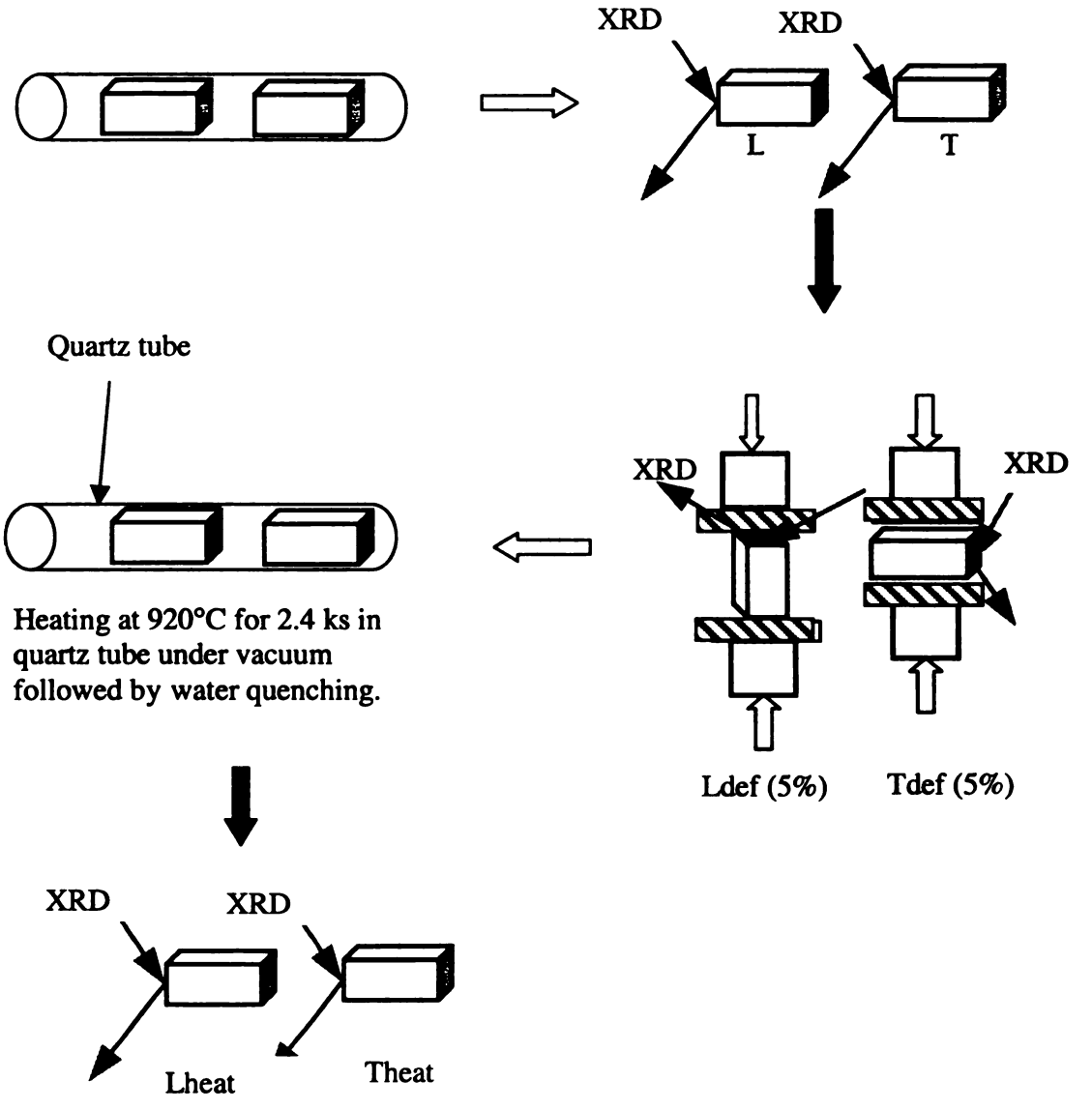

Figure 2.5 Schematic representation of the specimen preparation procedures, from as-received wire, deformed state, to solution treated conditions. All the texture measurements were taken on the exact same surface plane after different processing and deformation conditions, from as received, deformed, to heat-treatment to monitor the surface texture evolutions. See table 2.2 for detailed nomenclatures. The arrow mark referred to specimens' orientations for texture measurements.

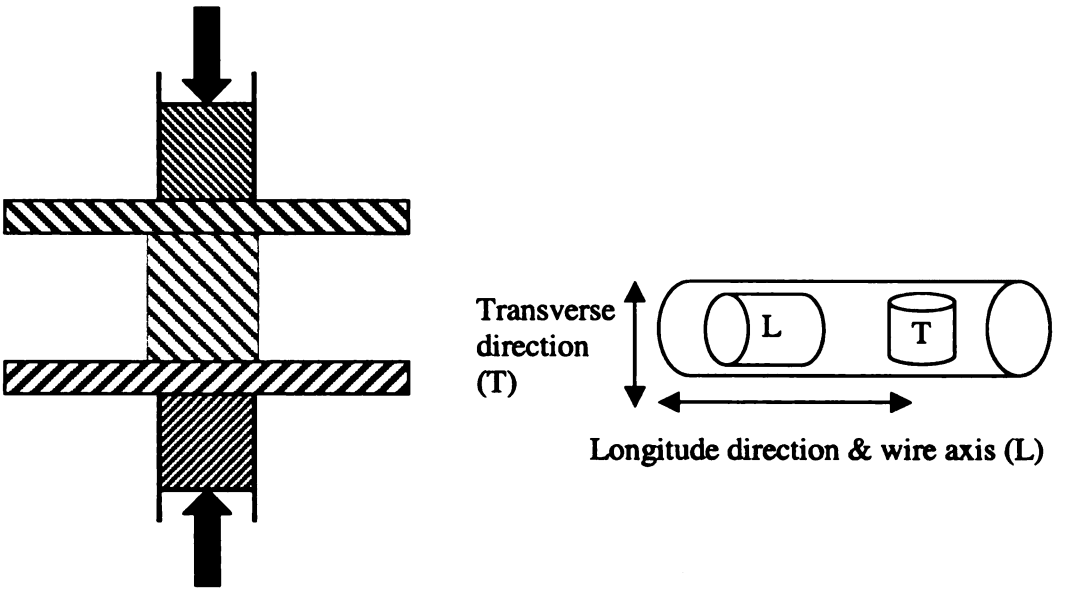

Figure 2.6 Representation of the experimental set up used for normal compression test (a) and related specimen orientation (b). The two cylinders inside the wire represent the actual orientation corresponding to the original as-received wire and how they were sectioned using EDM. The cylinder with longitudinal direction (labeled as L) means the as-received wire axis is parallel to the cylinder axis, while the cylinder in transverse direction (labeled as T) means the as-received wire axis is perpendicular to the cylinder axis. The compression axis was always parallel to the specimens' axes.

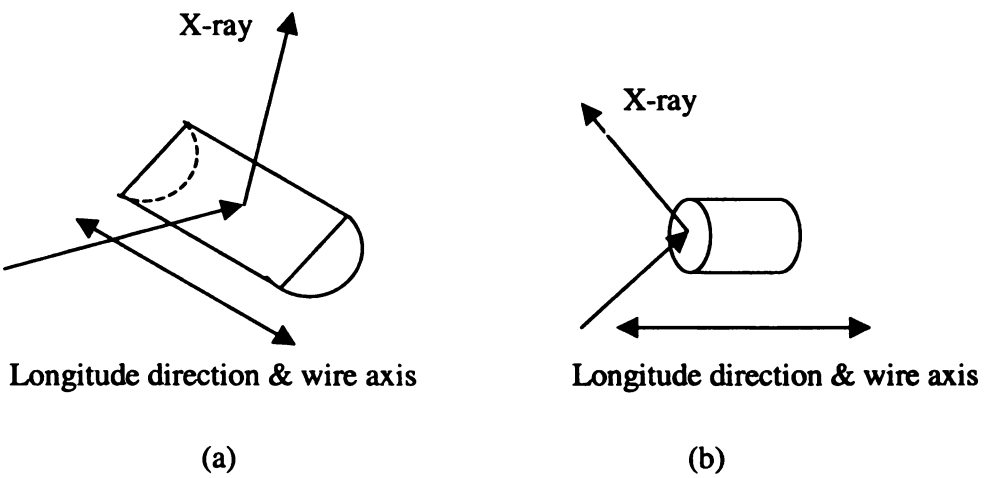

Figure 2.7 Schematic representations of the sample orientation for (a) X-ray diffraction techniques and (b) texture measurements used in the current study.

Chapter III

Effects of working and heat treatment on microstructural evolution and crystallographic texture of α and α" phases in Ti-6Al-4V

Overview

Crystallographic texture has been measured on titanium at several stages of a production process. As-received wire had a moderately strong fiber texture with prism plane normals aligned with the wire axis. The wire was worked by extrusion, solution heat-treated and water quenched, then aged. Extrusion strengthened the as-received texture. After solutionization and quenching, a secondary fiber with basal plane normals aligned with the wire axis emerged at the expense of the initial texture. This 90° rotation is similar to rotations observed in a rolled plate subjected to a super-β transus anneal, indicating strong variant selection occurred after solutionization and quenching. The development and selection of a particular variant after α→β→α transformation cycles is related to the least activeness of high temperature β phase slip system. Natural aging for a year led to the α" and β to transform back to the α phase. The relationship between the orientations of α, α", and the processing history are discussed in the context of the known physical metallurgy of titanium alloys.

3.1 Experiment results

In Ti-6Al-4V, a wide variety of phases can be generated at different stages of heat treatment and processing history, such as α', α", β, ω, α_2 and α phases, depending on the

particular thermomechanical treatment and interstitial (primarily oxygen) content [Boyer-A 1994]. From the measured and published crystal lattice constants the similarity between α", β and α phases, are illustrated in figure 3.1, which shows the coherent relationship between these phases. Although all the crystal structures of α', α", β, ω, α_2 and α phases are really similar, they fall into different crystallographic categories.

In this study, a set of specimens was collected at different stages of a typical manufacturing process. These specimens are identified in table 3.1, with Mex-sq60-a stands for middle of coil, followed by extrusion, solutionization and quenching at 920°C for 3.6 ks, and aging at 500°C for 14.4 ks. All specimens were examined using texture, x-ray diffraction, micro-hardness, and electron microscopy techniques.

3.1.1 As-received wire (B, M, and E)

Figure 3.2 shows the primary α phase pole figures of as-received wire from middle of the coil and the dominant crystal orientations within the specimen. The $(10\bar{1}0)_\alpha$ and $(0002)_\alpha$ α phase pole figures show that the primary α phase orientation is a strong fiber texture with 5.37 x random with the axisymmetric crystal orientations about the wire axis. The crystal prism plane normal direction, $(10\bar{1}0)_\alpha$, is aligned with the wire axis, and the $(0001)_\alpha$ plane normal direction is in the radial direction.

To evaluate the intrinsic texture variation in the original as-received wire, texture measurements were made on the wire at different locations. The overall texture in beginning, middle and end of the as-received wire is essentially the same with a strong fiber texture parallel to the wire axis. However, the intensity of preferred crystal orientation in the radial direction is higher in the ends of the coil than in the middle.

Figure 3.3 reveals the overall relationships between major texture intensities and the experiment processing steps.

In addition to texture evaluations, X-ray diffraction analyses performed on as-received specimens made from middle of the coil show primary α and β phases (Figure 3.4). In addition, TEM analysis on the M specimen revealed the same phase combinations, equilibrium α and metastable β phases (Figure 3.5). Besides the strong β phases reflections, the diffraction pattern from primary β phases shows typical ω phase diffuse streaking which is a typical characteristics of early β→ω transformations [Fan 1998], indicating that the primary metastable β phase has an ordering tendency to transform to a thermodynamically more stable ω phase. However, this β→ω transformation is not complete, otherwise, sharp ω-reflections would be revealed (Figure 3.5). Similar to the microstructure of M, X-ray diffraction and TEM analysis performed on B and E sectioned from beginning and end of coil revealed essentially the same phase combinations, phase morphology and spatial distributions.

3.1.2 Extruded specimens (Bex, Mex, and Eex)

The two α phase pole figures $(10\bar{1}0)_\alpha$ and $(0002)_\alpha$ of extruded Mex sectioned from middle of as-received wire show that the texture is the same as the as-received wire, but stronger in intensity (Figure 3.2(b) and 3.3) due to the ~30% reduction of area.

TEM examination of the extruded Mex material showed different microstructures in different specimens, one only contained primary α grains and the other only primary β grains (Figure 3.6). This may be due to non-uniform element and/or phase distribution in different regions, since the region examined in the two foils were originally 2 mm apart from each other. In some locations after the extruding operation, the specimen shows a

high dislocation density obscuring grain or phase boundaries in prior β regions (figure 3.6(a)). The inset diffraction patterns show streaked diffraction spots that imply a severely distorted crystal. At other locations, only non-equiaxed primary α grains (Figure 3.6(b)) were observed with high dislocation densities with an identifiable grain size of about 1 μm. The high dislocation density is expected from the extrusion process.

3.1.3 Quenching (M-sq20 & Mex-sq20 and M-sq60 & Mex-sq60)

After quenching, texture measurements show that a new α phase orientation developed; a fiber texture with the crystal basal plane $(0002)_\alpha$ normal direction aligned with the wire axis and the $(10\bar{1}0)_\alpha$ prism plane normal direction perpendicular to the wire axis (Figure 3.7). This introduction of a new orientation weakened the prior fiber texture (Figure 3.3). Figure 3.7(a) shows the α phase $(10\bar{1}0)_\alpha$ and $(0002)_\alpha$ pole figures of M-sq20 and related schematic showing the orientations. The new orientation is rotated 90° from the prior texture, suggesting that a transformation occurred during the solutionizing process. This transformation may be explained by the prior α phase transformed to β phase, and then retransformed back to α based upon a different $\{110\}_\beta$ plane 90° misoriented from the prior crystal while cooling, but in a favored way to cause a well defined $(0001)_\alpha$ plane normal aligned with the wire axis (Figure 3.3). In addition, it is apparent that a shorter solutionization time does not affect the texture significantly. However, the major texture intensities weakened. In contrast to the extruded condition where extrusion strengthened the major texture intensities, the texture intensities of the Mex-sq20 was weaker than that of M-sq20. A similar trend was observed for both short time solution and long time solution.

After quenching from 920°C, the as-received and extruded specimens show similar phases present, a mixture of primary α and hexagonal α' martensites which cause broadening of the $(10\bar{1}0)_\alpha$ and $(0002)_\alpha$ peak (Figure 3.4). This peak broadening was evidently caused by the presence of α' martensite, with lattice parameters that differed only slightly from the lattice parameters of the α phase due to compositional variations in these phases [Boyer-A 1994]. No orthorhombic α" martensites or retained β were observed. The TEM observations were consistent with the X-ray diffraction results with the presence of many needlelike hexagonal α' martensitic platelet with many finely divided interfaces (Figure 3.8). The diffraction pattern of a primary β grain showed both the primary α and β spots in figures 3.8(b) which shows the indexed β/α phases in the Burgers orientation relationship of $<111>_\beta \| <11\bar{2}0>_\alpha$ and $(\bar{1}10)_\beta \| (0001)_\alpha$. Figure 3.8 shows the TEM diffraction pattern from a primary β grain with [111] β zone pattern and three α $<11\bar{2}0>$ patterns superimposed.

3.1.4 Ageing

Texture measurements were made from specimens aged at 500°C for 14.4 ks, and summarized in figure 3.3. Similar to the as-quenched specimens, pole figures of aged specimens showed the secondary texture component with the crystal $(0002)_\alpha$ plane normal (c-axis) aligned with the wire axis, but the intensities of the components aligned with the wire axis were significantly reduced. The $(10\bar{1}0)_\alpha$ and $(0002)_\alpha$ pole figures for the M-sq60-a are shown in figure 3.7(b). The systematically decreased texture implies that aging caused a randomizing effect on the texture due to the decomposition of

hexagonal α' martensites which favors a decrease of existing orientations to form more randomly oriented new orientations. In addition, this texture decrease was more pronounced in the extruded specimens than in the as-received wire.

In addition to texture measurements, X-ray diffraction scans on the M-sq20-a, Mex-sq20-a, M-sq60-a, and Mex-sq60-a specimens revealed similar phase combinations, having a mixture of primary α phase with hexagonal α' and orthorhombic α" martensites with small amounts of retained β phase after aging (Figure 3.9). The TEM analyses show typical duplex microstructures with primary α and β grains (Figure 3.10(a)). The primary α and β phases have a grain size of approximately 2~3 μm. The complex diffraction pattern from a primary β grain of the aged M-sq60-a specimen shows distinct diffraction peaks from orthorhombic α" martensites, in agreement with X-ray diffraction analyses, and the orientation relationship between α and α" phases. The appearances of orthorhombic α" martensites and retained β phase after aging suggested a new transformation phenomenon occurred, $\alpha' \rightarrow \alpha'' + \beta$, assuming no phase transformation happened in the primary α phase.

Approximately one year later, similar X-ray diffraction were made on the same bulk M-sq20-a, Mex-sq20-a, M-sq60-a, and Mex-sq60-a specimens, and they revealed different phase combinations; a primary α phase without orthorhombic α" and retained β phases (Figure 3.9). On the normal X-ray diffraction scan, all α" and β diffraction peaks had consistently disappeared. During the prior year, all bulk and thin foil specimens were separately packed in a labeled envelopes without any mechanical, chemical, thermal processing, or damage.

The natural aging effect was also observed in the thin foil Ti-6Al-4V TEM specimens. TEM analyses were performed on the same M-sq20-a, thin foil specimens made one year previous. The diffraction patterns from the primary β phase showed only α phase spots without the prior orthorhombic α" and retained β phases (Figure 3.10). Similarly, TEM analyses of the thin foil Mex-sq20-a, M-sq60-a, and Mex-sq60-a specimens revealed the same effects.

The natural aging was also examined using micro-hardness tests. It is generally known that natural aging in Aluminum and Copper alloys leads to mechanical strengthening and a hardness increase. Micro-hardness measurements were performed on the same bulk M-sq20-a specimens using the same hardness tester, measurement conditions, and specimen orientations to compare micro-hardness values done one year previous. Using Student t test statistics, there is clearly a hardness increase from the mean 375 HV to 379 H_V with 90% confidence interval. Therefore, the X-ray bulk specimens' diffraction, TEM thin foils analyses, and micro-hardness testing all indicate that natural aging did occur in Ti-6Al-4V, leading to the transformation of orthorhombic α" martensite and retained β phases transform to the α phase.

In summary, from the current study, a series of phase transformation phenomenon can be proposed as follows:

- Quenching: $\beta \rightarrow \alpha'$,
- Artificial aging at elevated temperatures: $\alpha' \rightarrow \alpha'' + \beta$ and $\alpha' \rightarrow \alpha + \beta$,
- One-year natural aging at room temperatures: $\alpha'' + \beta \rightarrow \alpha$.

3.1.5 Crystal lattice measurements

Crystal lattice constants of major phases α, α" and β phases were carefully measured and calculated to determine the vanadium and oxygen concentration in the β and α phases, respectively (Table 3.2). Increasing vanadium concentration decreases the lattice parameter of β phase, while increasing interstitial elements, especially oxygen, increase the lattice parameters of the α phase by occupying a fraction of octahedral interstitial sites [Boyer-A 1994]. Initial vanadium concentration in the β phase was probably high and steadily decreased with further processing since the vanadium can diffuse into α phase at elevated temperatures. This is consistent with the TEM observation of diffuse ω streaking only in as-received wire since high concentration of vanadium in the β phase makes the formation of ω phase thermodynamically favorable.

3.2 Discussion

The texture and microstructural analyses show a new transformation phenomenon or mechanism occurred and 90° crystal orientation rotation from previous texture during the experimental processing. In Ti-6Al-4V, texture and microstructure can be adjusted and controlled separately [Peters 1980]. Therefore, it is of interest to investigate the microstructural transformation behavior and texture rotation separately in relation to previous Ti-6Al-4V alloys studies, physical metallurgy principles, and microstructure studies of other similar Titanium alloys.

3.2.1 Phase transformations in Ti-6Al-4V

A variety of phase transformations can occur in titanium alloys, depending on the particular thermo mechanical treatment and interstitial content. Some of the transformations are now better understood, while some others are not. A complete

review of all phase transformations that occur in Ti-6Al-4V is beyond the scope of this research, so only the most relevant findings are considered.

At temperatures above the $\alpha/\alpha+\beta$ transus, the equilibrium α phase can partially transform to a high temperature β phase. The subsequent quenching would lead to the formation of hexagonal α' phase instead of orthorhombic α'' since the V stabilizer concentration in primary β grains was lean at high solutionization temperature [Koul 1970]. Generally, upon aging, hexagonal α' decomposes into fine α and β by nucleation and growth process through the precipitation of β phase which is preferentially oriented along the basal directions within the α' plates [Gil 1995]. Davis et al. [1979] calculated the lattice strain between $\beta\rightarrow\alpha'$ and $\beta\rightarrow\alpha''$ transformations, and suggested the orthorhombic α'' structure was an intermediate structure between $\beta\rightarrow\alpha'$ transformation. However, the principle lattice strain between $\alpha'\rightarrow\alpha''+\beta$ is significantly larger than $\alpha'\rightarrow\alpha+\beta$ due to large 2-θ difference between α' and α'' peaks in the X-ray scan, suggesting the transformation $\alpha'\rightarrow\alpha''+\beta$ is thermodynamically unfavorable.

However, many authors reported that orthorhombic α'' structure could form by the spinodal decomposition of retained β phase during aging into $\beta_{V\ rich}$, and $\beta_{V\ lean}$ phase, $\beta\rightarrow\beta_{lean}+\beta_{rich}\rightarrow\alpha''+\beta_{rich}$. Therefore, it is certainly possible that the β phase precipitated from the decomposition of α' could further decompose into the α'' and β_{rich} phases, $\alpha'\rightarrow\alpha+\beta\rightarrow\alpha+\beta_{lean}+\beta_{rich}\rightarrow\alpha+\alpha''+\beta_{rich}$.

The disappearing of α'' and β_{rich} phases might be caused by the following reasons: (1) Room temperature diffusions of α'' and β phases. Generally, upon aging, the orthorhombic α'' martensite can decompose via spinodal precipitation into $\alpha+\beta$ through

$\alpha'' \rightarrow \alpha''_{lean} + \alpha''_{rich} \rightarrow \alpha + \beta$ [Davis 1979], or transform directly to α phase, depending on the concentration of β stabilizer [Boyer-I 1994]. Thus, during the approximate one-year period, the α'' may further decompose into $\alpha+\beta$ or α phase. To the author' knowledge, no room temperature V diffusion data is available. The typical diffusion distance for V in a year is less than 10^{-5} μm based on extrapolation of high temperature diffusivity and activation energy, indicating diffusion cannot account for the aging. In addition, the β phase obtained from artificial and/or natural aging is metastable at room temperature assuming the V concentration in the β phase is less than 15-wt%. Thus, the β phase may eventually transform back to stable α phase, leading to the natural aging effect. (2) Hydrogen absorption. Hydrogen absorption can lead to the shifting of α'' peaks to α phase and disappearing of β phase due to eutectoid decomposition [Fang 1998, Qazi 1965]. (3) Oxygen absorption. The absorption of oxygen in the β phase can reduce the β phase stability and promote the β phase transformation [Boyer-B 1994]. (4) Other unknown mechanism. In general, additional work is neededed to fully investigate the natural aging mechanism.

3.2.2 90° texture orientation rotation

3.2.2.1 Variant selections

According to the Burgers relationship (Figure 3.11) [Burgers 1934], upon heating each indivial α phase orientation can produce six cubic orientations with a $(110)_\beta$ plane parallel to the original $(0001)_\alpha$ plane and with the six possible combinations of parallel orientations, including two $<111>_\beta$ directions in the $(110)_\beta$ plane and three $<11\bar{2}0>_\alpha$ directions in the $(0001)_\alpha$ plane. On cooling to room temperature after solutionization,

each one of the six cubic orientations can generate another twelve orientations of the hcp α phase, only one of which is the original α phase orientation. Therefore, one orientation of α phase could ideally become 6×12=72 orientations of α phase texture, suggesting that a nearly random texture could be developed after the α→β→α transformation cycle. In contrast, the present study revealed a strong 90° rotation orientation with $(0001)_\alpha$ plane normal direction aligned with the wire axis, suggesting that a strong variant selection occurred during the solutionization and quenching. This is consistent with the prior result that upon heat treatment in the β phase field, the α phase texture developed without variant selection, while heat treatment in the α+β phase field, the resulting α phase texture had a strong variant selection at room temperature [Gey 1996, Moustahfid 1997].

3.2.2.2 Stress

It has long been realized that constraints, such as residual stress and oriented overgrowth, can affect the β→α transformation texture, resulting in only one of the six $(110)_\beta$ planes being favored while transforming to the $(0001)_\alpha$ with two strongly preferred orientations [Keeler 1956]. Upon heat treatment in the 920°C α+β phase field, approximately 40~60% of the primary α grains would transform to high temperature β grains [Kahveci 1986]. This α→β transformation leads to large internal stress build up between the β grains and the remaining α grains to avoid cracking due to changes in the atomic volumes of α and β phases [Rudman 1965]. This large internal stress can be reduced by volume contraction by as much as 0.55~2.6% through annihilation of transformation dislocations [Fujishiro 1980]. Thus the magnitude of internal stress would depend on the progress of α→β transformation and dislocation movement and recovery, which in turn depends largely on the solutionization temperature, time, solute

concentration, spatial phase distribution, initial stress state, high temperature texture evolution, grain sizes, grain growth behaviors and impurities. To the author' knowledge, the complicated physical metallurgy operating upon heating and solutionization is not available in open literature, and this might be more complex than the transformation process occurring during the $\beta \rightarrow \alpha$ transformation [Moustahfid 1997].

In addition, the α grain has a large anisotropic thermal expansion coefficient. For example, the linear thermal expansion coefficient along the c-axis is 20% higher than perpendicular to the c-axis [Boyer-J 1994]. Upon cooling prior to martensitic transformation, the large anisotropic thermal expansion of the existing α grains can lead to internal stress between different orientations of α grains, as well as with β grains that would shrink by transformation, assuming the stress state at the end of solutionization is zero. Prior to the beginning of $\beta \rightarrow \alpha'$ transformation at approximately 800°C, the β and α grains would shrink, with α grains shrinking preferentially along the c-axis. Figure 3.12 shows a schematic representation of in plane (radial and hoop) stresses that develop upon cooling prior to $\beta \rightarrow \alpha'$ transformation. The stresses in the β grains could be tensile, zero or negative magnitudes, depending on the exact arrangements of the α and β grains, in planes perpendicular to the wire axis. However, in the present research, the majority of α grains in as-received wire were orientated with the c-axis along the radial direction, suggesting that internal stresses might be highest in the plane perpendicular to the wire axis in the high temperature β grains (Figure 3.12), prior to transformation.

Based on this assumption, heat treatment in the β phase field would result in uniformly distributed β grains which have isotropic thermal expansion, leading to minimal internal stress between each β grain upon cooling prior to martensitic

transformation. This is consistent with the results that solution treating in the α+β phase field results in higher value of internal friction than solution treating in the β phase field [Ouchi 1999].

3.2.2.3 Texture of high temperature β phase

Unfortunately, the direct measurement of high temperature β texture was not possible with our texture system. However, the high temperature β phase texture can also be inferred from the α→β transformation based on the Burgers relationship without variant selection relationship (Figure 3.13(a)). It is expected that the majority of the $(110)_\beta$ plane normal angles with the original wire axis would be 0, 30, 60, or 90°, assuming variant selection does not apply (Figure 3.13(b)). Furthermore, the angle of 0, 60, or 90° could come from the same β orientation. In addition, the high temperature β phase texture that resulted in the 90° texture rotation can be inferred based on Burgers relationship (Figure 3.13(c)). The particular $(110)_\beta$ plane that can become the $(0002)_\alpha$ plane aligned along wire axis in the β→α transformation was always parallel to the radial directions, suggesting majority of $(110)_\beta$ planes normals aligned with the wire axis. Thus, the β phase $(110)_\beta$ plane normal having 30° angles with wire axis, did not exist after the α→β transformation due to variant selections, or it disappeared due to β grain growth resulting in shrinking of the non-favored β orientations. Therefore, the majority of the β phase is orientated with one of their six $(110)_\beta$ planes normals aligned with the wire axis. However, it is almost impossible to determine if variant selection occured in the α→β transformation.

3.2.2.4 Variant selections and activeness of slip system

As mentioned above, the internal stresses most likely build up along the radial directions. These radial internal stresses could potentially and locally deform the existing high temperature β phase prior to transformation. Most importantly, from the lack of change in the original α component of the texture, the change must have occurred in the part of the microstructure that transformed from α→β→α such that the majority of the β phase was orientated with one of their six $(110)_\beta$ planes normal aligned with the wire axis. Given this β fiber texture, then there would be little if any shear stresses from expansion mismatch resolved on the $(110)_\beta$ plane that became the transformation planes to form α. Thus, based on the proposed model by Gey et al. [1996, 1997] who conclude that the most active slip system correlates to a high density of defect sites that would favor the transformation texture, the other four $(110)_\beta$ planes would have had shear stresses resolved on them to generate dislocations that would favor them becoming the $(0002)_\alpha$ plane after the β→α transformation. However, this was not the case. In the current study, the data suggests that β→α transformation preferentially concentrated on the particular $(110)_\beta$ - $(0002)_\alpha$ plane with its normal parallel to the wire axis. The differences might be explained by the following reasons:

(1) Different processing history. In the experiment developed by Gey et al. [1996, 1997], high temperature "continuous dynamic recrystallization" with small equiaxed β grains was observed before further cooling down to room temperature. In addition, the cooling rate was chosen to give micro-sized (≥1 μm thick) α platelets (as compared to ~0.05 μm thick in the present research), suggesting that direct quenching was not used. Thus, upon cooling, those newly nucleated equiaxed β grains can further grow,

precipitate α platelet via nucleation and growth, and affect or even determine the subsequent variant selections [Keeler 1956]. However, in the current research, direct quenching was employed to eliminate any possible diffusion or nucleation prior to the martensitic transformation (which is not thermally activated) and takes place at high (temperature-independent) speed. Therefore, hot rolling in the β phase field with more than 30% reductions leading to the α phase texture with variant selection might be better categorized as a recrystallization texture instead of transformation texture [Gey 1996, 1997].

(2) Internal stresses level. The internal stresses that developed in β grains may not have been high enough to generate a large number of defects on $(110)_\beta$ planes, thus, there may be other criteria to determine the favored transformation texture. The present studies suggest that the other five $(110)_\beta$ planes under local stress that can be activated for slip were not activated to induce the formation of the α phase upon cooling, and in contrast to prior work, the development of a preferred variant is apparently related to the least active slip system. Further investigations are needed to determine if there was any reason to expect pre-existing dislocations to be present on the $(110)_\beta$ planes that became the basis for the observed transformation, that may have resulted from variant selections from $\alpha \rightarrow \beta$, development of high temperature β phase texture, and thus affected the $\beta \rightarrow \alpha$ transformation.

3.3 Conclusions

The present study investigated the effects of working and heat treatment on microstructural evolution and crystallographic texture of α phase in Ti-6Al-4V. Texture analysis revealed a 90° rotation from the prior texture emerges with the (0001) c-axis

aligned with the wire axis after quenching, which can be correlated to the least active slip system within the high temperature β phase as it accommodated differential thermal contraction in α during cooling.

Microstructural analysis showed α' martensitic plates formed after solutionization and quenching. The subsequent artificial aging process led to the formation of metastable α" and β, but natural aging for a year caused α" and β to transform back to the α phase.

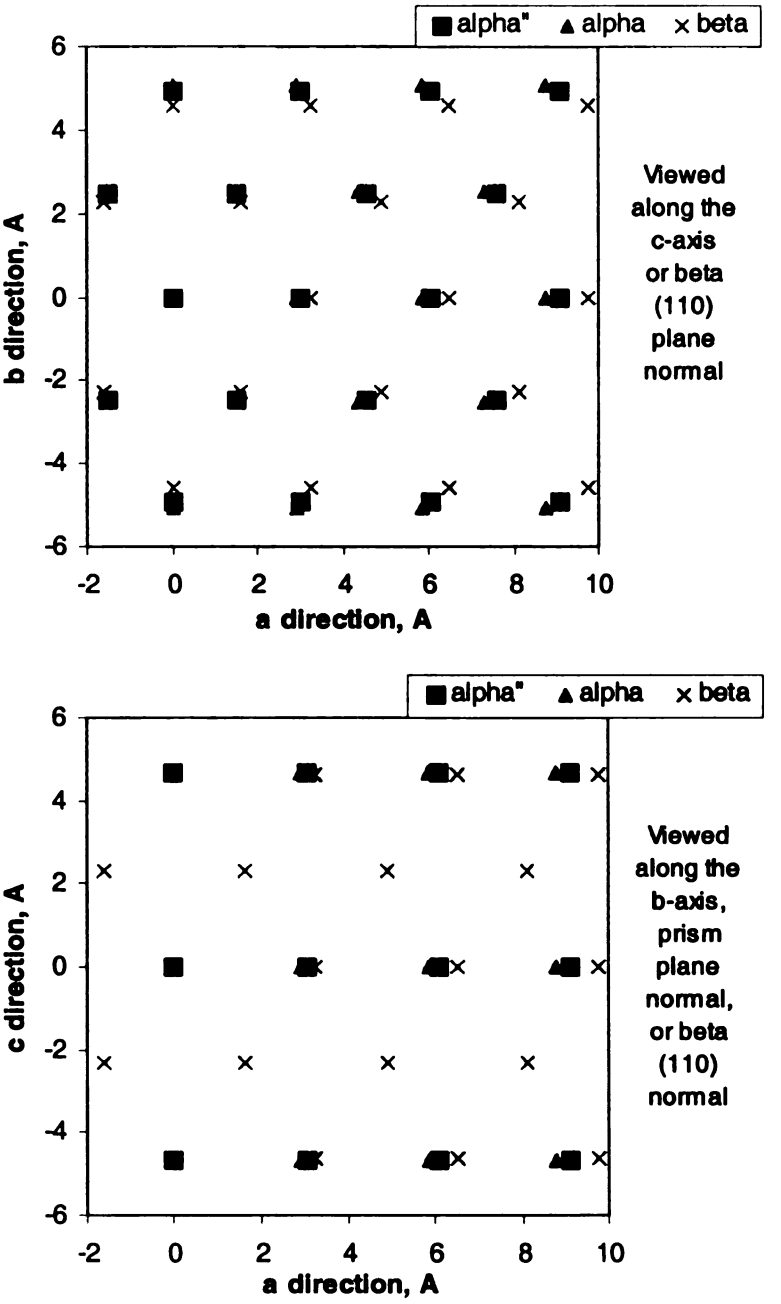

Figure 3.1 Crystal phases and their coherency relationship to each other.

Table 3.1 Specimens examined using X-ray diffractometer, texture measurements, and TEM technologies. Note, M stands for middle of the coil, ex for extruded, sq for solutionization and quenching, a for aging.

Process ID	Phase constituents	Processing conditions
B	α, β	Beginning of Coil
Bex	α, β	Beginning of Coil, Extrusion
M	α, β	Middle of Coil
Mex	α, β	Middle of Coil, Extrusion
E	α, β	End of Coil
Eex	α, β	End of Coil, Extrusion
M-sq20	α', α	Middle of coil, 920°C for 20 minutes,
Mex-sq20	α', α	Middle of coil, Extruded, 920°C for 20 minutes
M-sq60	α', α,	Middle of coil, 920°C for 60 minutes,
Mex-sq60	α', α,	Middle of coil, Extruded, 920°C for 60 minutes
M-sq20-a	α",α', α, β	Middle of Coil, 920°C for 20 minutes, Aged at 550°C for 4 hours
Mex-sq20-a	α",α', α, β	Middle of coil, Extruded, 920°C for 20 minutes, Aged at 550°C for 4 hours
M-sq60-a	α",α', α, β	Middle of Coil, 920°C for 60 minutes, Aged at 550°C for 4 hours
Mex-sq60-a	α",α', α, β	Middle of coil, Extruded, 920°C for 60 minutes, Aged at 550°C for 4 hours

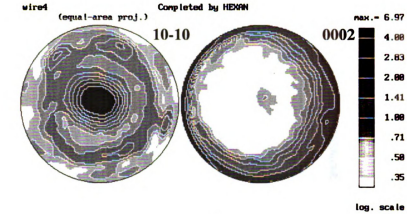

(a)

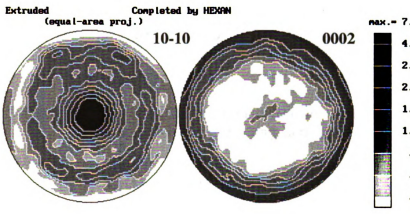

(b)

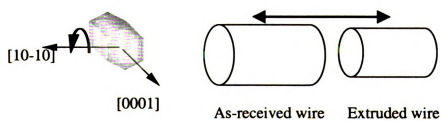

(c)

Figure 3.2 shows the primary α phase pole figures of (a) the as-received middle of wire M with wire axis out of page and (b) the extruded Mex with wire axis out of page sectioned from middle of as-received wire, and (c) the corresponding crystal orientations with specimens. The crystal prism plane normal direction, $(10\bar{1}0)_\alpha$, is aligned with the wire axis, and the $(0001)_\alpha$ plane normal direction is in the radial direction in the as-recived and extruded specimens.

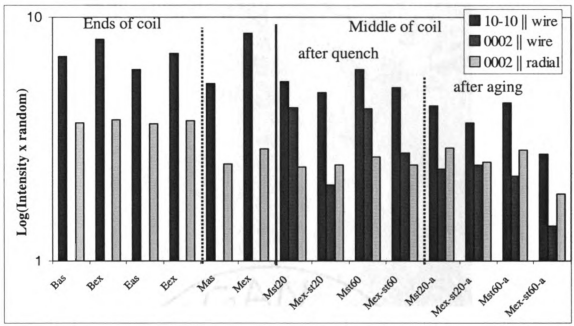

Figure 3.3 The overall texture variations from as-received wire through extrusion, solutionization and quenching, and aging.

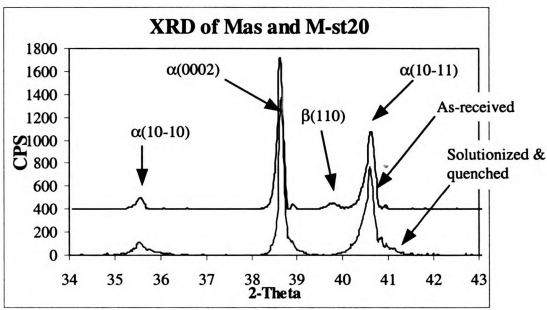

Figure 3.4 X-ray diffraction patterns of the wire M cut from middle of as-received coil showing primary α and β phases, and as-quenched M-sq20 specimens showing the peaks broadening due to the formation of α' martensites.

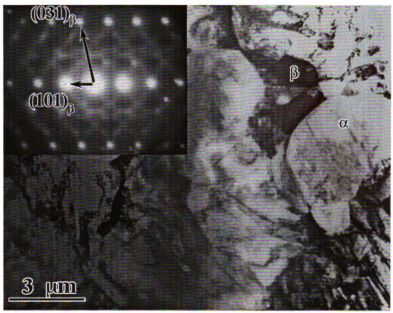

Figure 3.5 shows the TEM image of as-received middle of wire M and the related indexed diffraction pattern from primary β phase.

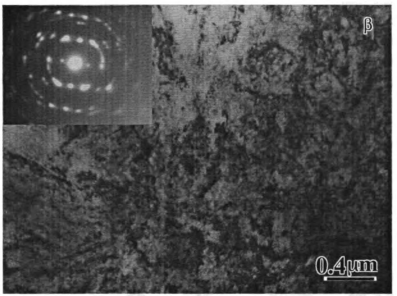

(a)

(b)

Figure 3.6 TEM micrographs of (a) the primary β phase in the extruded Mex specimens showing high dislocation densities and (b) the primary α grains in another thin foil. Inserts show the corresponding diffraction pattern from (a) primary β and (b) α phases.

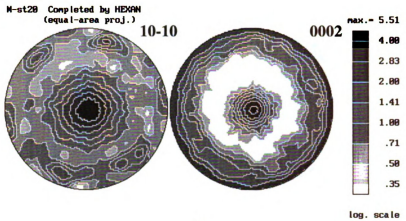

(a)

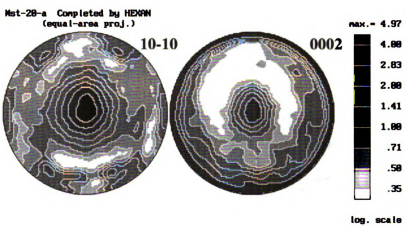

(b)

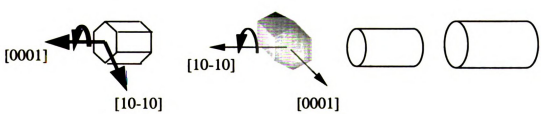

(c)

Figure 3.7 shows the primary α phase pole figures of (a) the as-quenched middle of wire Mex-sq60, (b) the aged Mex-sq60-a with wire axis out of page sectioned from middle of as-received wire, and (c) the corresponding crystal orientations with specimens. The pole figures indicated that a new fiber texture with the crystal basal plane $(0002)_\alpha$ normal direction aligned with the wire axis and the $(10\bar{1}0)_\alpha$ prism plane normal direction perpendicular to the wire axis after solutionization and quenching. This introduction of a new orientation weakened the prior fiber texture having $(0002)_\alpha$ normal direction aligned along radial directions.

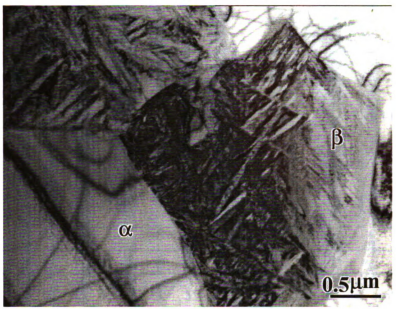

(a)

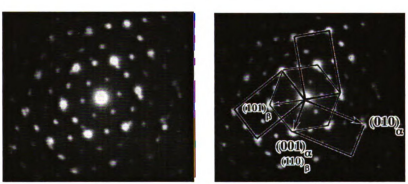

(b) (c)

Figure 3.8 shows (a) the TEM image of as-quenched M-sq60 sectioned from middle of wire (b) the related diffraction pattern from primary β phase showing a [111] β zone pattern and three α <11 $\bar{2}$ 0> patterns superimposed, and (c) is the schematic of (b).

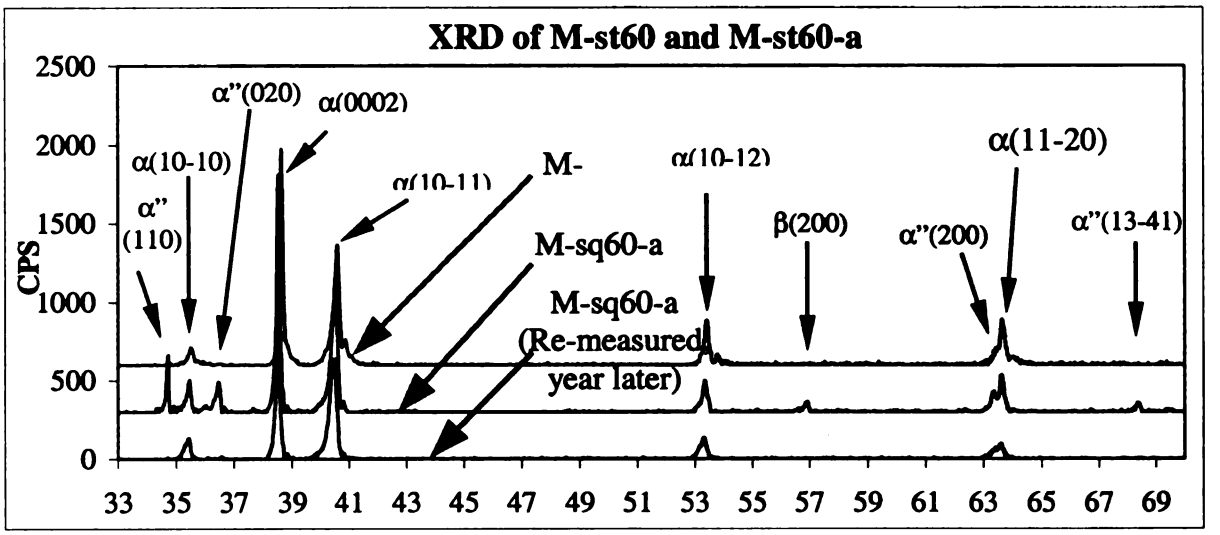

Figure 3.9 X-ray diffraction patterns of the as-quenched M-sq60, M-sq60-a and re-measured M-sq60-a (year later) specimens, showing the formation of orthorhombic α" martensites and β phases due to artificial aging, and disappear of α" martensites and β phases due to natural aging effect. Note, the M-sq60-a and re-measured M-sq60-a (after a year later) are the specimen measured at different time periods.

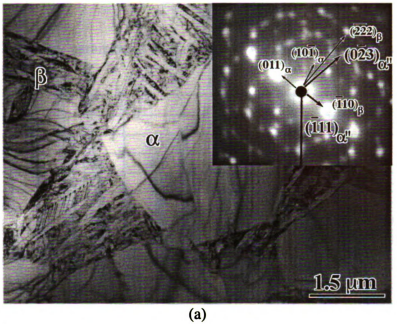

(a)

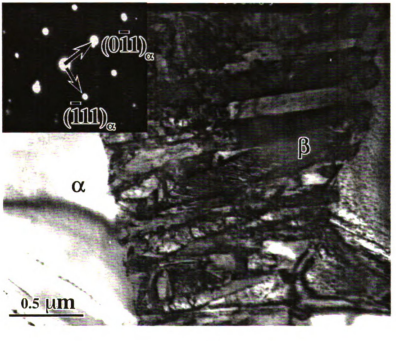

(b)

Figure 3.10 shows the TEM image of (a) the aged M-sq60-a specimens, and (b) the aged M-sq60-a specimens one year later. Inserts show the corresponding diffraction pattern from the corresponding indexed diffraction pattern from primary β phase

Table 3.2 Lattice parameters of Ti-6Al-4V specimens at various experimental processing conditions.

Process	α (A)		β (A)	α" (A)		
	a	c		a	b	c
M	2.9131	4.6572	3.2415	------	------	------
Mex	2.9164	4.654	3.2463	------	------	------
M-sq60	2.9223	4.669	------	------	------	------
Mex-sq60	2.9217	4.6676	------	------	------	------
M-sq60-a	2.9214	4.6672	3.2552	3.0327	4.9238	4.6672
Mex-sq60-a	2.9212	4.6676	3.2553	3.0334	4.9246	4.6676
M-sq60-a (new)	2.9247	4.6708	------	------	------	------
Mex-sq60-a (new)	2.9251	4.6708	------	------	------	------

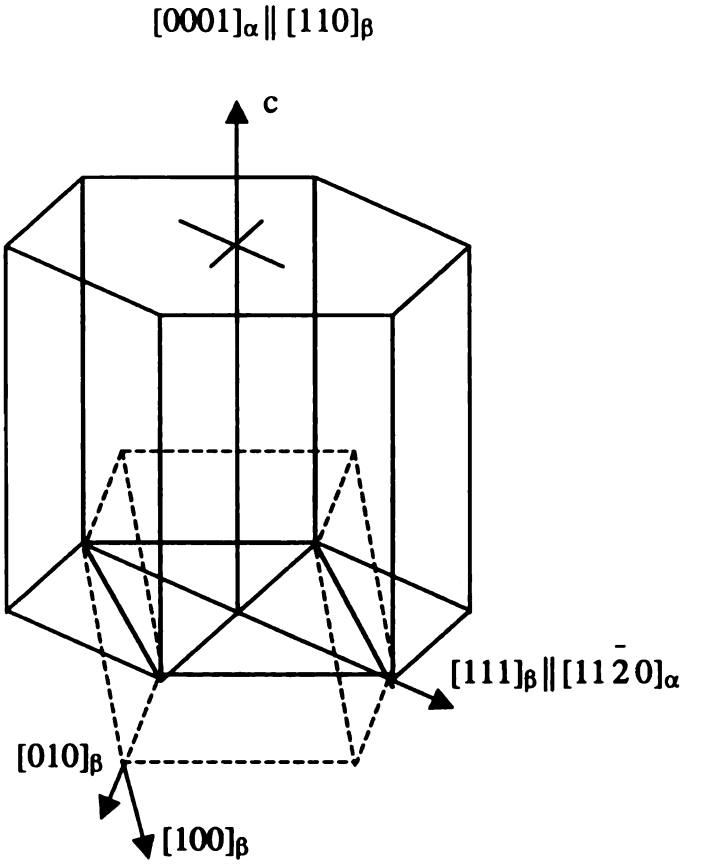

Figure 3.11 The lattice correspondence for β, and α'(α) transformations.

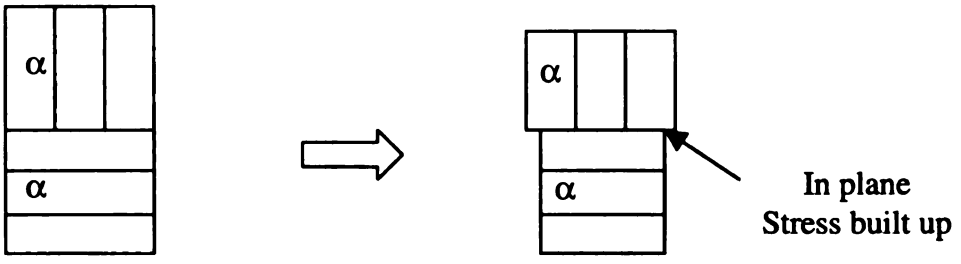

(a) Initial two α grains prior to cool down (b) In plane stress built up upon cooling

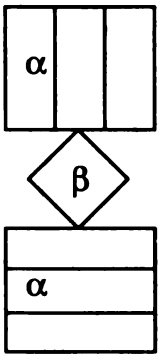

(c) In plane stress develops due to β grain shrink upon cooling prior to β→α' transformation

Figure 3.12: Schematic representation of internal stress build up between different orientations of α grains, as well as with β grains upon cooling prior to transformation to maintain compatibility due to large anisotropic thermal expansion difference between the a and c-axis. Initially, (a) assuming these two hexagonal α grains are well annealed at high temperature, and have a 90° mis-orientation. The (b) large anisotropic thermal contraction along c-axes leads to the development of in plane or radial stress between α grains upon cooling. In addition, if a β grain is located between these two α grains, the in plane tensile stress could develop in the β grain due to cooling. Note: the a-axes of the two α grains drawn are out of the page or radial directions are in plane.

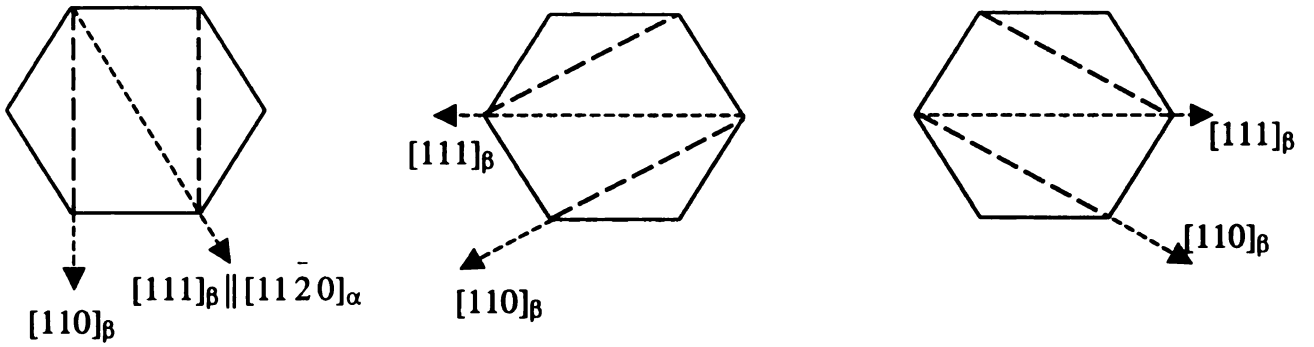
[110]β
[111]β ‖ [11 2̄ 0]α
[111]β
[110]β
[111]β
[110]β

(a)

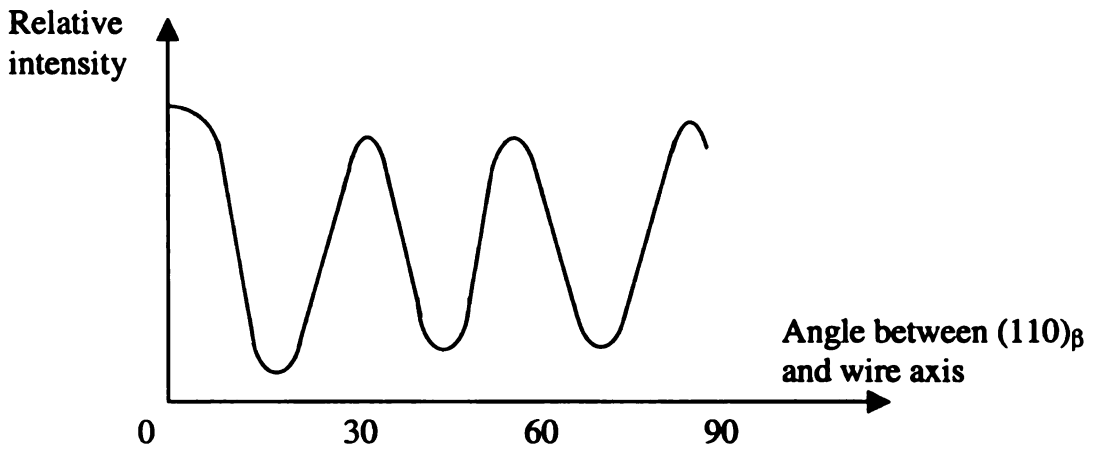
Relative intensity
Angle between (110)β and wire axis
0
30
60
90

(b)

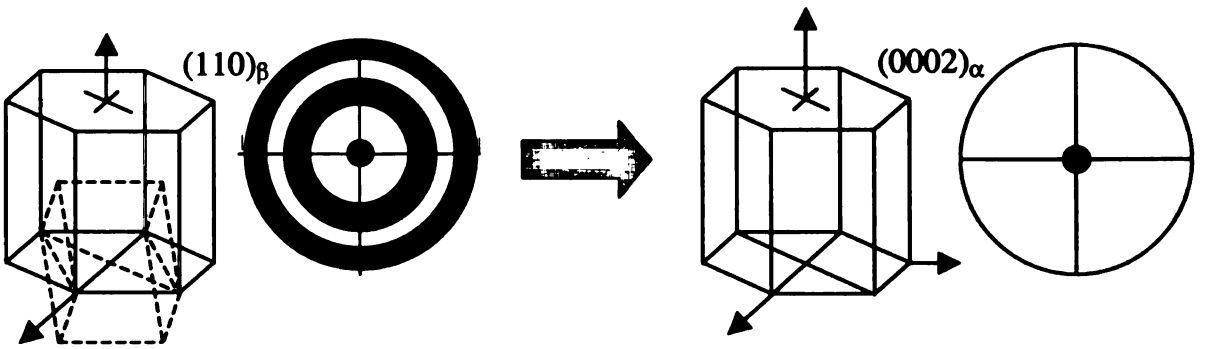
(110)β
(0002)α

(c)

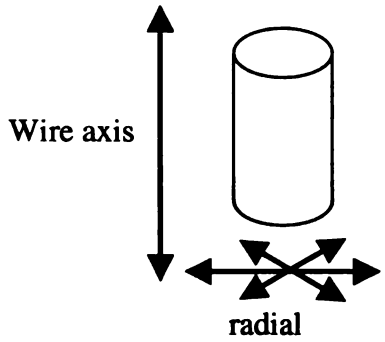

(d)

Figure 3.13 Schematic represent the possible (a) high temperature β phase texture, and (b) the angles of $(110)_\beta$ with wire axis based on the Burgers relationship [Burgers] from $\alpha \rightarrow \beta$, (c) high temperature β phase texture could lead to the formation of α phase texture with the c-axis normal along the wire axis upon quenching, and (d) the corresponding crystal orientations with specimens.

Chapter IV

Effects of solution temperature and time on crystallographic texture and mechanical properties in Ti-6Al-4V wire

Overview

Effects of solution temperature and time on crystallographic texture of the α phase and mechanical properties in Ti-6Al-4V were systematically and comprehensively examined using a series of microstructural and texture examinations and mechanical property tests. The wire was worked by extrusion, solution heat-treated and water quenched, then aged. As-received and extruded wire had a moderately strong fiber texture with prism plane normal aligned with the wire axis. After solutionization and quenching, a secondary fiber with the basal plane normal aligned with the wire axis emerged and consistently increased with solutionization temperatures and times. This implies more favored 90° mis-orientations developed from prior texture after higher solutionization temperatures and longer time heat treatments. Microstructural analysis revealed that the β phase volume fraction increased with solutionization temperature independent of solutionization times. The 0.2% yield strength increased consistently in both wire and radial directions with increasing solutionization temperatures and times, while Young's Modulus was consistently higher in the radial direction than that in the wire direction. The relationship between the variant selections of α phase, and the effects of dislocations are discussed in the context of the known physical metallurgy of titanium and other alloys.

4.1 Introduction

In chapter III, the effects of working and heat treatment on crystallographic texture of the α phase revealed that strong variant selections or 90° texture rotations from the prior texture emerged with the (0001) c-axis aligned with the wire axis after solutionization and quenching. However, many questions about the underlying transformation texture mechanisms and microstructure development remain unanswered. First, despite the fact that solutionization and quenching has been shown to cause variant selections, it is not clear if a higher solutionization temperature would cause a stronger 90° texture rotation with c-axis normal along the wire axis. This is because higher solutionization temperature in the α-β field could potentially generate increased amount of high temperature β phase, leading to different α phase orientations upon subsequent quenching and aging. Second, although a longer solutionization time and quenching has been shown to enhance the preferred variant selection, it is not clear if this strong 90° texture rotation is caused more by the β→α transformation variant selection, or whether it depends on the complicated physical metallurgy involved with the α-β solutionization process. Third, it is not clear if a different 90° orientation rotation from the prior orientations having the (0001) c-axis along the radial directions could occur which would maintain the prior texture. This is because there are two perpendicular orientation changes with 90° rotation from a prior orientation in 3-D space. From a review of the literature, the physical mechanisms of the α→β transformation that operates with heating and solutionization may be more complex than the process occurring during β→α transformation, because the α→β transformation is not well documented. Last, the

effects of texture rotations on the mechanical property development have not been fully investigated.

Therefore, the purpose of this set of experiments was to comprehensively and intensively assess the effects of process variables on the transformation texture, microstructure, and mechanical property development in Ti-6Al-4V wire after solutionization, quenching, and aging. The as-received wire specimens were partially extruded, solutionized in the two-phase region at temperatures of 905, 925, 940 and 960°C for either of 1.2, 2.4, 3.6, or 4.8 ks in an industrial shaker furnace designed to solutionize and quench specimens in a continuous process, followed by aging treatments in air at 500°C for 28.8 ks and air-cooling. Cross-sectional OM, SEM, and TEM were used to investigate the microstructure development, including primary α and β grain sizes, aspect ratio, and volume fractions. Mechanical compression tests were conducted with different specimen orientations, with the wire axis parallel or perpendicular to the compression axis. $(10\bar{1}0)_\alpha$ and $(0002)_\alpha$ pole figure measurements were used to investigate the effect of heat treatment variations on the texture after solutionization and transformation. X-ray diffraction of selected specimens with the surface normal parallel to the wire axis was assessed with serial sectioning to examine the effects of alloy and microstructure variations that could cause differences in peaks (phases), peak shape (defects), peak position (stress), and intensity (texture).

4.2 Experiment results

4.2.1 Texture of as-received and extruded specimens

As in previous studies of Ti-6Al-4V wire in chapter III, two α phase pole figures $(10\bar{1}0)_\alpha$ and $(0002)_\alpha$ of the as-received wire in diameter of 4.9 mm revealed that the

primary α phase orientation is a strong fiber texture with the axisymmetric crystal orientations about the wire axis (Figure 4.1(a)). After extrusion, the primary α phase texture was strengthened. The crystallographic direction $[10\bar{1}0]_\alpha$ in primary α grains is parallel or nearly parallel to the wire axis, and the $[0001]_\alpha$ direction is in the radial direction, similar to the texture of as-received wire (Figure 4.1(b)).

4.2.2 Texture of solution treated, quenched, and aged (SQA) specimens

Figure 4.2(a) reveals the overall relationships between major texture intensities and the solutionization conditions. After SQA, the β phase orientations could not be measured due to very small amount of β phase existing. The texture measurements show that the α phase orientation consisted of two fiber textures; one newly emerged fiber texture with the crystal basal plane $(0001)_\alpha$ normal direction aligned with the wire axis and the other prior fiber texture orientation with the basal plane $(0001)_\alpha$ normal aligned perpendicular to the wire axis (Figure 4.1(c)). The new fiber texture has a 90° rotation from the prior texture, suggesting that a transformation texture and variant selection occurred, leading to a crystal orientation with $(0001)_\alpha$ plane normal aligned with the wire axis after the transformation cycle $\alpha \rightarrow \beta \rightarrow \alpha$. Therefore, the presence of 90° mis-orientations from the prior texture may be a transformation related texture rotation, or possibly the result of a recrystallization process that causes a preferred orientation.

The intensities of the newly emerged fiber texture change dramatically with different solutionization times and temperatures. The intensities of the original fiber texture with the basal plane $(0001)_\alpha$ normal aligned perpendicular to the wire axis are essentially the same for all SQA specimens (Figure 4.2 (b)). However, the intensities of

the newly emerged fiber texture with the crystal basal plane $(0001)_\alpha$ normal aligned with the wire axis is strengthened with increasing solutionization times and temperatures (Figure 4.2 (c)), indicating that special 90° misoriented orientations relative to the prior as-received crystal orientation are more favorable at higher solutionization temperatures and longer times.

4.2.3 Microstructure of SQA specimens

In addition to texture examinations, OM, SEM, and TEM were done to provide detailed microstructural analysis of SQA specimens. After SQA, all specimens show typical duplex microstructures, consisting of equiaxed primary α and transformed β grains. The transformed β grains reveal martensites with an intertwined mixture of needle or platelet shaped domains with many finely divided interfaces or twins, each having a different orientation variant (Figure 4.3). Diffraction patterns taken from one of the primary β grain regions reveals the Burgers orientation relationship of $<111>_\beta \| <11\bar{2}0>_\alpha$ and $(\bar{1}10)_\beta \| (0001)_\alpha$ between α and β phases, consistent with other studies in bcc↔hcp transformation systems. No orthorhombic α" martensites or ω phases were observed. A diffraction pattern of a primary α grain (Figure 4.3) reveals this particular α grain is oriented to the [221]-zone axis of the hexagonal α phase without extra superlattice reflections due to the precipitation of α_2 phase.

In addition, grain size, aspect ratio, and volume fractions of the primary α and β phases were examined using cross-sectional OM and SEM observations since large areas can be chosen and are therefore more representative. After SQA, the primary α and β grains size were essentially the same and equiaxed. No abnormal grain growth was

observed. Figure 4.4(a) shows the overall relationships between the grain sizes, prior β phase ratio, and the experiment solutionization conditions. As expected, with increasing solutionization times and temperatures, the primary α and β grain size and volume fractions of prior β phase increased consistently. However, Figure 4.4(a)) shows that the volume fractions of the primary α and β phases are independent of the solutionization time in the present studies, suggesting the kinetics of α→β transformation is very fast. Therefore, with increasing solutionization temperature, more primary α phase transformed quickly to high temperature β phase, so more retransformed back to α phase upon cooling, resulting in more of the variant that is misoriented 90° from the prior crystal orientation. In summary, the effects of solutionization time and temperature increase the amount of texture rotations, the grain size and the volume fraction of prior β grains.

4.2.4 X-ray diffraction of serially sectioned SQA specimens

Three representative parts were chosen for X-ray diffraction studies of serially sectioned specimens; a sample solutionized at 905°C for 1.2 ks and aged at 500°C for 14.4 ks, a sample solutionized at 905°C for 4.8 ks and aged at 500°C for 14.4 ks, and a sample solutionized at 960°C for 4.8 ks and aged at 500°C for 14.4 ks. The d-spacing of $(10\bar{1}0)_\alpha$ and $(0002)_\alpha$ α phase peaks, $d_{(10\bar{1}0)\alpha}$ and $d_{(0001)\alpha}$ values changed with measurement locations (500 μm apart), indicating that lattice parameters vary with positions (Figure 4.5). However, both the α phase $(10\bar{1}0)_\alpha$ and $(0002)_\alpha$ lattice spacing decreased by about 0.2% after solutionization for 1.2 to 4.8 ks at 905°C, indicating that changes occurred in dislocation density, internal strain, substitutional Al and V atom concentrations, or

impurities (primary O) with time. The short time solutionization (905°C for 1.2 ks) led to an increase of the unit cell size and volume and a decrease of the c/a ratio from the extruded condition. The extrusion showed a larger c/a ratio (Figure 4.6(b)) which was evidently caused by a macro residual stress from extrusion which generated a tensile stress along wire axis direction and compression in the radial directions. After SQA the variation in the *ratios* of the d spacings (Figure 4.5) were smaller by an order of magnitude than variations in the *d spacings* (Figure 4.6(b, c)), indicating that the *proportionality* of the α phase unit cell did not change, though the d-spacings varied with time and position. In comparison, the variation in the d spacings and the ratios of the planes were consistently higher in the extruded wire than those of SQA specimens, indicating more consistency in the c/a ratio and d spacings in the SQA specimen than in the extruded wire.

4.2.5 Mechanical properties of SQA specimens

Figure 4.7 shows the (a) overall relationships and the related statistical analysis identifying the effects of solutionization temperature (b) and time (c) on 0.2% yield stress and the apparent Young's modulus along directions of parallel and perpendicular to the wire axes for compression tests. Clearly, after SQA the 0.2% yield stress at room temperature increased consistently in the wire directions with increasing solutionization temperatures and times due to the increasing β volume fraction during the α→β→α transformation, but in the radial direction, yield stress minima were observed at 940°C. However, the yield stresses in the radial direction are significantly higher than in the wire direction at lower solutionization temperatures where there was less material with the c-axis aligned with the wire axis (Compare Figures 4.2(a) and 4.7(a)). The apparent

Young's Modulus was consistently higher in the radial direction than that in the wire direction. Young's modulus along both wire and radial directions goes through a maximum point for the present alloys quenched from approximately 925°C and aging. The existence of this maximum in stiffness and minimum in yield stress has not been reported before.

4.3 Discussion

The present study investigated the effects of solution temperature and time on crystallographic texture and microstructure evolution such as 90° texture rotations, grain size, volume fraction of prior β grains, and the associated mechanical properties. Two main questions arise about the relationship between transformation texture, recrystallization, and microstructure development. First, it is not clear why the texture intensities of crystal orientation of $(10\bar{1}0)_\alpha$ aligned along wire axis were essentially the same since less primary α phase was retained with increasing solutionization temperature (Figure 4.2(b) and 4.4(b)). For example, the specimen texture intensity of $(10\bar{1}0)_\alpha$ along wire axis after solutionization at 960°C had less than 10% volume fraction of residual primary α phase, but the intensity of the $(10\bar{1}0)_\alpha$ along wire axis is the same as that of specimens solutionized at 905°C which had around 50% α phase. Secondly, despite the fact that the volume fraction of the primary β phase is independent of the solutionization time, it is not clear why the texture intensities of crystal orientation of $(0001)_\alpha$ aligned along wire axis were consistently increasing with time (Figure 4.2(c) and 4.4(a)). It is assumed that the longer time solutionization may lead to the further β grain re-orientation or recrystallization or grain growth of β grains, making the 90° mis-orientation with

$(0001)_\alpha$ along wire axis thermodynamically more favorable upon cooling. Therefore, it is of interest to concurrently investigate the microstructural transformation and texture rotation behaviors in relation to previous Ti-6Al-4V alloys studies, physical metallurgy principles related to recrystallization, grain growth and phase transformations, and similar microstructure studies of Titanium alloys.

4.3.1 Variant selections and mechanical properties

The present studies indicated that, with increasing solutionization temperature, the resulting intensity of the α phase orientations with $(0002)_\alpha$ along the radial directions was the same (Figure 4.2) even with much less α phase existing at high temperature, suggesting that some of the β phase transformed epitaxially back onto the existing parent α phase variants with $(0002)_\alpha$ along radial directions. If this were not so, after cooling the resulting α phase texture with $(0002)_\alpha$ aligned along radial directions would decrease with increasing solutionization temperatures. This assumption is based upon experimental results from rolling where one single α phase variant can generate many α phase variants after $\alpha \leftrightarrow \beta$ transformation cycles, including two perpendicular variants both having 90° mis-orientations from prior orientation (Figure 4.8) [Moustahfid 1997]. Therefore, it is expected that at elevated temperatures the α phase transforms to β phase, followed by transformation to two or more favorable α variants occurring during quenching, based on the Burgers relationship [Burgers 1934].

With increasing solutionization temperatures and times, the yield stress difference between wire and radial directions decrease consistently (Figure 4.7) and can be explained qualitativly: When the solutionization temperatures are increased, the volume fraction of high temperature β phase becomes higher, leading to more 90° α phase

rotation from the dominant prior crystal orientation, so the $(0001)_\alpha$ hard orientation of the α phase is aligned along the wire axis rather than only along the radial direction. This development of nearly equal fractions in the two orientations has a homogenization effect on the modulus and microyielding processes, leading to the almost equalized yield stress in both wire and radial directions. It is assumed that this larger difference in the effect of solutionization on Young's modulus is due to differences in the effects of microstructure and crystal orientation on bond strength. Generally, Young's modulus of polycrystalline materials is mainly determined by a weighted average of the modulus for the constituent crystals, which depends on the crystal orientation. Comparison of Figures 4.2(a) with 4.7(a) show a strong correlation between modulus values, and texture measurements, indicating that texture measurements are qualitatively representative of the volume fraction of crystal orientations. However, yield stress is more strongly affected by the material's microstructures than the crystal orientations.

4.3.2 Grain growth behaviors

At elevated temperatures, grain growth occurred after the $\alpha \rightarrow \beta$ transformation. For many materials, the isothermal grain growth can be represented by equation of the form $d^n - d_0^n = Kt$,

Where d denotes the mean grain diameter, d_o represents the starting diameter, t denotes the time, K denotes the constant, and n denotes the grain growth exponent.

The driving force for the α and β grain growth is a reduction of grain boundary energy. This process occurs by an exchange of elements or fluxes of the constituents such as Ti, Al and V between different phases. The phase boundary interfaces move by the process of conversion of one phase to another. Thus, regions of α phase convert to β

phase with diffusion of V from α to β grains, and Al away from the β phase grains, resulting in overall α and β grain growth while maintaining a constant volume ratio [Grewl 1989, 1990]. Since the rate-controlling mechanism requires exchange of V and Al between phases, this process is the same for both α and β grains, so the growth behaviors of both α and β phases should be the same, consistent with the experimental results. The average diffusion distances of Ti, Al and V in the β phase under experimental solutionization conditions were faster than those in α phase (Figure 4.4(c)), and the diffusion distances in the α phase are comparable to the rate of boundary migration shown in figure 4.4(a). However, the grain growth exponents at different solutionization temperatures were significantly different, ranging from 7.5 at 900°C, to 2.5 at 960°C, indicating different diffusion rate controlling mechanisms, though the trends of average diffusion distances of Ti, Al and V in α and β phases were similar at different solutionization temperatures.

Furthermore, the grain growth behavior strongly affects the texture. A strongly textured material contains low angle grain boundaries, having reduced grain boundary mobility and driving force for grain growth. During the current research, increasing grain sizes leads to the slowing down of growth rate based on grain growth exponential exponent, suggesting decreasing in grain boundary mis-orientations or local grouping of similar grain boundaries [Boswell 1995]. Therefore, it is highly possible that grain growth by grain rotation or preferential migration of certain boundary misorientations could decrease grain boundary area and strengthen the pre-existing β phase fiber textures, resulting in preferred α phase orientations with $(0002)_\alpha$ along wire axis upon quenching.

4.3.3 Dislocations and α↔β transformation

The changes in the unit cell size, c/a ratio and d-spacings after short time solutionization were due to changes in residual stress and dislocation density, and not due to compositional changes. The lattice parameter of the α phase is unaffected by heat treatment because the composition is very stable [Boyer-A 1994]. Since Al atoms are bigger and V atoms are smaller than Ti atoms, an increase of Al and a decrease in V in the α phase should increase the size of the unit cell slightly with increasing solutionization time, in contrast to the observations in figure 4.6(a). Since the α-β transformation occurred quickly (Figure 4.4(a), and since grain growth occurred at a rate similar to Al and V diffusion in α (Figure 4.4(c)), this implies that the dislocation density increased due to the transformation, such that the unit cell was still large after the short time solutionization after extrusion process. With longer time and higher temperature solutionization, a reduction of dislocation density occurred that is shown by the reduced unit cell volume and the reduced and well established c/a ratio. Thus, the high temperature solutionization process can be viewed as the combinations of α→β transformation and primary recrystallization processes which resulted in a reduction of dislocation density.

Because the α→β transformation proceeds with the superimposed recrystallization process [Divinski 1998], the α→β transformation and differential thermal expansion mismatch stresses could generate dislocations at or near the α/β phase boundaries, resulting an increasing of dislocations densities after short time solutionization (Figure 4.5 and 4.6). This internal strain/stress can be reduced by volume contraction through annihilation of nearby transformation dislocations [Fujishiro 1980], but the subsequent grain growth by α↔β phase transitions can continually exert internal stress as long as

grain growth continues. Thus, it is expected that micro-strains would always exist at α/β phase boundaries; while their magnitude would decrease due to the slowing down of the grain growth and recrystallization behaviors, consistent with our serial sectioning X-ray diffraction studies and internal friction measurement that higher solutionization in the $\alpha+\beta$ phase field results in lower internal friction [Ouchi 1999].

Cahn [1953] demonstrated that the dissipation of strain associated with dislocations via the formation of a secondary phase is facilitated by preferential phase nucleation on slip planes with dislocations. It is expected that the $\beta \rightarrow \alpha$ transformation could start from the α/β boundaries. The alternative (transformation starting from β/β boundaries) is not reasonable, because if the transformation started from β/β boundaries, similar to solutionization in the Ti-6Al-4V β phase field, the resulting α phase texture would develop without variant selection [Gey 1996, 1997]. The most pronounced difference between α/β and β/β boundaries is that strains evolve at α/β boundaries, accommodated by dislocations, suggesting that dislocations near boundaries could facilitate the transformation. Hence, the dislocations on the $\{110\}_\beta$ planes with high dislocation densities could provide the martensite nucleation sites [Furuhara 2001].

Thus, the most favorable variant is likely to be the one which has the resulting transformation strain accommodated most effectively with the pre-existing dislocations to minimize the required nucleation energy for transformation [Humbert 2002]. For example, if specific $\{110\}_\beta$ planes have lattice strains of approximately 1.38%, 9.9%, or –3.4%, then these specific $(110)_\beta$ planes are more likely transform to basal $(0002)_\alpha$, $(1\bar{1}00)_\alpha$, or pyramidal $(10\bar{1}1)_\alpha$ planes, respectively, during the subsequent $\beta \rightarrow \alpha$ transformation since the required lattice distortion and energy is minimized with this

correlation (see Table 4.1). In addition, the direction of the maximum misfit strain field between the parent and the secondary phase ($<111>_\beta \| <11\bar{2}0>_\alpha$) tends to develop along the direction of Burgers vector of dislocations, located either at the boundary or inside the β crystal [Furuhara 2001]. In addition, the habit plane of the newly formed α phase tends to be parallel to the dislocation line [Luo 1987], which cannot be determined due to the lack of measureable β phase after quenching in this study.

Furthermore, Furuhara et al. [2001] studied the grain boundary α precipitates from β matrix via low temperature aging of β titanium alloy. The α precipitates maintained Burgers orientations with their parent β grains, and coherency relations with nearby β grains via maintaining the maximum misfit direction, $<111>_\beta \| <11\bar{2}0>_\alpha$, parallel to the closest β/β grain boundary plane. Thus, it is expected that coherency could also be maintained between the newly formed α and the pre-existing neighboring α grain, in addition to the Burgers orientations of the newly formed α and parent β grain. Therefore, it is expected that the metallurgical state of high temperature α and β phases, and boundary dislocations could affect or determine the subsequent variant selections.

4.3.4 Conceptual model for the β→α transformation

The dislocation arrangement could strongly affect the β→α transformation. The grain growth behaviors via α↔β boundary movement resulted in the same grain sizes of α and β, independent of solutionization temperature and time, implying the transformations of α→β and β→α were essentially the same. Thus, it is likely that overall, α→β and β→α boundary misfit dislocations were similar at all times, although dislocations inside grains and α/β boundary reactions could affect the misfit boundary

dislocations. The texture analyses revealed the presence of 90° mis-orientations from the prior texture, implying that a common texture rotation occurred, suggesting that the α/β boundary dislocations have an intrinsic feature which could result in the 90° mis-orientations. This is consistent with results that the development of the new α texture component is independent of cooling rate or β→α transformation mechanisms, either martensitic or diffusional, as pointed out by many authors [Fujishiro 1980, Bieler 2000].

In the current study where longer time solutionization resulted in more strongly favored variant selection can be explained by a dislocation reaction effect. Upon solutionization, β phase boundary sweeping across α grains containing defects could maintain existing dislocation structures, since the boundary is coherent, or generate transformation-induced dislocations. In addition, dislocations inherited from primary α phase or caused by transformation could disappear by recrystallization in the high temperature β phase, leaving near-perfect β crystals, as indicated by the reduction in the unit cell dimension in figures 4.5 and 4.6. Thus, for short solutionization times, the dislocations in the boundary may have more variations, as indicated by the larger unit cell dimension with 20 minutes than 80 minues in figure 4.6, resulting in more variant selections of the β-α transformation, making the resultant texture is less pronounced. Thus, the longer the solutionization time, only the most stable boundary dislocations would remain, leading to a more favored 90° variant selection. This indicates that the variant selection process is strongly affected by β phase primary recrystallization processes that reduce the dislocation density during solutionization. However, further investigations are needed to fully characterize the change in metallurgical state of α and β

grains, especially regarding the relationship between crystal orientations, dislocation orientations and variant selections.

4.4 Conclusion

The present study systematically investigated the effects of heat treatment on mechanical, microstructural and crystallographic texture evolution of the α phase in Ti-6Al-4V using compression tests, OM, SEM, TEM and X-ray diffraction techniques. Texture analysis reveals 90° rotation from the prior texture after solutionization and quenching with the c-axis aligned with the wire axis. The 90° rotation consistently increased with solutionization temperatures and times, in a manner consistent with compression tests showing that the yield strength difference between wire and radial directions consistently decreased. The transformation texture is mainly determined by the orientation of dislocations, located either at phase boundary or inside the grains. The presence of 90° mis-orientations, independent of solutionization temperatures and times, can be intepreted as a common transformation related texture rotation due to the intrinsic α/β boundary dislocations.

Table 4.1 lattice strain or linear dimensional changes in $\beta \rightarrow \alpha$ transformation.

β phase Lattice plane distance (A)		α phase Lattice plane distance (A)		Linear dimensional changes (%)
$(110)_\beta$	2.3 →	(0001)	2.33	1.38
$(\bar{1}10)_\beta$	2.3 →	$(1\bar{1}00)$	2.53	9.9
$(110)_\beta$	2.3 →	$(01\bar{1}1)$	2.22	-3.4
$(01\bar{1})_\beta$	2.3 →	$(\bar{1}011)$	2.22	-3.4
$(10\bar{1})_\beta$	2.3 →	$(0\bar{1}11)$	2.22	-3.4
$(011)_\beta$	2.3 →	$(10\bar{1}1)$	2.22	-3.4

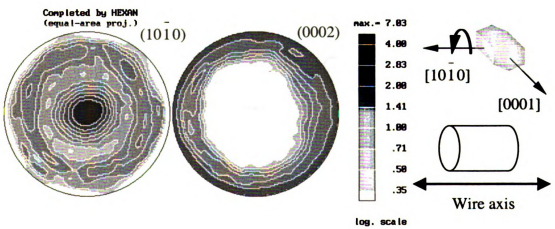

(a)

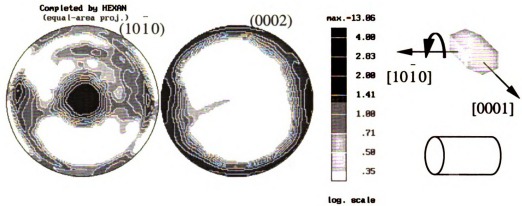

(b)

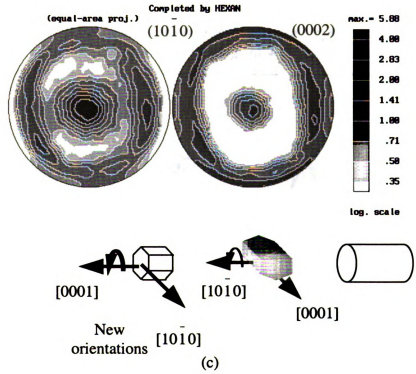

(c)

Figure 4.1 The primary α phase $(10\bar{1}0)$ and (0002) pole figures and schematic crystal orientations of (a) as-received wire, (b) extruded specimens, and (c) extruded specimens after solutionization at 925°C for 20 minutes and aging (SQA) with wire axis out of the page.

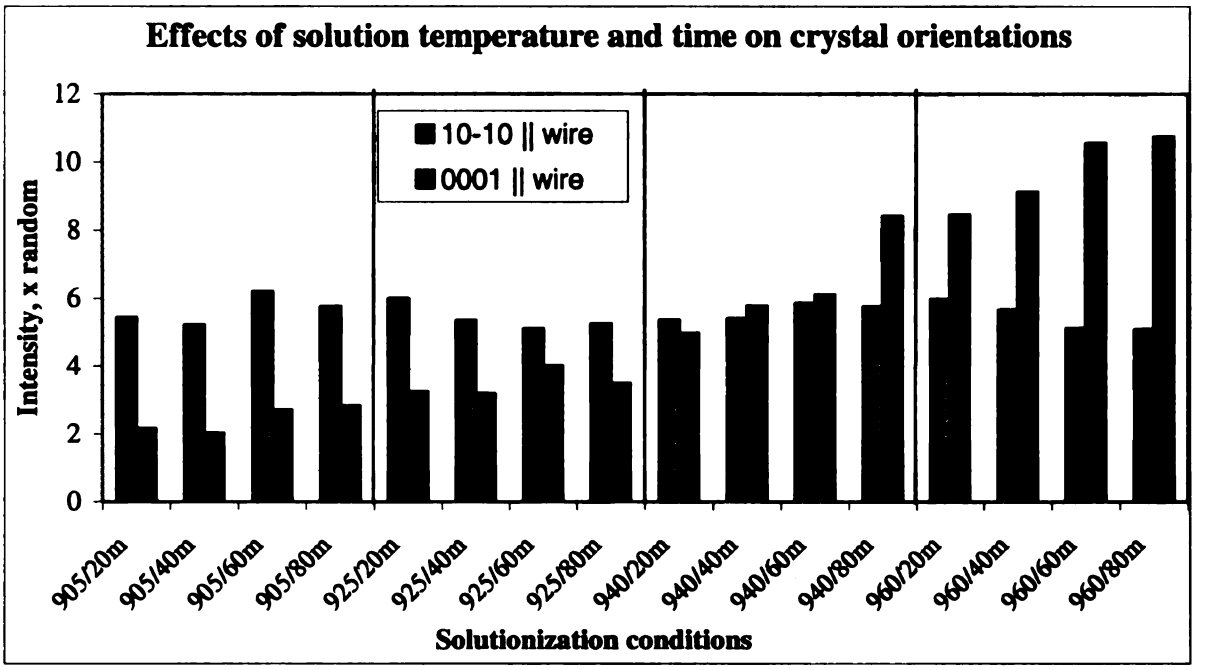
Effects of solution temperature and time on crystal orientations
Intensity, x random
12
10
8
6
4
2
0
10-10 || wire
0001 || wire
905/20m
905/40m
905/60m
905/80m
925/20m
925/40m
925/60m
925/80m
940/20m
940/40m
940/60m
940/80m
960/20m
960/40m
960/60m
960/80m
Solutionization conditions

(a)

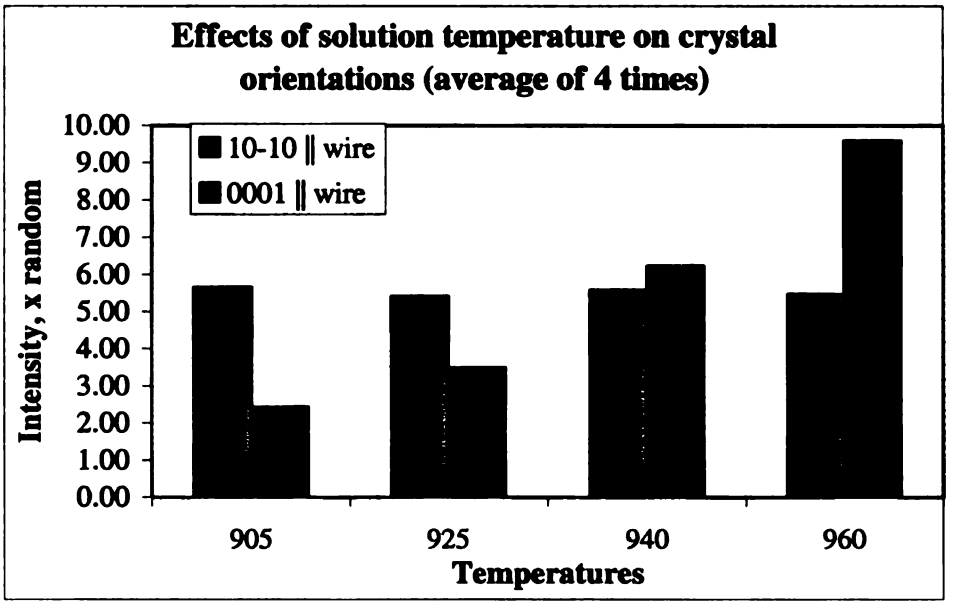
Effects of solution temperature on crystal orientations (average of 4 times)
Intensity, x random
10.00
9.00
8.00
7.00
6.00
5.00
4.00
3.00
2.00
1.00
0.00
10-10 || wire
0001 || wire
905
925
940
960
Temperatures

(b)

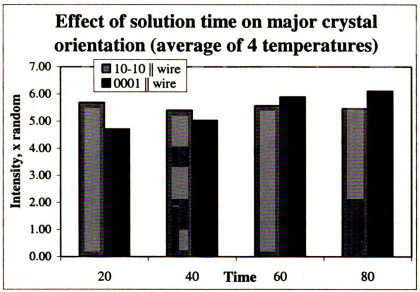

(c)

Figure 4.2 The overall relationships (a) between major texture intensities and the experiment solutionization conditions, and (b) the effects of solutionization temperature and (c) time on the major texture intensities using statistical analyzes via averaging the corresponding texture intensities of the same temperature of different times and same times of different temperatures, respectively.

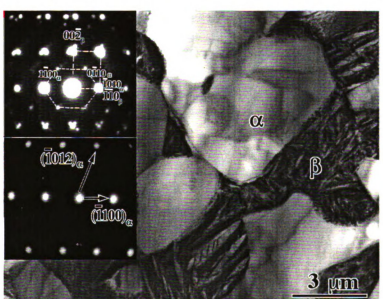

Figure 4.3 TEM image of specimen after solution treated at 925°C for 2.4 ks and aging at 500°C for 28.8 ks showing typical duplex microstructure, consisting of equiaxed primary α and β grains. Diffraction patterns taken from one of the transformed β grain regions reveals the Burgers orientation relationship of $<111>_\beta \| <11\bar{2}0>_\alpha$ and $(\bar{1}10)_\beta \| (0001)_\alpha$ between α and β phases, consistent with other studies in bcc↔hcp transformation systems.

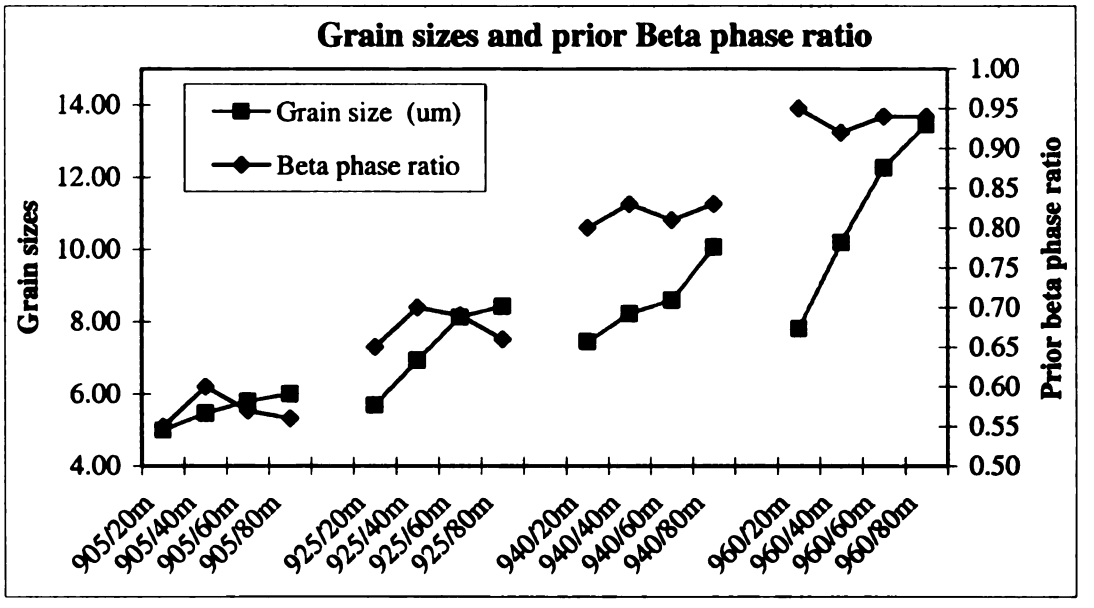
Grain sizes and prior Beta phase ratio
Grain size (um)
Beta phase ratio
Grain sizes
Prior beta phase ratio
14.00
12.00
10.00
8.00
6.00
4.00
1.00
0.95
0.90
0.85
0.80
0.75
0.70
0.65
0.60
0.55
0.50
905/20m
905/40m
905/60m
905/80m
925/20m
925/40m
925/60m
925/80m
940/20m
940/40m
940/60m
940/80m
960/20m
960/40m
960/60m
960/80m

(a)

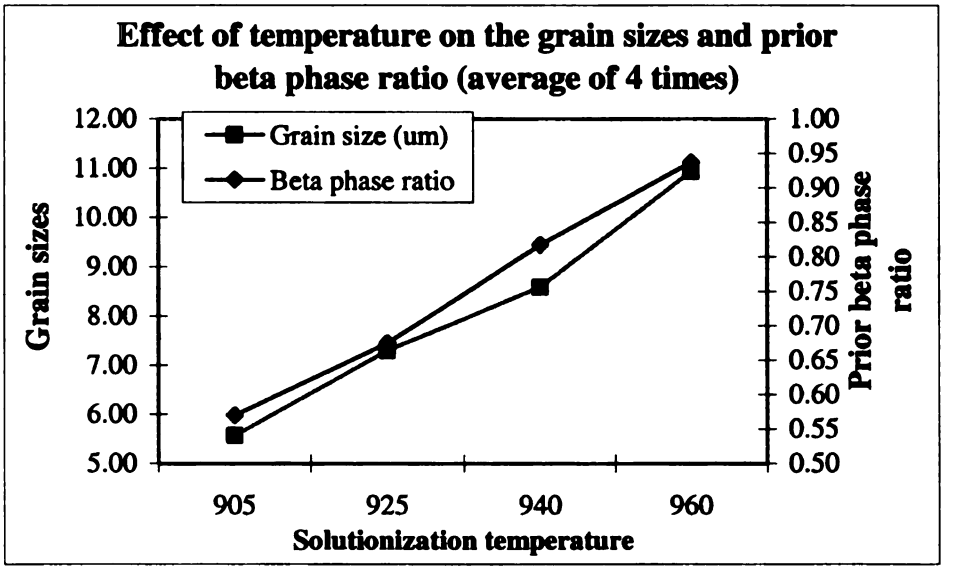
Effect of temperature on the grain sizes and prior beta phase ratio (average of 4 times)
Grain size (um)
Beta phase ratio
Grain sizes
Prior beta phase ratio
12.00
11.00
10.00
9.00
8.00
7.00
6.00
5.00
1.00
0.95
0.90
0.85
0.80
0.75
0.70
0.65
0.60
0.55
0.50
905
925
940
960
Solutionization temperature

(b)

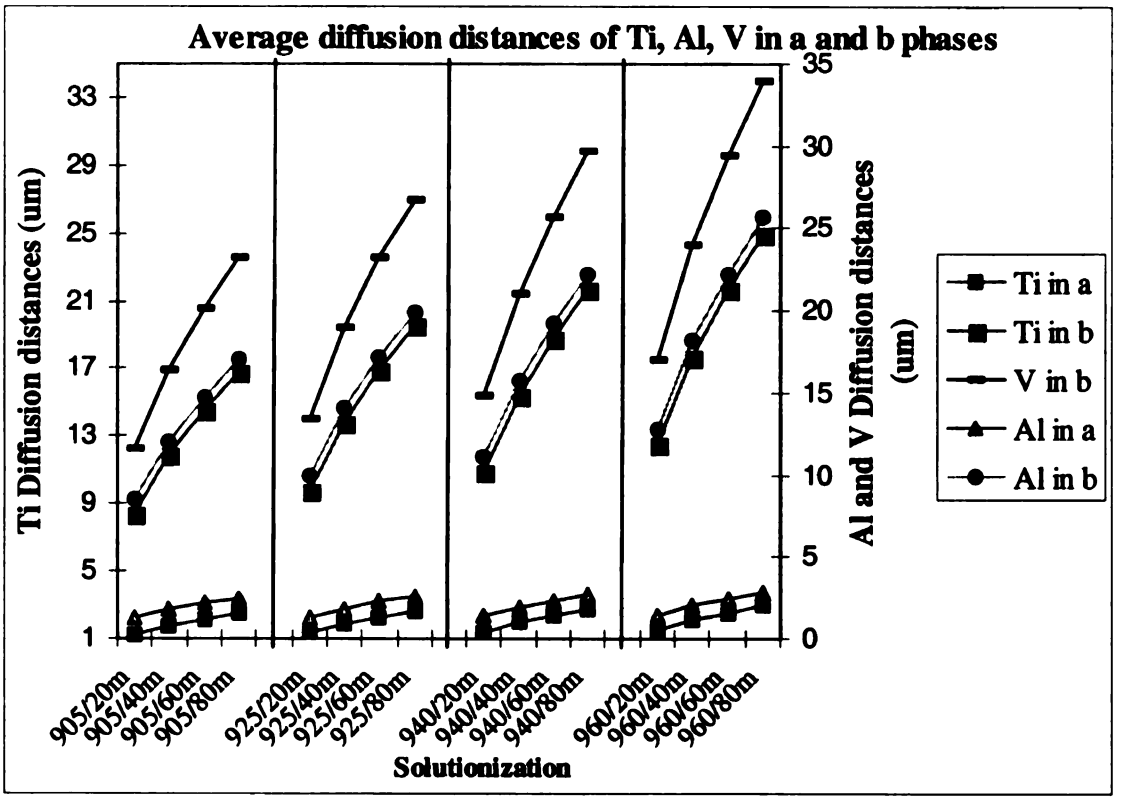

(c)

Figure 4.4 The overall relationships (a) between the grain sizes, prior β phase ratio, and the experiment solutionization conditions, (b) the effects of solutionization temperature on the grain sizes and prior β phase ratio using statistical analyzes via averaging the corresponding grain sizes and prior β phase ratio of the same temperature of different times, and (c) the average diffusion distances of Ti, Al, V in α and β phases under the experimental solutionization conditions.

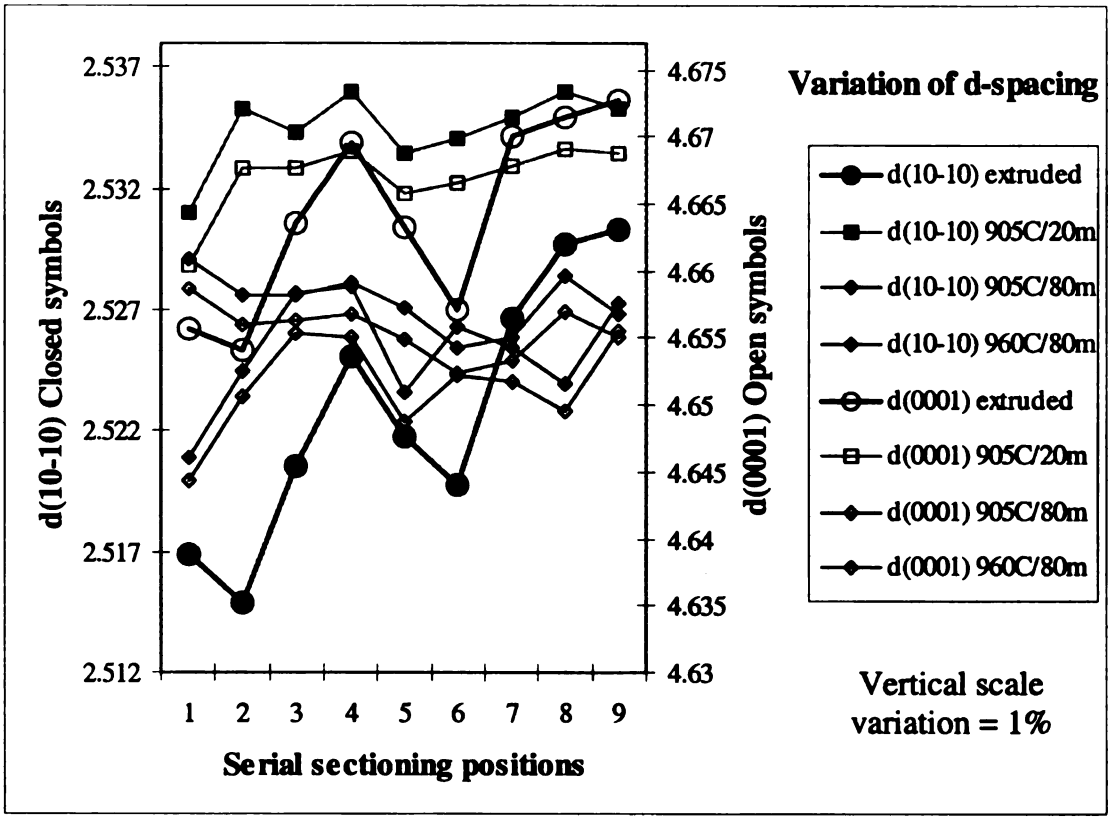

(a)

Temperature/time	Mean		Sigma	
	$(10\bar{1}0)$	(0001)	$(10\bar{1}0)$	(0001)
Extruded	2.5228	4.6642	5.46E-03	7.16E-03
905°C/20m	2.5345	4.6670	1.55E-03	2.68 E-03
905°C/80m	2.5253	4.6515	2.30 E-03	3.68 E-03
960°C/80m	2.5273	4.6556	1.19 E-03	1.95 E-03

(b)

Figure 4.5 shows the gradual sectioning of X-ray diffraction studies of specimens. The (a) zigzag relationship between d-spacing of $d_{(10\bar{1}0)\alpha}$ and $d_{(0001)\alpha}$, and (b) the related mean, and standard deviation (sigma) of the $d_{(10\bar{1}0)\alpha}$ and $d_{(0001)\alpha}$ under different solutionization conditions were identified.

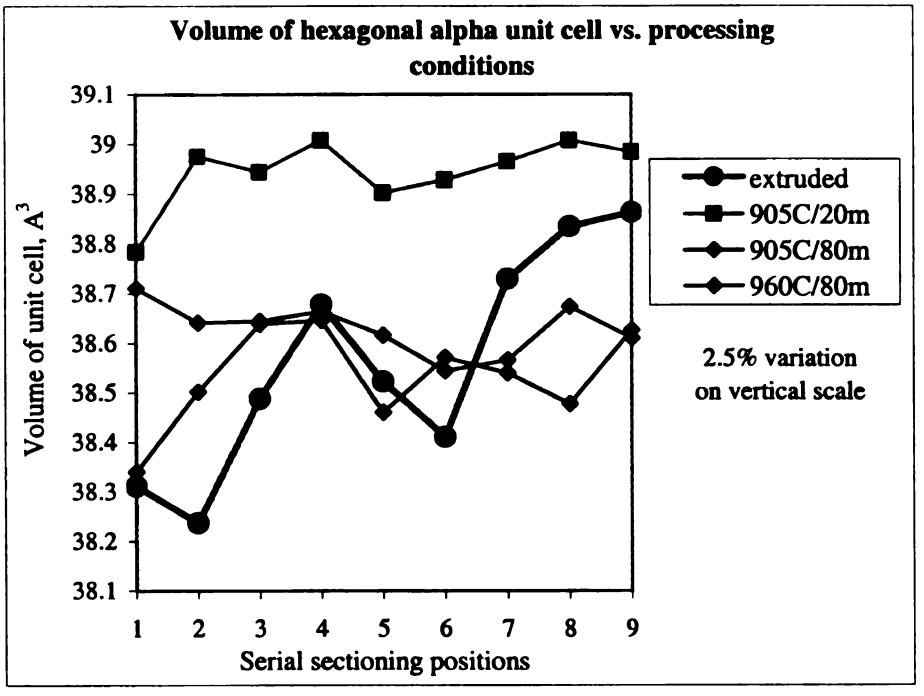
Volume of hexagonal alpha unit cell vs. processing conditions
Volume of unit cell, A3
39.1
39
38.9
38.8
38.7
38.6
38.5
38.4
38.3
38.2
38.1
1 2 3 4 5 6 7 8 9
Serial sectioning positions
extruded
905C/20m
905C/80m
960C/80m
2.5% variation on vertical scale

(a)

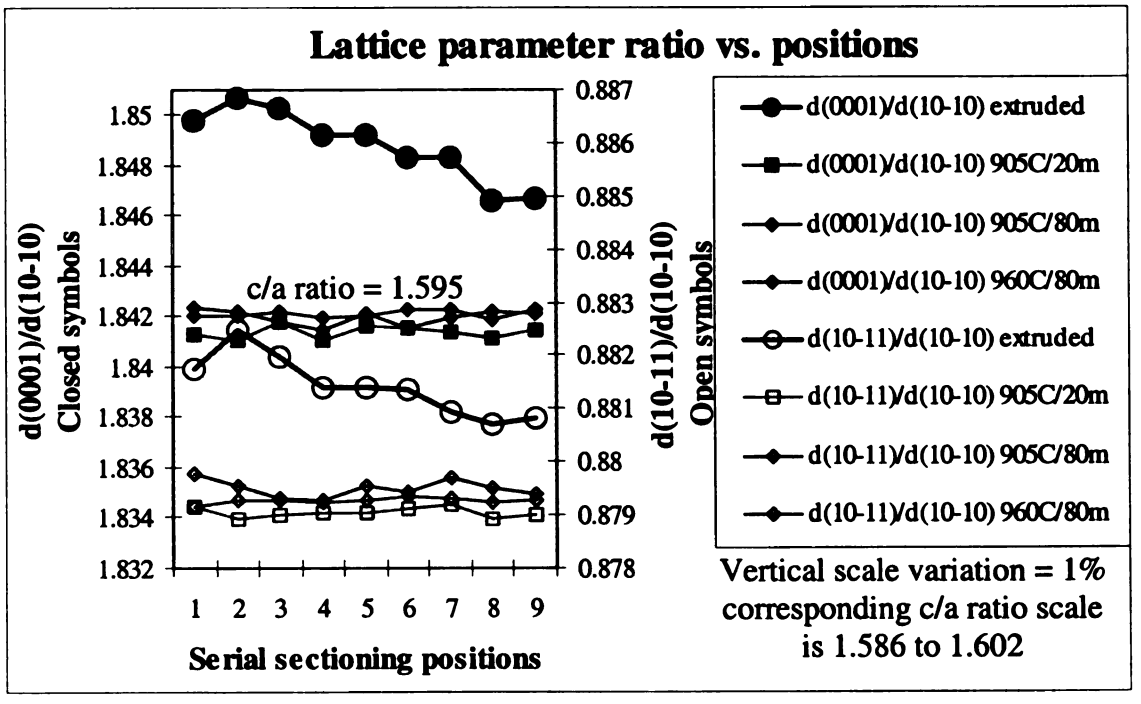
Lattice parameter ratio vs. positions
d(0001)/d(10-10) Closed symbols
1.85
1.848
1.846
1.844
1.842
1.84
1.838
1.836
1.834
1.832
c/a ratio = 1.595
d(10-11)/d(10-10) Open symbols
0.887
0.886
0.885
0.884
0.883
0.882
0.881
0.88
0.879
0.878
1 2 3 4 5 6 7 8 9
Serial sectioning positions
d(0001)/d(10-10) extruded
d(0001)/d(10-10) 905C/20m
d(0001)/d(10-10) 905C/80m
d(0001)/d(10-10) 960C/80m
d(10-11)/d(10-10) extruded
d(10-11)/d(10-10) 905C/20m
d(10-11)/d(10-10) 905C/80m
d(10-11)/d(10-10) 960C/80m
Vertical scale variation = 1% corresponding c/a ratio scale is 1.586 to 1.602

(b)

Temperature/time	Mean		Sigma	
	$d_{(0001)}/d_{(10\text{-}10)}$	$d_{(10\text{-}11)}/d_{(10\text{-}10)}$	$d_{(0001)}/d_{(10\text{-}10)}$	$d_{(10\text{-}11)}/d_{(10\text{-}10)}$
Extruded	1.849	0.881	1.44E-03	5.67E-04
905°C/20m	1.841	0.879	2.57E-04	0.93E-04
905°C/80m	1.842	0.8795	3.16E-04	1.60E-04
960°C/80m	1.842	0.8793	6.6E-08	0.56E-04

(c)

Figure 4.6 The serial sectioning X-ray diffraction studies show, (a) the volume of hcp unit cell vs. processing conditions, (b) the variations of d spacings $d_{(0001)\alpha}/d_{(10\bar{1}0)\alpha}$ and $d_{(10\bar{1}1)\alpha}/d_{(10\bar{1}0)\alpha}$, (c) the related mean and sigma of the $d_{(0001)\alpha}/d_{(10\bar{1}0)\alpha}$ and $d_{(10\bar{1}1)\alpha}/d_{(10\bar{1}0)\alpha}$ with solutionization temperatures and times. For comparison, the large variations of d spacings for as-received and extruded wire suggested that macro-residual stress might cause the lattice strain variations.

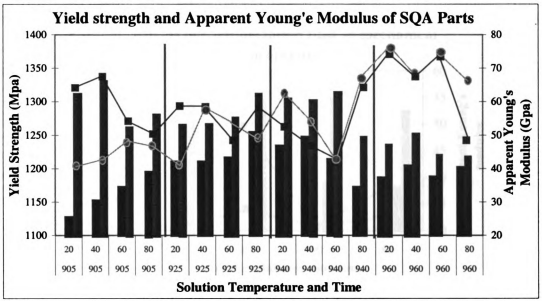
Yield strength and Apparent Young'e Modulus of SQA Parts
Yield Strength (Mpa)
Apparent Young's Modulus (Gpa)
1400
1350
1300
1250
1200
1150
1100
80
70
60
50
40
30
20
20 40 60 80 20 40 60 80 20 40 60 80 20 40 60 80
905 905 905 905 925 925 925 925 940 940 940 940 960 960 960 960
Solution Temperature and Time

(a)

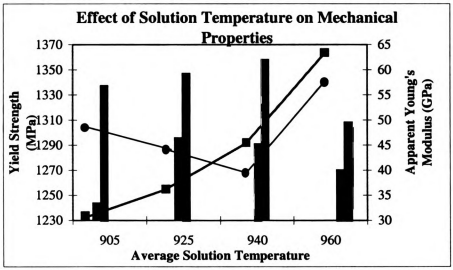
Effect of Solution Temperature on Mechanical Properties
Yield Strength (MPa)
Apparent Young's Modulus (GPa)
1370
1350
1330
1310
1290
1270
1250
1230
65
60
55
50
45
40
35
30
905 925 940 960
Average Solution Temperature

(b)

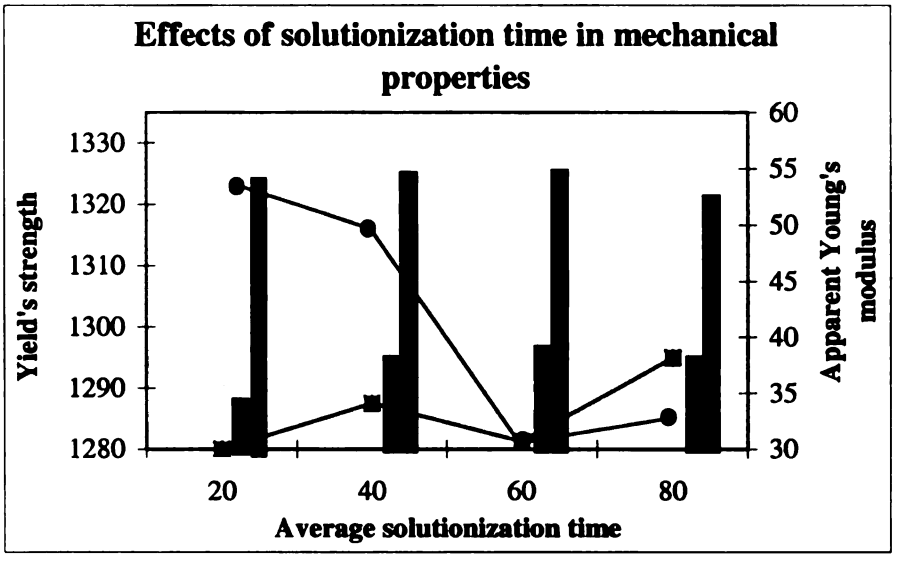

(c)

Figure 4.7 The overall (a) relationship between solutionization conditions and Young's Modulus and yield stress in the radial and wire directions, the (b) effects of solutionization temperature and (c) time on the mechanical properties using statistical analysis. The black line indicates the yield strength along radial directions and gray line indicates the yield strength along wire directions. The black column indicates the Young's modulus strength along wire directions and gray line indicates the Young's modulus along radial directions.

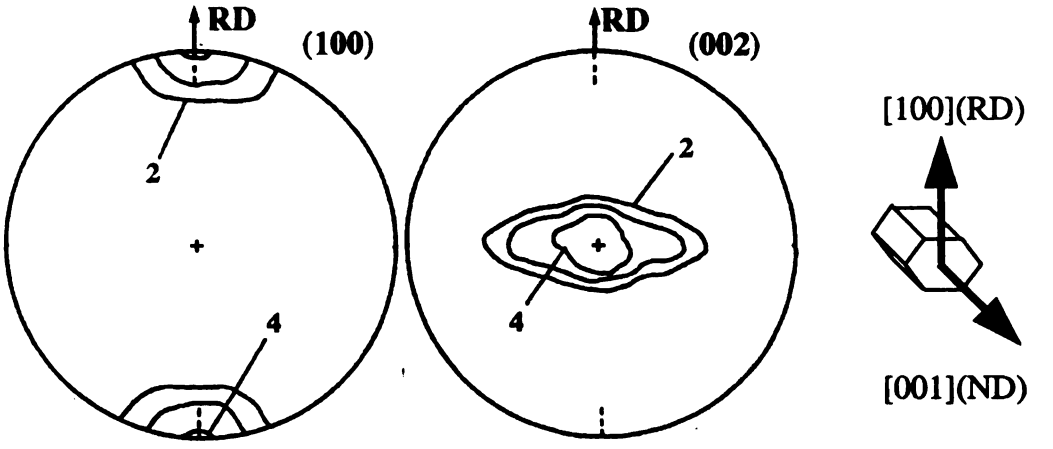

(a) Initial single α phase orientation prior to solutionization

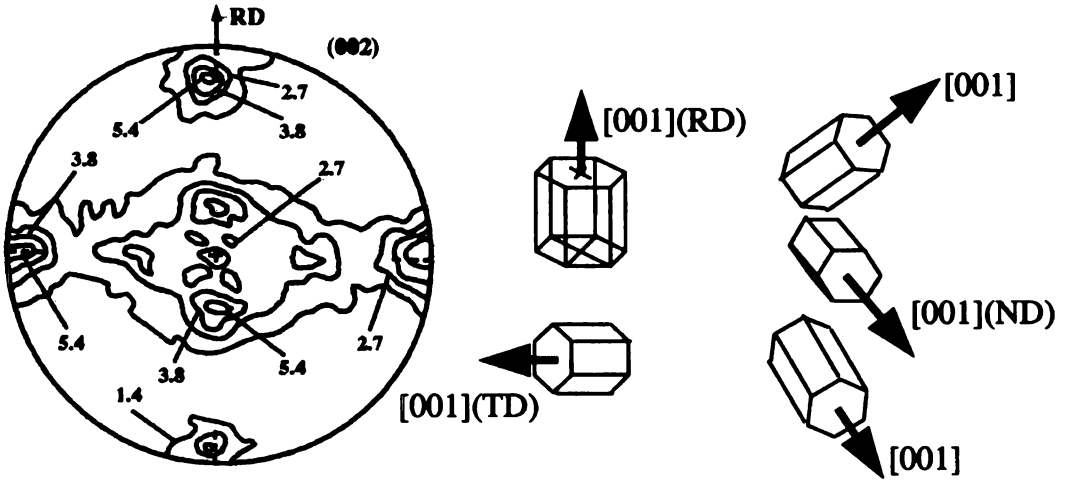

(b) Final α phase orientations after solutionization and quenching

Figure 4.8 Pole figures and schematic crystal orientations representations of the Ti-6Al-4V plates showing that one single α phase variant can generate three or four α phase variants after ST or α↔β transformation cycles in the α+β phase field, including two perpendicular variants both have 90° mis-orientations from prior orientations, and one variant having 30° mis-orientations from prior orientation in the RD plane [After Moustahfid 1997].

Chapter V

Variant selections during $\alpha \leftrightarrow \beta$ transformations in Ti-6Al-4V

Overview

The effects of low temperature annealing and different deformation directions on crystallographic texture evolution after solutionization and quenching of the α phase in Ti-6Al-4V wire specimens with $<10\bar{1}0>$ axisymetric texture were investigated using X-ray diffraction techniques. As-received specimens were either annealed or compressed 5% along the wire or radial directions. The specimens were solutionized in a sealed quartz tube, followed by water quenching. Texture analysis reveals residual β phase and 90° α phase mis-orientations from the prior as–received texture that are lowest for annealed specimens, and highest for specimens deformed along radial directions. Variant selection criteria, based on dislocation transformations between $\alpha \leftrightarrow \beta$ phases, and dislocation reactions related to α/β phase boundary transformation dislocations, are discussed in detail. Apparently, the dislocations generated by room temperature deformation are fairly stable during heating prior to the $\alpha \rightarrow \beta$ phase transformation, resulting in dislocation assisted high temperature β phase variant selections. Thus, dislocations in the α or β phase could still exist in β or α phase, respectively, after the $\alpha \leftrightarrow \beta$ transformation based on the fact that the α and β phase boundaries are coherent. In addition, the dislocation reactions and residual stress in the β phase lead to preferred concentration of dislocations on certain $(110)_\beta$ planes that cause preferred variant selection

that depends on details of initial dislocation population and recovery and recrystallization in the β phase during solutionization.

5.1 Introduction

The study in chapter IV indicates that of 90° mis-orientations from the prior texture are due to a common texture rotation related to intrinsic dislocations. The Burgers vector of the $<111>_\beta \| <11\bar{2}0>_\alpha$ dislocations that promote nucleation of α phase in β grains should be on planes of maximum shear. Due to the anisotropic thermal expansion of the α phase, it is expected that specific $\{110\}_\beta$ planes of high temperature β phase parallel and perpendicular to radial planes could have a significant amount of dislocations present that facilitates formation of α phase orientations with the c-axis parallel to the wire axis or radial directions that are observed experimentally. However, the detailed underlying transformation texture mechanisms, especially the effect of either prior or thermal expansion induced dislocations on variant selections remains unanswered. Thus, the purpose of this chapter is to assess the role of dislocations on the α/β texture transformation mechanisms in Ti-6Al-4V wire during solutionization and quenching.

To accomplish this goal, two sets of experiments were performed. First, as-received wire and annealed wire (525°C 6 hrs, furnace cooled) were subsequently solutionized for either 1 or 40 minutes and quenched to evaluate the effects of prior annealing and solutionization time on transformation texture changes. Secondly, a different set of as-received Ti-6Al-4V wire specimens were deformed in different directions, resulting in operation of different deformation modes, to determine if this would cause different variant selections after solutionization and quenching.

Compression in the wire direction would activate mainly prism slip, since the dominant orientation has the c-axes nearly perpendicular to the compression direction, and since prism slip has the lowest CRSS [Jones 1981]. Compression in the radial direction would cause a variety of slip responses; some grains would have the c-axis nearly aligned with the compression direction, resulting in very little strain due to it being an orientation where only <c+a> slip can be activated; some grains would be favorably oriented for only prism slip, where the c-axis is nearly perpendicular to the compression axis, while grains with orientations in between would be favorably oriented for a mixture of basal and prism slip. The texture measurements were made on the exact same specimen surfaces after each processing condition to eliminate the effects of intrinsic texture variation. Therefore, the objective of these experiments is to investigate the effects of dislocations on the transformation texture and how they are correlated with:

- Deformation mode
- Dislocation reactions
- Variant selections of $\alpha \rightarrow \beta$ and $\beta \rightarrow \alpha$ transformation texture
- Development of high temperature β phase
- $\alpha \leftrightarrow \beta$ phase transformation mechanism.

5.2 Experiment results

5.2.1 Texture of as-received and annealed specimens

As in Chapters III and IV, solutionization and quenching caused two α phase fiber texture components, one newly emerged fiber texture with the crystal basal plane $(0001)_\alpha$ normal aligned with the wire axis and the as-received fiber texture with the $(10\bar{1}0)_\alpha$ normal along wire axis (Figure 5.1(b)). The length of solutionization time had a much

larger effect than annealing, where the new orientation had about twice the intensity with 40 minutes as at 1 minute at the solutionization temperature. This shows that even 1 minute is enough time to establish a significant amount of the new orientation, but that a longer time causes more of the β phase transformation, recovery, and/or recrystallization. The effect of annealing was less dramatic, but the intensity of the new $(0001)_\alpha$ orientation in the annealed + solutionized specimens was 70-80% of the as-received specimens (Figure 5.1(a)). Clearly, annealing must have decreased point defects and dislocation densities to cause a lesser amount of the new component, since annealing at 525°C should not change the microstructure and texture significantly.

5.2.2 Texture of solutionized specimens after deformation

Figure 5.2 shows that 5% compression deformation in the radial direction caused much more of the new 90° rotated texture component than deformation in the longitudinal direction, after solutionization for 40 minutes at 920°C and quench in a sealed quartz tube. Compression alone along the longitudinal wire direction (L def) strengthened the $(0001)_\alpha$ fiber texture component along the wire axis by a factor of 5, but weakened the other main components, but solutionization and quench increased the initial deformation texture component back to 80-90% of their undeformed values. The new component was 10 times stronger (2.5 x random), and the retained β peak was 50% stronger (5.5 x random). The specimens deformed in the radial direction followed by solutionization and quenching showed a slightly larger reduction in the initial deformation texture components, and a 46 times stronger new component (13.4 x random), and a 3.7 times stronger retained β peak (9.2 x random). The crystal orientation intensities of $(0001)_\alpha$ and $(110)_\beta$ fiber texture components aligned along wire axis were

5.3 and 1.7 times higher than the corresponding texture intensities of specimens deformed along the wire axis and heat treated under the exact same conditions.

5.3 Discussion

The present study investigated the effects of dislocation defects on crystallographic texture evolution. Therefore, it is of interest to investigate the texture development in relation to previous Ti-6Al-4V alloys studies, physical metallurgy principles related to deformation modes, dislocation theories, and phase transformations.

5.3.1 Effects of Dislocations

The difference in 90° mis-orientations between annealed and as-received specimens followed by solutionization and quenching (Figure 5.1) indicates that defects, especially dislocations, affect the variant selections, assuming the same initially low density of $(0001)_\alpha$ orientations were aligned with the wire axis prior to heat treatment. The difference in texture development after heat treatment was most likely due to the difference in deformation defect structures along radial and wire directions (Figure 5.2). It is assumed that deformation in the as received wire caused microstructural changes such as residual stress, point defects and dislocations. More importantly, different deformation directions led to different residual stress and dislocation orientation/arrangement that could assist or hinder the subsequent transformation texture. A few conclusions about the effects of dislocations on the development of 90° texture mis-orientations can be identified as follows:

(1) The dislocations were kept without annihilation during the $\alpha \rightarrow \beta$ phase transformation and the subsequent grain/phase growth (described in Chapter IV). If this were not the case, the high temperature β phase and α phase $(0001)_\alpha$ texture along wire

axis would be the same, independent of deformation orientations. Also, annealing and solutionization time would not have had an effect on transformation textures. Although the $\alpha \rightarrow \beta$ transformation and grain growth were accomplished through movement of pre-existing grain boundaries [Ivasishin 1999], the pre-existing dislocations inherited from room temperature could also be kept through the transformation and at least part of the solutionization process, or they would react with the moving phase boundary to form new dislocations even after other grain or phase boundaries swept across the grain.

(2) The dislocations are fairly stable even at high temperatures, as shown by the effect of solutionization time in figure 5.1. The movements of dislocations are fairly slow even at high solutionization temperatures, resulting in stable dislocation arrangements and the subsequent dislocation assisted variant selections [Ivasishin 1999].

5.3.2 Deformation modes in β phase

It is expected that the deformation systems in β along the wire and radial directions are the same as other bcc metals, i.e. {110}, {112}, and {123} slip planes with <111> slip directions [Barrett 1966]. The diffraction studies of the initial β phase in as-received specimens, shown in Chapter III, revealed diffuse streaking that was different from ω phase reflections, in addition to sharp β reflections, suggesting <111> slip rather than twinning in β was the dominant deformation mode [Hanada 1986, 1987]. Therefore, in the current study the <111> dislocations in the β phase help accommodate compression along wire and radial directions.

5.3.3 $\alpha \rightarrow \beta$ transformation and dislocation-interface interactions

The cold deformation-induced dislocations could affect the development of high temperature β phase and the subsequent α transformed texture. The $\alpha \rightarrow \beta$ transformation

and grain growth were accomplished by α/β boundary movement. Thus, it is expected that the existing dislocations in primary α and β phases could affect the α/β boundary movement, and thus affect texture development. This assumption is further supported by the titanium α↔β transformation theory of Ivasishin [1999]. The lattice reconstruction stress of the α↔β transformation is close to a simple shear of low values that would not cause recrystallization in the transformed high temperature β phase, especially with initially low dislocation densities. Thus, the required transformation stresses are too low to destroy the orientation relationship between α and β phases, in contrast to the fcc → bcc transformation in steel, where the reconstruction stresses are too high to maintain the orientation relationship. In addition, the α phase is more resistant to relaxation and recrystallization due to the lower symmetry of the hexagonal α phase [Ivasishin 1999]. Therefore, it is possible that room temperature deformation induced dislocations could be kept or partially kept through the transformation, and that it may be easier for the α phase dislocations to be transferred to β than from β to α phase. Also, since diffusion is much faster in the β phase, climb/recovery reactions are likely to be faster in the β phase.

Furthermore, Priester [2001] stated that matrix dislocations could be directly transferred from one phase to the neighboring phase without annihilation at the phase boundary. This direct dislocation transfer across the phase boundary requires that the traces of slip planes from each side of the grain boundary are parallel at the grain boundary plane. Thus, if the Burgers vectors of the incoming and outgoing dislocations are parallel ($b_{in}=b_{out}$), no residual dislocation is left at the grain boundary. Otherwise, a residual dislocation is left with $b_{in}=b_{out}+b_{residual}$. Also, in-situ TEM studies on stainless steel, titanium and Ni_3Al alloys performed by Lee et al. [1990] indicated that direct

dislocation transfer requires (1) the angle between the slip plane traces in the grain boundary plane should be as small as possible, (2) minimum residual dislocation products are left at the phase boundary, and (3) the resolved shear stress on the outgoing dislocation must be high. However, the stress state near the α/β phase boundary is unknown.

Thus if we neglect the stress requirements, the basal $\vec{a}$ dislocations in figure 5.5 in the primary α phase are most likely to transform to the 1/2<111> type dislocations in a horizontal $(110)_\beta$ plane in the β phase upon the $\alpha \rightarrow \beta$ transformation. This transformation will accomplish 1.38% strain in <111> directions on the $(110)_\beta$ plane. In the specimen deformed radially, many grains oriented favorably for basal slip will transform that are full of basal plane dislocations, while only a few grains with only *c+a* dislocations will transform, although the *c+a* dislocations will not survive the transformation. Only half of the prism dislocations are likely to survive the transformation, since only one of the prism planes will be parallel to a $<112>_\beta$ plane (see Figure 1.2). The third $(10\bar{1}0)_\alpha \| (\bar{1}10)_\beta$ prism plane had very low resolved shear stress and no likely dislocation activity, and even if there were some dislocations, the burgers vector would be the less mobile $<001>_\beta$, but they would be less likely to survive since the two planes are not parallel. The grains with predominantly *c+a* and prism dislocations will have a lower density of surviving dislocations in the β phase than the grains with basal dislocations. The grains with lower dislocation density will thus have a growth advantage and may consume the grains having the inherited basal dislocations by a primary recrystallization process.

In the current study, $\alpha \rightarrow \beta$ transformation after compression along the wire direction (approximately normal to the page in figure 5.5 for example) could generate $1/2(1\bar{1}2)_\beta[1\bar{1}\bar{1}]$ type dislocations. Although $\vec{a}$ screw dislocations could cross slip onto $(101)_\beta$, $(\bar{1}01)_\beta$ planes via $\alpha \rightarrow \beta$ transformation, it is not expected that edge dislocations could directly transfer from the prism plane of the α phase onto $(101)_\beta$, $(\bar{1}01)_\beta$ planes. On the other hand, transformation after compression along radial directions would generate wide variety of dislocations, such as $1/2[\bar{1}11]$ or $1/2[1\bar{1}\bar{1}]$ type dislocations on the $(110)_\beta$ planes that correlate with basal $(0001)_\alpha$ planes, and $(1\bar{1}2)_\beta 1/2[1\bar{1}\bar{1}]$. Thus, different dislocations evolved after the high temperature $\alpha \rightarrow \beta$ transformation, which could further affect the subsequent grain growth. Since the kinetics of grain growth depends on the chemistry of high temperature phases [Ivasishin 1999] and the diffusion of Ti, Al and V [Grewl 1989, 1990], the development of high temperature β phase texture by grain growth could be enhanced depending upon the arrangements of dislocations.

5.3.4 Slip activity and dislocation reaction mechanism

Dislocation reactions in the β phase could also determine the subsequent α transformed texture. In ferrous alloys, the dislocation model criteria for variant selection during the austenite to martensite transformation can be summerized as: (1) variant selection according to slip activity on appropriate corresponding active slip system, and (2) dislocation reaction, which corresponds to certain variants related to dislocations with inactive Burgers vectors or a Burgers vector on a plane that has no slip activity at all [Wittridge 2001, Butron-Guillen 1996, 1998, Sum 1999]. However, no experimental

work proves that dislocations are actually present at the austenite/martensite interface and thus plays the roles proposed above [Wittridge 2001]. However, in bcc alloys, although a 1/2[111] dislocation spreads into three 1/6 [111] cores, these partial dislocations do not bound a stable stacking fault, unlike Shockley partial dislocations in fcc alloys [Hull 1986]. Thus, the available dislocation dissociations in bcc β phase are very limited.

Therefore, the dislocation and interface reactions after radial compression (compression along any line roughly in the plane of the page in figure 5.5) and heat treatment could result in the formation of $1/2(110)_\beta[\bar{1}\,1\,\bar{1}]$, $1/2(110)_\beta[1\,\bar{1}\,\bar{1}]$, $1/2(1\,\bar{1}\,2)_\beta[1\,\bar{1}\,\bar{1}]$ or $1/2(1\,\bar{1}\,\bar{2})_\beta[1\,\bar{1}\,1]$ dislocations, while compression in the axial direction (out of page in Figure 5.5) would not provide dislocations on $(110)_\beta$ planes. None of these dislocations could assist transformation leading to the 90° mis-orientation from prior as-received texture, since this would require that mobile dislocations are present on $(\bar{1}\,10)$ planes. The $1/2(110)_\beta[1\,\bar{1}\,\bar{1}]$ and $1/2(110)_\beta[1\,\bar{1}\,\bar{1}]$ dislocations could only lead to the formation of the original as-received fiber texture. In addition, the $\beta\rightarrow\alpha$ transformation could occur with shear movements of atoms on the $(1\,\bar{1}\,2)_\beta$ plane with $[1\,\bar{1}\,\bar{1}]$ direction (Figure 1.7), resulting in as-received fiber texture ($(1\,\bar{1}\,2)_\beta$ is perpendicular to $(110)_\beta$ plane) [Gey 1997]. Thus, the system with the most slip activity would not be associated with the newly formed α variants in the current study.

However, the perfect dislocation reactions in common bcc metals, such as the β phase can have the following types [Zhi]:

$$(1)\ \frac{a}{2}<111>+\frac{a}{2}<\bar{1}\bar{1}1>\longrightarrow a<001>$$

(2) $\frac{a}{2}<111>+\frac{a}{2}<11\bar{1}>\longrightarrow a<110>$

(3) $a<110>+a<010>\longrightarrow a<110>$

(4) $\frac{a}{2}<110>+\frac{a}{2}<1\bar{1}0>\longrightarrow a<110>$

(5) $\frac{a}{2}<0\bar{1}1>+\frac{a}{2}<10\bar{1}>\longrightarrow a<1\bar{1}0>$

(6) $\frac{a}{2}<110>+\frac{a}{2}<00\bar{1}>\longrightarrow a<11\bar{1}>$

All of the dislocation reactions listed above can occur theoretically in either co-planner or a non-coplanar manner [Zhi 1992], suggesting the same type of dislocation reactions could occur in wide varieties of different combinations of planes (Figure 5.6). Zhi [1992] calculated 864 combinations of planes for just the first type of dislocation reactions. For example, the following type of dislocation Burgers reaction could occur in any of the correlated planes listed beneath the Burgers reaction (Figure 5.6):

$$\frac{a}{2}[111]+\frac{a}{2}[\bar{1}\bar{1}1]\longrightarrow a[001]$$

$(\bar{1}01)$	(101)	(100)
$(0\bar{1}1)$	(011)	(010)
$(1\bar{1}0)$	$(1\bar{1}0)$	$(1\bar{1}0)$
$(2\bar{1}\bar{1})$	$(2\bar{1}0)$	(110)

It is possible that multiple dislocation reactions under residual stress or $\alpha\leftrightarrow\beta$ transformation stress could lead to appreciable dislocation concentration on $(\bar{1}10)_\beta$ planes that are necessary to stimulate a dislocation generated 90° mis-orientation from prior as-received texture. The necessary dislocations have to be $1/2(11\bar{2})_\beta[111]$, $1/2(\bar{1}10)_\beta[111]$, or $1/2(\bar{1}10)_\beta[11\bar{1}]$, which were different from the dislocations expected from the prior

deformation; $1/2(1\bar{1}2)_\beta[\bar{1}\bar{1}1]$, $1/2(110)_\beta[\bar{1}1\bar{1}]$ or $1/2(110)_\beta[1\bar{1}\bar{1}]$. However, it is possible that the $1/2(110)_\beta[\bar{1}1\bar{1}]$, $1/2(110)_\beta[1\bar{1}\bar{1}]$, and $1/2(1\bar{1}2)_\beta[1\bar{1}\bar{1}]$ dislocations could cross slip or move onto $1/2(11\bar{2})_\beta[111]$ and $1/2(11\bar{2})_\beta[111]$ planes via dislocation reactions under residual stress or $\alpha\leftrightarrow\beta$ transformation stress. As mentioned in chapter III, the $\alpha\leftrightarrow\beta$ transformation could result in volume contraction by as much as 0.55~2.6%. The transformation stress could be roughly estimated by the equation

$$\sigma = \frac{E}{3(1-2\nu)} * \frac{\Delta V}{V_0}$$ [Barsoum 1997],

where E denotes Young's modulus (100GPa for Ti-6Al-4V), ν denotes Poisson's ratio (0.26~0.36), $\Delta V/V_0$ volumetric change in materials.

Thus, the residual stress in titanium alloys is on the order of 0.03~3.1 GPa, which potentially could push dislocations onto certain planes. In addition, the thermal expansion differences between α and β phases could generate strain on the level of ~0.15 % upon heating and cooling process. Furthermore, $1/2(110)_\beta[\bar{1}1\bar{1}]$ or $1/2(110)_\beta[1\bar{1}\bar{1}]$ dislocations resulting from basal slip could easily survive through the solutionization; while prism slip less is likely to survive the transformation. Therefore, the dislocations in β phase after wire axis deformation and followed by heat treatment could assist transformation to the same α phase orientation as the original fiber orientations.

Even though the $(\bar{1}10)_\beta$ plane is properly oriented to facilitate the observed 90° transformation based upon $1/2[11\bar{1}]$ or $1/2[111]$ dislocations, there appears to be a relatively low probability of developing such dislocations on this plane via dislocation

reactions. Instead, an epitaxial retransformation appears to be favored using the existing dislocations. However, the fact that the 90° mis-orientation occurred implies that (1) $1/2[11\bar{1}]$ or $1/2[111]$ dislocations somehow got onto the $(\bar{1}10)_\beta$, and that even fewer dislocations existed on the $(110)_\beta$ plane that favored the epitaxial reverse transformation, or (2) variant selection was associated with the planes having the least slip and dislocation density that is opposite of the currently accepted theory. However, two other possibilities to consider are (1) a recovery/recrystallization process that removes dislocations from the grains with high dislocation density, which is required to reduce the epitaxial retransformation possibility, and (2) dislocations may have been generated on $(\bar{1}10)_\beta$ planes during the heating and cooling process due to thermal stresses.

Primary recrystallization occurs by motion of grain boundaries through grains having a high dislocation density, from grains with a preferred nucleation orientation or grains with a preferred boundary mobility. If an existing minority orientation that was not oriented for easy slip existed, then there is little expectation that a highly preferred recrystallized orientation would result, per the observation. In contrast, an existing orientation that had a low dislocation density could have a growth advantage into grains with a high transformed dislocation density, e.g. grains with primary prism slip would have fewer dislocations than grains with primary basal slip dislocations. Such grains would have a misorientation of about 45° about $(100)_\beta$ axis, and growth of these β orientations would still result in $(110)_\beta$ type planes rotated about the wire axis. Given this possibility, this still requires that remaining dislocations on {112} planes would have to cross slip onto $(\bar{1}10)_\beta$ planes, but the burgers vector would still be out of the $(\bar{1}10)_\beta$

plane. Thus recrystallization seems unlikely to provide a basis for dislocation-assisted transformation using mobile dislocations on $(\bar{1}10)_\beta$ planes. However, recrystallization does cause disappearance of dislocations that would favor epitaxial retransformation.

Next we consider the effect of thermal expansion and contraction stresses during heating and cooling that could generate dislocations on $(\bar{1}10)_\beta$ planes. Since thermal contraction is greatest along the c axis, this provides a basis for generation of shears on $(\bar{1}10)_\beta$ planes shown in figure 5.7. Shears on the $(\bar{1}10)_\beta$ planes can be envisioned in β grains between α grains aligned along the wire axis with different c-axis orientations, but not within β grains between α grains along the radial direction. The resulting stress and deformation could be substantial due to small amount of prior β phase upon heating (Figure 5.7(a)). Thus the generation of dislocations could be kept without annihilation during the subsequent grain growth. In addition, similar stress and dislocations could be generated upon cooling in the β phase (Figure 5.7(b)). Therefore, the generation of dislocations that cause preferred variant selection may occur upon heating and cooling rather then during the β phase solutionization part of the process. This would imply that some of the β transforms epitaxially in some regions, but transforms by 90° in others. However, further investigations including analytical instruments and finite element analysis are needed to characterize the distribution and magnitude of thermal stresses upon cooling.

Therefore, as pointed out in Chapter IV, the lattice similarities of a specific plane of prior phase with a certain dislocation arrangement with a correlating plane of the subsequent phase determines the latter transformation variants. Thus, local

concentrations of reacted or freshly generated dislocations on the $(\bar{1}10)_\beta$ plane (parallel to the radial plane) determined the new transformation variants since the $\beta \rightarrow \alpha$ transformation starts from the β/α grain boundaries and high dislocation density sites inside the β grains.

5.4 Conclusion

The present study systematically investigated the effects of deformation direction and dislocations on crystallographic texture evolution of α phase in Ti-6Al-4V using X-ray diffraction techniques. Deformation along different orientations resulted in different dislocation types, leading to different texture development after the $\alpha \rightarrow \beta \rightarrow \alpha$ transformation cycle. Texture analysis revealed 90° mis-orientations from the prior texture that were consistently higher for specimens deformed along radial directions, than specimens deformed along wire directions, respectively, followed by the same solutionization and quenching. The required low stress for lattice reconstruction of $\alpha \rightarrow \beta$ transformation suggests that the α and β phases are reluctant to recrystallize, leading to high dislocation stabilities. The variant selection mechanisms based on dislocation reactions and thermal residual stresses during cooling were discussed to show that generation of dislocations that facilitate the 90° misorientation observed are not easily envisioned.

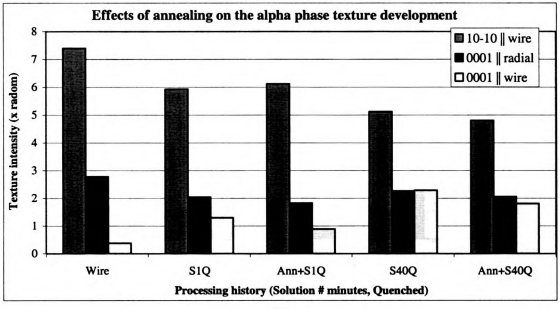

(a)

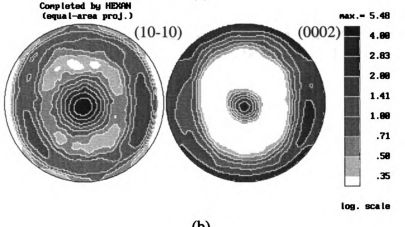

(b)

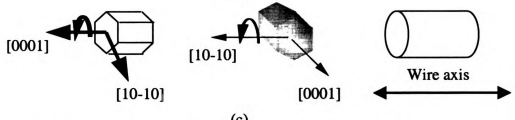

(c)

Figure 5.1(a) reveals the overall relationships between major texture intensities and the experiment conditions, (b) the experimental $(10\bar{1}0)_{\alpha}$, $(0002)_{\alpha}$, and $(\bar{1}10)_{\beta}$ pole figures with wire axis out of the page for specimen S40Q after solutionization without prior annealing, and (c) the schematic α crystal orientations. The levels of 90° mis-orientations from prior texture were consistently lower in the prior annealed and followed by solutionization and quenching specimens than that of the as received one without annealing, indicating the effects of defects on texture development.

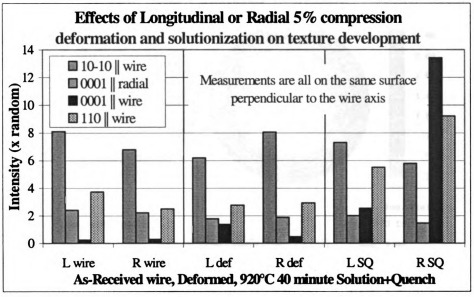

Figure 5.2 reveals the overall relationships between major texture intensities and the experiment processing conditions after solutionization for 40 minutes at 920°C. Different deformation directions, followed by the same heat treatment resulted in different texture development.

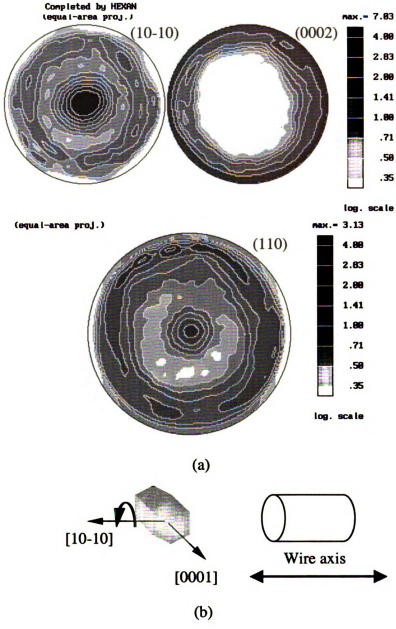

Figure 5.3 showing (a) the $(10\bar{1}0)_\alpha$, $(0002)_\alpha$, and $(110)_\beta$ pole figures of as–received wire with wire axis out of the page, and the (b) schematic α crystal orientations. The α phase consisted of one fiber texture with $(0002)_\alpha$ plane normal along radial directions. The β phase consisted of a fiber texture with the axisymmetric $(110)_\beta$ crystal orientations about the wire axis, and a few of rotated or tilted $(110)_\beta$ fiber texture aligned approximately 30° from the wire axis.

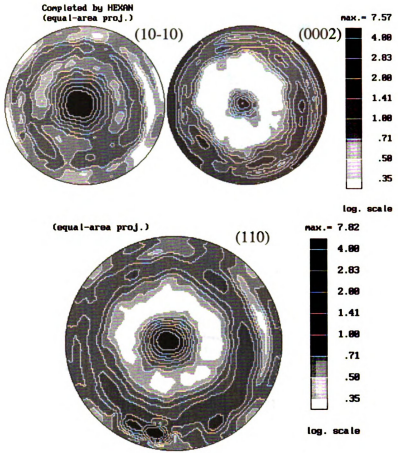
Completed by HEXAN
(equal-area proj.)
(10-10)
(0002)
max.= 7.57
4.00
2.83
2.00
1.41
1.00
.71
.50
.35
log. scale
(equal-area proj.)
(110)
max.= 7.82
4.00
2.83
2.00
1.41
1.00
.71
.50
.35
log. scale

(a)

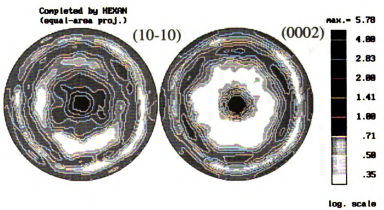
Completed by HEXAN
(equal-area proj.)
(10-10)
(0002)
max.= 5.70
4.00
2.83
2.00
1.41
1.00
.71
.50
.35
log. scale

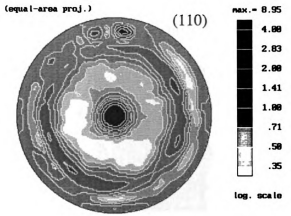

(b)

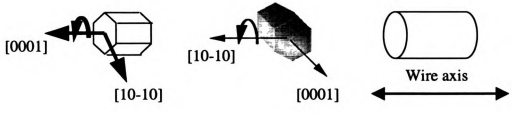

(C)

Figure 5.4 showing the $(10\bar{1}0)_{\alpha}$, $(0002)_{\alpha}$, and $(110)_{\beta}$ pole figures with wire axis out of the page of heat-treated specimens (a) L heat and (b) T heat after solutionization for 40 minutes at 920°C, followed by quenching in sealed quartz tube, and (c) the schematic α crystal orientations for both cases. Note, the crystal orientation of $(0001)_{\alpha}$ and $(110)_{\beta}$ plane normal along wire axis of T heat (deformed along transverse direction and heat treated) is 13.42 and 9.21 X random, respectively, which is 5.3 and 1.7 times higher than the corresponding textures of specimens L heat deformed along longitude direction and heat treated under the exact same conditions.

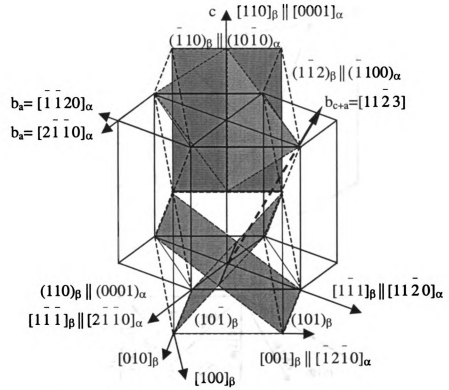

Figure 5.5 showing dislocations mutations based on the geometric and Burgers relationship between α and β phases. Compression along the wire axis is roughly out of the page. Compression in radial directions imposes compressive stresses in directions roughly in the plane of the page. Neither would activate much prism slip on $(10\bar{1}0)_\alpha$ planes. The prism $\vec{a}$ dislocations transform into $[1\bar{1}1](11\bar{2})_\beta$ dislocations, but they cannot mutate onto $(110)_\beta$ planes after $\alpha \rightarrow \beta$ transformation. However, either basal or prismatic $\vec{a}$ screw dislocations could cross slip onto the two inclined $(101)_\beta$, $(\bar{1}01)_\beta$ planes after $\alpha \rightarrow \beta$ transformation. The $\vec{c}+\vec{a}$ dislocations could be directly transferred onto β phase $(101)_\beta$, $(\bar{1}01)_\beta$ planes, but would have a large irrational Burgers vector.

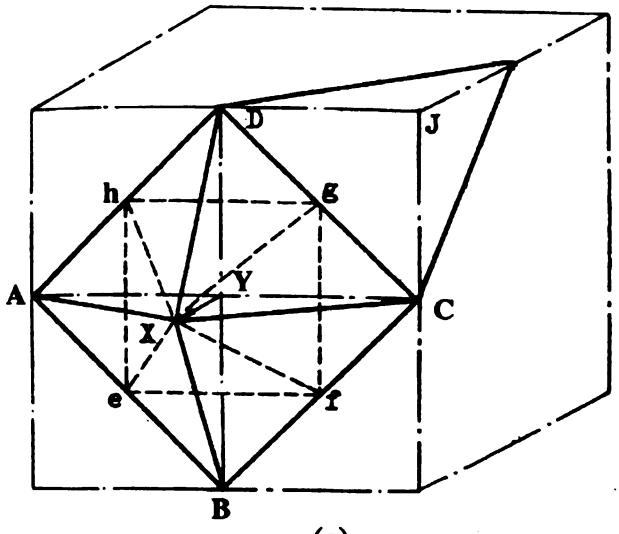

(a)

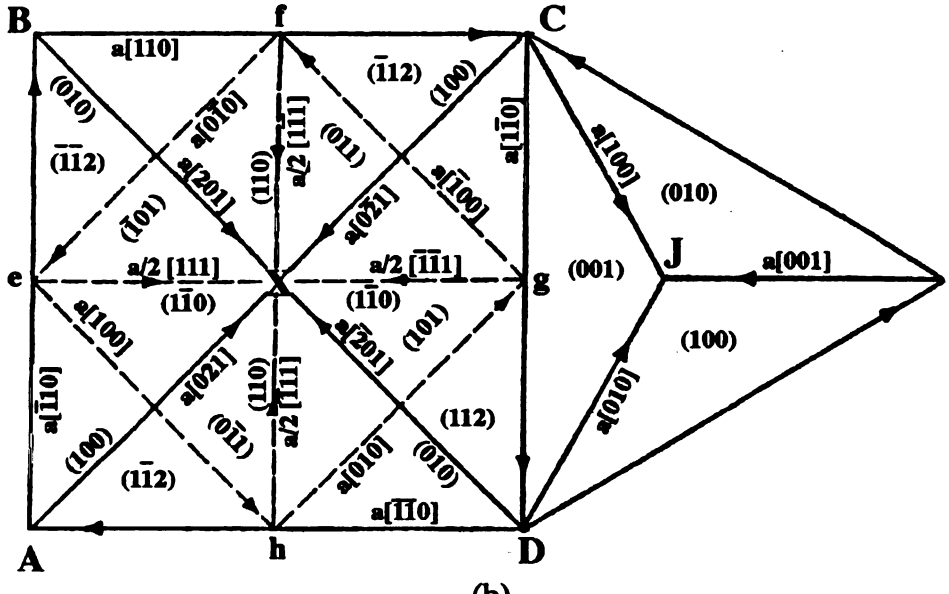

(b)

Figure 5.6 shows the spatial construction of <100>, <110>, and <111> directions and {100}, {110}, and {112} planes in bcc metal, and (b) planer representation for projections of the ABCDX pyramids [After Zhi 1992]. In the ABCDX pyramids, sides of hexahedron represents {100} planes, sides of the dashed line pyramids represents {110} planes, and sides of the solids line pyramids represents {112} planes.

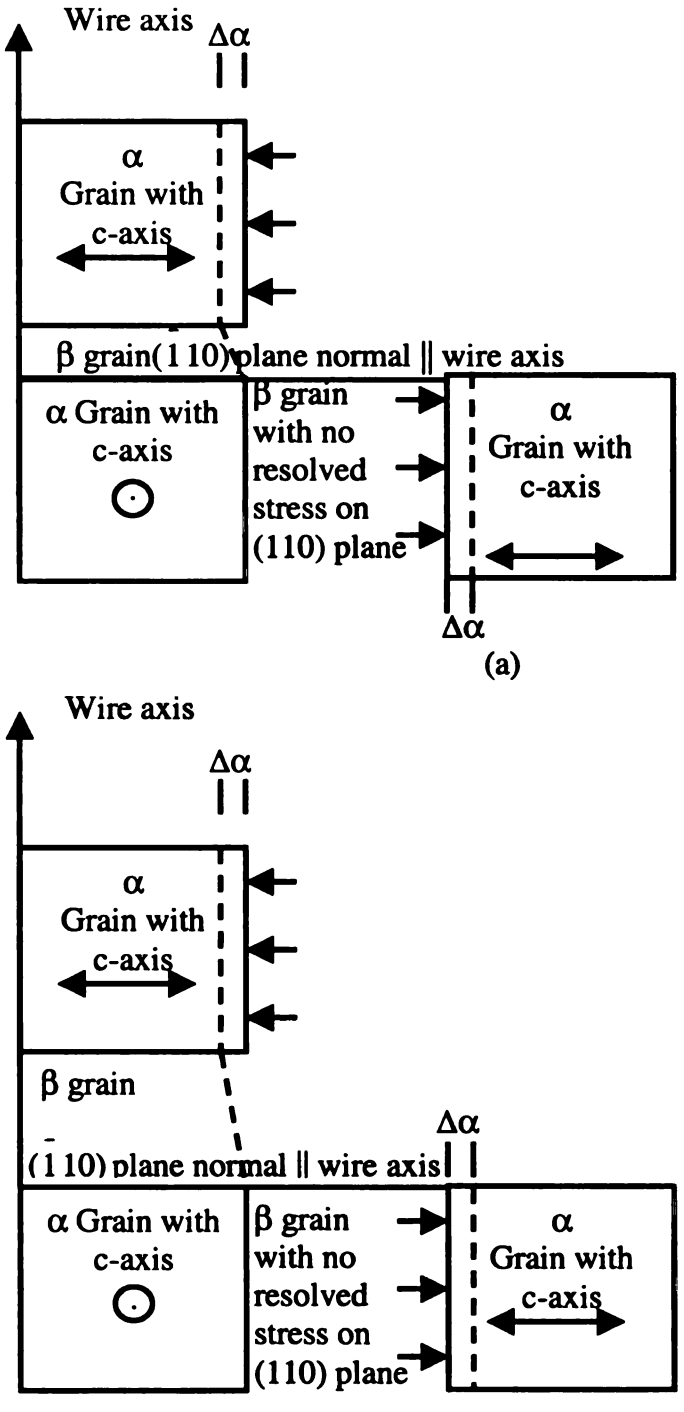

Figure 5.7 Schematic descriptions of effect of differential thermal expansion and contraction of primary α grains (shaded boxes) on state of shear in β grains during (a) heating and (b) cooling process.

References

Akhtar, A., *Metallurgical Transactions*, 6A(1975) 1105.

Anderson, S., *Acta Chem. Scand.*, 11(1957) 1641.

Babel, H.W., Frederick, S.F., *JOM*, October 20 (1968) 32.

Barrett, C.S., Massalski, T.B., *Structure of Metals*, 3rd Ed., McGraw, N.Y. 1966.

Barsoum, M.W., *Fundamentals of ceramics*, New York, McGraw Hill, 1997. p. 502.

Bieler, T.R., Semiatin, S.L., J.J. Jonas symposium, COM 2000, proceeding, CIM, Montreal, 2000, pp. 253-64.

Boswell, E., Strangwood, M., Pate, P.S., *Titanium'95 Science and Technology*, 1995, p. 2446.

Boyer, R.R., *Titanium'95 Science and Technology*, 1995, p. 41.

Boyer-A, R., Welsch, G., Colling, E.W., *Materials Properties Handbook: Titanium Alloys*, ASM International, Materials Park, OH, 1994, p. 483-491.

Boyer-B, R., Welsch, G., Colling, E.W., *Materials Properties Handbook: Titanium Alloys*, ASM International, Materials Park, OH, 1994, p. 1053-1054.

Boyer-C, R., Welsch, G., Colling, E.W., *Materials Properties Handbook: Titanium Alloys*, ASM International, Materials Park, OH, 1994, p. 1113.

Boyer-D, R., Welsch, G., Colling, E.W., *Materials Properties Handbook: Titanium Alloys*, ASM International, Materials Park, OH, 1994, p. 611-612.

Boyer-E, R., Welsch, G., Colling, E.W., *Materials Properties Handbook: Titanium Alloys*, ASM International, Materials Park, OH, 1994, p. 606-607.

Boyer-F, R., Welsch, G., Colling, E.W., *Materials Properties Handbook: Titanium Alloys*, ASM International, Materials Park, OH, 1994, p. 263.

Boyer-G, R., Welsch, G., Colling, E.W., *Materials Properties Handbook: Titanium Alloys*, ASM International, Materials Park, OH, 1994, p. 599.

Boyer-H, R., Welsch, G., Colling, E.W., *Materials Properties Handbook: Titanium Alloys*, ASM International, Materials Park, OH, 1994, p. 62-63.

Boyer-I, R., Welsch, G., Colling, E.W., *Materials Properties Handbook: Titanium Alloys*, ASM International, Materials Park, OH, 1994, pp. 56.

Boyer-J, R., Welsch, G., Colling, E.W., *Materials Properties Handbook: Titanium Alloys*, ASM International, Materials Park, OH, 1994, pp. 516.

Burgers, W.G., *Physica*, 1(1934)561.

Butron-Guillen, M.P., Da Costa, Viana, C.S., Jonas, J.J., in Z.D. Liang, L. Zuo. Y.Y. Chu (Eds.), *Proceeding of the Eleventh International Conference on Texture of Materials*, ICOTOM-11, Xian, China, Sept. 16-20, 1996, International Academic Publishers, 137 Chaonei Dajie, Beijing 100010, China.

Butron-Guillen, M.P., Da Costa, Viana, C.S., Jonas, J.J., *Materials Science Forum*, 273-275 (1998) 151.

Cahn, J.W., *Acta Metall.*, 5(1953) 169.

Cahn, R.W., Haasen, P., *Physical Metallurgy*, Fourth Edition, Elsevier Science B.V., North-Holland, 1996, pp. 1531.

Chesnutt, J.C., Rhodes, C.G., Williams, J.C., Fractography-Microscpic Cracking Processes, ASTM STP 600, p. 99, 1976.

Churchman, A.T., *Proc. Roy. Soc.*, A226(1954) 216.

Cullity, B.D., *Elements of X-ray Diffraction*, Second Edition, Addison-wesley publishing company, Inc., October, 1978, pp. 295-300.

David, D., Garcia, E.A., Beranger, G., *Titanium '80, Science and Technology*, H. Kimura and O. Izumi (Eds.), *TMS/AIME*, 1980, p. 537.

Davis, R., Flower, H.M., West, D.R.F., *Journal of Materials Science*, 14(1979) 712.

Davis, R., Flower, H.M., West, D.R.F., *Acta Metallurgica*, 27(1979) 1041.

Divinski, S.V., Dnieprenko, V.N., Ivasishin, O.M., *Materials Science and Engineering*, A243 (1998) 201.

Fan, Z., *Scripta Metallurgica et Materialia*, 31(11)(1994) 1519.

Fang, T.Y., Wang, W.H., *Materials Chemistry and Physics*, 56(1998) 35.

Fujishiro, S., Nadiv, S., "Effect of Transformation on the Texture of Titanium", *Titanium'80*, 1980, p. 899.

Furuhara, T., Maki, T., *Materials Science & Engineering A*, 312(2001) 145.

Gehlen, P.C., *The Science, Technology and Applications of Titanium*, p. 349, Pergamon Press, 1970.

Gey, N., Humbert, M., *Acta Materialia.*, 50 (2002) 277.

Gey, N., Humbert, M., Moustahfid, H., *Scripta mater.*, 42(2000)525.

Gey, N., Humbert, M., Philippe, M.J., Combres, Y., *Materials Science and Engineering*, A219 (1996) 80.

Gey, N., Humbert, M., Philippe, M.J., Combres, Y., *Materials Science and Engineering*, A230 (1997) 68.

Gil, F.G., Manero, J.M., Plannell, J.A., *Titanium'95 Science and Technology*, 1995, p. 2454.

Grewl, G., Ankem, S., *Acta Met. Mater.*,38(9)(1990) 1607.

Grewl, G., Ankem, S., *Metallurgical Transactions A*, 20A (1989) 39.

Grewl, G., Ankem, S., *Metallurgical Transactions A*, 21A (1990) 1645.

Hanada, S., Izumi, O., *Metallurgical Transactions*, 18A(1987) 265.

Hanada, S., Izumi, O., *Metallurgical Transactions*, 17A(1986) 1409.

Hu, H., Cline, R.S., *Transactions of The Metallurgical Society of AIME*, 242 (1968) 1013.

Hull, D., Bacon, D.J., *Introduction to Dislocations*, Third Edition, Pergamon press, 1986, p. 121-126.

Humbert, M., Gardiola, B., Esling, C., Flemming, G., Hensger, K.E., *Acta Materialia*, 50 (2002)1741.

Inouye, K., Iijima, Y., Hirano, K., *Titanium '80, Science and Technology*, H. Kimura and O. Izumi (Eds.), TMS/AIME, 1980, pp. 569-76.

Ivasishin, O.M., Teliovich, R.V., *Materials Science and Engineering*, A263 (1999) 142.

Jones, I.P., Hutchinson, W.B., *Acta Metallurgica.*, 29(1981)951.

Kahveci, A.I., Welsch, G.E., *Scripta Metallurgica*, 20(9)(1986)1287.

Ke, H., Ning, C., Jia, D., Zhou, Y., Song, G., *Nonferrous Metals* (China), vol. 53, no. 4, pp. 8-14, Nov. 2001.

Keeler, J.H., Geisler, A.H., *JOM*, February, 8 (1956) 80.

Koul, M.k., Breedis, J.F., *Acta Metallurgica*, 18(1970) 579.

Lasalmonie, A., Loubradou, M., *Journal of Materials Science*, 14(1979) 2589.

Lee, T.C., Robertson, I.M., Birnbaum, H.K., *Philosophical Magazine* A, 62(1) (1990) 131.

Libanati, C.M., Dyment, F., *Acta Met.*, 11(1963)1263.

Luo, C.P., Weatherly, G.C., *Acta Metall.*, 35(1987) 1963.

Maykuth, D. J., Monroe, R.E., Favor, R.J., Moon, D.P., *Titanium base alloys: 6Al-4V; processes and properties handbook*, Columbus, Ohio : Battelle Memorial Institute, Defense Metals Information Center, 1971, Chapter I: Physical metallurgy, Page, I-II.

Moustahfid, H., Gey, N., Humbert, M., Philippe, M.J., Metallurgical and Materials Transactions A, 28A (1997) 51.

Murayama, Y., Suzuki, Y., Shimura, M., *Titanium'80*, 1980, p. 965.

Murdock, J.F., Lundy, T.S., Stansbury, E.E., *Acta Met.*, 12(1964)1033.

Murdock, J.F., McHarque, C.J., *Acta Met.*, 16(1968)493.

Naka, S., *Phil Mag A*, 57(5)(1994)717.

Orr, R.D., de Bruijn, J.D., Davies, J.E., *Cells and Materials* (USA), vol. 2, no. 3, pp. 241-251, 1992.

Ouchi, C., Fukai, H., Hasegawa, K., *Materials Science and Engineering*, A263 (1999) 132.

Ouchi, K., Iijima, Y., Hirano, K., *Titanium '80, Science and Technology*, H. Kimura and O. Izumi (Eds.), TMS/AIME, 1980, pp. 559-68.

Paton, N.E., Backofen, W.A., *Trans. TMS-AIME*, 245(1969) 1369.

Paton, N.E., Backoffn, W.A., *Metallurgical Transactions*, 1A(1970) 2839.

Peters, M., Luetjering, G., *Titanium'80*, 1980, p 925.

Priester, L., *Materials Science and Engineering*, A309-310 (2001) 430.

Qazi, J.I., Senkov, O.N., Rahim, J., Genc, A., Froes, F.M., *Metallurgical and Materials Transactions A*, 32A (2001) 2453.

Rabinkin, A., Talianker, M., Botstein, O., *Metallurgical*, 29(1981) 691.

Regnier, P., Dupouy, J.M., *Physica status solidi*, 39(1970)79.

Rhodes, C.G., Paton, N.E., *Metallurgical Transactions*, 8A(1977) 1749.

Rhodes, C.G., Williams, J.C., *Metallurgical Transactions*, 6A(1975) 2103.

Rosenbaum, H.S., *Deformation twinning*, Gorden and Breach, New York, 1964, p. 43.

Rosi, F.D., Perkins, F.C., Seigle, L.L., *Trans. TMS-AIME*, 197(1953) 257.

Rudman, P.S., Trans. AIME, 233(1965) 864.

Silcock, J.M., Davis, M.H., Hardy, H.K., *A symposium, Monograph and Report Series No. 18*, p. 93, Inst. Of Metals, London (1956).

Spedding, F.H., Hanak, J.J., Daane, A.H., *J. Less common Metals*, 3(1961)110.

Sum. M., Jonas, J.J., *Textures Microstr.*, 31(1999) 187.

Tanabe, A., Nishimura, T., Fukuda, M., *Titanium'80*, 1980, p. 938.

Toth, L.S., Gilormini, P., Jonas, J.J., *Acta Metall.*, 36(12)(1988) 3077.

Welsch, G., Lutjering, G., Gazioglu, K., Bunk, W., *Metallurgical Transactions*, 8A(1977) 169.

Williams, J.C., Blackburn, M.J., *Metallurgical Transactions*, 60 (1967) 373.

Williams, J.C., Hickman, B., *Metallurgical Transactions*, 1(1970) 2648.

Williams, J.C., Sommer, A.W., Tung, P.P., *Metallurgical Transactions*, 3(1972) 2979.

Wittridge, N.J., Jonas, J.J., Root, J.H., *Metallurgical and Materials Transactions A*, 32A (2001) 889.

Zhi, Z.F., *Phys Status Solidi A* 130 (1): K19-K24 MAR 16 1992.